EIEлектротехніка і Eлектромеханіка

Electrical Engineering
& Electromechanics

Електричні машини та апарати
Електротехнічні комплекси та системи
Промислова електроніка
Теоретична електротехніка
Інженерна електрофізика.
   Техніка сильних електричних та магнітних полів

Electrical Engineering & Electromechanics

Scientific Journal was founded in 2002
Founder – National Technical University «Kharkiv Polytechnic Institute» (Kharkiv, Ukraine)

no. 6, 2024

Table of Contents

Y. Hakmi, H. Miloudi, M. Miloudi, A. Gourbi, M.H. Bermaki

Frequency experimental identification approach for single-phase induction motor common-mode parameters

Introduction. *The presence of broad-spectrum and high-amplitude electromagnetic interference (EMI) within a single-phase induction motor (SPIM) drive poses a significant threat to both the system and other electronic equipment. High-frequency (HF) models of electrical motors play a critical role in overcoming these challenges, as they are essential for characterizing electromagnetic compatibility (EMC) in drives and designing effective EMI filters.* ***The novelty*** *of this study proposes an enhanced HF motor model based on transfer functions (TFs) to accurately represent the motor's behavior at HFs for frequency-domain analyses in the range of 100 Hz to 30 MHz.* ***Purpose.*** *The equivalent HF model for a SPIM is discussed in this paper. The suggested equivalent circuit describes a motor's common-mode (CM) properties.* ***Methodology.*** *HF model was developed by a frequency-domain analysis utilizing an experimental setup and MATLAB software. The motor impedance analysis is based on the measurement of variations in motor characteristics as a function of frequency in the CM setup.* ***Originality.*** *TF has been tuned using an asymptotic identification method of Bode to match the behavior of the real impedances of the motor parameters as a function of the frequency in the CM configuration. This tuned TFs are then synthesized into a comprehensive wideband EMC equivalent circuit model using the Foster network technique, which can be then simulated in any Spice-based simulator tools.* ***Results.*** *The proposed mathematical model was employed to conduct simulations, and the resulting predictions were validated against experimental data. CM response of the EMC equivalent circuit at low, medium, and HFs were compared between simulations and experimental measurements using Lt-Spice simulator software.* ***Practical value.*** *It is observed that results show satisfactory agreement with the measurements over a large frequency bandwidth [100 Hz–30 MHz], and the equivalent model of SPIM can be cascaded with other electronic and electrical modules to form a complete single-phase electric drive system model for fast analysis and prediction of system level EMI and electromagnetic sensitivity.* References 37, table 5, figures 13.
Key words: **common-mode, electromagnetic compatibility, experimental impedance measurement, high frequency, single-phase induction motor.**

Вступ*. Наявність широкоспектральних та високоамплітудних електромагнітних перешкод (ЕМП) в однофазному асинхронному електродвигуні (ОАЕД) становить значну загрозу як для системи, так і для іншого електронного обладнання. Високочастотні (ВЧ) моделі електродвигунів відіграють вирішальну роль у подоланні цих проблем, оскільки вони необхідні для характеристики електромагнітної сумісності (ЕМС) у приводах та проєктування ефективних фільтрів ЕМП.* ***Новизна*** *цього дослідження полягає в тому, що пропонується вдосконалена модель ВЧ-двигуна на основі передатних функцій (ПФ) для точного представлення поведінки двигуна на ВЧ для аналізу частотної області в діапазоні від 100 Гц до 30 МГц.* ***Мета****. У статті обговорюється еквівалентна ВЧ-модель для ОАЕД. Запропонована еквівалентна схема описує властивості двигуна у синфазному режимі (СР).* ***Методологія****. ВЧ-модель була розроблена за допомогою аналізу у частотній області з використанням експериментальної установки та програмного забезпечення MATLAB. Аналіз імпедансу двигуна заснований на вимірюванні змін характеристик двигуна в залежності від частоти встановлення СР.* ***Оригінальність****. ПФ були налаштовані за допомогою асимптотичного методу ідентифікації Боде для відповідності поведінці реальних імпедансів параметрів двигуна залежно від частоти конфігурації СР. Надалі ці налаштовані ПФ синтезуються в комплексну модель еквівалентної схеми ЕМС з використанням методу мережі Фостера, яку потім можна моделювати в будь-яких інструментах симулятора на основі Spice.* ***Результати****. Запропонована математична модель використовувалася щодо моделювання, а отримані прогнози було перевірено з урахуванням експериментальних даних. Реакція СР еквівалентної схеми ЕМС на низьких, середніх та високих частотах порівнювалась між моделюванням та експериментальними вимірами з використанням програмного забезпечення симулятора Lt-Spice.* ***Практична цінність****. Результати показують задовільне співпадіння з вимірюваннями у значному діапазоні частот [100 Гц-30 МГц], а еквівалентна модель ОАЕД може бути каскадована з іншими електронними та електричними модулями для формування повної моделі однофазної системи електроприводу для швидкого аналізу та прогнозування ЕМП на рівні системи та електромагнітної чутливості. Бібл. 37, табл. 5, рис. 13.*
Ключові слова: **синфазний режим, електромагнітна сумісність, експериментальний вимір імпедансу, висока частота, однофазний асинхронний двигун.**

Abbreviations

CM	Common-Mode	PSCM	Permanent Split Capacitor Motor
EMC	Electromagnetic Compatibility	PWM	Pulse Width Modulation
EMI	Electromagnetic Interference	SPIM	Single-Phase Induction Motor
FEM	Finite Element Method	TF	Transfer Function
HF	High-Frequency		

Introduction. Electric motors account for more than 53 % of electricity consumption in developed nations and approximately 65 % in the industrial sector [1]. SPIMs boast efficiencies ranging from 30 % to 65 %, rendering them popular for low power applications [2]. SPIM drivers find applications in a wide range of equipment, including domestic and industrial settings, for controlling pumping operations [3], variable speed fans [4], compressors [5] and vehicle electric systems [6].

Using a variable frequency driver with SPIM (Fig. 1) offers numerous advantages in terms of speed control, energy efficiency, starting torque, noise and vibration [4]. This combination is finding increasing use in a wide range of applications [3–6].

Researchers are investigating diverse driving technologies to improve the performance and efficiency of SPIMs, prompted by concerns regarding operational costs and energy consumption [7, 8]. Adapting SPIM speed to loading conditions optimizes energy savings and system performance through PWM inverter control (Fig. 1). However, internal HF switching in PWM inverters induces significant voltage changes (dv/dt), causing serious CM EMI issues. These challenges have a substantial impact on the EMC of the system. SPIMs play a central role in amplifying these disturbances as they serve as the primary conduit for the propagation of CM currents.
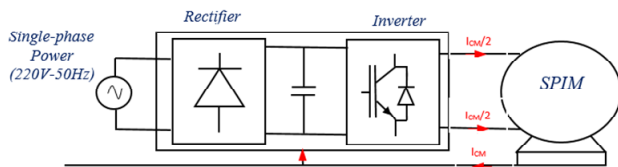
Fig. 1. Topology of SPIM driven by the single-phase inverter

Furthermore, the presence of CM voltage in the motor's output can give rise to various issues, including leakage current, shaft voltage, and bearing currents. These complications not only substantially reduce the life cycle of machines and drives but also have the potential to violate international EMI standards [9–12]. Therefore, responsible management of these technologies is crucial to both maximize the benefits and mitigate the risks associated with EMI.

Given the complexity of power generation and transmission in electric drive systems, conventional post processing methods relying on experience and experimentation are insufficient for precisely identifying and addressing EMC issues [13–15]. Therefore, establishing advanced system level EMI simulation, prediction, and optimization design methods is imperative during the early stages of SPIM driver development.

In this context, assessing CM impedance characteristics at HFs for the SPIM is crucial. The CM impedance of SPIMs significantly influences the magnitude of CM currents induced by the CM voltage of the inverter in SPIM drive systems. SPIMs contribute to CM currents due to their intrinsic asymmetry and the presence of parasitic capacitance and inductance inherent in their design. At HFs, these parasitic elements become more pronounced and can substantially affect the CM impedance of the motor. The impedance of these parasitic elements varies with frequency, resulting in complex networks and changes in the overall CM impedance of the motor. Understanding CM impedance up to 30 MHz is essential to ensure compliance with stringent EMC standards established by organizations like the International Special Committee on Radio Interference [16], which govern conducted EMI assessments across frequencies ranging from 150 kHz to 30 MHz.

Previous research on SPIMs has primarily concentrated on design optimization [8, 17], fault diagnosis [18, 19], and control methodologies [2, 4–7, 20], resulting in notable enhancements in SPIM performance and operational efficiency. However, there exists a notable gap in understanding the electromagnetic behavior of SPIMs from an EMC perspective. While some studies have explored EMC aspects, such as the work of [9], which focused on EMC characterization of capacitor start SPIMs using a HF model based on a genetic algorithm, further research is needed to address this gap. **This paper aims** to address this gap by introducing a pioneering study on the electromagnetic behavior of SPIMs with start capacitors from an EMC perspective. Through the development of a comprehensive HF model tailored specifically for start capacitor SPIMs based on motor port impedance characteristics, the objective is to investigate their electromagnetic characteristics, including CM impedance and propagation paths. By incorporating advanced simulation and predictive modeling techniques, this model enhances the electromagnetic environment of adjustable drive systems, enabling accurate investigation

and proactive resolution of EMI issues. Specifically, the model effectively addresses critical EMI concerns such as motor terminal overvoltage ringing and bearing discharge current, facilitating the design of effective dv/dt filters and improving overall EMC performance.

HF SPIM model. Researchers have proposed diverse EMI modeling approaches for various electrical machines, including three phase induction motors [21–28], DC motors [11, 29], and permanent magnet machines [12, 30–32]. These approaches fall into two main categories: FEM and measurement-based methods, a numerical technique, adeptly capture the intricate geometry and material characteristics of machines. Employed in the preliminary design phase, engineers use FEM to assess the impact of motor design choices on undesirable HF phenomena, establishing a 3D or 2D electromagnetic analysis that requires an understanding of the motor's geometric structure and electromagnetic parameters [12, 30, 31]. However, this method not only increases the workload for researchers, but also places limitations on the model's accuracy at higher frequencies.

In contrast, measurement-based methods rely on experimental data from impedance measurements, usually in common and differential modes, and involve a parameterization process. They provide higher accuracy than numerical models, do not require detailed motor geometry, and are well-suited for system level simulations predicting HF phenomena such as overvoltage and conducted emissions. The main types of measurement-based models are the physics-based circuits, and the behavioral or black-box models. Physics-based circuits use pre-defined equivalent circuit topologies with parameters that reflect the physical components of the machine to represent the real HF behavior of the machine. Some examples of physics-based circuit models can be found in [22, 23, 26, 29]. Although they have a rather low number of circuit elements and therefore low complexity, they need an extraction procedure to determine the unknown circuit parameters, and most of them are only validated up to 10 MHz. Black-box models adeptly represent dynamic behaviors, especially in HF resonances, accounting for complex internal structures and parasitic coupling in electrical machines. Rational functions achieve this by easily converting to equivalent electric circuits, accurately reproducing measured behaviors at terminals [14, 25, 27, 28, 33].

In [20] was presented a broadband equivalent circuit model for three phase AC motors using the vector fitting algorithm. Despite its high accuracy in capturing resonance behavior across a broad frequency range, the method's complexity in mathematical procedures may constrain its practical application.

In summary, previous relevant studies in EMC and HF electrical machine modeling have identified several limitations. These include:

1. A notable gap in HF modeling, particularly tailored for SPIM, despite facing analogous challenges to three phase motors.

2. The precision of existing modeling approaches relies heavily on the detailed internal structural features of the machine.

3. The proposed modeling methods face challenges in meeting EMI requirements, primarily because of constraints in effectively handling the required frequency ranges (150 kHz – 30 MHz).

Addressing the aforementioned issues, this paper proposes a measurement-based wide-frequency EMC model for the PSCM, treating the motor as a black box. The model accurately depicts CM characteristics from 100 Hz to 30 MHz, offering key analyses of EMI emission and coupling mechanisms in a single-phase electric drive system. A 175 W SPIM with PSCM is utilized as a case study. The CM port impedance, is mathematically fitted using Bode's asymptotic identification method. The resulting tuned TF is synthesized into an EMC equivalent circuit using the RLC Foster network.We validate the model's effectiveness and accuracy by comparing it with experimental results using the Lt-Spice simulator. Besides modeling the behavior of the PSCM, this article explores the influence of internal parameters on the EMC behavior of the motor. Crucially, it identifies dominant effects at specific frequencies. The analysis encompasses CM of dominant parasitic capacitances within the electric machine critical for understanding primary motor-to-ground CM pathways.

Key properties of the proposed model:

1. The model identification process is straightforward, achieving high accuracy by relying only on the impedance magnitude and phase angle of the structure's parasitic parameters, independent of motor manufacturer data.

2. The equivalent circuit model seamlessly integrates with other components to form complete electric drive system models, enabling thorough assessment of conducted emissions and ensuring EMC compliance. It accurately predicts stator winding overvoltage and bearing discharge current, facilitating optimal design of mitigation measures such as dv/dt filters.

3. The methodology is versatile and can be extended to each individual component in the drive system (e.g., cable, inverter), allowing its application across a wide range of motors.

The proposed method provides the capability to characterize the motor impedance over a wide frequency range, which is one of its key practical advantages. This enables designers to more effectively adjust the motor parameters to ensure optimal performance under varying operating conditions, a crucial necessity for many industrial and commercial applications such as pumping or ventilation. Given that variable speed drives operate at HF, it becomes imperative to find a HF model of the motor associated with the variable speed drive. This method thus allows for modeling the motor behavior under extreme conditions.

CM measurement setup for PSCM. SPIM, resembling the design of a three-phase motor, consists of a stator and a squirrel-cage rotor with two perpendicular windings: primary «running» and auxiliary «starting». Upon motor initiation, a centrifugal switch disconnects the auxiliary winding at around 75 % of the nominal speed [8, 20]. PSCM is a specialized variant known for its incorporation of a start split capacitor [2]. In this configuration, the auxiliary winding, and capacitor are connected in series, enhancing the motor's starting efficiency. The capacitor plays a crucial role in optimizing the initial startup process. Specific motor characteristics examined in this paper are detailed in Table 1.

The Wayne Kerr 6500B precision impedance analyzer for impedance analysis are used. This analyzer offers high resolution measurements from 100 Hz to 30 MHz, meeting the IEEE Std 112-2017 reliability requirements. With an impressive impedance accuracy of ±0.05 %.

Table 1
PSCM parameters

Rated voltage, V	Rated power, W	Rated current, A	Speed, rpm	Rated torque, N·m	Efficiency, %
230	<175	<1.5	1400	<4	87

To anticipate HF behavior, the impedance between the motor terminals and the housing was assessed using the configuration shown in Fig. 2. This approach provided insights into the CM characteristics of the tested PSCM.
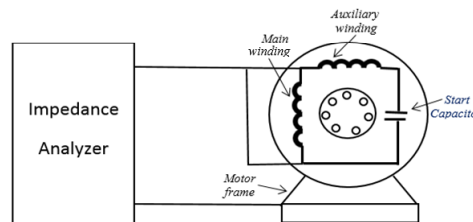
Fig. 2. CM test configuration

Figures 3, 4 show that this impedance starts to be capacitive due to the parasitic capacitance between the stator windings and the motor frame. Then, at medium frequency, the parasitic inductance becomes more dominant, so that the CM impedance drops at a certain frequency, and multiple peaks and drops can occur thereafter. However, at HFs, beyond the antiresonance frequency f_n, Z_{CM} demonstrates a weaker increase and exhibits inductive behavior.
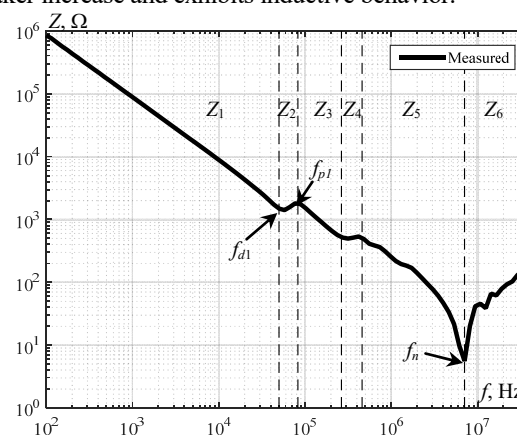
Fig. 3. CM impedance magnitude measurement
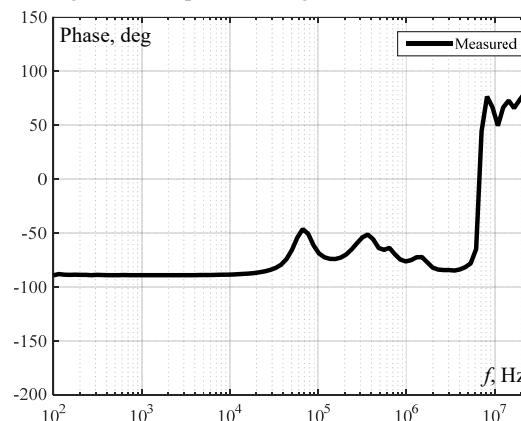
Fig. 4. CM impedance phase measurement

HF modeling of the CM impedance of the PSCM. The obtained measurement results facilitate the progression to the subsequent stage, where the TF is modeled. Specifically, Bode's asymptotic identification method is applied to model the magnitude and phase of the CM

impedance. The approach involves extracting the impedance TF for PSCM, utilizing the identification method. The modeling strategy is grounded in the observation that the overall magnitude curve of the impedance measurement undergoes a change in slope at each break frequency. Additional details about the method can be found in [34–36].

The modeling process involves the following succinct steps:

1. Identify break frequencies (pole and zero positions) from measured data, as depicted in Fig. 3.

2. Define the slopes of asymptotes and terms for the corresponding TF segments.

3. Derive the comprehensive system TF by multiplying the TFs at different frequencies.

From the characteristics of the magnitude depicted in Fig. 3, several break frequencies f_{d1}, f_{p2},..., f_n related to the poles and zero's locations have been exhibited. The asymptotic magnitude Bode plots of basic TFs terms are used to obtain the approximate plot for the real CM impedance.

Before the first dipping frequency f_{d1}, the magnitude curve decreases with a slope of -1, and the phase is $-90°$:

$$Z_1(s) = 1 / s, \qquad (1)$$

where s is the Laplace transform variable or complex frequency; $Z_1(s)$ is the TF of the pole at the origin.

At the first dipping and peaking frequencies (f_{d1} and f_{p2}) suggest the presence of 2nd-order systems (ξ_2 and ξ_3 are the damping ratios). The corresponding terms are calculated by:

$$Z_2(s) = \left[\left(\frac{1}{w_{n2}^2} \right) \cdot s^2 + \frac{2 \cdot \xi_2}{w_{n2}} \cdot s + 1 \right], \qquad (2)$$

where $Z_2(s)$ is the TF of a 2nd-order system; the undamped natural frequency w_{n2} is given by:

$$w_{n2} = 2 \cdot \pi \cdot f_{d1}, \qquad (3)$$

$Z_3(s)$ is for 2nd-order system with two poles:

$$Z_3(s) = \frac{1}{\left[\left(\frac{1}{w_{n3}^2} \right) \cdot s^2 + \frac{2 \cdot \xi_3}{w_{n3}} \cdot s + 1 \right]}, \qquad (4)$$

where the undamped natural frequency w_{n3} is given by:

$$w_{n3} = 2 \cdot \pi \cdot f_{p2}. \qquad (5)$$

Applying the same analysis to each pair of remaining dipping and peaking frequencies in the CM impedance measurement yields TFs at different frequencies. The complete TF is obtained by:

$$Z_{CM}(s) = Z_1(s) \cdot Z_2(s) \cdots Z_n(s). \qquad (6)$$

The estimated CM TF can be expressed as a ratio of two frequency-dependent polynomial representations:

$$Z_{CM}(s) = \frac{b_m \cdot s^m + b_{m-1} \cdot s^{m-1} + \cdots + b_1 \cdot s + b_0}{a_n \cdot s^n + a_{n-1} \cdot s^{n-1} + \cdots + a_1 \cdot s + a_0}, \qquad (7)$$

where a_n, $b_m \in \mathrm{Re}$ are the unknown polynomial coefficients; n is the order of the desired model.

The coefficients of the Z_{CM} TF are given in Table 2.

Table 2

Coefficients of the 5th-order TF

a_0	a_1	a_2	a_3	a_4	a_5
0	$9.322 \cdot 10^{20}$	$1.088 \cdot 10^{16}$	$1.844 \cdot 10^{11}$	$3.692 \cdot 10^5$	1

b_0	b_1	b_2	b_3	b_4	b_5	b_6
$8.245 \cdot 10^{28}$	$1.152 \cdot 10^{24}$	$2.756 \cdot 10^{19}$	$6.49 \cdot 10^{13}$	$2.491 \cdot 10^8$	6.849	$4.908 \cdot 10^6$

Figures 5, 6 display the frequency response of the estimated TF compared to the measurement curves. This comparison reveals the superposition of curves for both the magnitude and phase of the CM impedance from 100 Hz to 30 MHz, sufficiently confirming the validity of the modeling principle in the CM frequency range. To achieve a better approximation, introducing more poles and zeros into the TF is advisable. However, our primary aim is to obtain a less complex yet more physically accurate model.
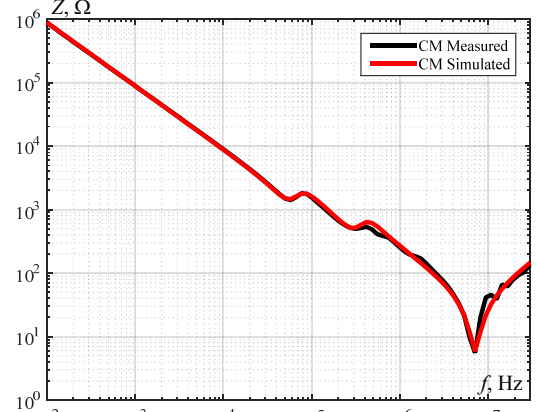
Fig. 5. Measured and simulated magnitudes of CM impedance
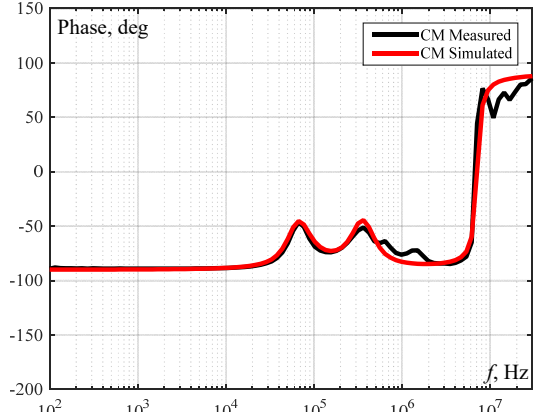
Fig. 6. Measured and simulated phases angle of CM impedance

Figure 7 shows the pole-zero distribution in the complex frequency plane. As we can see, all the poles of the polynomial function are located on the left half-plane, which gives us sufficient information about the stability of the system.
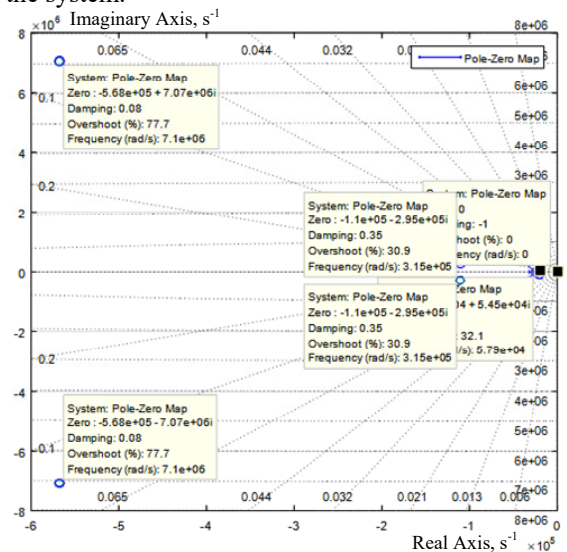
Fig. 7. Zero and pole locations of the CM impedance

Approach to get PSCM equivalent circuit. This section delves into the practical approach for the successful passive network synthesis of the TF of PSCM, utilizing the approximate Foster equivalent method. The goal is to propose a Spice-compatible equivalent circuit that accurately reproduces the frequency response of the CM impedance. To achieve this, a series of steps must be undertaken, starting with the expansion of the previously derived TF into a partial fraction representation, specifically pole-residue pairs. Subsequently, this representation is synthesized into a series of parallel combinations of resistance, inductance, and capacitance, as illustrated in Fig. 8, at which the subscripts r and c indicate the real and complex numbers and their orders are Nr and Nc for real and pair complex poles respectively.
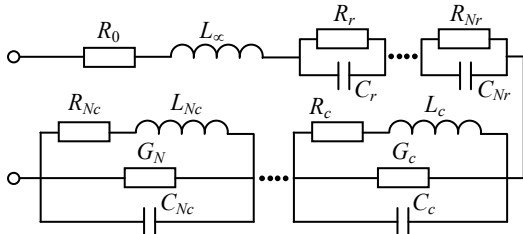
Fig. 8. Equivalent circuit synthesis for the Foster expansion of TF

Pole-residue formulation. The process of obtaining the partial fraction expansion of the CM TF (7) simply involves reexpressing the ratio of the polynomial representation into a sum of simpler positive real functions $Z_1(s), Z_2(s),\ldots, Z_n(s)$, as follows:

$$Z_{CM}(s) = \frac{\sum_{m=0}^{M} b_m \cdot s^m}{\sum_{n=0}^{N} a_n \cdot s^n} = d + e \cdot s + \sum_{n=1}^{N_r} \frac{r_{rn}}{s - p_{rn}} +$$

$$+ \sum_{n=1}^{N_c}\left(\frac{r_{cn}}{s - p_{cn}} + \frac{r_{cn}^*}{s - p_{cn}^*} \right); \tag{8}$$

where d is the real value constant; e is the s-proportional term; N_r, N_c are the numbers of real poles and complex conjugate pole pairs; p_{rn}, r_{rn} are the real poles and residues; p_{cn}, p_{cn}^*, r_{cn}, r_{cn}^* are the pairs of complex and conjugate poles and residues respectively.

Equivalent circuit synthesis. Converting the partial fraction expansion (8) into an equivalent circuit compatible with Spice [37]. Table 3 summarizes the synthesis methods for real-pole and complex-pole pair terms.

Table 3

The equivalent circuit synthesis of Z_{CM} TF

$Z(s)$	Equivalent circuit model	Parameters
$d + e \cdot s$		$R_0 = d$; $L_\infty = e$
$r_r/(s - p_r)$		$R_r = -r_r/p_r$; $C_r = 1/r_r$
$\dfrac{r_c}{s - p_c} + \dfrac{r_c^*}{s - p_c^*}$		$R_c = \dfrac{L_c(r_c p_c^* + r_c^* p_c)}{r_c + r_c^*}$ $L_c = \dfrac{r_c + r_c^*}{p_c p_c^* + \left[-(p_c^* + p_c) + \dfrac{r_c p_c^* + r_c^* p_c}{r_c + r_c^*} \right]\dfrac{r_c p_c^* + r_c^* p_c}{r_c + r_c^*}}$ $G_c = \dfrac{r_c + r_c^*}{-(p_c^* + p_c) + \dfrac{r_c p_c^* + r_c^* p_c}{r_c + r_c^*}}$ $C_c = 1/\left(r_c + r_c^*\right)$

A calculation was conducted to determine the values of the circuit components. The extracted poles and residues are presented in Table 4, while the synthesized component values for the equivalent circuit HF model of the PSCM – in Table 5.

Table 4

Poles and residues of the TF of Z_{CM}

$d = 5.03626$; $e = 4.90827 \cdot 10^{-6}$	
Poles p_i	Residues r_i
$p_r = 0$	$r_r = 5.5573 \cdot 10^8$
$p_c = -1.769 \cdot 10^5 \pm i \cdot 4.442 \cdot 10^5$	$r_c = 1.957e8 \pm i \cdot 3.537 \cdot 10^7$
$p_c = -9.831 \cdot 10^5 \pm i \cdot 2.321 \cdot 10^6$	$r_c = 3.002e8 \pm i \cdot 8.108 \cdot 10^7$

The frequency responses obtained from measurements and the equivalent circuit using the Lt-Spice simulator are compared in Fig. 9, 10.

Table 5

Component values of the equivalent circuit

$R_0 = 5.0362 \ \Omega$		$L_\infty = 7.8117 \cdot 10^{-7} \ \text{H}$	
Real branch no.		R_r, Ω	C_r, F
1		0	$1.7994 \cdot 10^{-9}$
Branch no.	L_c, H	R_c, Ω	C_c, F	G_c, S
1	$1.04 \cdot 10^{-4}$	37.01	$1.66 \cdot 10^{-9}$	3730
2	$1.92 \cdot 10^{-3}$	185.7	$2.55 \cdot 10^{-9}$	1522.4

As depicted in Fig. 9 and detailed in Table 5, the variation in CM impedance for PSCM with frequency is effectively represented by a series connection of the components: resistance R_0, inductance L_∞ and capacitance C_r. This model is particularly relevant in the frequency range of 100 Hz to 7 MHz, where C_r signifies the capacitive interaction between the stator windings and the

motor frame. Above 7 MHz, the predominantly inductive behavior is attributed to the inductance L_∞, wherein the main impact is observed in the internal and external feed lines of the motor. Simultaneously, resistance R_0 plays a crucial role in damping the resonance that results from the interaction between L_∞ and C_r. Two additional *R-L-C-G* branches are introduced, cascading with the previous components to capture further resonant phenomena. The first cell resonates at 80 kHz, while the second cell represents the resonance frequency at 446 kHz.
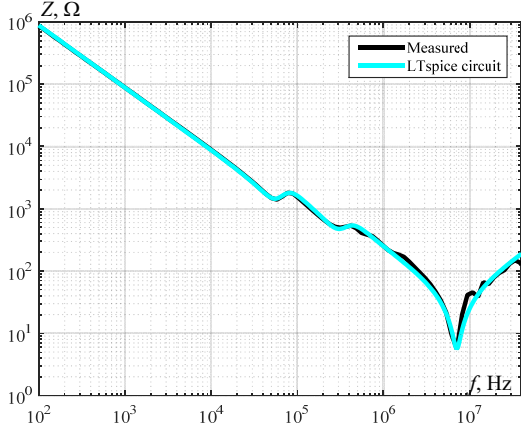
Fig. 9. Comparison of measurement and simulated magnitude of a Foster equivalent circuit for CM impedance
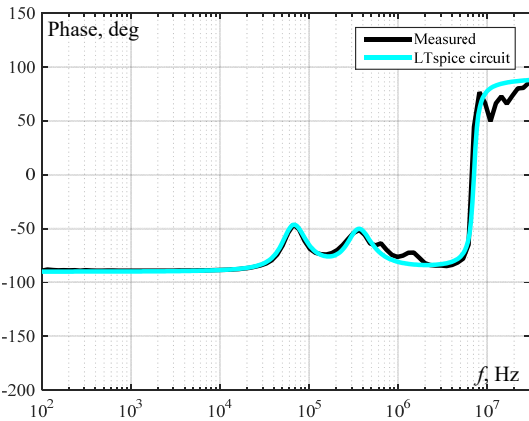
Fig. 10. Comparison of measurement and simulated phase of a Foster equivalent circuit for CM impedance

CM impedance analysis in PSCM based on motor parameters. Graphing impedance characteristics of the main winding Z_m, auxiliary winding Z_a and start capacitor Z_c in a CM up to 30 MHz offers insights into the frequency-dependent behavior of the SPIM. In Fig. 11 the measurement configurations for motor parameters are described, and the impedance frequency responses are presented in Fig. 12, 13. The measurement setup involves connecting the two probes of the precision impedance analyzer between the terminals of each parameter shorted together and the motor frame.

Initial impedance comparison observations reveal a decline in spectrum amplitudes with slopes of (–1) at low frequencies. The impedances of the CM Z_{CM}, main Z_m and auxiliary Z_a windings overlap, indicating capacitive behavior attributed primarily to parasitic capacitances between conductors and slot walls. Their impact is minimal at 100 Hz due to typically large impedance. However, as frequency increases, impedance decreases, promoting the circulation of CM current.
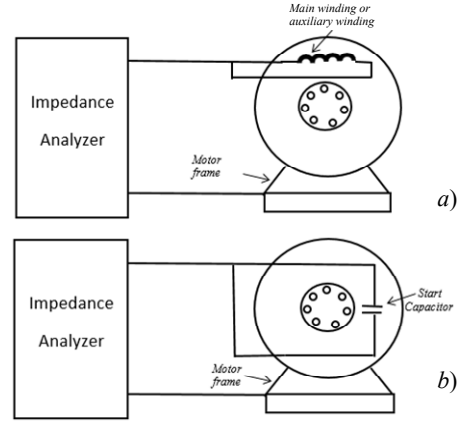
Fig. 11. Measurement setups of the main or auxiliary winding (*a*) and start capacitor (*b*)
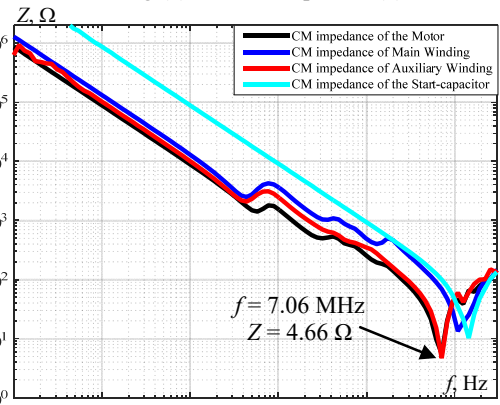
Fig. 12. Magnitude evolution of the PSCM parameters
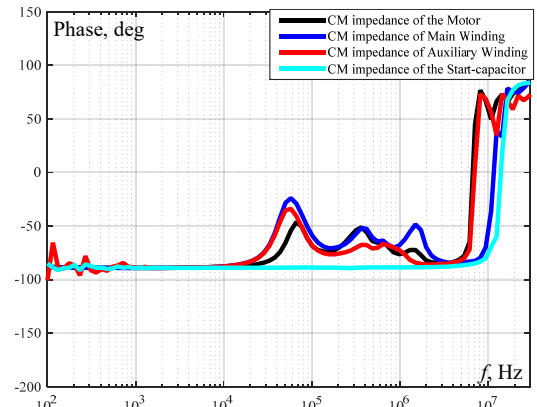
Fig. 13. Phase angle evolution of the PSCM parameters

In the medium-frequency range, interactions among inductive, resistive, and capacitive elements govern motor impedances, exhibiting multiple resonances and anti-resonances in the impedance modulus. This spectrum distribution highlights electromagnetic diversity within the motor. Results show a parallel trend in the number and shape of resonances between the CM impedance of PSCM and the main impedance, indicating the significant influence of dominant parasitic capacitances from the main winding. This profoundly impacts PSCM's CM impedance behavior, with parasitic capacitances in the main winding becoming the primary path for CM currents at specific frequencies.

At higher frequencies, impedances continue to decrease with slopes of (–1), signifying reduced impedance of parasitic capacitances and decreased CM current resistance. Results emphasize the significant impact of the auxiliary

winding on shaping the motor's CM impedance characteristics within this frequency range. This underscores the substantial influence of the auxiliary winding on the CM impedance of PSCM, with associated parasitic capacitances creating a low impedance route and establishing new current flow paths within the motor. Notably, at the antiresonance frequency of 7 MHz, the motor impedance is only 4.66 Ω, representing the lowest impedance path for CM leakage current across the frequency range. At this frequency, CM current through the auxiliary winding can be significant, posing a risk of stator winding failure. Therefore, careful consideration in EMC design is required to assess the current driven by the CM voltage of the voltage source inverter. Additionally, the start capacitor has no significant effect on total CM impedance, allowing its influence on the HF model to be neglected.

Understanding these paths is vital for assessing risks linked to CM current. CM noise circulation, driven by dominant parasitic capacitances at specific frequencies, poses threats to motor efficiency and interconnected equipment performance. Increased motor heating from CM current may lead to premature aging, while interference with control circuits can cause erratic behavior and reduced system reliability. To mitigate risks, consider strategies like filters, optimized grounding, and shielding.

This study examined the implications of modeling results for practical applications, such as environmental impact, potential effects of SPIM, and the mode of circulation of common currents in SPIMs. The models could be used to improve the electromagnetic environment of adjustable drive systems, thus ensuring optimal operation while avoiding EMC compatibility issues. Furthermore, these results could be used to develop a model for an adjustable drive system. On the other hand, by considering the model of the motor implanted in a variable speed drive system, researchers could identify conducted emissions generated by this system. Through simulation, engineers can quantify EMI noise amplitude and propagation paths within the system, including overvoltage amplitude and waveform. This requires developing an accurate HF model of key motor driving components, SPIM, cables, and inverters. Consequently, EMI reduction techniques can then be proposed based on such HF EMI models, minimizing interference risks and enhancing EMC of the system.

Conclusions. This paper introduces a practical method to model the common-mode impedance of permanent split capacitor motor across a wide range of frequencies relevant to conductive common-mode electromagnetic interference. Common-mode impedance for single-phase induction motor with 175 W has been measured, tested and utilized to synthesize the motor equivalent circuit. The simulated data closely aligns with the experimental data up to 30 MHz. The accuracy relies on the order of approximation. Moreover, the impact of each parameter of the permanent split capacitor motor on the common-mode impedance has been investigated in a wide frequency range. Results indicate that the auxiliary winding notably influences the main path of the high-frequency common-mode current, as this is the key for the electromagnetic compatibility optimization. The model is presented as Spice circuits, allowing for direct inclusion into a circuit model suitable for predicting terminal overvoltage and addressing electromagnetic interference issues.

Additionally, it can predict and address high-frequency problems and aid in designing electromagnetic interference filters to enhance electromagnetic compatibility in cable-fed motor-drive systems.

Conflict of interest. The authors of the article declare that there is no conflict of interest.

REFERENCES
1. Gómez J.R., Quispe E.C., Castrillón R. del P., Viego P.R. Identification of Technoeconomic Opportunities with the Use of Premium Efficiency Motors as Alternative for Developing Countries. *Energies*, 2020, vol. 13, no. 20, art. no. 5411. doi: https://doi.org/10.3390/en13205411.
2. Jannati M., Anbaran S.A., Asgari S.H., Goh W.Y., Monadi A., Aziz M.J.A., Idris N.R.N. A review on Variable Speed Control techniques for efficient control of Single-Phase Induction Motors: Evolution, classification, comparison. *Renewable and Sustainable Energy Reviews*, 2017, vol. 75, pp. 1306-1319. doi: https://doi.org/10.1016/j.rser.2016.11.115.
3. Bojang D., Nhantumbo E., Verma M., Kulkarni A. PV-Fed Single-Phase Induction Motor for Irrigation Application. *Journal of The Institution of Engineers (India): Series B*, 2024, vol. 105, no. 2, pp. 335-342. doi: https://doi.org/10.1007/s40031-023-00975-z.
4. Kiriella K.K.C.S., Karunadasa J.P., Rodrigo W.D.A.S. Design and Implementation of an Electronic Fan Regulator for Reduced Harmonics and Ripple Free Speed. *Engineer: Journal of the Institution of Engineers*, Sri Lanka, 2023, vol. 56, no. 4, pp. 13-22. doi: https://doi.org/10.4038/engineer.v56i4.7588.
5. Önceler A.A., Taşkin S. Modeling and analysis of single-phase induction motor drive for variable capacity control of a refrigerator compressor. *Sigma Journal of Engineering and Natural Sciences*, 2020, vol. 38, no. 3, pp. 1509-1526.
6. Rusdi M., Jayadi J., Mangera P., Ponadi A., Wakole P. Speed Control of Induction Motor Using Variable Frequency Driver (VFD) Method Based On Arduino Nano. *MATEC Web of Conferences*, 2022, vol. 372, art. no. 06001. doi: https://doi.org/10.1051/matecconf/202237206001.
7. Phurahong T. Design of 2-Leg Inverter for Controlling of A Single Phase Induction Motor. *2020 3rd International Conference on Power and Energy Applications (ICPEA)*, 2020, pp. 117-120. doi: https://doi.org/10.1109/ICPEA49807.2020.9280147.
8. Rahman S., Meraj M., Iqbal A., Tariq M., Maswood A.I., Ben-Brahim L., Al-ammari R. Design and Implementation of Cascaded Multilevel qZSI Powered Single-Phase Induction Motor for Isolated Grid Water Pump Application. *IEEE Transactions on Industry Applications*, 2020, vol. 56, no. 2, pp. 1907-1917. doi: https://doi.org/10.1109/TIA.2019.2959734.
9. Miloudi H., Miloudi M., Ardjoun S.A.E.M., Mahmoud M.M., Telba A.A., Denaï M., Khaled U., Ewais A.M. Electromagnetic Compatibility Characterization of Start-Capacitor Single-Phase Induction Motor. *IEEE Access*, 2024, vol. 12, pp. 2313-2326. doi: https://doi.org/10.1109/ACCESS.2023.3349018.
10. Zeghoudi A., Slimani H., Bendaoud A., Benazza B., Bechekir S., Miloudi H. Measurement and analysis of common and differential modes conducted emissions generated by an AC/DC converter. *Electrical Engineering & Electromechanics*, 2022, no. 4, pp. 63-67. doi: https://doi.org/10.20998/2074-272X.2022.4.09.
11. Bermaki D.M.H., Miloudi D.H., Miloudi D.M., Gourbi D.A., Bendaoud P.D.A. High-frequency Differential Mode Modeling of Universal Motor's Windings. *International Journal of Electrical and Electronics Research*, 2023, vol. 11, no. 4, pp. 1057-1064. doi: https://doi.org/10.37391/ijeer.110425.
12. Ruiz-Sarrio J.E., Chauvicourt F., Gyselinck J., Martis C. Impedance Modeling Oriented Toward the Early Prediction of High-Frequency Response for Permanent Magnet Synchronous Machines. *IEEE Transactions on Industrial Electronics*, 2023, vol. 70, no. 5, pp. 4548-4557. doi: https://doi.org/10.1109/TIE.2022.3189075.
13. Zheng F., Wang A., Wu Z., Gao T., Wang Z., Zhao X. Capacitor Tolerance Criterion for Three-Phase EMI Filters to Attenuate Noise of PWM Inverters. *IEEE Transactions on Power Electronics*, 2021, vol. 36, no. 8, pp. 9080-9092. doi: https://doi.org/10.1109/TPEL.2020.3048272.
14. Xiong Y., Li X., Zhou W., Li N., Jiao M., Li Y., Du X., Nie X., Ji X. Broadband Electromagnetic Compatibility Modeling for Three-Phase

Synchronous Motor of Armored Vehicle. *Acta Armamentarii*, 2022, vol. 43, no. 7. pp. 1467-1477. doi: https://doi.org/10.12382/bgxb.2021.0387.

15. Han D., Li S., Wu Y., Choi W., Sarlioglu B. Comparative Analysis on Conducted CM EMI Emission of Motor Drives: WBG Versus Si Devices. *IEEE Transactions on Industrial Electronics*, 2017, vol. 64, no. 10, pp. 8353-8363. doi: https://doi.org/10.1109/TIE.2017.2681968.

16. CISPR 22. *Information technology equipment – Radio disturbance characteristics – Limits and methods of measurement*. Edtion 6.0, August 2008.

17. Sharma U., Singh B. Improved Design for High Efficiency of Single-Phase Induction Motor for Industrial Exhaust Fan. *2021 IEEE 4th International Conference on Computing, Power and Communication Technologies (GUCON)*, 2021, pp. 1-5. doi: https://doi.org/10.1109/GUCON50781.2021.9573780.

18. Ganguly B., Chatterjee A., Chatterjee A., Paul S. Diagnosis of Stator Winding Fault of Single-Phase Induction Motor Employing Wavelet Induced Residual-Convolutional Neural Network. *2020 IEEE International Conference on Power Electronics, Drives and Energy Systems (PEDES)*, 2020, pp. 1-5. doi: https://doi.org/10.1109/PEDES49360.2020.9379665.

19. Alviento E.V., Cabais J.B., Fajardo J.M.M., Garcia R.G., Ballado A.H. Early Detection of Single-Phase Induction Motor Failure through the use of Accelerometer and Temperature Sensor via Arduino. *2021 IEEE 17th International Colloquium on Signal Processing & Its Applications (CSPA)*, 2021, pp. 64-69. doi: https://doi.org/10.1109/CSPA52141.2021.9377285.

20. Golsorkhi M.S., Binandeh H., Savaghebi M. Online Efficiency Optimization and Speed Sensorless Control of Single-Phase Induction Motors. *Applied Sciences*, 2021, vol. 11, no. 19, art. no. 8863. doi: https://doi.org/10.3390/app11198863.

21. Miloudi H., Miloudi M., Gourbi A., Bermaki M.H., Bendaoud A., Zeghoudi A. A high-frequency modeling of AC motor in a frequency range from 40 Hz to 110 MHz. *Electrical Engineering & Electromechanics*, 2022, no. 6, pp. 3-7. doi: https://doi.org/10.20998/2074-272X.2022.6.01.

22. Zhao Z., Fan F., Sun Q., Jie H., Shu Z., Wang W., See K.Y. Physics Informed Neural Network-based High-frequency Modeling of Induction Motors. *Chinese Journal of Electrical Engineering*, 2022, vol. 8, no. 4, pp. 30-38. doi: https://doi.org/10.23919/CJEE.2022.000036.

23. Zhao Z., Fan F., Sun Q., Tu P., See K.Y. High-Frequency Modeling of Induction Motor Using Multilayer Perceptron. *2022 Asia-Pacific International Symposium on Electromagnetic Compatibility (APEMC)*, 2022, pp. 222-224. doi: https://doi.org/10.1109/APEMC53576.2022.9888414.

24. Karakasli V., Ye Q., Griepentrog G., Wei J. A Parameterization of 6-Port High-Frequency Delta- and Star-Connected Induction Motor Model. *2020 International Symposium on Electromagnetic Compatibility - EMC EUROPE*, 2020, pp. 1-6. doi: https://doi.org/10.1109/EMCEUROPE48519.2020.9245646.

25. Li L., He W., Wang Y., Li X. Modelling of the wide frequency equivalent circuit of the three-phase AC motor based on vector fitting method. *International Journal of Electric and Hybrid Vehicles*, 2019, vol. 11, no. 1, pp. 12-22. doi: https://doi.org/10.1504/IJEHV.2019.098722.

26. Toulabi M.S., Wang L., Bieber L., Filizadeh S., Jatskevich J. A Universal High-Frequency Induction Machine Model and Characterization Method for Arbitrary Stator Winding Connections. *IEEE Transactions on Energy Conversion*, 2019, vol. 34, no. 3, pp. 1164-1177. doi: https://doi.org/10.1109/TEC.2019.2891349.

27. Jia K., Bohlin G., Enohnyaket M., Thottappillil R. Modelling an AC motor with high accuracy in a wide frequency range. *IET Electric Power Applications*, 2013, vol. 7, no. 2, pp. 116-122. doi: https://doi.org/10.1049/iet-epa.2012.0127.

28. Idir N., Weens Y., Moreau M., Franchaud J.J. High-Frequency Behavior Models of AC Motors. *IEEE Transactions on Magnetics*, 2009, vol. 45, no. 1, pp. 133-138. doi: https://doi.org/10.1109/TMAG.2008.2006006.

29. Liu J., Wang X., Nan J. Application of Ant Colony Algorithm to the Analysis of Common Mode EMI Model of DC Motor. *Energy and Power Engineering*, 2011, vol. 3, no. 2, pp. 96-106. doi: https://doi.org/10.4236/epe.2011.32013.

30. Ruiz-Sarrio J.E., Chauvicourt F., Gyselinck J., Martis C. High-Frequency Modelling of Electrical Machine Windings Using Numerical Methods. *2021 IEEE International Electric Machines & Drives Conference (IEMDC)*, 2021, pp. 1-7. doi: https://doi.org/10.1109/IEMDC47953.2021.9449561.

31. Rahimi A., Kanzi K. Improved High-Frequency Modeling of PMSM Using 3-D Finite Element Analysis. *2019 International Power System Conference (PSC)*, 2019, pp. 71-78. doi: https://doi.org/10.1109/PSC49016.2019.9081510.

32. Zhang D., Kong L., Wen X. A measurement based modeling method of interior permanent magnet motor considering the rotor position for EMI analysis. *2014 IEEE Conference and Expo Transportation Electrification Asia-Pacific (ITEC Asia-Pacific)*, 2014, pp. 1-6. doi: https://doi.org/10.1109/ITEC-AP.2014.6941033.

33. Stevanovic I., Wunsch B., Skibin S. Behavioral high-frequency modeling of electrical motors. *2013 Twenty-Eighth Annual IEEE Applied Power Electronics Conference and Exposition (APEC)*, 2013, pp. 2547-2550. doi: https://doi.org/10.1109/APEC.2013.6520654.

34. Thomas R.E., Rosa A.J., Toussaint G.J. *The Analysis and Design of Linear Circuits*. John Wiley & Sons, 2011. 928 p.

35. Nise N.S. *Control Systems Engineering*. Wiley Publ., 2015. 944 p.

36. Miloudi H., Bendaoud A., Miloudi M., Dickmann S., Schenke S. A novel method of transfer-function identification for modeling DM impedance of AC motor. *2017 International Symposium on Electromagnetic Compatibility - EMC EUROPE*, 2017, pp. 1-5. doi: https://doi.org/10.1109/EMCEurope.2017.8094770.

37. Antonini G. Spice equivalent circuits of frequency-domain responses. *IEEE Transactions on Electromagnetic Compatibility*, 2003, vol. 45, no. 3, pp. 502-512. doi: https://doi.org/10.1109/TEMC.2003.815528.

Yassine Hakmi[1]*, PhD,*
Houcine Miloudi[1]*, Professor,*
Mohamed Miloudi[2]*, Lecturer,*
Abdelkader Gourbi[3]*, Lecturer,*
Mohammed Hamza Bermaki[1]*, Lecturer,*
[1] Djillali Liabes University, Algeria,
e-mail: yassine.hakmi@univ-sba.dz (Corresponding Author);
el.houcine@yahoo.fr;   bermaki.hamza@gmail.com
[2] Relizane University, Algeria,
e-mail: mohamed.miloudi@univ-relizane.dz
[3] Ahmed Ben Bella University, Algeria,
e-mail: aekett@yahoo.fr

R. Araria, M.B. Guemmour, K. Negadi, A. Berkani, F. Marignetti, M. Bey

Design and evaluation of a hybrid offshore wave energy converter and floating photovoltaic system for the region of Oran, Algeria

Introduction. *This paper presents **the novel** design and analysis of a hybrid renewable energy system that combines a wave energy converter (WEC) with a floating photovoltaic (FPV) system for offshore installation, with a specific focus on Oran as a case study. The purpose of integrating these two technologies is to harness both wave and solar energy, thereby maximizing energy output and enhancing the reliability of renewable energy sources in offshore environments.* ***The goal*** *of this study is to develop a hybrid system that leverages the complementary nature of WEC and FPV technologies to maximize energy output and improve reliability. By integrating these technologies, the system aims to overcome the limitations of standalone energy systems.* ***The methodology*** *includes selecting suitable WEC and FPV technologies, optimizing their configurations, and analyzing their combined performance under various environmental conditions. To assess the energy production potential, structural stability, and economic feasibility of the hybrid system, computational simulations and data analysis are employed. This comprehensive approach ensures rigorous testing and optimization for real-world applications.* ***The results*** *demonstrate substantial improvements in energy yield and system resilience compared to standalone WEC or FPV systems. The hybrid system shows enhanced performance, particularly in consistent energy output and structural robustness. These findings indicate that combining WEC and FPV technologies can lead to more reliable and efficient offshore renewable energy solutions.* ***The practical values*** *are significant, providing insights into efficient and sustainable offshore renewable energy solutions. By focusing on Oran, it offers a localized perspective that can be adapted to similar coastal areas globally, contributing to the advancement of renewable energy technologies. The hybrid system's enhanced reliability and efficiency support the broader goal of sustainable energy development in marine environments, highlighting its potential for widespread application and impact.* References 23, tables 4, figures 17.
Key words: **wave energy converter, maximum power point tracking, hybrid system, floating photovoltaic system.**

Вступ*. У статті представлено нову конструкцію та аналіз гібридної системи відновлюваної енергії, яка поєднує в собі перетворювач хвильової енергії (WEC) з плавучою фотоелектричною (FPV) системою для морської установки, з особливим акцентом на регіоні Оран як тематичному дослідженні. Призначенням інтеграції цих двох технологій є використання хвильової та сонячної енергії, таким чином максимізуючи вихід енергії та підвищуючи надійність відновлюваних джерел енергії в морському середовищі.* ***Метою*** *цього дослідження є розробка гібридної системи, яка використовує взаємодоповнюючий характер технологій WEC і FPV для максимізації виходу енергії та підвищення надійності. Інтегруючи ці технології, система має на меті подолати обмеження автономних енергетичних систем.* ***Методологія*** *включає в себе вибір відповідних технологій WEC і FPV, оптимізацію їх конфігурацій і аналіз їх спільної продуктивності в різних умовах навколишнього середовища. Для оцінки потенціалу виробництва енергії, структурної стабільності та економічної доцільності гібридної системи використовується обчислювальне моделювання та аналіз даних. Цей комплексний підхід забезпечує ретельне тестування та оптимізацію для реальних застосувань.* ***Результати*** *демонструють суттєві покращення у виході енергії та стійкості системи порівняно з автономними системами WEC або FPV. Гібридна система демонструє покращену продуктивність, зокрема стабільну вихідну енергію та міцність конструкції. Ці висновки вказують на те, що поєднання технологій WEC і FPV може призвести до більш надійних і ефективних рішень для морських відновлюваних джерел енергії.* ***Практичні значення*** *є значними, що дають змогу зрозуміти ефективні та стійкі рішення для відновлюваних джерел енергії в морських умовах. Зосереджуючись на Орані, пропонується локальна перспектива, яку можна адаптувати до подібних прибережних районів у всьому світі, сприяючи розвитку технологій відновлюваної енергії. Підвищена надійність і ефективність гібридної системи підтримує більш широку мету сталого енергетичного розвитку в морському середовищі, підкреслюючи її потенціал для широкого застосування та впливу.* Бібл. 23, табл. 4, рис. 17.
Ключові слова: **перетворювач енергії хвиль, відстеження точки максимальної потужності, гібридна система, плавуча фотоелектрична система.**

Introduction. This paper presents the design and analysis of a hybrid renewable energy system combining a wave energy converter (WEC) and a floating photovoltaic (FPV) system for offshore installation, specifically focusing on Oran, Algeria as a case study. The integration of these two technologies aims to harness both wave and solar energy, maximizing the energy output and improving the reliability of renewable energy sources in offshore environments [1]. The design process involves the selection of suitable WEC and FPV technologies, optimization of their configurations, and analysis of their combined performance under varying environmental conditions [2]. Computational simulations and experimental data are utilized to assess the energy production potential, structural stability, and economic feasibility of the hybrid system. Results indicate significant improvements in energy yield and system resilience compared to standalone WEC or FPV systems. The findings provide valuable insights into the development of efficient and sustainable offshore renewable energy solutions, contributing to the advancement of hybrid energy systems for coastal regions [3].

The control and the power management of hybrid power generation systems involves sophisticated strategies to ensure seamless integration of diverse energy sources such as solar, wind, and energy storage with the electric grid. Centralized, decentralized, and hierarchical control methods are deployed to balance efficiency, reliability, and scalability. Advanced energy management systems, leveraging artificial intelligence and machine learning, optimize power flows and storage utilization, enhancing overall system performance [4]. Load forecasting and demand response techniques play a pivotal role in maintaining grid stability by adjusting loads based on generation availability. Additionally, peak shaving and load leveling techniques help in managing demand and reducing grid strain.

Compliance with interconnection standards is essential to ensure safety, reliability, and interoperability of hybrid systems with the grid. These systems can also provide ancillary services like voltage regulation, frequency control, and reactive power support,

contributing to grid resilience. Case studies demonstrate successful applications of hybrid systems in various settings, from island communities to industrial plants, highlighting their versatility and benefits. Current research is focused on improving control algorithms, power electronics, and integrating emerging technologies such as block chain and advanced data analytics to enhance system reliability and transparency.

The goal of the paper is to develop a comprehensive hybrid renewable energy system combining wave energy and floating solar panels. The study aims to optimize the design for effective offshore deployment, considering the unique environmental and oceanographic conditions of Oran. By analyzing the performance and integration of these technologies, the paper seeks to enhance energy efficiency and sustainability. The ultimate objective is to provide a viable solution for clean energy generation in coastal regions, contributing to the reduction of carbon emissions. The case study of Oran serves as a practical example to validate the system's feasibility and potential benefits.

Subject of investigations. This paper involves a comprehensive exploration of integrating WECs with FPV systems for offshore energy production. The research delves into the design and engineering aspects, assessing the structural and functional synergy between these renewable energy technologies. Key investigations include analyzing the performance, efficiency, and durability of the hybrid system under the specific marine conditions of Oran. Additionally, the study examines the economic viability and environmental impact of deploying such a system offshore. The goal is to identify the potential benefits and challenges, providing insights for future applications in similar coastal regions.

Designs of hybrid FPV-WEC technologies. Hybrid projects combining floating solar panels and WECs have the technological capacity to produce a large portion of the world's annual electricity [5, 6]. This hybrid solution is particularly suitable for countries with abundant wave energy resources. Developers can utilize existing infrastructure, such as transmission lines, if the floating solar farm is built near WECs. An innovative technology using floating solar with battery storage and wave energy was proposed for coastal regions. The intermittent floating solar resource is integrated with a battery energy storage system to meet peak demands. Colocation with WECs will help to boost the generation of such assets and smooth out the generation curve. The addition of a floating solar system near a WEC compensates for the unstable generation of these systems by adjusting wave energy production, while PV systems can compensate for the wave energy shortfall in the medium to long term [7]. This hybrid FPV-wave energy system is flexible and complementary. A schematic of a hybrid FPV-WEC system is shown in Fig. 1.
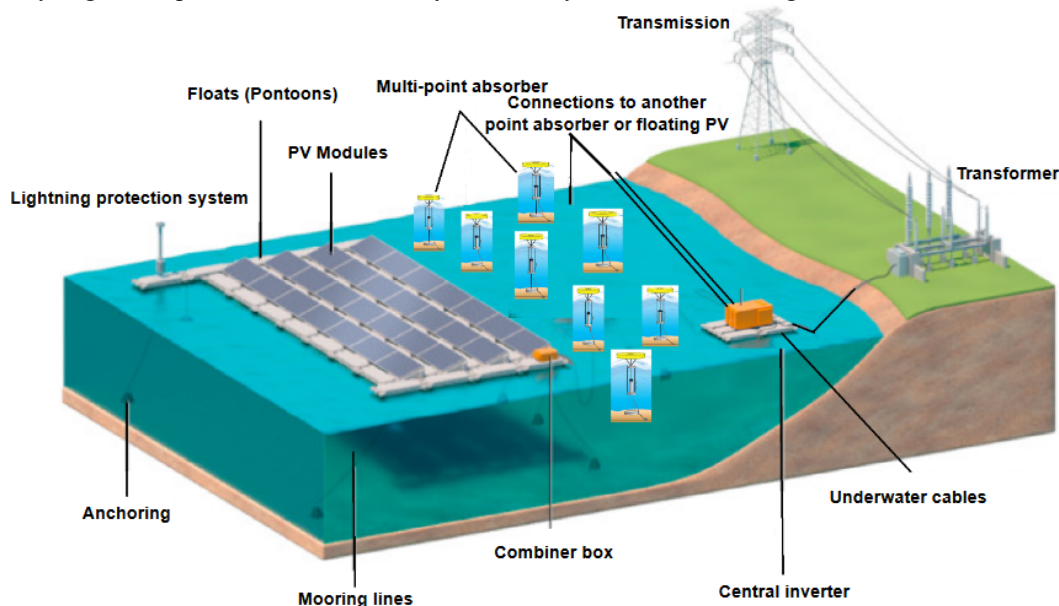
Fig. 1. Illustration of a hybrid FPV and WEC system

Study region, data and wave models. The study concentrated on the area with the highest wave energy potential in Algeria, specifically the northwest coast in the Oran region. Figure 2 of the map highlights the Oran region in Algeria, identified for its high wave energy potential and favorable solar conditions. This strategic location is ideal for installing a hybrid station combining FPV panels and WEC. The hybrid system aims to harness both solar and wave energy to provide a reliable and sustainable power supply to the Oran region. The map illustrates the targeted area for exploitation, showcasing the geographical advantages that make Oran a prime candidate for this innovative energy solution.

Table 1 provides comprehensive information about the Mediterranean coasts of Oran, detailing the potential for installing FPV systems and utilizing wave energy in this region. It includes key metrics such as average solar irradiance and wave energy density, highlighting the dual renewable energy resources available. The table also outlines suitable coastal areas for FPV installation, considering factors like water depth and proximity to the shore. Seasonal data on wave heights and periods further emphasize the region's capacity for wave energy exploitation.

This combination of solar and wave energy data underscores the feasibility of developing a hybrid renewable energy system in Oran to ensure a sustainable and efficient power supply.

Fig. 2. Map of potential deployment sites in the region of Oran

Table 1
Potential for wave energy utilization in the region of Oran

Parameters	Values
Average wave height, m	1.5-2.5
Wave period, s	5-7
Peak sun hours, h/day	5
Distance from shore (FPV), m	500
Distance from shore (WEC), km	1-5
Surface area available, km^2	≈ 20
Wave energy flux, kW/m	10-20
Water depth, m	20-50
Seabed conditions	Sandy to rocky
Environmental impact	Low to moderate
Proximity to grid, km	5-10
Accessibility	Good
Number of WEC units	10
Grid connection proximity, km	5
CO_2 emissions avoided, tons/year	80000

Hydrodynamics modelling of multi-point absorber. One kind of WEC that uses energy from ocean waves is a point absorber. A point absorber is modeled from both an electrical and hydrodynamic perspective. The following are the essential formulas for point absorber modeling. To illustrate the idea and layout of a WEC, a simple sketch might be utilized. The primary purpose of a WEC is to convert the kinetic and potential energy of waves in the ocean into electrical power that can be used [8, 9]. In the sketch, you might illustrate how a buoyant building rises and falls in response to the passing waves. Figure 3 serves as a typical illustration of a self-reacting point absorber, showcasing how the device efficiently harnesses ocean wave energy for power generation.

Fig. 3. OPT © power buoy device serves as a typical illustration of a self-reacting point absorber [10]

This buoy is connected to a mechanical linkage that, as shown in Fig. 4, transforms the vertical motion into mechanical motion. This mechanical linkage is often in the form of a piston or hydraulic system. Since WEC hydrodynamic modeling is the subject of numerous research, this paper only offers a general review of point absorber hydrodynamic modeling [11].
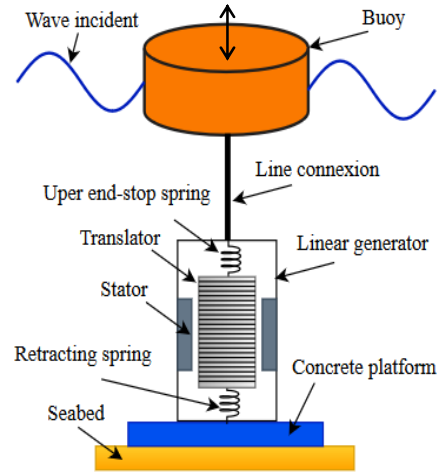
Fig. 4. Concept and layout of the WEC in a sketch

Wave equation. The incoming wave motion affects the point absorber's motion. Equation (1) from linear wave theory can be used to characterize the wave elevation [12]. Figure 5 depicts a smooth, periodic oscillation pattern representing a sinusoidal wave, characterized by its consistent amplitude and wavelength:

$$\eta(x,t) = A\cos(kx - \omega t), \qquad (1)$$

where η is the free surface elevation with respect to $z = 0$ (m); A is the amplitude of the wave (m); k is the number of wave (rad/m); ω is the frequency of angular motion (rad/s); x is the horizontal position (m); t is time (s).
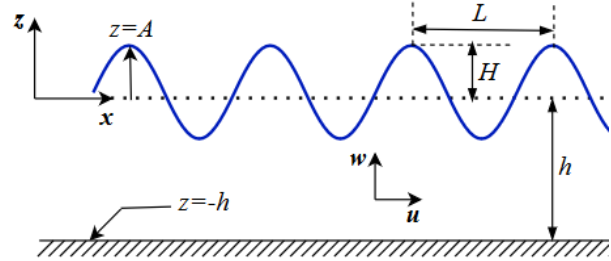
Fig. 5. Sinusoidal incidence wave form

Particle velocity. The particle velocity of the water particles beneath the absorber is given by:

$$u(x,t) = \frac{A\omega}{k}\sin(kx - \omega t). \qquad (2)$$

This velocity is important for estimating the kinetic energy of the incident waves.

Buoyancy force. The buoyancy force acting on the point absorber can be calculated using Archimedes' principle [13]:

$$F_b = \rho_\omega g V, \qquad (3)$$

where F_b is the force of buoyancy (N); ρ_ω is the water's density (kg/m^3); g is the acceleration brought on by gravity (m/s^2); V is the volume that the point absorber has displaced (m^3).

Power capture. The electrical power captured by the point absorber can be calculated as [14]:

$$P_e = \frac{1}{2} \rho_\omega g V H_s C_d v^3 P_g, \qquad (4)$$

where P_e is the output of electrical power (W); H_s is the noteworthy wave height (m); C_d the coefficient of power capture; v is the difference in velocity between the waves and the absorber (m/s); P_g is the effectiveness of the generator.

To investigate the nonlinear effects of the device, time domain models are required. All the forces acting on a wave energy device are captured by (5), without going into detail about how they interact.

Then, considering a floating body that is just limited in heave motion, Newton's second law is considered. It says that the total force of the body, or F_{net}, is equal to the mass times the translational acceleration (the same laws apply to moments, which are not discussed here):

$$F_{net} = m \frac{d^2 z(t)}{dt^2} = F_g(t) + F_{FK}(t) + F_{rad}(t) + \\ + F_{res}(t) + F_{PTO}(t) + F_{spring}(t) + F_{add}(t), \qquad (5)$$

where F_{net} is the total force exerted on the buoy (N); m is the point absorber's mass (kg); $z(t)$ relates to the point absorber's vertical movement over time (m); $F_g(t)$ is the force of gravity (N); $F_{FK}(t)$ is the force of Froude-Krylov (N); $F_{rad}(t)$ is the force of radiation (N); $F_{res}(t)$ is the force of viscosity (N); $F_{PTO}(t)$ is the power take-off (PTO) force (N); $F_{spring}(t)$ is the force of mooring (N); $F_{add}(t)$ is the additional force (N); F_{add} is another force operating on the structure, such as drift, wind, tidal, or other body-water interactions.

Gravity force. The gravitational force exerted on the point absorber:

$$F_g(t) = -mg. \qquad (6)$$

Froude-Krylov force. The hydrodynamic force due to the motion of the point absorber. It depends on the acceleration of the point absorber:

$$F_{FK} = -m \frac{d^2 z(t)}{dt^2}. \qquad (7)$$

Radiation force. The force brought on by the waves that the point absorber's motion radiated. It is also dependent on the velocity of the absorber. The radiation force F_{rad} depletes the system's energy, as was previously stated. Since of this, F_{rad} is proportional to the floater's velocity in the following manner since it is functioning as a damper [15]:

$$F_{rad}(t) = -b \frac{dz(t)}{dt}, \qquad (8)$$

where b is the radiation damping coefficient (kg/s); $dz(t)/dt$ is the first time derivative of the vertical displacement of the buoy, i.e. the velocity (m/s).

The restoring force F_{res} according to Archimedes' law of buoyancy, is taken proportional to the vertical displacement of the buoy according to:

$$F_{res}(t) = -cz(t), \qquad (9)$$

where c is the coefficient of restoration (kg/s^2); z is the buoy's vertical displacement (m).

Power take-off (PTO) force. The force produced by the PTO system, which uses the point absorber's motion to extract energy. These forces, like the PTO damping force F_{PTO}, radiation force F_{rad}, mechanical spring force F_{spring} and restorative force F_{res} are produced by:

$$F_{spring}(t) = -k_{SP} z(t); \qquad (10)$$

$$F_{PTO}(t) = -\beta \frac{dz(t)}{dt}, \qquad (11)$$

where k_{sp} is the spring coefficient in mechanical terms (kg/s^2); β is the damping coefficient of the PTO (kg/s).

Additional force. Any other forces – like drift, wind, tidal forces, or other body-water interactions – that can have an impact on the point absorber. As implied by its name, the additional mass force F_{add} acts in addition to the buoy's absolute mass. As a result, it is assumed to be proportionate to the floater's acceleration as:

$$F_{add}(t) = -a \frac{d^2 z(t)}{dt^2}, \qquad (12)$$

where a is the mass coefficient added (kg); $d^2 z(t)/dt^2$ is the acceleration (m/s^2), or the second time derivative of the buoy's vertical displacement $z(t)$.

Gaining insight into the behavior and energy conversion efficiency of the point absorber can be achieved by solving (5) of motion using suitable numerical techniques while taking into account the unique features and design of the device.

Modeling of the PV array. Many similar circuits have been devised thus far to simulate solar cells. Generally speaking, they can be divided into two main categories: single- and two-diode. The single diode model (Fig. 6) is one of the most widely used equivalent circuits for PV cells [16].
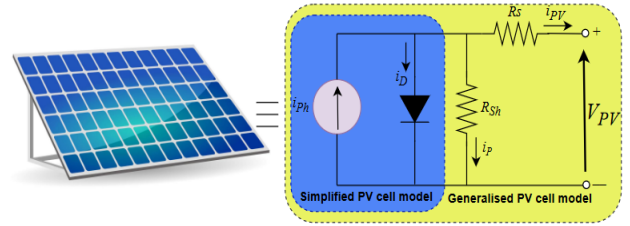
Fig. 6. The equivalent circuit of a PV cell

The PV current i_{Ph}, diode current i_D, series resistance R_S, parallel resistance R_{Sh} and net cell current i_{PV} are shown in Fig. 6. When the equivalent circuit of the PV panel is considered, equation (13) produces the net cell current i_{PV}:

$$i_{PV} = i_{Ph} - i_D - i_P. \qquad (13)$$

Using the established linkages in [17], the final mathematical Eq. (14) of this model, which characterizes the I–V properties of the solar panel, can be found as:

$$i_D = i_0 \left(\exp\left(\frac{V_{PV} + R_s i_{PV}}{nv} \right) \right); \qquad (14)$$

$$i_P = i_0 \left(\frac{V_{PV} + R_s i_{PV}}{R_P} \right); \qquad (15)$$

$$i_{PV} = i_{Ph} - i_0 \left(\exp\left(\frac{V_{PV} + R_s i_{PV}}{nv} \right) - 1 \right) - \frac{V_{PV} + R_s i_{PV}}{R_P}, \qquad (16)$$

where i_{PV} is the PV output current that flows through the series resistance R_S; V_{PV} is the PV output voltage; i_{Ph} is the photo generated current; i_D is the diode saturation current; i_0 is the reverse saturation current; i_P is the current passing via shunt resistance R_{Sh}; n is the number of series connected solar PV cells; v is the junction thermal voltage.

The open circuit voltage of the PV panel is given by:

$$V_{OC} = \frac{a \cdot k \cdot T}{q} \log\left(\frac{i_{Ph}}{i_D} + 1\right), \qquad (17)$$

where a is the ideality constant of a diode; q is the charge of an electron ($1{,}602 \cdot 10^{-19}$ C); k is the Boltzmann constant ($1{,}381 \cdot 10^{-23}$ J/K); T is the p-n junction's temperature.

As demonstrated by the equations above, the PV cell current is a complex function of temperature and photon intensity. Since the power produced by PV cells is the result of the product of cell current and voltage, the power of a PV cell is a complex function of temperature and radiation intensity [18, 19].

Figure 7 illustrates the varying electrical output of a PV cell as it responds to changes in light intensity, highlighting the relationship between irradiation and power generation efficiency [20, 21].
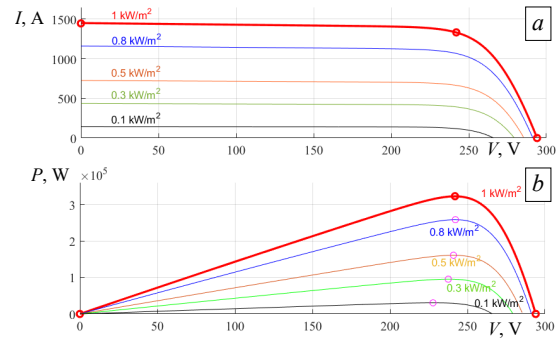
Fig. 7. Characteristics of the PV cell at different irradiation levels: $a - I = f(V)$; $b - P = f(V)$

Control strategy applied to the PFV-WEC. The control strategy for the PFV-WEC hybrid system (Fig. 8), designed to supply the Oran region in Algeria, involves several advanced algorithms.
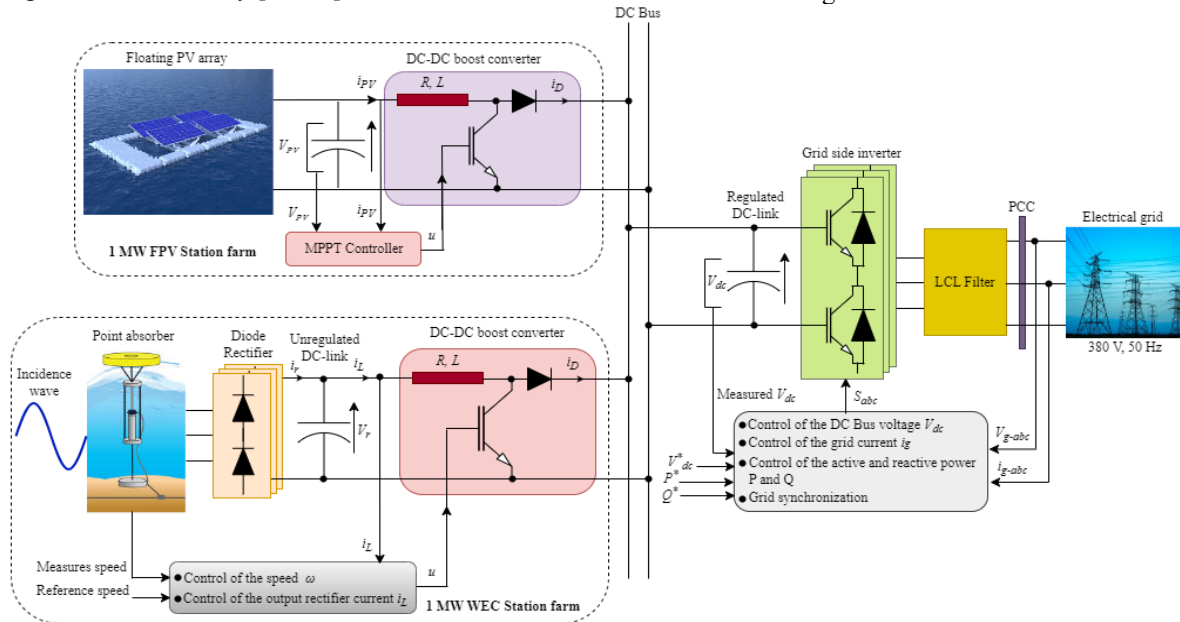
Fig. 8. Different control strategies applied to the hybrid conversion chain

Maximum power point tracking optimizes the energy harvested from the FPV panels. The DC bus voltage regulation ensures stable operation and efficient energy conversion [22, 23]. Additionally, the control of active and reactive power balances the power supply and maintains grid stability. These algorithms work in tandem to maximize energy output and ensure a reliable power supply to the Oran region from the hybrid FPV and WEC system.

Simulation results and discussion. The hybrid FPV and multi-point absorber model with grid connection simulation aims to accomplish three things: first, it will investigate the behavior of important system variables over time; second, it will verify that power produced by the FPV-PTO is successfully injected into the grid; and third, it will verify that current is injected into the grid with unity power factor. It was determined that a 25-second simulation period was sufficient to achieve these objectives. Figure 9 displays a number of variables as trends over time, including the applied wave form with an amplitude of 1 m, the rod speed, the buoy's position, the force produced (250 kN), and the point absorber's response. The parameters used in this simulation are shown in Tables 2–4.

Table 2

Detailed specifications of solar PV station

Parameters	Values
Maximum power, W	255.74
Parallel strings	180
Series connected modules per string	7
Open circuit voltage V_{oc}, V	42
Short circuit current i_{sc}, A	8.03
Cell per module N_{cell}	60
Voltage at maximum power point V_{mp}, V	34.56
Current at maximum power point i_{mp}, A	7.4
Temperature coefficient of V_{oc}	0.361
Temperature coefficient of i_{oc}	0.007

Table 3

Detailed specifications of WEC station

Parameters	Values
Wave amplitude, m	0.8 – 1.2
Number of the PTO	4
Stator resistance R_s, Ω	0.01
Armature inductance, µH	80
Flux linkage, Wb	0.8
Moment of inertia, kg·m^2	0.002008
Viscous friction coefficient, kg·s^{-1}	0.0028
Pole pairs	18

Electric filter and grid parameters

Parameters	Values
Resistance of the filter, Ω	10
Inductance of the filter, H	0.5
Grid voltage, V	380
Frequency, Hz	50
DC capacitor, mF	10
DC link voltage, V	1200

The simulation results evaluating the transient and steady-state performance of the controllers under sudden changes in wave speed are illustrated in Fig. 9. Both controllers perform effectively in steady-state conditions, as evidenced by Fig. 10,*a*, which shows the linear permanent magnet synchronous generator (LPMSG) rotational velocity response to wave speed using the model controllers. The electromagnetic torque generated by the LPMSG is illustrated in Fig. 10,*b*. Figure 10,*c* presents the active and reactive power components of the LPMSG. The employed control strategy demonstrates a satisfactory decoupling between these components. This approach ensures a high active power yield and a highly stable direct bus voltage by maintaining the reactive power at zero throughout the simulation period.
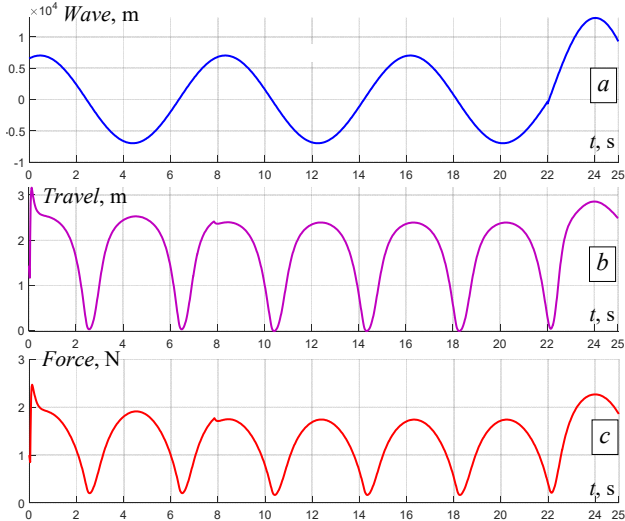
Fig. 9. Time evolution of important parameters in the multi-point absorber based on WEC:
a – sinusoidal wave signal; *b* – travel curve; *c* – force curve

Figure 11 displays the voltage and current outputs of the LPMSG along with detailed zoomed-in views of these waveforms. The main plots show the overall behavior, while the zooms highlight finer details such as amplitude and frequency. This provides insight into the LPMSG's performance and stability under various conditions.

The DC bus voltage varies with amplitude of approximately 1200 V, showing fluctuations of about 1.5 % of the nominal value, which corresponds to changes in the applied wave's waveform. As illustrated in Fig. 12, the performance of the PV station is analyzed under different levels of solar irradiation. The surface temperature of the PV array is maintained at a constant 25 °C during the simulation. As depicted in Fig. 12, the performance of the PV system is primarily influenced by the cell's temperature and the level of irradiation received. Higher temperatures reduce efficiency. Figure 12,*a* illustrates the variation in solar irradiation, showing how sunlight changes throughout

the day and the effect of a cloud casting a shadow, for example. Figures 13,*a,b* depict the grid voltage and current, illustrating that the signals are purely sinusoidal. The voltage amplitude remains constant at 380 V, and the current amplitude is 20 A.
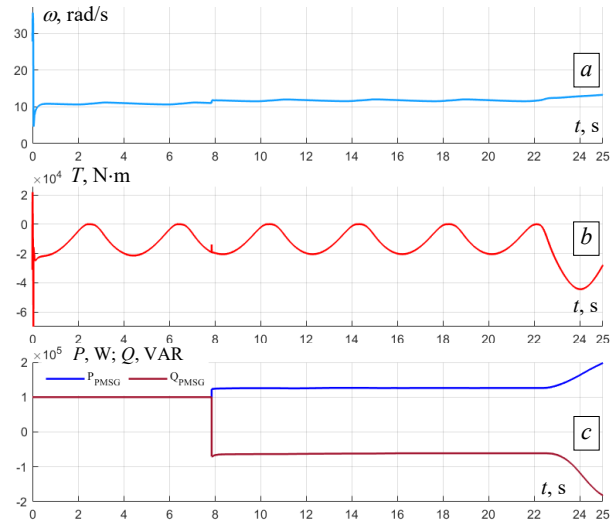
Fig. 10. LPMSG electrical variables during the maritime substation test: *a* – speed; *b* – electromagnetic torque; *c* – active and reactive power
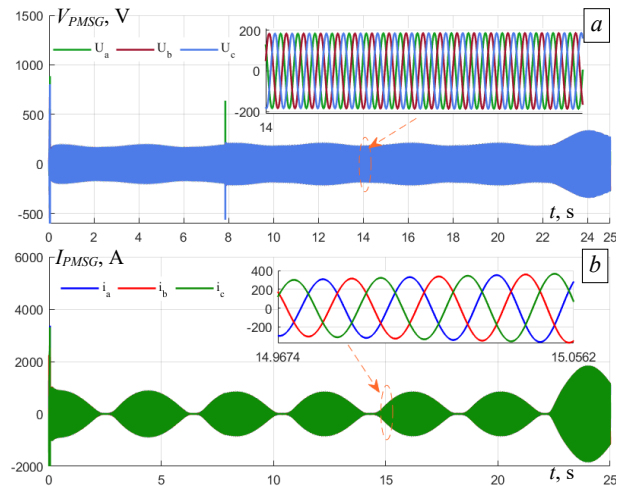
Fig. 11. In a normal maritime operation, the LPMSG's output of three phases of voltage (*a*) and current (*b*)
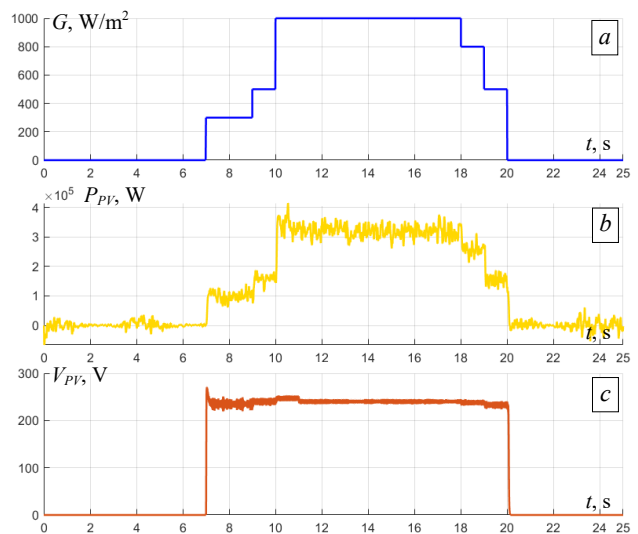
Fig. 12. Performance of FPV farm: *a* – solar irradiance profile; *b* – generated power; *c* – PV voltage
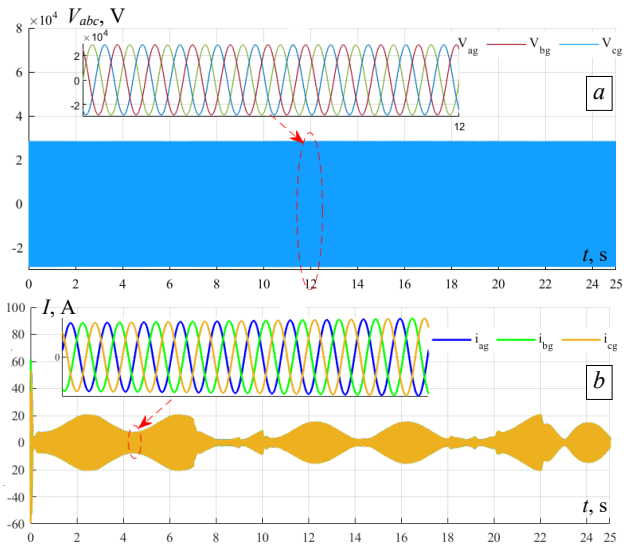
Fig. 13. FPV-WEC hybrid system performance at point of common coupling bus: *a* – grid voltages; *b* – grid current

Figure 14 shows the three-phase voltage and current outputs of the inverter, including detailed zoomed-in views of the waveforms. The main plots illustrate the overall behavior of the voltage and current, revealing their consistent and balanced nature across all phases. The zoomed-in views highlight finer details, such as waveform amplitude and frequency, providing a closer look at the inverter's performance. This comprehensive depiction emphasizes the inverter's ability to deliver stable and efficient power output under various operating conditions.

When the applied wave oscillates, Fig. 15,*a* and Fig. 16 show the waveforms of the active power grid and DC link voltage, respectively. Figures 15,*a*,*b* indicate the apparent active power and reactive power as 1 MW and 0 VAR, respectively.

Energy management is maintained throughout this study (Fig. 17). The power demanded by the load equals the sum of the power generated by the combined FPC-WEC system and the power supplied by the public grid.
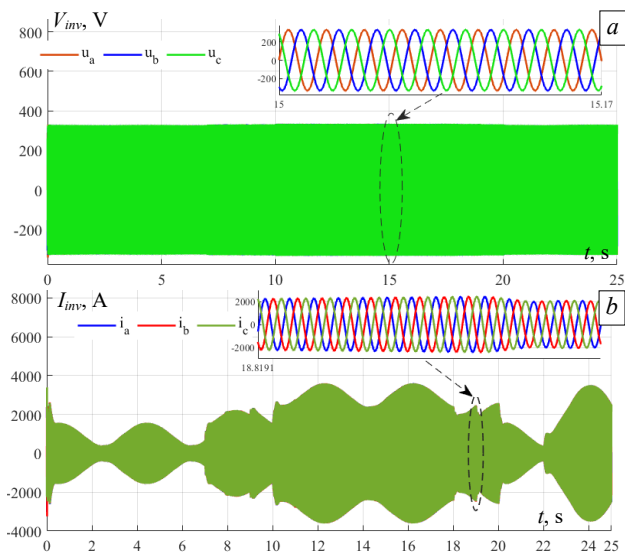
Fig. 14. Three phase voltage (*a*) and current (*b*) of the output of inverter
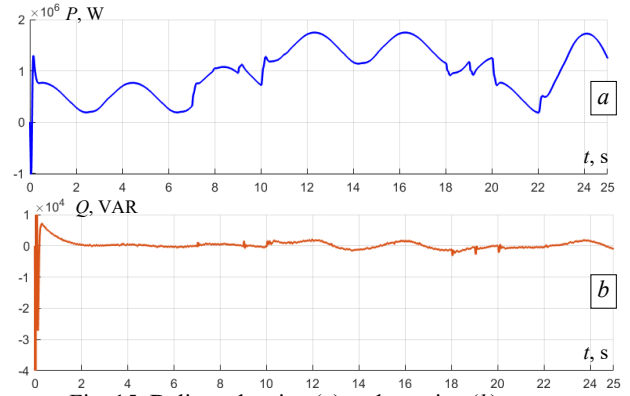
Fig. 15. Delivered active (*a*) and reactive (*b*) power
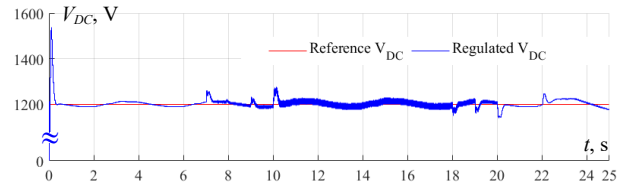
Fig. 16. DC link voltage
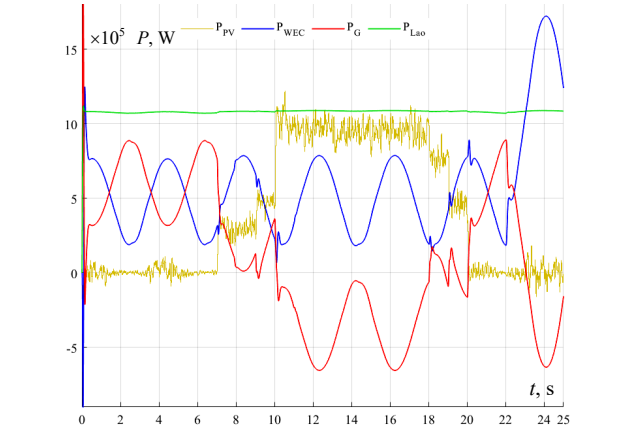
Fig. 17. Actual active power flow between the load, grid, and hybrid system

Conclusions. This paper presents the design and analysis of a hybrid wave energy converter (WEC) and floating photovoltaic (FPV) system specifically designed for offshore deployment in the Oran region. By integrating WEC and FPV technologies, a synergistic approach is achieved, harnessing both wave and solar energy to enhance energy output and improve system reliability. The comprehensive design process involved identifying suitable WEC and FPV components and optimizing their configurations to meet the unique environmental and operational conditions of the Oran site. Computational simulations and numerical data were utilized to assess the performance, structural stability, and economic feasibility of the hybrid system. The findings of this study show substantial enhancements in energy yield and system resilience compared to standalone WEC or FPV installations. The hybrid system leverages the complementary nature of wave and solar energy, offering a more consistent and reliable energy supply, thereby addressing the intermittency challenges common to renewable energy sources. Additionally, the economic analysis suggests that the hybrid system is a viable investment, offering potential cost savings and enhanced energy production efficiency in the long term. These findings highlight the potential of hybrid renewable energy systems as a sustainable solution for offshore energy generation.

This research provides valuable insights into the design and implementation of hybrid WEC and FPV systems for offshore use. The Oran case study exemplifies how such integrated renewable energy solutions can be effectively applied to similar coastal regions, highlighting their feasibility and benefits. Future research should focus on further optimization, scaling, and real-world deployment of these hybrid systems to maximize their potential in achieving a sustainable and low-carbon energy future.

Conflict of interest. The authors of the article declare that there is no conflict of interest.

REFERENCES

1. Alcañiz A., Monaco N., Isabella O., Ziar H. Offshore floating PV–DC and AC yield analysis considering wave effects. *Energy Conversion and Management*, 2024, vol. 300, art. no. 117897. doi: https://doi.org/10.1016/j.enconman.2023.117897.

2. Ghigo A., Faraggiana E., Sirigu M., Mattiazzo G., Bracco G. Design and Analysis of a Floating Photovoltaic System for Offshore Installation: The Case Study of Lampedusa. *Energies*, 2022, vol. 15, no. 23, art. no. 8804. doi: https://doi.org/10.3390/en15238804.

3. Parimalasundar E., Jayanthi R., Suresh K., Sindhuja R. Investigation of efficient multilevel inverter for photovoltaic energy system and electric vehicle applications. *Electrical Engineering & Electromechanics*, 2023, no. 4, pp. 47-51. doi: https://doi.org/10.20998/2074-272X.2023.4.07.

4. Patil A., Mamatha G., Kulkarni P.S., Verma A. Analysis of Hybrid Floating Photovoltaic and Hydro-Power plant with HOMER Pro Software. *2022 IEEE International Conference on Power Electronics, Drives and Energy Systems (PEDES)*, 2022, pp. 1-6. doi: https://doi.org/10.1109/PEDES56012.2022.10080502.

5. Xiong L., Le C., Zhang P., Ding H., Li J. Harnessing the power of floating photovoltaic: A global review. *Journal of Renewable and Sustainable Energy*, 2023, vol. 15, no. 5, art. no. 052701. doi: https://doi.org/10.1063/5.0159394.

6. Priyanka G., Surya Kumari J., Lenine D., Srinivasa Varma P., Sneha Madhuri S., Chandu V. MATLAB-Simulink environment based power quality improvement in photovoltaic system using multilevel inverter. *Electrical Engineering & Electromechanics*, 2023, no. 2, pp. 43-48. doi: https://doi.org/10.20998/2074-272X.2023.2.07.

7. Solomin E., Sirotkin E., Cuce E., Selvanathan S.P., Kumarasamy S. Hybrid Floating Solar Plant Designs: A Review. *Energies*, 2021, vol. 14, no. 10, art. no. 2751. doi: https://doi.org/10.3390/en14102751.

8. Al Shami E., Zhang R., Wang X. Point Absorber Wave Energy Harvesters: A Review of Recent Developments. *Energies*, 2018, vol. 12, no. 1, art. no. 47. doi: https://doi.org/10.3390/en12010047.

9. Alnujaie A., Berkani A., Negadi K., Hadji L., Ghazwani M.H. Enhancing the Performance and Coordination of Multi-Point Absorbers for Efficient Power Generation and Grid Synchronization Control, *Journal of Applied and Computational Mechanics*, 2024, vol. 10, no. 3, pp. 422-442. doi: https://doi.org/10.22055/jacm.2024.44960.4293.

10. Zhou B., Wang Y., Hu J., Jin P., Wang L. Evaluation and optimization of a hybrid wave energy converter using excited motion response in two degrees of freedom. *Journal of Hydrodynamics*, 2023, vol. 35, no. 1, pp. 145-154. doi: https://doi.org/10.1007/s42241-023-0013-3.

11. Berkani A., Ghazwani M.H., Negadi K., Hadji L., Alnujaie A., Ghazwani H.A. Predictive control and modeling of a point absorber wave energy harvesting connected to the grid using a LPMSG-based converter. *Ocean Systems Engineering*, 2024, vol. 14, no. 1, pp. 017-52. doi: https://doi.org/10.12989/ose.2024.14.1.017.

12. Sathish C., Chidambaram I.A., Manikandan M. Intelligent cascaded adaptive neuro fuzzy interface system controller fed KY converter for hybrid energy based microgrid applications. *Electrical Engineering & Electromechanics*, 2023, no. 1, pp. 63-70. doi: https://doi.org/10.20998/2074-272X.2023.1.09.

13. Vervaet T., Stratigaki V., De Backer B., Stockman K., Vantorre M., Troch P. Experimental Modelling of Point-Absorber Wave Energy Converter Arrays: A Comprehensive Review, Identification of Research Gaps and Design of the WECfarm Setup. *Journal of Marine Science and Engineering*, 2022, vol. 10, no. 8, art. no. 1062. doi: https://doi.org/10.3390/jmse10081062.

14. Tagliafierro B., Martínez-Estévez I., Domínguez J.M., Crespo A.J.C., Göteman M., Engström J., Gómez-Gesteira M. A numerical study of a taut-moored point-absorber wave energy converter with a linear power take-off system under extreme wave conditions. *Applied Energy*, 2022, vol. 311, art. no. 118629. doi: https://doi.org/10.1016/j.apenergy.2022.118629.

15. Ravichandran N., Ravichandran N., Panneerselvam B. Floating photovoltaic system for Indian artificial reservoirs – an effective approach to reduce evaporation and carbon emission. *International Journal of Environmental Science and Technology*, 2022, vol. 19, no. 8, pp. 7951-7968. doi: https://doi.org/10.1007/s13762-021-03686-4.

16. Jee H., Noh Y., Kim M., Lee J. Comparing the Performance of Pivotless Tracking and Fixed-Type Floating Solar Power Systems. *Applied Sciences*, 2022, vol. 12, no. 24, art. no. 12926. doi: https://doi.org/10.3390/app122412926.

17. Bourenane H., Berkani A., Negadi K., Marignetti F., Hebri K. Artificial Neural Networks Based Power Management for a Battery/Supercapacitor and Integrated Photovoltaic Hybrid Storage System for Electric Vehicles. *Journal Europeen des Systemes Automatises*, 2023, vol. 56, no. 1, pp. 139-151. doi: https://doi.org/10.18280/jesa.560118.

18. Khan S.A., Mahmood T., Awan K.S. A nature based novel maximum power point tracking algorithm for partial shading conditions. *Electrical Engineering & Electromechanics*, 2021, no. 6, pp. 54-63. doi: https://doi.org/10.20998/2074-272X.2021.6.08.

19. Noureldeen O., Ibrahim A.M.A. Performance Analysis of Grid connected PV/Wind Hybrid Power System during Variations of Environmental Conditions and Load. *International Journal of Renewable Energy Research*, 2018, vol. 8, no. 1, pp. 208-220. doi: https://doi.org/10.20508/ijrer.v8i1.6702.g7347.

20. Themozhi G., Srinivasan K., Arun Srinivas T., Prabha A. Analysis of suitable converter for the implementation of drive system in solar photovoltaic panels. *Electrical Engineering & Electromechanics*, 2024, no. 1, pp. 17-22. doi: https://doi.org/10.20998/2074-272X.2024.1.03.

21. Viola A., Franzitta V., Trapanese M., Curto D. Nexus Water & Energy: A Case Study of Wave Energy Converters (WECs) to Desalination Applications in Sicily. *International Journal of Heat and Technology*, 2016, vol. 34, no. S2, pp. S379-S386. doi: https://doi.org/10.18280/ijht.34S227.

22. Yang B., Duan J., Chen Y., Wu S., Li M., Cao P., Jiang L. A critical survey of power take-off systems based wave energy converters: Summaries, advances, and perspectives. *Ocean Engineering*, 2024, vol. 298, art. no. 117149. doi: https://doi.org/10.1016/j.oceaneng.2024.117149.

23. Latreche K., Taleb R., Bentaallah A., Toubal Maamar A.E., Helaimi M., Chabni F. Design and experimental implementation of voltage control scheme using the coefficient diagram method based PID controller for two-level boost converter with photovoltaic system. *Electrical Engineering & Electromechanics*, 2024, no. 1, pp. 3-9. doi: https://doi.org/10.20998/2074-272X.2024.1.01.

Rabah Araria[1]*, Doctor of Technical Science,*
Mohamed Boutkhil Guemmour[2]*, Doctor of Technical Science,*
Karim Negadi[1]*, Full Professor,*
Abderrahmane Berkani[1]*, Doctor of Technical Science,*
Fabrizio Marignetti[3]*, Full Professor,*
Mohamed Bey[1]*, Doctor of Technical Science,*
[1] L2GEGI Laboratory, Department of Electrical Engineering, Faculty of Applied Science, University of Tiaret, Algeria, e-mail: rabah.araria@univ-tiaret.dz; karim.negadi@univ-tiaret.dz (Corresponding Author); abderrahmane.berkani@univ-tiaret.dz; mohamed.bey@univ-tiaret.dz
[2] Industrial Technologies Research Laboratory, Department of Mechanical Engineering, Faculty of Applied Science, University of Tiaret, Algeria, e-mail: mohamed.guemmour@univ-tiaret.dz
[3] Department of Electrical and Information Engineering, University of Cassino and Southern Lazio, Italy, e-mail: marignetti@unicas.it

M. Irwanto, L.K.W. Kita

An application of multi-magnetic circular planar spiral relay to improve the performance of wireless power transfer system

*Introduction. The system of delivering electricity without wires is known as wireless power transfer (WPT). The WPT system has been extensively used in a number of industries, health, telecommunications, and transportation. However, the distance between the transmitter and receiver coils has a significant impact on its efficiency. Lower power can be generated between coils the farther apart they are, and vice versa. **The novelty** of the proposed work is innovative in that it develops a multi-magnetic circular planar spiral relay to improve the WPT system's performance and designs circular planar spiral coils to achieve an appropriate inductance value for the 5 kHz matching frequency. **The goal** of paper is to create a circular planar spiral coil with an appropriate inductance value for the 5 kHz matching frequency. **Methods.** The transmitter circuit, receiver circuit, and DC voltage source are parts of the WPT system. The inverter circuit uses the inductive coupling technique to transform the DC power source into AC voltage on the transmitter coil. The suggested coil is additionally employed as a multi-magnetic circular planar spiral relay in order to increase the mutual inductance between the receiver and transmitter coils. **Results.** To monitor the power improvement that results from adding a multi-magnetic relay to the system, the transmitter coil, receiver coil, and multi-magnetic relay are positioned at specific distances from each other. With $V_{dc} = 30$ V and $d_{tr} = 21$ cm, the power received at the receiver coil can therefore be improved by up to 67 %. **Practical value.** The multi-magnetic circular planar spiral relay applied in the WPT system has been investigated in an experimental study and it can be applied for DC load. References 26, table 1, figure 18.*
Key words: **wireless power transfer, performance improvement, magnetic relay, multi-magnetic circular planer spiral relay.**

*Вступ. Система доставки електроенергії без дротів відома як бездротова передача енергії (WPT). Система WPT широко використовується у ряді галузей промисловості, охорони здоров'я, телекомунікацій та транспорту. Однак відстань між передавальною та приймальною котушками істотно впливає на її ефективність. Чим далі котушки один від одного, тим нижча потужність, і навпаки. **Новизна** запропонованої роботи полягає в розробці багатомагнітного круглого плаского спірального реле для покращення продуктивності системи WPT і в проєктуванні круглих пласких спіральних котушок для досягнення відповідного значення індуктивності для частоти узгодження 5 кГц. **Метою** роботи є створення кругової плоскої спіральної котушки з відповідним значенням індуктивності для частоти узгодження 5 кГц. **Методи.** Схема передавача, схема приймача та джерело постійної напруги є частинами системи WPT. Схема інвертора використовує метод індуктивного зв'язку перетворення джерела постійного струму в змінну напругу на котушці передавача. Пропонована котушка додатково використовується як багатомагнітне кругле плоске спіральне реле для збільшення взаємної індуктивності між приймальною і передавальної котушками. **Результати.** Для контролю поліпшення потужності, яке відбувається в результаті додавання багатомагнітного реле в систему, котушка, що передає, приймальна котушка і багатомагнітне реле розташовуються на певних відстанях один від одного. При $V_{dc} = 30$ В і $d_{tr} = 21$ см потужність, яка приймається приймальною котушкою, може бути покращена до 67 %. **Практичне значення.** Багатомагнітне кругле плоске спіральне реле, що застосовується в системі WPT, було досліджено експериментально, і його можна застосовувати для постійного навантаження. Бібл. 26, табл. 1, рис. 18.*
Ключові слова: **бездротова передача живлення, підвищення продуктивності, магнітне реле, багатомагнітне спіральне пласке реле.**

Introduction. Nowadays, there is a growing amount of work being done on the development and applications of wireless power transfer (WPT) in numerous fields. For instance, wireless power transmission has been effectively applied in a number of industries, including biomedicals [1, 2], battery chargers [3–6], the electrical industry, and even the transportation industry, including electric vehicles [7–9]. Activities are made simpler and more efficient by doing this. Additionally, it helps reduce the expense of using wires as a power conductor.

WPT system typically has three primary parts: the transmitter circuit, receiver circuit and DC voltage source [10, 11]. An inverter circuit and coil make up the transmitter circuit; the inverter circuit converts the primary DC power source to AC voltage [12, 13], which is then connected to the transmitter coil. AC power produced at the transmitter coil is then transferred to the receiver coil using the principle of inductive coupling. The transmitted AC power is determined by the quantity of magnetic flux that reaches the receiver coil, which in turn is determined by the magnetic field created by the transmitter coil. The transmitter coil diameter is the final factor that influences this [14].

Power transfer of inductive coupling occurs by conducting an alternating magnetic field on the transmitter coil [15, 16]. Consequently, in the receiver coil, the magnetic flux produced will be transformed into an electric current. The electric current that the transmitter coil delivers is always greater than the electric current that the receiver coil generates. The receiver coil receives less current the farther apart the two coils are [17–20]. The entire magnetic field that flows through the transmitter and receiver coil is measured as magnetic flux. The centre of the coils is where the flux is always focused. The distance between the transmitter and receiver coil impacts the amount of AC power that the receiver coil can receive; the greater the distance, the lower the AC power that can be obtained on the receiver coil [21, 22] and it can be classified in a low power electrical device and also as an electrical energy harvested [23]. To prevent the magnetic field from passing out of the centre between the transmitter and reception coils, the flux level can still be increased. To maximize the flux and raise the AC power on the reception coil, a multi-magnetic relay must be positioned between the transmitter and the receiver coil.

The goal of this study is to create a circular planar spiral coil with an appropriate inductance value for the 5 kHz matching frequency. The usage of a higher frequency will result in a lower coil inductance since frequency and coil inductance have an inversely proportionate relationship. Conversely, the coil's inductance is directly correlated with

its number of turns, meaning that an increase in turns will result in a larger coil inductance. To achieve the matching frequency of 5 kHz, a suitable type of coil and its inductance value are needed because the shape of the coil impacts the value of its inductance. With reference to [6], the receiver coil's AC power is always low, and the greater the distance between the transmitter and the coil, the lower the AC power is on the coil. Consequently, mutual inductance is needed to increase the induction between the transmitter and receiver coils in order to increase the power of 5 kHz WPT system. To obtain the mutual inductance in this instance, a multi-magnetic circular planar spiral relay is utilized. Because of this, the main focus of this study will be on enhancing the power of 5 kHz wireless power transmission through the use of mutual inductance to reinforce the magnetic field between the transmitter and receiver coils as well as multi-magnetic circular planar spiral relays.

Methodology. This section offers the design of a circular planar spiral coil for getting a sufficient inductance value for the matching frequency of 5 kHz. The construction of WPT system with inclusion of a multi-magnetic circular planar spiral relay is detailed in this part. This section also explains the assessment of the measurement findings of the WPT system's performances with and without the multi-magnetic circular planar spiral relay.

A block diagram of a proposed WPT system with a multi-magnetic relay is displayed in Fig. 1. The multi-magnetic planer spiral relay, receiver circuit, and transmitter circuit make up its three primary components. Circular planer spiral coils are the shapes of the magnetic planer spiral relay, transmitter coil, and receiver coil.
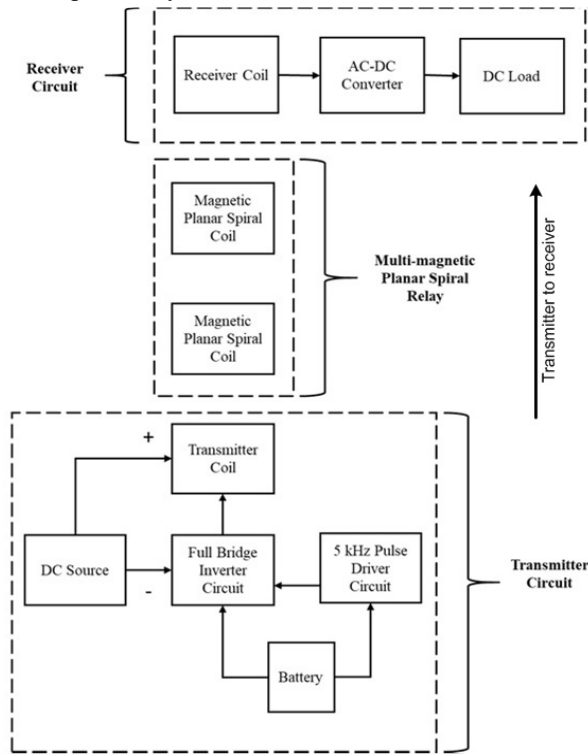
Fig. 1. Block diagram of proposed WPT system with multi-magnetic relay

The transmitter coil, full bridge inverter circuit, and 5 kHz pulse driver circuit make up the transmitter circuit. The PIC16F628A-I/P microcontroller, which powers the entire bridge inverter circuit, is responsible for creating

the 5 kHz pulse wave and driving the MOSFETs' gate terminals. The primary purpose of the complete bridge inverter circuit is to change the DC voltage source into an AC voltage of 5 kHz for the transmitter coil.

The receiver coil, AC-DC converter, and DC load make up the receiver circuit. A 5 kHz AC voltage is applied to the receiver coil as a result of mutual magnetic flux leaking from the transmitter coil into the receiver coil. A rectifier (AC-DC converter) is needed when DC electrical is applied in the system [24, 25]. In this research, a rectifier rectifies 5 kHz AC voltage, which is then applied by the DC load.

Increasing the strength of the magnetic field between the transmitter and receiver coils is the primary purpose of a multi-magnetic relay. As a result, the receiver coil's AC voltage, current, and power can all be increased. This indicates that the WPT system performs better when using a multi-magnetic relay than when it does not.

Proposed design of circular planar spiral coil. The occurrence of an electromagnetic force in a conducting wire or coil as a result of variations in the magnetic force lines (magnetic flux) is known as electromagnetic induction. The fundamental idea of electromagnetic induction between transmitter and receiver coils is depicted in Fig. 2. Furthermore, Fig. 2 depicts the idea design of coils, including the wire diameter (d_w), the distance between turns (s), the inner diameter (d_{in}), and the outer diameter (d_{out}).
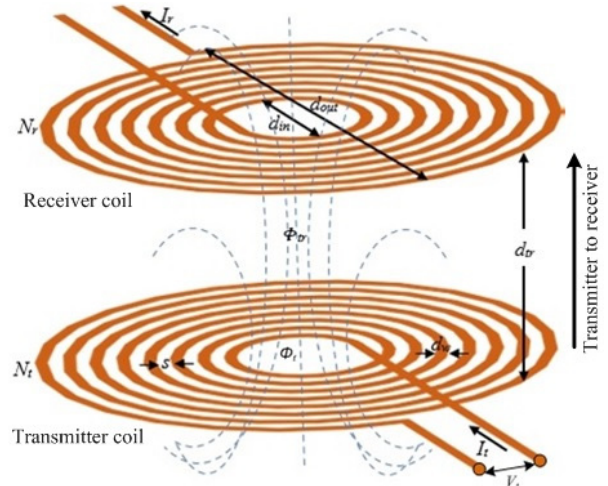
Fig. 2. The fundamental idea of transmitter and receiver coils

In this design, the turn numbers of the transmitter coil N_t and the receiver coil N_r are the same ($N_t = N_r = N$). The distance d_t separates the coils of the transmitter and receiver. Following (1) [18], the transmitter coil produces the magnetic flux Φ_t when an AC voltage V_t is supplied to it. This causes the AC current to pass through the transmitter coil.

$$V_t = -N_t \frac{\mathrm{d}\Phi_t}{\mathrm{d}t}. \tag{1}$$

The magnetic flux flows to the receiver coil through the air medium and produce the mutual magnetic flux Φ_{tr}. Thus, an induced voltage V_r is generated on the receiver coil and the current I_r flows through the receiver coil if it is a closed loop circuit.

In this setup, the circular planer spiral coil and a capacitor C are linked in parallel to yield a math frequency f of 5 kHz. Therefore, (2) can be used to compute the coil inductance L [17, 26]:

$$L = \frac{1}{4\pi^2 f^2 C} .\qquad(2)$$

The specifications and computations of the parameter utilized in the following (2) must be understood before constructing the circular planer spiral coil design. Table 1 displays the characteristics of the circular planar spiral coil that was utilized in the experiment.

Table 1

Specification of the proposed circular planar spiral coils

Parameter	Value
Wire diameter d_w, mm	1.25
Inner diameter d_{in}, mm	20
Number of turns N	66
Spacing between turns s, mm	0.001
Outer diameter d_{out}, mm	185.131
Capacitance of capacitor C, µF	3
Inductance of coil L, µH	338

The circular planar spiral coil, which can be utilized as a multi-magnetic relay as well as a transmitter and receiver coil, is depicted in Fig. 3. Up to four circular planar spiral coils with the same inductance value L and number of turns N can be used in the WPT system created in this study. The coil was built using computations from the formulas given in this section and the design concept.

Fig. 3. Proposed circular planar spiral coil

Hardware construction of 5 kHz WPT system. A WPT system requires more than just the coils that are employed, circuit design and construction are essential for system application. It is important to build the circuits in a way that allows the WPT system to function correctly and in accordance with the intended mechanism. As a result, the construction of the circuits that are employed, such as the receiver side AC-DC converter and the transmitter side full bridge inverter is covered in this part.

Pulse driver circuit. The frequency of operation for the WPT system in this study is 5 kHz. The PIC16F628A-I/P microcontroller serves as the primary driver in the pulse driver circuit, which generates the frequency. The PIC compiler software's C language is used to program the PIC16F628A-I/P microcontroller to operate at a frequency of 5 kHz. Consequently, the complete bridge inverter is driven by the ensuing pulse wave.

A schematic representation of the pulse driver circuit employed in this study is presented in Fig. 4. The D1 1N4007 diode protects the battery's polarity and permits a current flow of 1 A before the 12 V voltage source from the battery enters the LM7805 voltage regulator. The LED, which serves as a voltage indication in the circuit, is connected in parallel to the LM7805 output terminal. On the other side of the connection, pins 4 and 14 are the positive 5 V terminal of the PIC16F628A-I/P microcontroller and pin 5, which is the negative terminal, where the 5 V output voltage that results from the regulation of the LM7805 is filtered by capacitors C1 and C2 to reduce noise. Conversely, pins 15 and 16 represent the oscillator terminals that are linked to the crystal, together with two parallel capacitors C3 and C4. With the use of a coding program, this oscillator determines the speed at which the processor will execute instructions to create two pulse waves at a frequency of 5 kHz, corresponding to pin numbers 11 and 12.
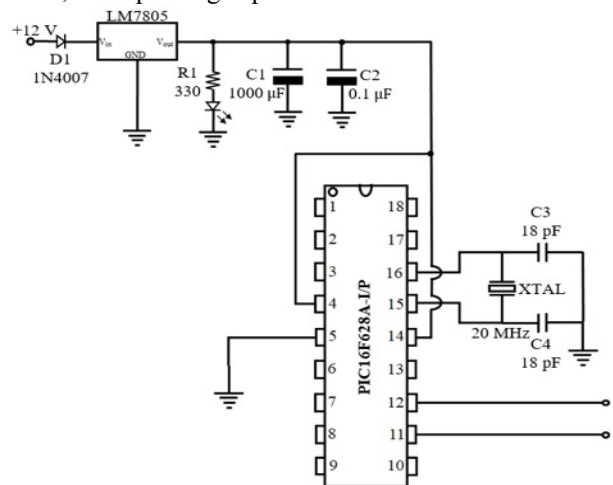
Fig. 4. Schematic diagram of pulse driver

Full bridge inverter circuit. As illustrated in Fig. 5, this study employs a full bridge inverter with four power MOSFET switches. Pins 11 and 12 of the pulse driver are connected to the input terminal of the full bridge inverter by terminals A and A'. The terminals B and B' link the full bridge inverter to the DC voltage source, enabling the nominal voltage to be set by the DC input provided at the transmitter side.
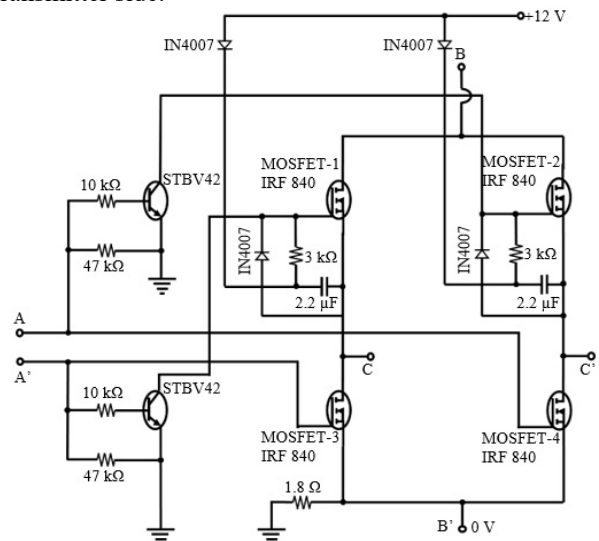
Fig. 5. Full bridge inverter schematic diagram

Four IRF 840 MOSFETs transform the DC input voltage into an AC voltage so that the inverter's output side (terminals C and C') can generate a full waveform output at a frequency of 5 kHz. In order to get a pure sinusoidal waveform, the outputs of the C and C' terminals can be routed to a 3 μF filter capacitor and a 100 μH inductor before being sent to the transmitter coil.

Receiver circuit. A DC waveform must be created by rectifying the 5 kHz AC voltage waveform that was received at the receiver coil on the receiving side. As a result, a device is required to change the waveform from AC to DC. As seen in Fig. 6, this study uses a full wave AC-DC converter with four diodes acting as switches.
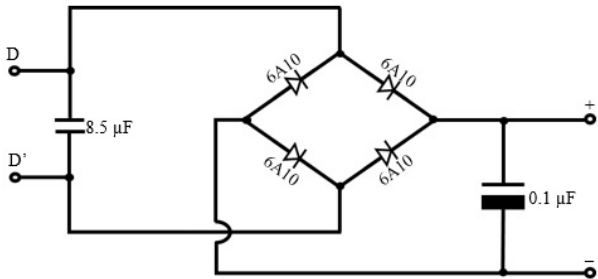
Fig. 6. Full bridge rectifier circuit

In accordance with the schematic diagram in Fig. 6, the connections at input terminals D and D' originate from the receiver coil. An 8.5 μF capacitor filters the input power that the receiver side of the circuit receives before it is sent to the full wave converter. A full wave AC-DC converter using four 6A10 diodes as switches rectifies AC-DC waveforms. Before connecting the DC load through the output terminals (+ and –), the AC-DC waveform's rectification results are filtered by a 0.1 μF capacitor to lessen noise.

Overall hardware and experimental setup of WPT system. The overall design and experimental configuration of the 5 kHz WPT system suggested in this study are described in this section. Figure 7 depicts the overall hardware of the suggested WPT system. As seen in Fig. 4, the battery may supply 5 V of DC voltage to the pulse driver circuit after the LM7805 reduces 12 V to 5 V. In Fig. 5 the battery supplies 12 V of DC voltage to the entire bridge circuit. As seen in Fig. 5, the DC voltage source (V_{dc} source) has the ability to supply the DC voltage source to the entire bridge inverter circuit at terminals B and B'.
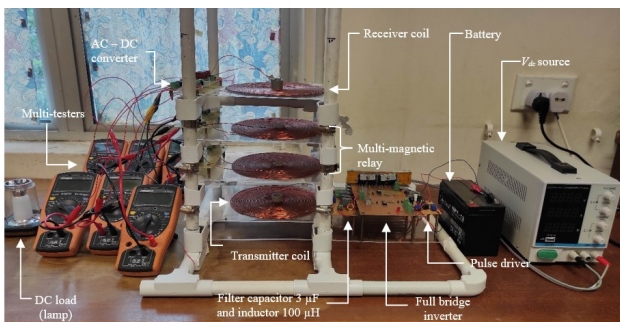
Fig. 7. Overall design of the proposed WPT system

The design of multiple experimental setups, ranging from the production of a 5 kHz pulse wave to the power transfer procedure utilizing the WPT system suggested in this study. In order to collect the required data, various settings were used in each experiment. This experiment involves setting a number of parameters, including the number of circular planar spiral coils utilized in the WPT system, variations in the DC voltage source (V_{dc} source), and variations in the distance between coils.

The waveform and frequency received on each coil must be verified to show that the proposed WPT system in this experiment operates at a frequency of 5 kHz in the form of a sine voltage waveform. Consequently, the system is set by connecting each coil to the oscilloscope as shown in Fig. 8. The multi-magnetic relay is connected to channels 2 and 3, respectively, and the transmitter coil is connected to oscilloscope channel 1. While the oscilloscope's channel 4 is linked to the receiver coil. In this experiment, the DC voltage is set to 15 V, and the coil spacing is adjusted to be 0 cm, 15 cm, 30 cm, and 45 cm. Verifying the waveform and frequency value that occur in each coil is the aim of this experiment.
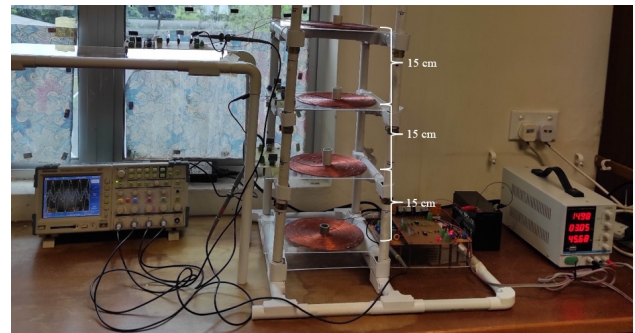
Fig. 8. Verification of waveform and frequency on all coils

There are just two coils (the transmitter coil and the receiver coil) used in the experiment shown in Fig. 9. The two coils are positioned vertically between three and thirty centimeters apart. Additionally, a voltage value ranging from 3 V to 30 V is supplied to the specified V_{dc} source. This arrangement allows findings on many parameters, including voltage, current, and power, to be obtained and shown graphically for the additional analysis.
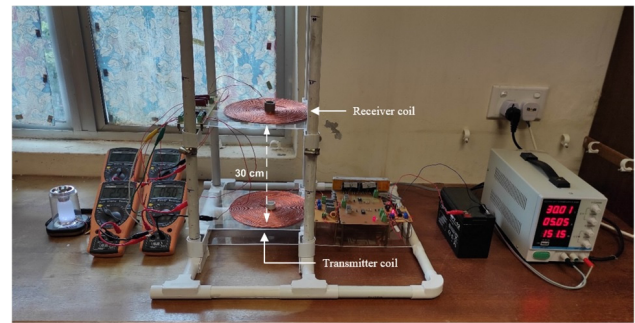
Fig. 9. WPT system without multi-magnetic relay

As illustrated in Fig. 10, this experiment is similar to the setup discussed previously, but it adds a multi-magnetic relay consisting of two circular planer spiral coils positioned between the transmitter and receiver coils. The four coils that are being used are separated by 7 cm due to the multi-magnetic relay's positioning between 7 and 14 cm. The transmitter side's input voltage (V_{dc} = 30 V) and the reception coil's distance (d_{tr} = 21 cm) are both fixed at the DC voltage source. This setup makes use of the output obtained on the receiver side to determine how adding a multi-magnetic relay affects the created WPT system's performance.
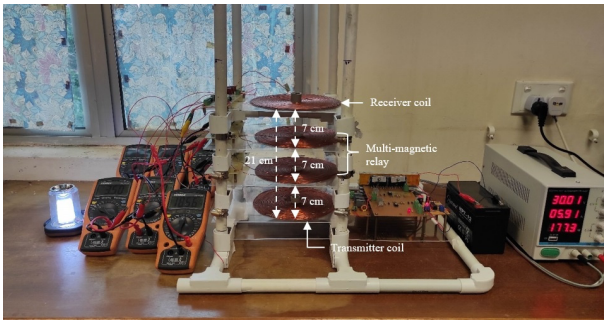
Fig. 10. WPT system with multi-magnetic relay

Results. The study findings are covered in this section, beginning with the development of a 5 kHz frequency in the pulse driver circuit using the microcontroller PIC16F628A-I/P. Additionally, the hardware produced in this research has been used in studies to convert DC to AC as the result waveform on full bridge inverters. Above all, the analysis results of the power development tests are provided by this section, which examines the power output data from the transmitter, receiver, and multi-magnetic relay sides.

Generation of 5 kHz pulse wave. The pulse driver circuit, which has the microcontroller PIC16F628A-I/P as its primary component, produces the 5 kHz frequency. In order to achieve a frequency of 5 kHz, this pulse driver circuit applies frequency through the MOSFETs' gate terminals. Four MOSFETs make up the entire bridge inverter circuit utilized in the driver circuit.

The configuration of the four MOSFETs allows for continuous operation. Simultaneous driving of MOSFET-1, MOSFET-4, MOSFET-2 and MOSFET-3 is observed. In order to provide the transmitter coil with an AC voltage, this is done to reverse the direction of current flow through the coil. This is a result of MOSFET-1 and MOSFET-4 having identical phase angles, ranging from 0° to 180°, configured. In contrast, the phase angles of MOSFET-2 and MOSFET-3 are arranged from 180° to 360°. Stated otherwise, MOSFET-2 and MOSFET-3 are «OFF» when MOSFET-1 and MOSFET-4 are «ON». Conversely, MOSFET-1 and MOSFET-4 are «OFF» when MOSFET-2 and MOSFET-3 are «ON». Thus, Fig. 11 displays the result of the coordination of these four MOSFETs as an output of the hardware that was constructed.
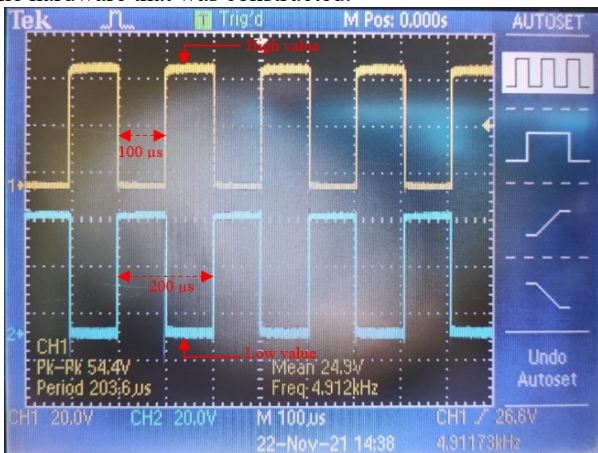
Fig. 11. 5 kHz pulse wave generations

AC voltage waveform and magnetic flux generated on the transmitter coil. The four MOSFETs' rectification produced an AC voltage on the transmitter coil, but it is still not entirely functional. Consequently, in order to change the square waveform into a sinusoidal waveform, a filter is required. Here, the wave filters are a 3 µF capacitor and a 100 µH inductor. Furthermore, when an inductor has electricity flowing through it, it can also produce a magnetic field. The entire magnetic field that flows through the transmitter and receiving coil is measured as magnetic flux. As a result, it is important to choose an inductor value that will produce the intended result. When an excessively big inductor is used, the transmitter coil experiences a lower voltage but a better waveform (sinusoidal waveform). On the other hand, even though the voltage that results is larger, an inductor that is too small cannot provide a perfect sinusoidal waveform.

The results of the transmitter coil voltage pulse waveform in the simulation can be seen in the form of a sine voltage waveform with a half cycle formed in 100 µs and one cycle formed in 200 µs. On the other hand, the pulse waveform generated in the experiment is also a sine wave with a frequency of 4.9 kHz where it is very close to get 5 kHz. Figure 12 shows the rectification result of the square waveform into a sine waveform that occurs in the full bridge inverter and filtering by 3 µF capacitors and 100 µH inductors. Based on the oscilloscope's scale, this is clear. One cycle sine wave's length is composed of two divisions, each taking 100 µs of time. Afterwards, 200 µs is needed to generate one cycle of the AC sine voltage waveform. This indicates that the AC sine voltage waveform has 5000 cycles in a second.
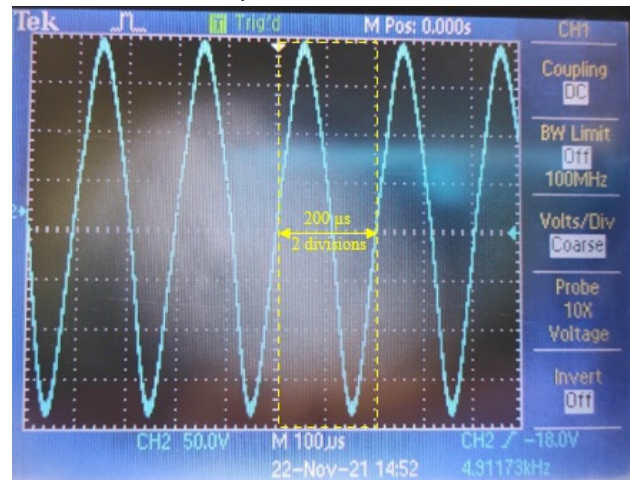
Fig. 12. 5 kHz sine voltage waveform of transmitter coil

In order to generate the magnetic flux (Fig. 13,*b*) following (1), the sine voltage waveform in Fig. 12 is formed (Fig. 13,*a*) with a peak voltage of 50 V. The link between the coil's number of turns and the integral of the voltage on the transmitter coil side is represented by the magnetic flux. The waveform and frequency broadcast in the system are identical to the sine voltage waveform that forms at a frequency of 5 kHz in the transmitter coil.

AC voltage waveform on the transmitter coil, multi-magnetic relay and receiver coil. Verification of the waveform on the multi-magnetic relay and receiver coil has also been done in order to confirm the waveform created in the transmitter coil. Figure 14 displays the verification outcomes for each coil's frequency and waveform.
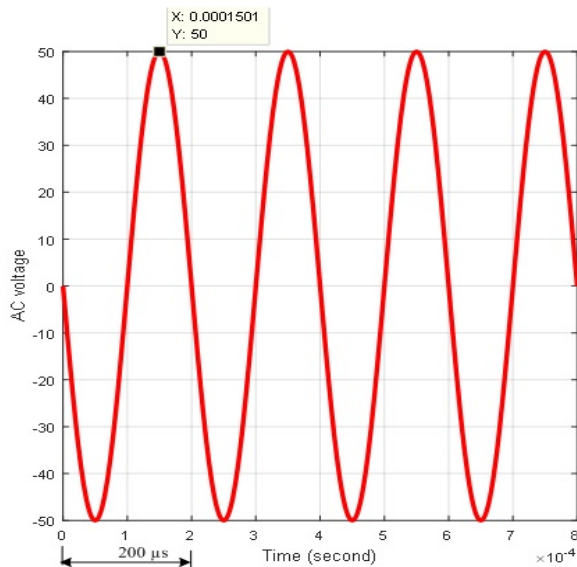
a) sine voltage
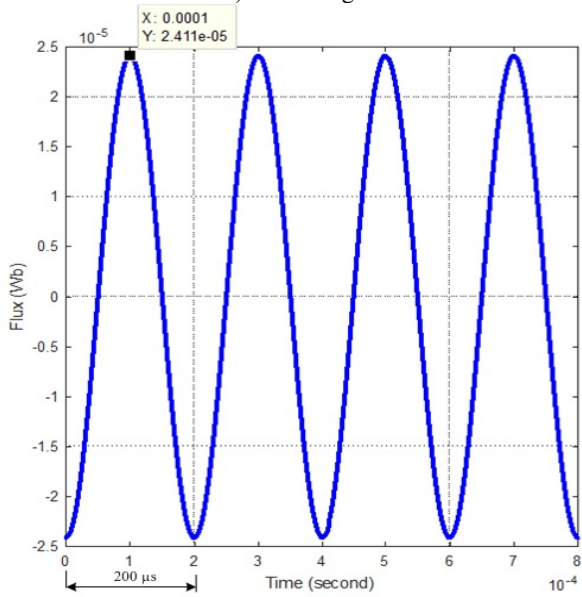
b) magnetic flux

Fig. 13. 5 kHz sine voltage (*a*) and magnetic flux (*b*) waveform on the transmitter coil following (1)
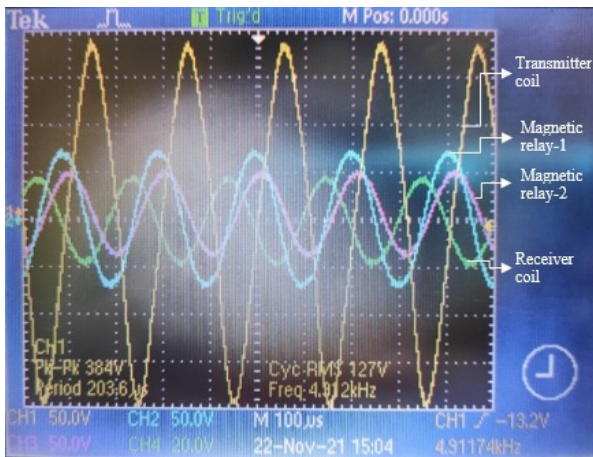
Fig. 14. Waveform and frequency on all coils

The output of the transmitter coil is represented by channel 1 of the oscilloscope, the multi-magnetic relay is represented by channels 2 and 3, and the waveform produced in the reception coil is represented by channel 4.

The output waveform and frequency reported in Fig. 14 reveals almost 5 kHz. It is shown that the WPT system and all coils are working properly and the experiment is ready to proceed in the data gathering and analysis stage.

Performance improvement of 5 kHz WPT system. The impact of incorporating a multi-magnetic relay on the designed WPT system's performance is covered in this subsection. This part also covers the performance comparison between the WPT system with and without multi-magnetic relays based on the output produced in the experiment. The transmitter and receiver coil distances, the constant V_{dc} at 30 V, and the d_{tr} constant at a distance of 21 cm are the settings for the tests conducted in this section. This is done to monitor the performance and determine the best spacing between multi-magnetic relays.

WPT performance with the addition of one magnetic relay. This configuration is done to see how adding a magnetic relay affects the output voltage, current, and power in the receiver side of the developed WPT system. The experiment is set up with the DC voltage source V_{dc} = 30 V, and the distance between the transmitter and receiver coil d_{tr} = 21 cm. Additionally, one magnetic relay is placed between the transmitter and receiver coils with distances set at 3 cm, 6 cm and 9 cm. As a result, a graph of the receiver side output comparison based on the system configuration with a magnetic relay added is displayed in Fig. 15. In contrast, Fig. 16 illustrates the percentage improvement of the WPT system with a magnetic relay added when compared to the WPT system without one.
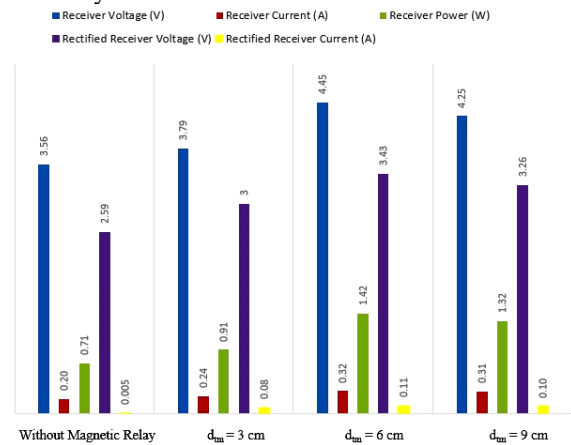
Fig. 15. WPT performance with the addition of one magnetic relay
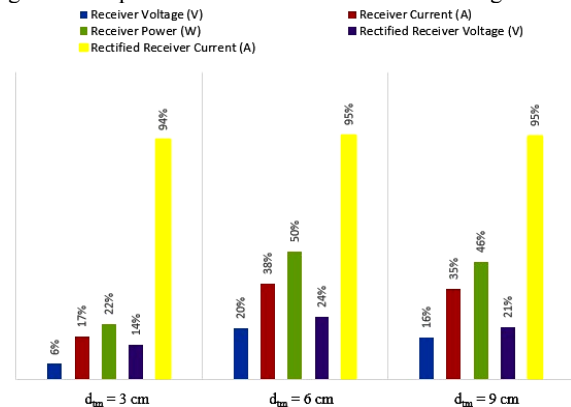
Fig. 16. Improvement of WPT by addition of one magnetic relay in percent (%)

The output of the receiver coil produced from the experiment without a magnetic relay is 3.56 V and 0.2 A

with a power of 0.71 W. However, after adding a magnetic relay, the observed parameters have increased. The power achieved at the magnetic relay point (d_{tm} = 3 cm) is 0.91 W at 3.79 V of voltage and 0.24 A of current. When the magnetic relay is positioned at d_{tm} = 3 cm (Fig. 16) the receiver coil's output improves by 22 % in power, 6 % in voltage, and 17 % in current. Conversely, however, there was also improvement at d_{tm} = 6 and 9 cm. The resulting output experiences a 20 % voltage rise, a 38 % current increase, and a 50 % power gain at d_{tm} = 6 cm. At d_{tm} = 9 cm, there is a 16 % increase in voltage, a 35 % increase in current, and a 46 % increase in power.

The magnetic relay placed 6 cm away from the transmitter coil produced the maximum output that was measured. Stated otherwise, this is the best position relative to other positions. The amount of flux that the magnetic relay can capture can be large at the distance between the transmitter and the magnetic relay, d_{tm} = 3 cm, but the flux cannot completely reach the receiver coil due to the distance between the magnetic relay and the receiving coil being relatively far. Conversely, the output obtained is marginally less than the distance d_{tm} = 6 cm at d_{tm} = 9 cm or higher. This is due to the transmitter coil's action, which is where the flux is initially generated. As a result, the magnetic coil acts to retain the flux in the magnetic field between coils before it escapes. Because of this, the flux received at d_{tm} = 6 cm is more than at d_{tm} = 9 cm or higher, but it is still capable of reaching the receiver coil with magnetic flux. As is well known, mutual induction involves a magnetic coil in addition to the transmitter and receiver coils in this experiment.

This experiment involves rectifying the waveform from AC to DC in addition to the process of power transfer between the coils. Rectifiers or AC-DC converters are used in the rectification process. Because the created WPT system operates at a frequency of 5 kHz and prevents it from being delivered directly to the load, this rectification procedure is necessary. The trend of the observed DC voltage and the AC parameters in the receiver coil are consistent (Fig. 15, 16). But the outcome of the rectification is marginally less than the input, which in this instance is the receiver coil. This results from a decrease brought on by the rectifier circuit's kind of diodes' threshold voltage value.

WPT performance with the addition of multi-magnetic relay. This experiment is comparable to the one discussed previously, but it adds a multi-magnetic relay (two coils). The distance between the transmitter and receiver coils, d_{tr} = 21 cm, and the DC voltage source, which serves as the transmitter side's DC input voltage, are both fixed at V_{dc} = 30 V. The multi-magnetic relay is positioned at a distance of 7 and 14 cm from the transmitter and receiving coils, respectively. By using the output received on the receiver side, this setup is done to observe how adding a multi-magnetic relay affects the created WPT system's performance. Consequently, a comparison graph of the WPT system's performance that was enhanced by the addition of a multi-magnetic relay is displayed in Fig. 17. Furthermore, a comparison of the percentage improvement that happens when the system uses a multi-magnetic relay is shown in Fig. 18.

The performance of the WPT system with a multi-magnetic relay is compared to the experiment without a magnetic relay and with the addition of one magnetic relay

(one coil) in Fig. 17. Using one magnetic relay at d_{tm} = 6 cm, the maximum receiver power in the experiment is utilized as a comparison, with reference to Fig. 17, 18. As a result, with a voltage gain of 0.58 V (12 %) and a current improvement of 0.11 A (26 %), the receiver power received at the receiver coil by 0.74 W, or 34 %. Concurrently, the experiment's receiver power increased by roughly 1.45 W, or 67 %, from the system without a magnetic relay to the one with a multi-magnetic relay added. The system also had a higher voltage difference of 1.47 V, or 29 % higher, and a higher current difference of 0.12 A, or 53 % higher, than the system without a multi-magnetic relay.
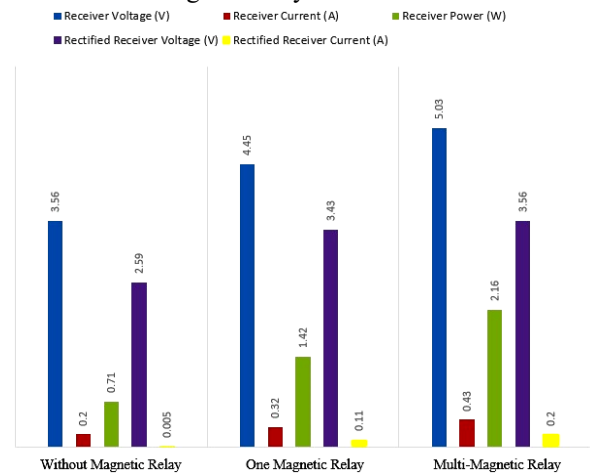
Fig. 17. WPT performance with the addition of multi-magnetic relay
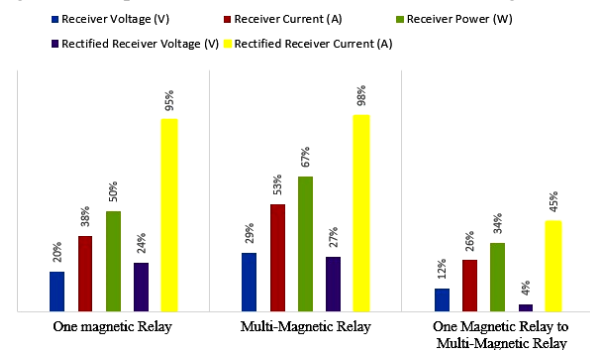
Fig. 18. Improvement of WPT by addition of multi-magnetic relay in percent (%)

Conclusions. The purpose of this research is to create a circular planar spiral coil with an appropriate inductance value for the 5 kHz matching frequency. The following conclusions can be been conducted.

1. A circular planar spiral coil is developed by designing and calculating a number of parameters, including the number of turns, inner and outer diameter, wire diameter and the spacing between turns. According to the findings, 338 µH is the proper circular planar spiral coil inductance value for the 5 kHz WPT system.

2. System performance is improved when a multi-magnetic circular planar spiral relay is incorporated into the WPT system. Consequently, there was a 67 % improvement in the power received at the receiver coil, going from 0.71 W to 2.16 W.

3. The percentage error between simulation and experiment is still less than 10 %, according to the validation data. This indicates that the WPT system hardware created for this investigation is dependable and matches the simulation.

Conflict of interest. The authors declare that they have no conflicts of interest.

REFERENCES

1. Ouacha B., Bouyghf H., Nahid M., Abenna S. DEA-based on optimization of inductive coupling for powering implantable biomedical devices. *International Journal of Power Electronics and Drive Systems (IJPEDS)*, 2022, vol. 13, no. 3, pp. 1558-1567. doi: https://doi.org/10.11591/ijpeds.v13.i3.pp1558-1567.
2. Meor M., Yusop Y., Saat S., Hasan K.K. Performance comparison of capacitive power transfer between Matching Resonant Circuit π1a and π1b at 13.56 MHz Operating Frequency. *International Journal of Power Electronics and Drive Systems (IJPEDS)*, 2022, vol. 13, no. 3, pp. 1614-1624. doi: https://doi.org/10.11591/ijpeds.v13.i3.pp1614-1624.
3. Vidya R., Keshavan B.K. Optimizing Performance Parameters of Stationary Wire Free Power Transfer Circuit. *International Journal of Power Electronics and Drive Systems (IJPEDS)*, 2023, vol. 14, no. 3, pp. 1309-1321. doi: https://doi.org/10.11591/ijpeds.v14.i3.pp1309-1321.
4. Hasan K.K., Saat S., Yusop Y., Awal M.R. Development of Self-Charging Unmanned Aerial Vehicle System Using Inductive Approach. *International Journal of Power Electronics and Drive Systems (IJPEDS)*, 2022, vol. 13, no. 3, pp. 1635-1644. doi: https://doi.org/10.11591/ijpeds.v13.i3.pp1635-1644.
5. Ragab A., Marei M.I., Mokhtar M., Abdelsattar A. Design and performance evaluation of a PV interface system based on inductive power transfer. *International Journal of Power Electronics and Drive Systems (IJPEDS)*, 2021, vol. 12, no. 1, pp. 364-373. https://doi.org/10.11591/ijpeds.v12.i1.pp364-373.
6. Obais A.M., Ruzij A.F. Design and Implementation of An Efficient WPT System. *International Journal of Power Electronics and Drive System (IJPEDS)*, 2020, vol. 11, no. 2, pp. 711-725. doi: https://doi.org/10.11591/ijpeds.v11.i2.pp711-725.
7. Lee C.H., Jung G., Hosani K.A., Song B., Seo D., Cho D. Wireless Power Transfer System for an Autonomous Electric Vehicle. *2020 IEEE Wireless Power Transfer Conference (WPTC)*, 2020, pp. 467-470. doi: https://doi.org/10.1109/WPTC48563.2020.9295631.
8. Nama J.K., Kumar Verma A. An Efficient Wireless Charger for Electric Vehicle Battery Charging. *2020 IEEE 9th Power India International Conference (PIICON)*, 2020, pp. 1-5. doi: https://doi.org/10.1109/PIICON49524.2020.9112972.
9. Siddique M.N.I., Ahmed N., Abdullah S.M., Khan M.Z.R. An automated transmitter positioning system for misalignment compensation of capacitive-coupled electric vehicles. *International Journal of Electrical and Computer Engineering (IJECE)*, 2022, vol. 12, no. 4, pp. 3505-3516. doi: https://doi.org/10.11591/ijece.v12i4.pp3505-3516.
10. Butar-Nutar A.H., Leong J., Irwanto M. Effect of DC voltage source on the voltage and current of transmitter and receiver coil of 2.5 kHz wireless power transfer. *Bulletin of Electrical Engineering and Informatics*, 2020, vol. 9, no. 2, pp. 484-491. doi: https://doi.org/10.11591/eei.v9i2.2060.
11. Yamaguchi K., Okamura R., Terada H., Iida K. Experimental Review of An Improving System on Wireless Power Transfer Via Auto Tuning of Frequency. *International Journal of Electrical and Computer Engineering (IJECE)*, 2023, vol. 13, no. 2, pp. 1314-1319. doi: https://doi.org/10.11591/ijece.v13i2.pp1314-1319.
12. Janardhan G., Surendra Babu N.N.V., Srinivas G.N. Single phase transformerless inverter for grid connected photovoltaic system with reduced leakage current. *Electrical Engineering & Electromechanics*, 2022, no. 5, pp. 36-40. doi: https://doi.org/10.20998/2074-272X.2022.5.06.
13. Parimalasundar E., Muthukaruppasamy S., Dharmaprakash R., Suresh K. Performance investigations of five-level reduced switches count H-bridge multilevel inverter. *Electrical Engineering & Electromechanics*, 2023, no. 6, pp. 58-62. doi: https://doi.org/10.20998/2074-272X.2023.6.10.

14. Gu H.-S., Choi H.-S. Analysis of Wireless Power Transmission Characteristics for High-Efficiency Resonant Coils. *IEEE Transactions on Applied Superconductivity*, 2020, vol. 30, no. 4, pp. 1-4. doi: https://doi.org/10.1109/TASC.2020.2966424.
15. Nazieha Nanda N., Hajar Yusoff S., Fauziah Toha S., Fadzlin Hasbullah N., Shafina Roszaidie A. A brief review: basic coil designs for inductive power transfer. *Indonesian Journal of Electrical Engineering and Computer Science*, 2020, vol. 20, no. 3, pp. 1703-1716. doi: https://doi.org/10.11591/ijeecs.v20.i3.pp1703-1716.
16. Alghrairi M., Sulaiman N., Hasan W.Z.W., Jaafar H., Mutashar S. Efficient wireless power transmission to remote the sensor in restenosis coronary artery. *Indonesian Journal of Electrical Engineering and Computer Science*, 2022, vol. 25, no. 2, pp. 771-779. doi: https://doi.org/10.11591/ijeecs.v25.i2.pp771-779.
17. Irwanto M., Nugraha Y.T., Hussin N., Nisja I. Effect of temperature and solar irradiance on the performance of 50 Hz photovoltaic wireless power transfer system. *Jurnal Teknologi*, 2023, vol. 85, no. 2, pp. 53-67. doi: https://doi.org/10.11113/jurnalteknologi.v85.18872.
18. Tian Y., Lin Y., Tian J., Xiang L. Multi-thread sensing coil design for metal object detection of wireless power transfer systems. *Measurement*, 2021, vol. 184, art. no. 109952. doi: https://doi.org/10.1016/j.measurement.2021.109952.
19. Usikalu M.R., Adewole S.A., Achuka J.A., Adagunodo T.A., Abodunrin T.J., Obafemi L.N. Investigation into Wireless Power Transfer in near Field using Induction Technique. *Journal of Physics: Conference Series*, 2019, vol. 1299, no. 1, art. no. 012047. doi: https://doi.org/10.1088/1742-6596/1299/1/012047.
20. Okoyeigbo O., Olajube A.A., Shobayo O., Aligbe A., Ibhaze A.E. Wireless power transfer: a review. *IOP Conference Series: Earth and Environmental Science*, 2021, vol. 655, no. 1, art. no. 012032. doi: https://doi.org/10.1088/1755-1315/655/1/012032.
21. Kurniawan T.A., Gumilang R.B., Wibisono G. Coil Inductance Design for Low Power Hybrid Wireless Power Transfer. *IOP Conference Series: Materials Science and Engineering*, 2020, vol. 771, no. 1, art. no. 012014. doi: https://doi.org/10.1088/1757-899X/771/1/012014.
22. Ha-Van N., Simovski C.R., Asadchy V.S., Tretyakov S.A. Mid-range wireless power transfer: anapoles or magnetic dipoles? *Physica Scripta*, 2024, vol. 99, no. 2, art. no. 025518. doi: https://doi.org/10.1088/1402-4896/ad1b86.
23. Mohamad Yusoff A.A., Ahmad K.A., Sulaiman S.N., Hussain Z., Abdullah N. Air cavity-based vibrational piezoelectric energy harvesters. *Electrical Engineering & Electromechanics*, 2021, no. 5, pp. 39-45. doi: https://doi.org/10.20998/2074-272X.2021.5.06.
24. Krylov D.S., Kholod O.I. The efficiency of the active controlled rectifier operation in the mains voltage distortion mode. *Electrical Engineering & Electromechanics*, 2021, no. 2, pp. 30-35. doi: https://doi.org/10.20998/2074-272X.2021.2.05.
25. Krylov D.S., Kholod O.I. Active rectifier with a fixed modulation frequency and a vector control system in the mode of bidirectional energy flow. *Electrical Engineering & Electromechanics*, 2023, no. 6, pp. 48-53. doi: https://doi.org/10.20998/2074-272X.2023.6.08.
26. Irwanto M., Ali M.B., Nugraha Y.T., Ismail B., Nisja I., Leow W.Z. Analysis on the Effect of DC Current Changes on the Magnetic Field of Wireless Power Transfer. *2023 IEEE 14th Control and System Graduate Research Colloquium (ICSGRC)*, 2023, pp. 186-191. doi: https://doi.org/10.1109/ICSGRC57744.2023.10215406.

M. Irwanto[1], *PhD, Associate Professor,*
L.K.W. Kita[2], *MSc, Lecturer,*
[1] Department of Electrical Engineering,
Faculty of Science & Technology,
Universitas Prima Indonesia, Medan, Indonesia,
e-mail: muhammadirwanto@unprimdn.ac.id (Corresponding Author)
[2] Department of Electrical Engineering,
Politeknik Negeri Batam, Indonesia,
e-mail: wisnulalu@polibatam.ac.id

C.D. Tran, M. Kuchar, P.D. Nguyen

Research for an enhanced fault-tolerant solution against the current sensor fault types in induction motor drives

*Introduction. Recently, three-phase induction motor drives have been widely used in industrial applications; however, the feedback signal failures of current sensors can seriously degrade the operation performance of the entire drive system. Therefore, the motor drives require a proper solution to prevent current sensor faults and improve the reliability of the motor drive systems. **The novelty** of the proposed research includes integrating the current sensor fault-tolerant control (FTC) function according to enhanced technique into the field-oriented control loop for speed control of the motor drive system. **Purpose.** This research proposes a hybrid method involving a third difference operator and signal comparison algorithm to diagnose various types of current sensor faults as a positive solution to enhance the stability of the induction motor drive system. **Methods.** A hybrid method involving a third difference operator for the measured speed signals and a comparison algorithm between measured and estimated current signals are proposed to diagnose the current sensors' health status in the fault-tolerant process. After determining the faulty sensor, the estimated current signals based on the Luenberger observer are used immediately to replace the defective sensor signal. **Results.** The current sensor is simulated with various failure types, from standard to rare failures, to evaluate the performance of the FTC method implemented in the MATLAB/Simulink environment. Simultaneously, a fault flag corresponding to a defective sensor should be presented as an indicator to execute the repair process for faulty sensors at the proper time. **Practical value.** Positive results have proven the feasibility and effectiveness of the proposed FTC integrated into the speed controller to improve reliability and ensure the stable operation of the induction motor drive system even under current sensor fault conditions.* References 29, tables 3, figures 10.
Key words: **current sensor fault, estimated current, fault-tolerant control, field-oriented control, induction motor drive.**

*Вступ. Останнім часом трифазні приводи з асинхронними двигунами широко використовуються у промисловості; однак відмови сигналу зворотного зв'язку датчиків струму можуть погіршити експлуатаційні характеристики всієї системи приводу. Тому для електроприводів потрібне належне рішення для запобігання відмов датчиків струму та підвищення надійності систем приводу. **Новизна** пропонованого дослідження полягає в інтеграції функції відмовостійкого управління датчиком струму (FTC) відповідно до вдосконаленої методики в контур управління полем для управління швидкістю системи приводу. **Мета**. У цьому дослідженні пропонується гібридний метод, що включає оператор третьої різниці та алгоритм порівняння сигналів для діагностики різних типів відмов датчиків струму як позитивне рішення для підвищення стійкості системи приводу з асинхронним двигуном. **Методи**. Пропонується гібридний метод, що включає оператор третьої різниці для виміряних сигналів швидкості та алгоритм порівняння між виміряними та оціночними сигналами струму, для діагностики стану справності датчиків струму у відмовостійкому процесі. Після визначення несправного датчика сигнали оцінки струму на основі спостерігача Люенбергера негайно використовуються для заміни сигналу несправного датчика. **Результати**. Датчик струму моделюється з різними типами відмов, від стандартних до рідкісних відмов, з метою оцінки продуктивності методу FTC, реалізованого у середовищі MATLAB/Simulink. Одночасно прапорець несправності, що відповідає несправному датчику, повинен бути представлений як індикатор для виконання процесу ремонту несправних датчиків у належний час. **Практична цінність**. Позитивні результати довели здійсненність та ефективність пропонованого FTC, інтегрованого в регулятор швидкості, для підвищення надійності та забезпечення стабільної роботи системи приводу з асинхронним двигуном навіть в умовах несправності датчика струму.. Бібл. 29, табл. 3, рис. 10.
Ключові слова: **несправність датчика струму, розрахунковий струм, відмовостійке керування, орієнтоване на поле керування, привід з асинхронним двигуном.**

Introduction. Three-phase induction motors (3~IM) with the advantages of size, reliability, performance, and flexible control are currently widely used electrical machines in various fields [1, 2], such as industry, transportation, agriculture and so on. A system that includes a 3~IM connecting to the load, an inverter power, a sensor system, and a controller is called the induction motor drive (IMD). Modern speed control techniques applying inverter technology for IMD include two primary control groups: scalar and vector technique control [3, 4]. The principle of the scalar control method is based on keeping the flux according to the *V/f* ratio. This method has advantages: it is a simple control algorithm and has a low cost. However, the control performance is low and only used for simple applications. In contrast, the group of vector control methods, typically the field-oriented control (FOC) method, has high performance, but complex control algorithms and high costs are used for applications requiring high precision [5, 6]. Modern 3~IMD structure includes four main parts: motor, voltage source inverter, controller integrated control algorithm, and sensor system.

Problems and the relevance. All of the parts in the IMD's structure play an essential role in the system's stable operation. Hence, the accuracy of the sensors is vital to ensuring the stability of the drive system [7, 8]. Loss of connection or accuracy of sensor feedback signals can lead to function degradation or damage to the motor drive system. Therefore, it is necessary to develop functions against sensor faults to improve the reliability of the motor drive system; the function is called the fault-tolerant control (FTC) technique [9, 10]. A comprehensive sensor FTC function includes three distinct processes: fault diagnosis, fault signal isolation, and reconfiguration to maintain stable operation under fault conditions. During the fault diagnosis stage, the health status of the sensor should be determined, and any faulty sensor needs to be accurately located. Faulty sensors must be isolated immediately whenever a fault condition is identified. Immediately, the signal from this faulty sensor must be replaced with an estimated signal; in other words, switch from sensor control mode to sensorless control [11, 12].

Review of recent publications about the FTC and unsolved tasks. The sensor system in the motor drive system includes two types of sensors: the current sensor and the speed sensor. Therefore, research on sensor faults is also divided into two subjects: the speed sensor fault (SSF)

and the current sensor fault (CSF). Most research on sensor FTC focuses on completely damaged or disconnected faults, where the feedback signals to the controller become zero. Corresponding to this fault type, with SSF cases, diagnosis methods mainly rely on comparison algorithms between measured and estimated signals [13–15]; with the CSF cases, various techniques exist for diagnosing sensor failures, such as relying on the difference between the measured signal and the estimated signal [16], phase imbalance and missing error phase [17], or sudden changes in the measured signal [18, 19], or using a mixed evaluation index [20]. However, besides total damaged failure, several other types of fault can occur for current sensors, but most studies pay little attention to them.

Purpose of the paper. This research proposes a hybrid method involving a third difference operator (TDO) and signal comparison algorithm [21] to diagnose various types of current sensor faults, such as bias, drift, and gain fault [22] as a positive solution to enhance the stability of the IMD system. Once the faulty sensor is identified, current signals estimated based on direct estimators [23, 24] or observers like Luenberger [25, 26] are used instead of the faulty current signal.

FTC solution against the current sensor failure for 3~IMDs. This section briefly describes an IMD model integrating the current sensor-FTC function, various types of CSF, and the applied FTC algorithm. The motor modeling operations and the Clarke and Park transformations are also summarized to clarify the proposed FTC solution.

A. IMD model integrating the current sensor FTC function. The structure of the IMD includes a 3~IM connecting to the load, an inverter power, a sensor system, and a controller (Fig. 1). An FTC algorithm is integrated into the controller function to enhance the CSF protection feature (Fig. 1). FTC block receives the stator current and rotor speed as input signals for calculating the corresponding estimated quantities to implement the fault diagnosis algorithm (Fig. 2).
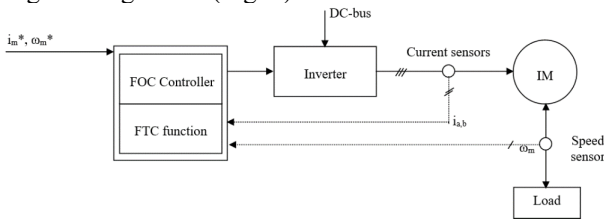
Fig. 1. 3~IMD integrated FTC function
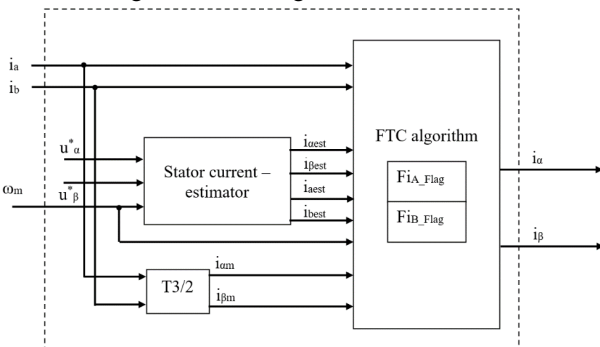
Fig. 2. FTC function block

In the FTC function block, the current estimator receives the measured motor speed and calculated stator voltage from the DC-link, combining inverter switching

impulse [27] to generate the estimated current by proper methods. The estimated and measured current signals are provided for implementing the CSF diagnosis algorithm [21] and providing proper current signals to the FOC controller. The estimation equation system of the virtual currents based on the Luenberger observer [28, 29] is presented briefly below:

$$\frac{di_{S\alpha}}{dt} = -E_1 i_{S\alpha} + E_2 \psi_{R\alpha} + E_3 \psi_{R\beta} + E_4 u_{S\alpha}^* - L_1 i_{S\alpha} + L_2 i_{S\beta} ; (1)$$

$$\frac{di_{S\beta}}{dt} = -E_1 i_{S\beta} - E_3 \psi_{R\alpha} + E_2 \psi_{R\beta} + E_4 u_{S\beta}^* - L_1 i_{S\beta} - L_2 i_{S\alpha} ; (2)$$

$$\frac{d\psi_{R\alpha}}{dt} = E_5 i_{S\alpha} - E_6 \psi_{R\alpha} - E_7 \psi_{R\beta} - L_3 i_{S\alpha} + L_4 i_{S\beta} ; (3)$$

$$\frac{d\psi_{R\beta}}{dt} = E_5 i_{S\beta} + E_7 \psi_{R\alpha} - E_6 \psi_{R\beta} + L_3 i_{S\beta} - L_4 i_{S\alpha} ; (4)$$

where

$$E_1 = \frac{\left(L_R^2 R_S + L_m^2 R_R\right)}{\sigma L_S L_R^2} ; \quad E_2 = \frac{L_m R_R}{\sigma L_S L_R^2} ; \quad E_3 = \frac{L_m \omega_r}{\sigma L_S L_R} ;$$

$$E_4 = \frac{1}{\sigma L_S} ; \quad E_5 = \frac{L_m R_R}{L_R} ; \quad E_6 = \frac{R_R}{L_R} ; \quad E_7 = \omega_r ;$$

$$L_1 = (h-1)\left(\frac{1}{\sigma T_S} + \frac{1}{\sigma T_R}\right) ; \quad L_2 = -(h-1)\omega_r ;$$

$$L_3 = \left(h^2 - 1\right)\left[\left(\frac{1}{\sigma T_S} + \frac{1}{\sigma T_R}\right)\frac{\sigma L_m L_S}{L_R} - \frac{L_m}{T_R}\right] +$$

$$+ \frac{\sigma L_m L_S}{L_R}\left(\frac{1}{\sigma T_S} + \frac{1}{\sigma T_R}\right)(h-1) ;$$

$$L_4 = -(h-1)\frac{\sigma L_m L_S}{L_R}\omega_r ; \quad T_S = \frac{L_S}{R_S} ; \quad T_R = \frac{L_R}{R_R} ;$$

$$\sigma = \frac{L_S L_R - L_m^2}{L_S L_R} ; \quad h = \text{const} > 1 ;$$

R_S, R_R are the stator and rotor resistance; L_S, L_R, L_m are the stator, rotor and magnetizing inductance; $\omega_r = p\omega_m$ is the rotor speed; p is the number of pole pairs; $i_{S\alpha}$, $i_{S\beta}$, $u_{S\alpha}^*$, $u_{S\beta}^*$, $\psi_{R\alpha}$, $\psi_{R\beta}$, are the stator current, voltage and rotor flux components in the stationary frame;

The real-time stator current can be converted to the stationary coordinate system using the Clarke formula (5) and the inverse transformation (6):

$$\begin{bmatrix} i_\alpha \\ i_\beta \end{bmatrix} = \begin{bmatrix} 1 & 0 \\ 1/\sqrt{3} & 2/\sqrt{3} \end{bmatrix}\begin{bmatrix} i_a \\ i_b \end{bmatrix} ; \quad (5)$$

$$\begin{bmatrix} i_a \\ i_b \end{bmatrix} = \begin{bmatrix} 1 & 0 \\ -1/2 & \sqrt{3}/2 \end{bmatrix}\begin{bmatrix} i_\alpha \\ i_\beta \end{bmatrix} . \quad (6)$$

B. Current sensor failure types. During the operation of the IMD, under the influence of various factors of the operating environment such as temperature, vibration, electromagnetic field impact, and deterioration of equipment life, sensors may be damaged or degraded function. A sensor is considered faulty when its signal to the controller seriously deviates beyond the available threshold compared with the actual signal. Some typical types of sensor faults considered in the FTC technique correspond to soft fault type: drift, scale, bias, precision degradation, and

hard fault type (total failures): constant feedback value, constant feedback value with noise, and bottom noise [22]. Suppose the measurement standard deviation of the sensors is ignored. In that case, the mathematical expressions describing the sensor fault types are presented in Table 1 and Fig. 3 according to the types of CSF signals.

Table 1
Mathematical expressions according to sensor fault types

Type	Expression	Note
Soft fault		- $i_m(t)$ is the measured phase current corresponding to the fault type;
Drift	$i_m(t)=i(t)+a+bt$	
Scale	$i_m(t)=Ki(t)$	
Bias	$i_m(t)=i(t)+K$	- $i(t)$ is the true value of the measured phase current;
Precision degradation	$i_m(t)=i(t)+e(t)$	
Hard fault		- a, b, K are the constants corresponding to the fault type;
Constant	$i_m(t)=K$	
Constant with noise	$i_m(t)=K+e(t)$	- $e(t)$ is the excessive random noise;
Bottom noise	$i_m(t)=0+e(t)$	- t is the time variable
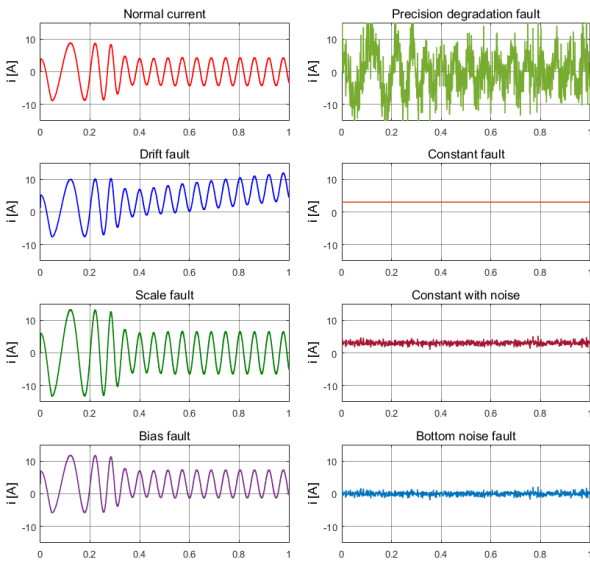
Fig. 3. Graphical signals of healthy state and fault state types of the phase current

C. FTC against current sensor failures. A hybrid method involving a TDO for the measured rotor speed and a comparison algorithm of estimated and measured current signals is applied to diagnose the current sensors' health status. First, the TDO algorithm corresponding to (7) is used to check whether there are signs of failure with the speed sensor:

$$\text{If } (TDO_w \geq Th_w) \ \{ F_{TDO_w} = 1 \}, \quad (7)$$

where $TDO_w = \left| \Delta^3 w(p) \right|$;

$$\begin{cases} 1^{st} \text{ operator}: \Delta^1 w(p) = w(p) - w(p-1); \\ 2^{nd} \text{ operator}: \Delta^2 w(p) = \Delta^1 w(p) - \Delta^1 w(p-1); \\ 3^{rd} \text{ operator}: \Delta^3 w(p) = \Delta^2 w(p) - \Delta^2 w(p-1); \end{cases}$$

where p is the current sampling time; $(p-1)$ is the previous sampling time; Th_w is the defined threshold selected to determine the fault state of the speed sensors. The threshold can be chosen with a value 10 % corresponding to the reference speed, as shown in [21].

Then, suppose the measured speed signal is determined the normality state. In that case, the estimated and measured

signal comparison algorithms are implemented to check the current sensor faults, as in (8) and (9):

$$\text{If } \left(\left| i_{j-m} - i_{j-est} \right| > Th_i \right) \{ F_{COMj} = 1 \}; \text{ else } \{ F_{COMj} = 0 \}, \quad (8)$$

$$\text{If } \left((! F_{TDO_w}) \text{ and } F_{COMj} \right) = 1; \ \{ F_j = 1 \}; \text{ else } \{ F_j = 0 \}, \quad (9)$$

where i_{j-m} are the measured current signals of i_a, i_b; i_{j-est} is the estimated current signals of $i_{a\ est}$, $i_{b\ est}$; F_j is the fault indication flag for each current sensor; Th_i is the threshold selected to determine the fault state of the current sensor with a value 10 %.

Remark: The «NOT» operator in (9) ensures that the measured rotor speed signal is in good condition, which means the estimated current signal is correct.

If the fault indication flags are low, the FTC function will transfer the feedback-measured current to the FOC controller. Otherwise, if the fault indication flags are high, the FTC unit will provide the corresponding estimated current signals for the speed control in IMD. The principle of the FTC unit is shown in Table 2.

Table 2
Judgment of FTC function

Fault indication flag	Current sensor status	The output
$F_{IA} = 0$, $F_{IB} = 0$	Normal	$i_{\alpha m}$, $i_{\beta m}$
$F_{IA} = 1$, $F_{IB} = 0$	A-phase fault	$i_{\alpha\ est}$, $i_{\beta\ est}$
$F_{IA} = 0$, $F_{IB} = 1$	B-phase fault	$i_{\alpha\ est}$, $i_{\beta\ est}$

Simulation results. The operation of the 3~IMD using the FOC method is carried out in the normal speed zones, and the failures corresponding to seven types of current faults are simulated to evaluate the performance of the FTC solution integrated into the controller. The machine parameters of the motor are shown in Table 3.

Table 3
Parameters of the induction motor

Rated power, W	2200
Rated voltage, V	400
Nominal speed, rpm	1420
Pole pairs number	2
Stator resistance, Ω	3.179
Rotor resistance, Ω	2.118
Stator inductance, H	0.209
Rotor inductance, H	0.209
Magnetizing inductance, H	0.192

A reference speed will be set, including acceleration from 0 to 500 rpm in 0.3 s, and kept constant throughout the operation. CSF types are simulated to test the speed controller's FTC performance. Corresponding to the soft faults of the current sensors, drift fault, scale fault, bias fault, and precision degradation are simulated to investigate the performance of the proposed FTC method.

In Fig. 4, the motor is operating stably; when 1.2 s a drift-fault occurs at phase A (Fig. 4,*a*), the FTC function immediately operates to diagnose the fault accurately and quickly, and the phase A current fault flag is pushed high while the corresponding phase B fault flag remains low (Fig. 4,*b*). The estimated current replaces the measured current signal, making the IMD stable.

In Fig. 5, similar to the first case, a scale fault occurs at phase B (Fig. 5,*a*); the FTC function immediately operates to diagnose the scale fault at the fault phase, and the phase B current fault flag is pushed high while the corresponding phase A fault flag remains low (Fig. 5,*b*).
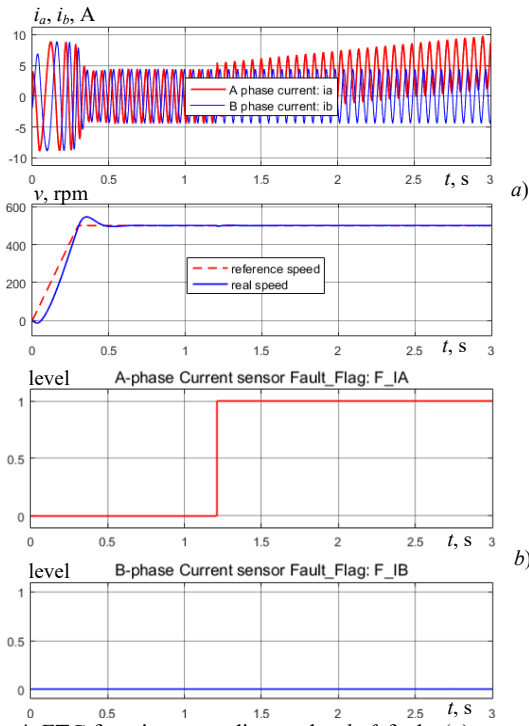
Fig. 4. FTC function according to the _drift_ fault: (*a*) measured phase currents and motor speed; (*b*) the fault-indication-flags
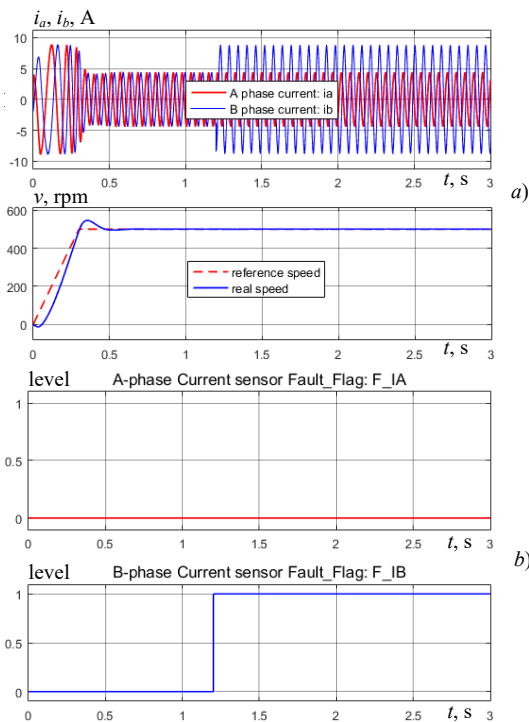
Fig. 5. FTC function according to the _scale_ fault: (*a*) measured phase currents and motor speed; (*b*) the fault-indication-flags

In Fig. 6, the bias fault occurs at phase A (Fig. 6,*a*), the FTC function diagnoses the fault at phase A, and the phase B fault flag remains low (Fig. 6,*b*).

In Fig. 7, the final fault in the soft fault group, the precision degradation fault, occurs at phase B (Fig. 7,*a*), and the FTC function operates precisely according to the proper indication fault flags (Fig. 7,*b*).

Next simulation cases corresponding hard fault types: a constant feedback value of the phase A current corresponds to a value of 3 A (Fig. 8,*a*), constant feedback value with

noise, phase B current value is a noise around the value 3 A (Fig. 9,*a*), bottom noise is around zero in phase A (Fig. 10,*a*). The FTC function accurately identified the faulty sensor locations in Fig. 8,*b*, 9,*b*, and 10,*b*, respectively. The estimated current is used instead of the measured current to supply the FOC loop and control the motor speed stably and accurately.
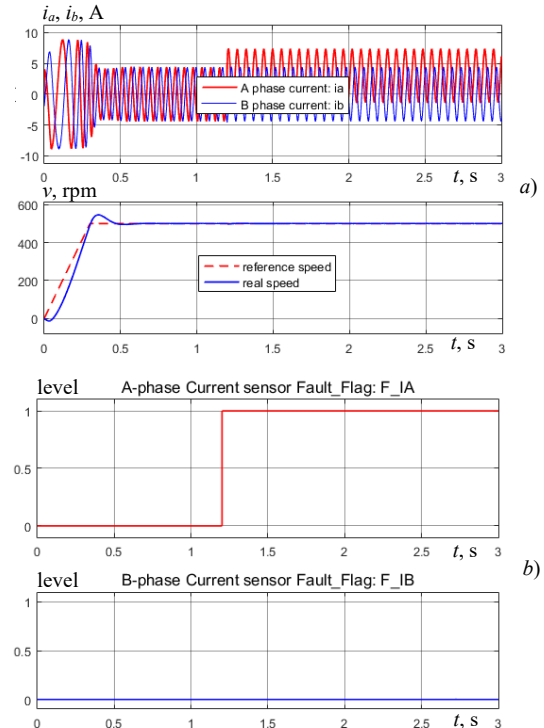
Fig. 6. FTC function according to the _bias_ fault: (*a*) measured phase currents and motor speed; (*b*) the fault-indication-flags
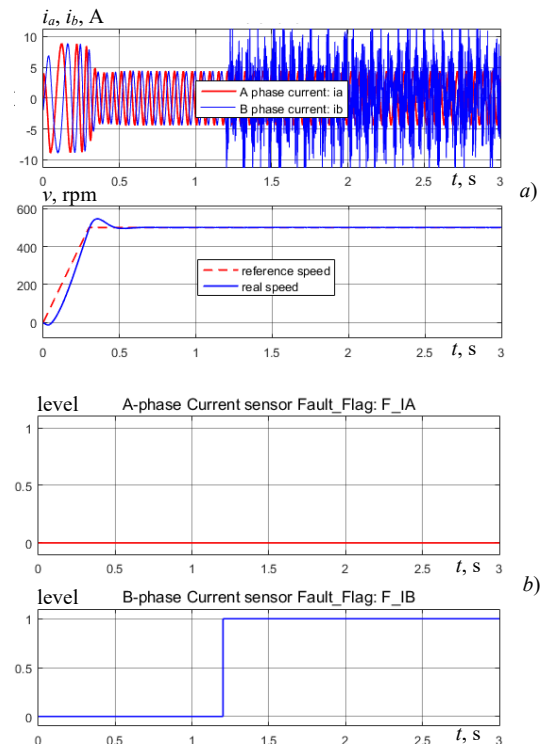
Fig. 7. FTC function according to the _precision degradation fault_: (*a*) measured phase currents and motor speed; (*b*) the fault-indication-flags
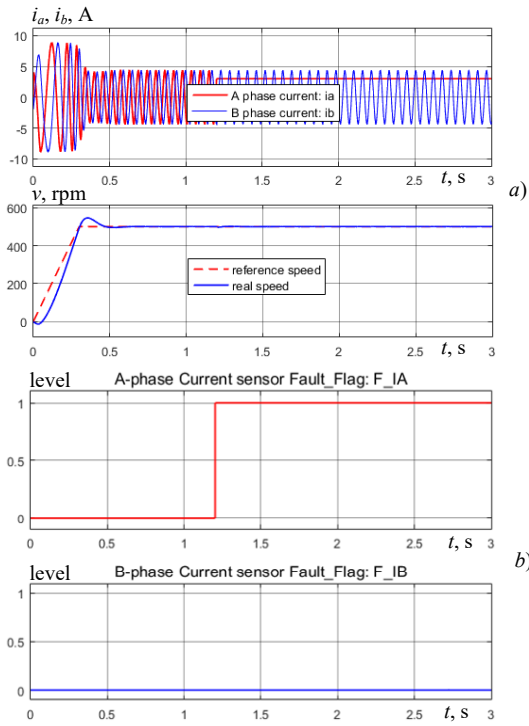
Fig. 8. FTC function according to the *constant feedback value*:
(*a*) measured phase currents and motor speed;
(*b*) the fault-indication-flags

Fig. 9. FTC function according to the *constant feedback value with noise*: (*a*) measured phase currents and motor speed;
(*b*) the fault-indication-flags

Fig. 10. FTC function according to the *bottom noise*:
(*a*) measured phase currents and motor speed;
(*b*) the fault-indication-flags

Then, the comparison algorithm between the measured and the estimated signals of each current phase is used to determine whether a discrepancy occurs or not. After determining the healthy status of each current sensor, if both current sensors are healthy, the measured currents are sent to the field-oriented control loop. If a failure occurs with any current sensors, the feedback signal corresponds to the estimated currents.

Through the results achieved, the proposed fault-tolerant control method has proven to be effective in accurately determining the health and location of the faulty phase currents in all simulation cases. The induction motor drive has enhanced stability and reliability in the motor control process, corresponding to the current sensor's health status.

Conflict of interest. The authors declare that they have no conflicts of interest.

REFERENCES
1. Chan T., Shi K. *Applied Intelligent Control of Induction Motor Drives*. John Wiley & Sons (Asia) Pte Ltd, 2011. 421 p. doi: https://doi.org/10.1002/9780470825587.
2. Ibrar A., Ahmad S., Safdar A., Haroon N. Efficiency enhancement strategy implementation in hybrid electric vehicles using sliding mode control. *Electrical Engineering & Electromechanics*, 2023, no. 1, pp. 10-19. doi: https://doi.org/10.20998/2074-272X.2023.1.02.
3. Pena J.M., Diaz E.V. Implementation of V/f scalar control for speed regulation of a three-phase induction motor. *2016 IEEE ANDESCON*, 2016, pp. 1-4. doi: https://doi.org/10.1109/ANDESCON.2016.7836196.

Conclusions. A hybrid method combining a third difference operator for the measured rotor speed and comparison algorithms of phase current signals is proposed to be applied to induction motor drive against various current sensor fault types. The third difference operator is used to check the signal quality status of the measured speed to ensure the estimated current calculated from the measured speed is accurate.

4. Zhang Z., Bazzi A.M. Robust Sensorless Scalar Control of Induction Motor Drives with Torque Capability Enhancement at Low Speeds. *2019 IEEE International Electric Machines & Drives Conference (IEMDC)*, 2019, pp. 1706-1710. doi: https://doi.org/10.1109/IEMDC.2019.8785159.

5. Mon-Nzongo D.L., Jin T., Ekemb G., Bitjoka L. Decoupling Network of Field-Oriented Control in Variable-Frequency Drives. *IEEE Transactions on Industrial Electronics*, 2017, vol. 64, no. 7, pp. 5746-5750. doi: https://doi.org/10.1109/TIE.2017.2674614.

6. Zerdali E. A Comparative Study on Adaptive EKF Observers for State and Parameter Estimation of Induction Motor. *IEEE Transactions on Energy Conversion*, 2020, vol. 35, no. 3, pp. 1443-1452. doi: https://doi.org/10.1109/TEC.2020.2979850.

7. Tran C.D., Kuchar M., Sobek M., Sotola V., Dinh B.H. Sensor Fault Diagnosis Method Based on Rotor Slip Applied to Induction Motor Drive. *Sensors*, 2022, vol. 22, no. 22, art. no. 8636. doi: https://doi.org/10.3390/s22228636.

8. Amin A.A., Hasan K.M. A review of Fault Tolerant Control Systems: Advancements and applications. *Measurement*, 2019, vol. 143, pp. 58-68. doi: https://doi.org/10.1016/j.measurement.2019.04.083.

9. Moussaoui L., Aouaouda S., Rouaibia R. Fault tolerant control of a permanent magnet synchronous machine using multiple constraints Takagi-Sugeno approach. *Electrical Engineering & Electromechanics*, 2022, no. 6, pp. 22-27. doi: https://doi.org/10.20998/2074-272X.2022.6.04.

10. Gouichiche A., Safa A., Chibani A., Tadjine M. Global fault-tolerant control approach for vector control of an induction motor. *International Transactions on Electrical Energy Systems*, 2020, vol. 30, no. 8, art. no. e12440. doi: https://doi.org/10.1002/2050-7038.12440.

11. Wang Z., Shao J., He Z. Fault Tolerant Sensorless Control Strategy With Multi-States Switching Method for In-Wheel Electric Vehicle. *IEEE Access*, 2021, no. 9, pp. 61150-61158. doi: https://doi.org/10.1109/ACCESS.2021.3072700.

12. Chaabane H., Khodja D.E., Chakroune S., Hadji D. Model reference adaptive backstepping control of double star induction machine with extended Kalman sensorless control. *Electrical Engineering & Electromechanics*, 2022, no. 4, pp. 3-11. doi: https://doi.org/10.20998/2074-272X.2022.4.01.

13. Gundewar S.K., Kane P.V. Condition Monitoring and Fault Diagnosis of Induction Motor. *Journal of Vibration Engineering & Technologies*, 2021, vol. 9, no. 4, pp. 643-674. doi: https://doi.org/10.1007/s42417-020-00253-y.

14. Niu G., Xiong L., Qin X., Pecht M. Fault detection isolation and diagnosis of multi-axle speed sensors for high-speed trains. *Mechanical Systems and Signal Processing*, 2019, vol. 131, pp. 183-198. doi: https://doi.org/10.1016/j.ymssp.2019.05.053.

15. Azzoug Y., Menacer A., Pusca R., Romary R., Ameid T., Ammar A. Fault Tolerant Control for Speed Sensor Failure in Induction Motor Drive based on Direct Torque Control and Adaptive Stator Flux Observer. *2018 International Conference on Applied and Theoretical Electricity (ICATE)*, 2018, pp. 1-6. doi: https://doi.org/10.1109/ICATE.2018.8551478.

16. Manohar M., Das S. Notice of Removal: Current Sensor Fault-Tolerant Control of Induction Motor Driven Electric Vehicle Using Flux-Linkage Observer. *2020 IEEE Transportation Electrification Conference & Expo (ITEC)*, 2020, pp. 884-889. doi: https://doi.org/10.1109/ITEC48692.2020.9161553.

17. Aib A., Khodja D.E., Chakroune S., Rahali H. Fuzzy current analysis-based fault diagnostic of induction motor using hardware co-simulation with field programmable gate array. *Electrical Engineering & Electromechanics*, 2023, no. 6, pp. 3-9. doi: https://doi.org/10.20998/2074-272X.2023.6.01.

18. Gholipour A., Ghanbari M., Alibeiki E., Jannati M. Speed sensorless fault-tolerant control of induction motor drives against current sensor fault. *Electrical Engineering*, 2021, vol. 103, no. 3, pp. 1493-1513. doi: https://doi.org/10.1007/s00202-020-01179-0.

19. Manohar M., Das S. Current Sensor Fault-Tolerant Control for Direct Torque Control of Induction Motor Drive Using Flux-Linkage Observer. *IEEE Transactions on Industrial Informatics*, 2017, vol. 13, no. 6, pp. 2824-2833. doi: https://doi.org/10.1109/TII.2017.2714675.

20. Zuo Y., Ge X., Chang Y., Chen Y., Xie D., Wang H., Woldegiorgis A.T. Current Sensor Fault-Tolerant Control for Speed-Sensorless Induction Motor Drives Based on the SEPLL Current Reconstruction Scheme. *IEEE Transactions on Industry Applications*, 2023, vol. 59, no. 1, pp. 845-856. doi: https://doi.org/10.1109/TIA.2022.3204733.

21. Huu Nguyen M.C., Tran C.D. An extended sensor fault tolerant control method applied to three-phase induction motor drives. *Bulletin of Electrical Engineering and Informatics*, 2024, vol. 13, no. 1, pp. 125-133. doi: https://doi.org/10.11591/eei.v13i1.5992.

22. Yi T.-H., Huang H.-B., Li H.-N. Development of sensor validation methodologies for structural health monitoring: A comprehensive review. *Measurement*, 2017, vol. 109, pp. 200-214. doi: https://doi.org/10.1016/j.measurement.2017.05.064.

23. Tran C.D., Nguyen T.X., Nguyen P.D. A field-oriented control (FOC) method using the virtual currents for the induction motor drive. *International Journal of Power Electronics and Drive Systems (IJPEDS)*, 2021, vol. 12, no. 4, pp. 2095-2102. doi: https://doi.org/10.11591/ijpeds.v12.i4.pp2095-2102.

24. Ho S.D., Brandstetter P., Palacky P., Kuchar M., Dinh B.H., Tran C.D. Current sensorless method based on field-oriented control in induction motor drive. *Journal of Electrical Systems*, 2021, vol. 17, no. 1, pp. 62-76.

25. Adamczyk M., Orlowska-Kowalska T. Self-Correcting Virtual Current Sensor Based on the Modified Luenberger Observer for Fault-Tolerant Induction Motor Drive. *Energies*, 2021, vol. 14, no. 20, art. no. 6767. doi: https://doi.org/10.3390/en14206767.

26. Azzoug Y., Pusca R., Sahraoui M., Ammar A., Romary R., Marques Cardoso A.J. A Single Observer for Currents Estimation in Sensor's Fault-Tolerant Control of Induction Motor Drives. *2019 International Conference on Applied Automation and Industrial Diagnostics (ICAAID)*, 2019, pp. 1-6. doi: https://doi.org/10.1109/ICAAID.2019.8934969.

27. Rahman T., Motakabber S.M.A., Ibrahimy M.I. Design of a Switching Mode Three Phase Inverter. *2016 International Conference on Computer and Communication Engineering (ICCCE)*, 2016, pp. 155-160. doi: https://doi.org/10.1109/ICCCE.2016.43.

28. Adamczyk M., Orlowska-Kowalska T. Postfault Direct Field-Oriented Control of Induction Motor Drive Using Adaptive Virtual Current Sensor. *IEEE Transactions on Industrial Electronics*, 2022, vol. 69, no. 4, pp. 3418-3427. doi: https://doi.org/10.1109/TIE.2021.3075863.

29. Azzoug Y., Sahraoui M., Pusca R., Ameid T., Romary R., Cardoso A.J.M. High-performance vector control without AC phase current sensors for induction motor drives: Simulation and real-time implementation. *ISA Transactions*, 2021, vol. 109, pp. 295-306. doi: https://doi.org/10.1016/j.isatra.2020.09.021.

C.D. Tran[1], *Doctor on Electrical Engineering,*
M. Kuchar[2], *Professor, Doctor on Electrical Engineering,*
P.D. Nguyen[2,3], *PhD Student,*
[1] Power System Optimization Research Group,
Faculty of Electrical and Electronics Engineering,
Ton Duc Thang University, Ho Chi Minh City, Vietnam,
e-mail: trandinhcuong@tdtu.edu.vn (Corresponding Author)
[2] Department of Applied Electronics,
Faculty of Electrical Engineering and Computer Science,
VSB-Technical University of Ostrava, Czech Republic,
e-mail: martin.kuchar@vsb.cz; phuong.nguyen.duy.st@vsb.cz
[3] Faculty of Electronics and Telecommunication,
Saigon University, Ho Chi Minh City, Vietnam,
e-mail: phuong.nd@sgu.edu.vn

A. Zorig, N. Hamouda, B. Babes, S. Mouassa

Improving the efficiency of a non-ideal grid coupled to a photovoltaic system with a shunt active power filter using a self-tuning filter and a predictive current controller

*Introduction. Recently, photovoltaic (PV) systems are increasingly favored for converting solar energy into electricity. PV power systems have successfully evolved from small, standalone installations to large-scale, grid-connected systems. When the nonlinear loads are connected to a grid-tied PV system, the power quality can deteriorate due to the active power supplied by the PV array, there's a noticeable decline in the quality of power delivered to consumers. Its combination with the shunt active power filter (SAPF) enhances system efficiency. Consequently, this integrated system is adept at not only powering local loads but also at compensating for reactive power and filtering out harmonic currents from the main grid. The **novelty** of the work describes how an operation of a small scale PV system connected to the low voltage distribution system, and nonlinear load can be achieved, the investigation aims to analyze the system's behavior and elucidate the advantages of employing various control algorithms. These proposed algorithms are designed to ensure a unity power factor for the utility grid while prioritizing high convergence speed and robustness against load power fluctuations across different levels of solar irradiation affecting the PV modules. The **purpose** of this work is to enhance the dynamic performance of the SAPF by cooperatively using a self-tuning filter (STF) based instantaneous active and reactive power method (PQ) with a novel predictive current control, enhance the system resilience, ensure optimal management of the total active power between the PV system, the electrical network and the non-linear load by integrating the functionalities of the SAPF under different levels of solar irradiation and maintain the DC-link capacitor voltage constant. **Methods**. A novel predictive current controller is designed to generate the switching signals piloted the three phase source voltage inverter, also a novel algorithm of instantaneous active and reactive power is developed, based on STF, to extract accurately the harmonic reference under non ideal grid voltage, also the perturb and observe algorithm is used to extract, under step change of solar irradiation, the maximum power point tracking of the PV module and the PI controller is used to maintain constant the DC-link capacitor voltage of the SAPF. **Results**. The efficacy of the proposed system is primarily centered on the grid side, and the performance evaluation of the control system is conducted using the STF based PQ algorithm and predictive current control. In addition, comprehensive testing encompasses all modes of operation, including scenarios involving distorted voltage sources, step changes in solar radiation, and variations in nonlinear loads. Results highlight superior performance in both transient and stable states, affirming the robustness and effectiveness of the proposed controllers. **Practical value**. The total harmonic distortion value of the grid current for all tests respects the IEEE Standard 519-1992. References 21, tables 7, figures 25.*

Key words: **photovoltaic system, shunt active power filter, active and reactive power algorithm, self-tuning filter, total harmonic distortion, predictive current control, maximum power point tracking.**

*Вступ. Останнім часом фотоелектричні (PV) системи все частіше використовуються для перетворення сонячної енергії на електрику. Фотоелектричні системи успішно еволюціонували від невеликих автономних установок до великомасштабних систем, підключених до мережі. Коли нелінійні навантаження підключені до мережевої фотоелектричної системи, якість електроенергії може погіршитися через активну потужність фотоелектричної матриці, що подається, спостерігається помітне зниження якості електроенергії, що постачається споживачам. Його поєднання із шунтуючим активним фільтром потужності (SAPF) підвищує ефективність системи. Отже, ця інтегрована система здатна як живити локальні навантаження, так і компенсувати реактивну потужність і відфільтровувати гармонійні струми з основний мережі. **Новизна** роботи описує, як можна домогтися роботи маломасштабної фотоелектричної системи, підключеної до розподільчої системи низької напруги та нелінійного навантаження, дослідження спрямоване на аналіз поведінки системи та з'ясування переваг використання різних алгоритмів управління. Ці алгоритми розроблені для забезпечення одиничного коефіцієнта потужності для комунальної мережі, при цьому віддаючи пріоритет високої швидкості конвергенції та стійкості до коливань потужності навантаження на різних рівнях сонячного опромінення, що впливає на фотоелектричні модулі. **Метою** даної роботи є підвищення динамічних характеристик SAPF шляхом спільного використання фільтра, що самоналаштовується (STF), на основі методу миттєвої активної та реактивної потужності (PQ) з новим предиктивним управлінням струмом, підвищення стійкості системи, забезпечення оптимального управління загальною активною потужністю між фотоелектричною системою, електричною мережею та нелінійним навантаженням шляхом інтеграції функцій SAPF при різних рівнях сонячного опромінення та підтримання постійної напруги конденсатора ланки постійного струму. **Методи**. Новий предиктивний контролер струму, призначений для генерації сигналів перемикання, пілотованих трифазним інвертором напруги джерела, також розроблений новий алгоритм миттєвої активної та реактивної потужності, заснований на самонастроюючому фільтрі, для точного вилучення гармонійного опорного значення при неідеальній напрузі мережі, також використовується алгоритм обурення та спостереження при ступінчастій зміні сонячного випромінювання, відстеження максимальної точки потужності фотоелектричного модуля, а ПІ-регулятор використовується для підтримки постійної напруги конденсатора постійного струму SAPF. **Результати**. Ефективність пропонованої системи в першу чергу зосереджена на стороні мережі, а оцінка продуктивності системи керування проводиться з використанням алгоритму PQ на основі STF та керування струмом. Крім того, комплексне тестування охоплює всі режими роботи, включаючи сценарії, що включають спотворені джерела напруги, ступінчасті зміни сонячного випромінювання та зміни нелінійних навантажень. Результати підкреслюють чудову продуктивність як у перехідних, так і у стабільних станах, підтверджуючи надійність і ефективність пропонованих контролерів. **Практична цінність**. Загальне значення гармонійних спотворень мережі для всіх випробувань відповідає стандарту IEEE 519-1992. Бібл. 21, табл. 7, рис. 25.*

Ключові слова: **фотоелектрична система, шунтуючий фільтр активної потужності, алгоритм активної та реактивної потужності, фільтр, що самоналаштовується, повне гармонічне спотворення, предиктивне управління струмом, відстеження точки максимальної потужності.**

Introduction. The increasing use of semiconductor devices and nonlinear loads (NLs) in industrial, residential, and commercial sectors has resulted in the degradation of power grid voltage and current waveforms. This, in turn, leads to harmonic distortion in the electrical system [1]. Such harmonics in the power network can cause significant issues including increased power losses, overloading of transmission lines, diminished power quality, reduced equipment efficiency, and disruptions in

---

device performance. Today, NLs are prevalent in both residential and office spaces [2].

Photovoltaic (PV) systems are increasingly favored for converting solar energy into electricity. In recent times, PV power systems have successfully evolved from small, standalone installations to large-scale, grid-connected systems. When the NLs are connected to a grid-tied PV system, the power quality can deteriorate due to the active power supplied by the PV array. As the adoption of NLs increases, there is a noticeable decline in the quality of power delivered to consumers [3–6]. The shunt active power filter (SAPF) emerges as an adaptable remedy for harmonic compensation. It operates by connecting parallel to the grid and consistently injecting currents that, at any given time, match the harmonic components caused by the NL. The sole use of SAPF is less attractive in practice due to the still high effort involved, especially for powerful systems to be filtered. Hence we are much more interested in filtering system coupled with PV system to ensure several advantages. Integrating a PV system into the grid to benefits local load supply, and its combination with the SAPF enhances system efficiency. Consequently, this integrated system is adept at not only powering local loads, but also at compensating for reactive power and filtering out harmonic currents from the main grid. This ensures that the grid current maintains a sinusoidal waveform and upholds a unity power factor (PF) [7–9].

The first task is to extract the power from the PV generator under varying weather conditions. Hence, employing maximum power point tracking (MPPT) method known perturb and observe (P&O), to maximize energy harvest from a PV generator across diverse radiation levels [10–12]. Then his control is integrated at the DC bus control level of the SAPF, which can be provide the power via an appropriate control of SAPF to fed the NL.

The effectiveness of the SAPF is judged by the shape of the signal which must be the inverted image of the harmonics to be compensated, contained in the load. Then the detection method of reference harmonics plays a role in active filtering because the detected signal presents a reference quantity for controlling the voltage source inverter (VSI) of the SAPF. Many algorithms have been used to generate these harmonics reference [1, 13, 14] and the most used is the instantaneous active and reactive power (PQ) algorithm, the primary algorithm on the grid side is dedicated to determining the optimal reference filter currents crucial for the proficient governance of the SAPF. And advanced approach leverages a self-tuning filter (STF), designed specifically to navigate the control intricacies of the SAPF when faced with voltage distortions [9], the major positive behavior of the STF lies in extracting the fundamental components of the voltage, which also facilitates the computation of an accurate harmonic reference current for scenarios involving non-ideal grid voltage, and fluctuating load conditions [15]. This, in turn, aids in producing compensator currents, achieved through the amalgamation of predictive current control (PCC) and supplementary algorithms [16–19].

The secondary controller utilizes a PI controller for ensuring the DC link voltage remains consistent around its predetermined reference value, especially during sudden load shifts or alterations in solar irradiation, and

its capability of has been investigated across all operational modes of the proposed system. Other hand, a novel control current loop applied of SAPF in order to generate the filter currents by thanks the PCC, the development of an efficient PCC design for active power filtering system. In order to extract, for such a system, the filter current and generates the switching signals of SAPF, the modified predictive current controller is considered here as an appropriate technique [20, 21].

The goal of the paper is to enhance the dynamic performance of the SAPF by cooperatively using a STF based PQ algorithm with a novel PCC, enhance the system resilience, ensure optimal management of the total active power between the PV system, the electrical network and the non-linear load by integrating the functionalities of the SAPF under different levels of solar irradiation and maintain the DC-link capacitor voltage constant.

Subject of investigations. This paper describes how an operation of a small scale PV system connected to the low voltage distribution system, and NL can be achieved, the investigation aims to analyze the system's behavior and elucidate the advantages of employing various control algorithms. These proposed algorithms are designed to ensure a unity PF for the utility grid while prioritizing high convergence speed and robustness against load power fluctuations across different levels of solar irradiation affecting the PV modules.

Topologies of an SAPF fed via PV system. The power circuit of the suggested topology of three-phase grid-connected PV and active power filter system can be viewed in Fig. 1. It is designed firstly to inject the real power generated by the PV system to the load on whole days [3]. This topology includes PV panels, a DC-DC boost converter, and a three-phase VSI linked to the low voltage grid via a link inductor. In addition, there's three-phase full bridge rectifier followed by a series resistor and inductor, in parallel with capacitor, which creating NL. The objectives that have been mainly focused in the proposed work are as follows:

1. To effectively demonstrate the multifunctional system's behavior across diverse operating modes and showcase its resilience under challenging conditions.

2. To maintain constant DC-link capacitor voltage of the SAPF under solar irradiance change.

3. To enhance the dynamics performance of SAPF by using STF based PQ algorithm and PCC.

4. To ensure the complete integration of the functionalities of SAPF to compensate the reactive power, suppress the harmonic currents and inject the surplus of active power in the utility grid.

PV array model and its MPPT controller. The combination of numerous PV cells arranged in series and parallel configurations forms a PV generator. Several articles in the literature extensively cover the modeling of these modules [9–11]. The prevalent adoption of a single diode model is attributed to its consistently favorable outcomes. Here, we use the single-diode model to describe the characteristics of PV cells (Fig. 2).

Figure 2 depicts the equivalent circuit of a solitary solar cell, featuring a single diode VD, a parallel resistor R_p, a series resistor R_s, and via Kirchhoff's current law, the output current of the solar PV cell can be expressed as [9]:

$$I_{pv} = I_{ph} - I_d - I_{R_p} ; \qquad (1)$$

$$I_{pv} = I_{ph} - I_0\left[\exp\left(A\left(V_{pv} + R_S I_{pv}\right)\right) - 1\right] - \frac{V_{pv} - R_S I_{pv}}{R_p} ; \qquad (2)$$

where I_{ph} is the solar-generated current; I_{pv} is the output current; I_d is the diode current; V_{pv} is the output voltage; I_0 is the diode reverse saturation current; A is the ideality factor of the diode ($1<A<2$).

Fig. 1.
Topology circuit of an SAPF powered by the PV system

Fig. 2. Equivalent circuit of PV panel

Figure 3 shows the generated outputs characteristics of PV module at T = 25 °C and diverse irradiance. To generate the specified voltage from the simulated model, 120 cells connected in series are required. This system achieves the desired voltage level by applying a gain on the cell voltage equal to the number of sum cells.

Fig. 3. Characteristic curves $P_{pv} = f(V_{pv})$ and $I_{pv} = f(V_{pv})$ of the PV module

The voltage is determined by ensuring that the PV array operates at its maximum power point (MPP). The P&O algorithm stands out as the most widely adopted MPPT technique, which is used in this work, due to its simplicity and easy implementation. It is based on tracking the MPP by comparing power at different samples times and by periodically perturbing voltage [12]. The working principle of the P&O algorithm is shown in Fig. 4.

Fig. 4. Flow chart of the P&O algorithm

When PV power P_{PV} and PV voltage V_{PV} increase, the perturbation step size Δd is added to the duty cycle, thus $d(k+1)$ is the next duty cycle value of perturbation, which forces the operating point to move towards the MPP and vice versa. Then, when power P_{PV} increases and V_{PV} decreases, the Δd will be subtracted for the next cycle of perturbation and vice versa. The process is repeated periodically until the MPP is reached. Once the MPP is located by extracting the optimum duty ratio of the boost converter $d(k)$.

The adjustment of the duty ratio for the boost converter is achieved by manipulating the IGBT switches. Gating signals for these IGBT switches are generated by a high carrier frequency pulse-width modulator block, operating at a frequency of 15 kHz (Fig. 5).
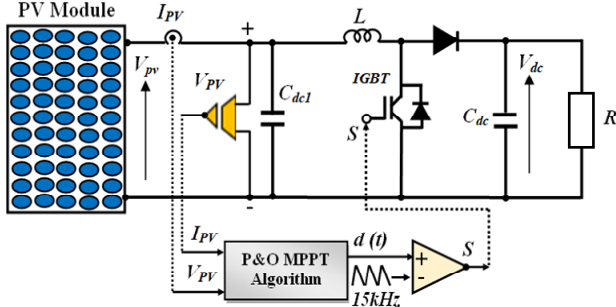
Fig. 5. Scheme control of the PV with DC-DC boost converter

The DC-DC boost converter is driven by the pulse-width modulator's control input $S(t)$. Its operating principle can be expressed by duty cycle D and switching period T_s as follows:

$$S(t) = \begin{cases} 0, & 0 \le t \le DT_s; \\ 1, & DT_s \le t \le T_s; \end{cases} \quad (3) \qquad V_{dc} = \frac{V_{pv}}{1-D} . \quad (4)$$

Dependent on the switching duty cycle and input voltage V_{pv}, when the IGBT is open, the input capacitor C_{dc1} is charged via the PV panel as per the input voltage, when the IGBT switches ON, current charges up through L, when the IGBT switches back OFF, an opposing voltage is generated and released, the inductor now acts as a voltage source in series with the supply voltage, the output voltage V_{dc} is now charged up to a higher voltage than before, therefore stepping up the voltage.

Indenting the reference harmonics currents. The PQ algorithm is based on a set of instantaneous power defined in the time domain, where the three-phase supply voltages (v_{s1}, v_{s2}, v_{s3}) and currents load (i_{l1}, i_{l2}, i_{l3}) are transformed using the Clarke transformation (α-β) [13], which are written as:

$$\begin{bmatrix} v_{s\alpha} \\ v_{s\beta} \end{bmatrix} = T_{32}^t \cdot \begin{bmatrix} v_{s1} \\ v_{s2} \\ v_3 \end{bmatrix} = \sqrt{\frac{2}{3}} \begin{bmatrix} \frac{1}{\sqrt{2}} & \frac{1}{\sqrt{2}} & \frac{1}{\sqrt{2}} \\ 1 & \frac{1}{2} & -\frac{1}{2} \\ 0 & \frac{\sqrt{3}}{2} & \frac{\sqrt{3}}{2} \end{bmatrix} \times \begin{bmatrix} v_{s1} \\ v_{s2} \\ v_3 \end{bmatrix}; \quad (5)$$

$$\begin{bmatrix} i_{l\alpha} \\ i_{l\beta} \end{bmatrix} = T_{32}^t \cdot \begin{bmatrix} i_{l1} \\ i_{l2} \\ i_{l3} \end{bmatrix} = \sqrt{\frac{2}{3}} \begin{bmatrix} \frac{1}{\sqrt{2}} & \frac{1}{\sqrt{2}} & \frac{1}{\sqrt{2}} \\ 1 & \frac{1}{2} & -\frac{1}{2} \\ 0 & \frac{\sqrt{3}}{2} & \frac{\sqrt{3}}{2} \end{bmatrix} \times \begin{bmatrix} i_{l1} \\ i_{l2} \\ i_{l3} \end{bmatrix}. \quad (6)$$

In scenarios where the sources voltage are distorted and unbalanced, the performance of the PQ algorithm is

degraded [13], for this a STF is involved and introduced to accurately cleaning the source voltage from these disturbances on the (α-β) axis. This new filter, initially developed in [14, 15] is designed to extract the fundamental component of source voltage amidst distorted and unbalanced conditions. The transfer function of the STF is obtained in the (α-β) axis, it can be expressed as:

$$H(s) = \frac{v_{s\alpha\beta F}}{v_{s\alpha\beta}} = K \frac{s + j\omega_c}{s^2 + \omega_c^2} . \quad (7)$$

The value of K is chosen via the frequency response of the STF (Fig. 6,a,b), when we plot the 3D Bode diagram of the STF for the gain and the phase. It can be noticed that at $\omega_c = 2\pi f_c$ ($f_c = 50$ Hz) and $K=20$, the phase angle is equal to 0, and gain is equal 0. This feature allowed us to judge that the fundamental components of the grid voltage are correctly extracted.
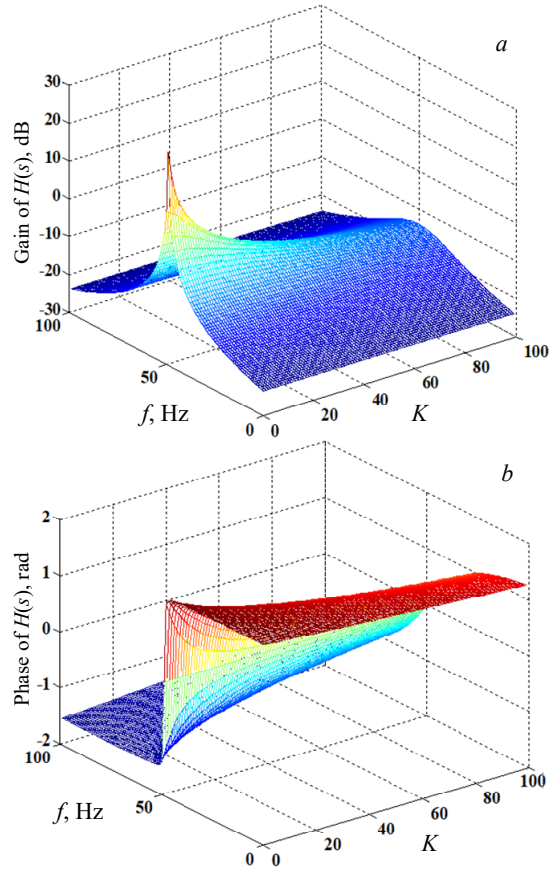
Fig. 6. Frequency response of the STF:
gain (*a*) and phase (*b*) of the $H(s)$ for the fundamental

The fundamental of the grid voltage on the (α-β) axis are extracted through (8), (9):

$$v_{s\alpha F} = \frac{20(s+20)}{(s+20)^2 + \omega_c^2} v_{s\alpha}(s) - \frac{20\omega_c}{(s+20)^2 + \omega_c^2} v_{s\beta}(s); \quad (8)$$

$$v_{s\beta F} = \frac{20 \cdot 20\omega_c}{(s+20)^2 + \omega_c^2} v_{s\alpha}(s) + \frac{20(s+20)}{(s+20)^2 + \omega_c^2} v_{s\beta}(s). \quad (9)$$

Then, the active and reactive instantaneous powers «*p*» and «*q*» are given in matrix form:

$$\begin{bmatrix} p \\ q \end{bmatrix} = \begin{bmatrix} v_{s\alpha F} & v_{s\beta F} & 0 \\ -v_{s\beta F} & v_{s\alpha F} & 0 \\ 0 & 0 & v_0 \end{bmatrix} \times \begin{bmatrix} i_{l\alpha} \\ i_{l\beta} \end{bmatrix}. \quad (10)$$

The currents reference in (α-β) axis is obtained as:

$$\begin{bmatrix} i_{h\alpha}^* \\ i_{h\beta}^* \end{bmatrix} = \frac{1}{v_{s\alpha F}^2 + v_{s\beta F}^2} \begin{bmatrix} v_{s\alpha F} & -v_{s\beta F} \\ v_{s\beta F} & v_{s\alpha F} \end{bmatrix} \times \begin{bmatrix} \tilde{p} \\ q \end{bmatrix}. \quad (11)$$

The three phase reference current of the SAPF can be obtained by applying the inverse Clarke transformation to the stationary reference currents as:

$$\begin{bmatrix} i_{h1}^* \\ i_{h2}^* \\ i_{h3}^* \end{bmatrix} = \sqrt{\frac{2}{3}} \times \begin{bmatrix} 1 & 0 \\ -1/2 & \sqrt{3}/2 \\ -1/2 & -\sqrt{3}/2 \end{bmatrix} \times \begin{bmatrix} i_{h\alpha}^* \\ i_{h\beta}^* \end{bmatrix}. \quad (12)$$

The three phase reference current of the active power filter can be obtained by applying the inverse Clarke transformation to the stationary reference currents as illustrated by (7).

The required active component I_c, essential for compensating switching losses, is derived from the DC voltage controller. The main task is assigned to the PI controller to maintain the DC-link voltage V_{dc} fixed and ensure the reduced of fluctuation voltage under step change of irradiance solar and sudden change of NL. Furth more the PI regulator provides good performance and high robustness in controlling the system. Voltage control loop diagram can be seen in Fig. 7. It delivered the active component i_c necessary to cover also the switching losses. The final reference harmonic is given as:

$$\begin{bmatrix} i_{f1}^* \\ i_{f2}^* \\ i_{f3}^* \end{bmatrix} = \begin{bmatrix} i_{h1}^* \\ i_{h2}^* \\ i_{h3}^* \end{bmatrix} - \begin{bmatrix} i_{c1} \\ i_{c2} \\ i_{c3} \end{bmatrix}. \quad (13)$$

A graphical representation of the STF based PQ algorithm for determining the reference current filter is depicted in Fig. 7. The resultant reference current derived from this process will be employed in the PCC block of the SAPF, as detailed in the subsequent section, where the STF based PLL is the modified phase looked loop and explained in [16].
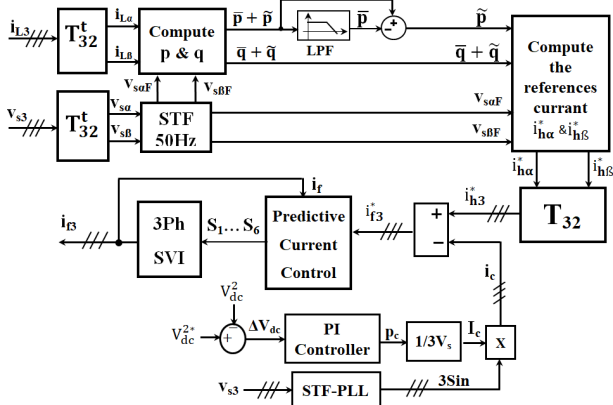
Fig. 7. Diagram of STF based PQ algorithm

Current loop regulation of SAPF using a new PCC. This section concentrates on developing a point of common connection strategy for PV systems feeding SAPFs, while also addressing the generation of reference currents [17, 21]. The initial step involves creating a predictive current model for the SAPF. By deriving the dynamic model of the SAPF from the equivalent single-phase circuit of a three-phase VSI connected to the point of common connection, the strategy is formulated in (14) and as shown in Fig. 8.
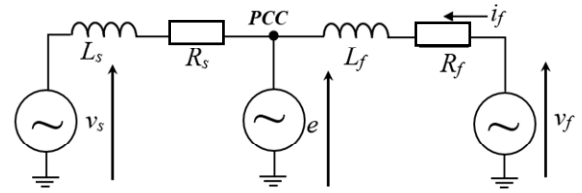
Fig. 8. Simplified scheme of an SAPF

$$\frac{di_f}{dt} + \frac{R_f}{L_f} i_f = \frac{e - v_f}{L_f}, \quad (14)$$

where e is the mains phase voltage at the point of common connection; i_f is the pertinent phase current drawn by the SAPF; v_f is the averaged value of SAPF leg voltage; R_f and L_f are the resistance and the inductance of AC filter inductors.

$$i_f(k+1) = i_f(k)e^{T_s(R_f/L_f)} + (E(k) - V_f(k)) \cdot \left(\frac{1 - e^{T_s/\tau}}{R_f} \right). \quad (15)$$

Introducing a and b parameters as:

$$a = e^{-T_s(R_f/L_f)} \approx 1 - \frac{R_f}{L_f} T_s;$$

$$b = \frac{1 - e^{-(T_s/\tau)}}{R_f} \approx \frac{1 - 1 + \left(\frac{R_f}{L_f} T_s \right)}{R_f} \approx \frac{T_s}{L_f},$$

where the coefficients a, b are approximated by a Taylor series. The time constant of the output stage of the SAPF is denoted as $\tau = L_f/R_f$.

The SAPF current at time instants k and $k+1$ is denoted by $i_f(k)$ and $i_f(k+1)$, respectively. The SAPF behavior may be then rewritten as:

$$i_f(k+1) = i_f(k) \cdot a + (E(k) - V_f(k)) \cdot b. \quad (16)$$

The discrete SAPF model for the sample period between the time instances $k+1$ and $k+2$ can be rewritten from (16) in order to design two-steps ahead PCC, as:

$$i_f(k+2) = i_f(k+1) \cdot a + (E(k+1) - V_f(k+1)) \cdot b. \quad (17)$$

It is remarked that point of common connection voltage is predictable to exhibit a quite sinusoidal waveform, for its prediction, a simple linear extrapolation algorithm was used according to:

$$E(k+1) = 2E(k) - E(k-1). \quad (18)$$

The aim of this PCC is to calculate for the next sampling period T_s between the time instances $k+1$ and $k+2$ such an SAPF voltage reference $V_f = V_i$ ($i = a, b, c$), which is the current error at the time instant $k+2$ is omitted as shown in Fig. 9.

Fig. 9. Predictive current controller

For the purposes of controlling the current error at the sampling period between the time instants $k+1$ and $k+2$ can be introduced as:

$$\Delta i_f(k+2) = i_f^*(k+2) - i_f(k+2), \quad (19)$$

where:

$$\Delta i_f(k+2) \cong 0. \quad (20)$$

The reference SAPF average voltage to eliminate current error at the time instant $k+2$, can then be given from (16) – (18) as:

$$V_f(k+1) = E(k+1) - \frac{1}{b}\left[i_f^*(k+2) - i_f(k+1)a\right]. \quad (21)$$

In applications of the SAPF, current references typically involve the 5th and 7th harmonics, resulting in a complex prediction of the current reference. To overcome this challenge, a polynomial extrapolation technique is suggested for generating current references during transient conditions. Typically, a second-order two-ahead extrapolation method utilizes values from previous sampling instants to estimate the current reference value at time instant $k+2$

$$i_f^*(k+2) = a_0 i_f^*(k) + a_1 i_f^*(k-1) + a_2 i_f^*(k-2) + \dots$$
$$\dots + a_n i_f^*(k-n), \quad (22)$$

where a_i ($i = 0\dots n$) are the polynomial coefficients to be calculated. There are 9 coefficients to be determined if a compensation of 5th, 7th and 11th harmonics is wanted. Those parameters have been chosen using a genetic algorithm optimization (GAO) based on the minimization of the subsequent fitness function given as:

$$\Delta i_f = \int \left| i_f^*(k) - i_f(k) \right|, \quad (23)$$

where $i_f^*(k)$ represents the predicted current reference at time instant k. The search results obtained using the GAO is summarized in Table 1.

Table 1
Reference generation based GAO parameters

h	5th	7th	11th
a_h	5.3695	–0.2398	11.4581
b_h	–7.1420	2.7384	18.2503
c_h	2.5985	–2.4251	12.8374

Considering the disparity between the modeled filter inductance L_f and its actual value L, the closed-loop transfer function for the current control loop can be described using the following three discrete equations in the z-domain. The first two equations illustrate the behavior of the PCC, while the 3rd equation characterizes the actual plant:

$$V_f(k)z = E(k)\frac{T_s}{L_f} - \left[i_f^*(k)z^2 - -i_f(k+1)\right]; \quad (24)$$

$$i_f(k+1) = E(k)\frac{T_s}{L_f} - V_f(k)L_f + i_f(k); \quad (25)$$

$$V_f(k)z = E(k)z^{-1} - \frac{L_f}{T_s}\left[i_f^*(k) - i_f(k)z^{-1}\right]. \quad (26)$$

From (24) – (26), taking into account the grid voltage as a disturbance, the closed current loop transfer function is:

$$\frac{i_f(z)}{i_f^*(z)} = \frac{\left(L_f/Lz^2\right)}{z^2 + \left(L_f/L^{-1}\right)}. \quad (27)$$

Ignoring the parameters mismatch (i.e $L_f/L = 1$) in (27) the closed current loop poles must to be moved from the origin to attain better noise rejection. In order to move the current loop closed loop poles from the origin, a new prediction method for the SAPF current at the instant $k+1$ is:

$$\begin{cases} i_f(k+1) = i_f(k) + i_f^*(k-1) + i_f^*(k) - \Delta i_f(k+1); \\ \Delta i_f(k+1) = i_f(k+1) + i_f^*(k-1); \\ i_f(k+1) = +i_f^*(k+1) + 0.5i_f^*(k) + 0.5i_f(k). \end{cases} \quad (28)$$

The block diagram of the overall control structure considering both the voltage, and current control loop is shown in Fig. 10. From this diagram we observe that the SAPF voltages reference values obtained from (21) are forwarded to a space vector modulator functioning in asymmetric [20].

Fig. 10. General control scheme of the SAPF

Simulation results. The efficacy of the proposed system is primarily centered on the grid side. The performance evaluation of the control system is conducted using the STF based PQ algorithm and PCC. Comprehensive testing encompasses all modes of operation, including scenarios involving distorted voltage sources, step changes in solar radiation, and variations in NLs. These assessments are carried out through the MATLAB/Simulink software. Key simulation parameters are outlined in Table 2, and additional details – in Table 3.

Table 2
Physical and electrical characteristics of the PV

Physical characteristic	BP MSX-150
Number of cell in series N_s	72
Number of cell in parallel N_p	1
Standard test conditions	1000 W/m^2, 25 °C
Maximum power P_{max}, W	200
Maximum point voltage V_{mpp}, V	65
Current at maximum point I_{mpp}, A	5.375
Open short circuit voltage V_{oc}, V	26.5

Table 3
System parameters simulated

Parameter	Value
Source resistor R_s, mΩ	20
Source inductance L_s, mH	0.5
DC-Link capacitance C_{dc}, µF	2300
Source frequency f, Hz	50
Source voltage V_s, V	100
Coupling inductance L_f, mH	4.3
Coupling resistor R_f, Ω	1
Load resistance R_d, Ω	290
Load inductance L_d, mH	2
Boost inductance L_b, H	0.04
Load capacitor C_d, µF	1800
K_I	0.1
K	15
T_s, ms	0.005

Testing performance of the proposed system under distorted grid voltage with irradiation $G = 900$ W/m². In this test, the solar irradiation is 900 W/m², the waveforms of the first phase of current load (i_{L1}), voltage source (v_{s1}), grid current (i_{s1}), filter current (i_{f1}), DC-link voltage (V_{dc}) and its reference (V^*_{dc}) are illustrate in Fig. 11, the first one, when the grid voltage is sinusoidal and before connected the SAPF into grid, the grid current is distorted with a total harmonic distortion (THD) of 28.27 % and the injected current ($i_{f1} = 0$), after switching ON the SAPF at $t = 0.05$ s and when the PQ algorithm is switched OFF, we observe that the grid current remain distorted and in phase opposite with the grid voltage, its THD pass to 25.14 % (Fig. 12,*b*), which mean the filter current contain only the fundamental (Fig. 12,*c*), in this case, there are no harmonics current filtering.
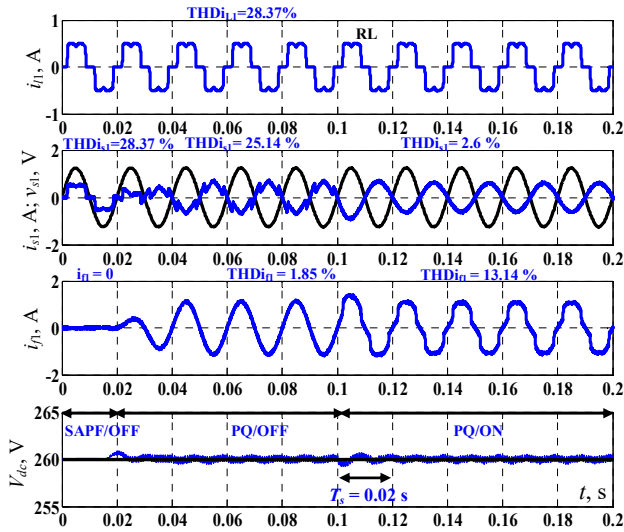
Fig. 11. Performances of the system with ideal grid voltage
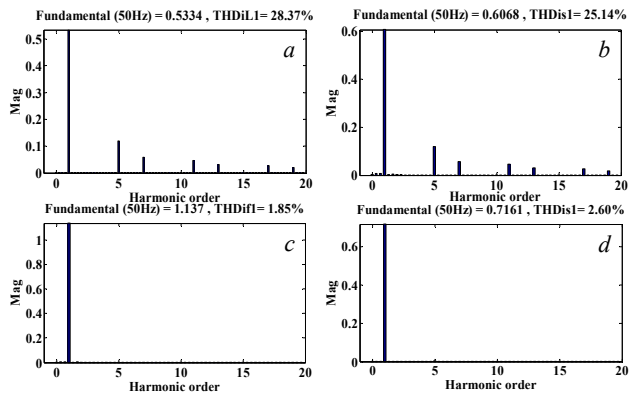
Fig. 12. Harmonic spectrum of i_{L1}, i_{s1} and i_{f1}

After the PQ algorithm is switched ON at 0.1 s, it can be observed that the grid current is sinusoidal with a THD of 2.6 % (Fig. 12,*d*) and the injected current became distorted with a THD of 13.1 % (Table 4), which mean that the SAPF have compensate the harmonic current and the reactive power and inject the fundamental current into grid, which justify the capability of the PCC to manage the dual functionality of the SAPF with the PV system; also we observe that the DC-link voltage track its reference value thanks the PI controller with a less fluctuations, which is dispersed after 0.02 s.

From Fig. 13, when the grid voltage became distorted at the instant 0.2 s with a THD of 9.35 % (Fig. 14,*a*), the grid current is distorted and its THD pass from 2.6 % to 8.96 % (Fig. 14,*c*), we can say that the PQ algorithm is not suitable to generate the reference harmonics current. But after turned ON the STF-PQ algorithm at the instant 0.03 s, the grid current recovers its sinusoidal wave form and noted an enhanced of its THD, it passes from 8.86 % to 2.72 % (Fig. 14,*d*). The detailed results are depicted in Table 4.
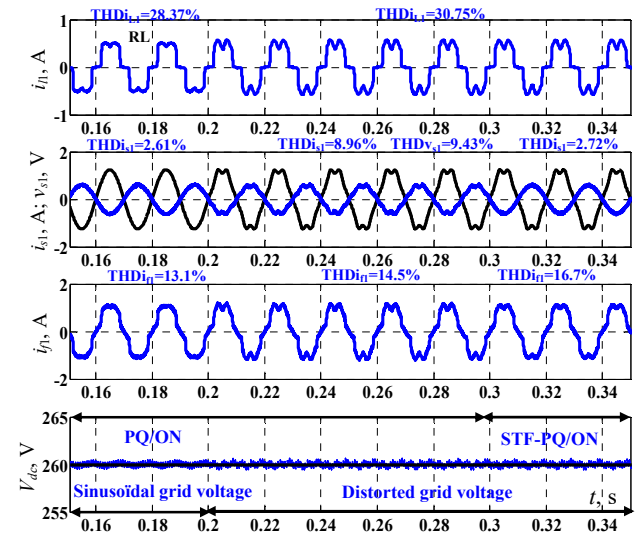
Fig. 13. Performance of the system with distorted grid voltage
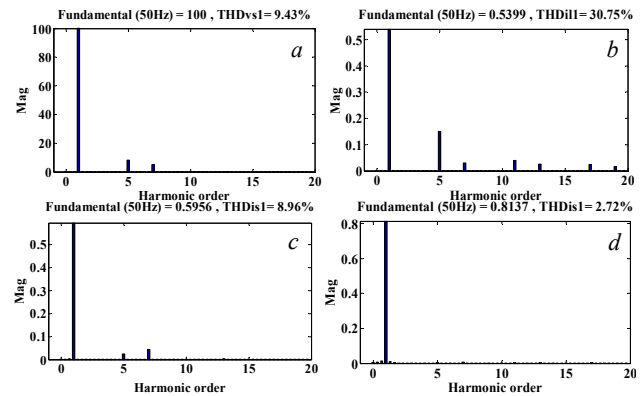
Fig. 14. Harmonic spectrum of v_{s1}, i_{L1} and i_{s1}

The flow of the active power and reactive power is illustrated in Fig. 15, which demonstrate clearly how the system control proposed have mange all the operation modes under distorted grid voltage.
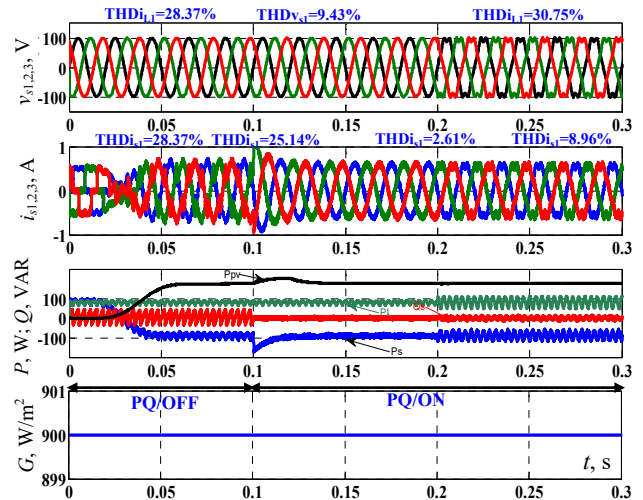
Fig. 15. Behavior the grid, PV and NL under distorted grid voltage

It can be seen that active power of grid P_s is negative after turned ON the SAPF, which mean that the active power P_{pv} generated by the PV is injected into the grid after satisfying the need of active power P_L of the NL; also reactive power of the grid is null, which means that the unity PF is reached. This major performance has been degraded when the grid voltage is distorted by the appearance of fluctuations of power system; values of the power are recapped in Table 4.

Table 4
Performance of the proposed system under distorted voltage

G, W/m²	900 W/m² [0 – 0.4 s] and R_d, L_d				
V_s, V	Sinusoidal [0 – 0.1 s]	Distorted THD = 9.43 %			
State/SAPF	SAPF/OFF	SAPF/ON [0.1 – 0.3 s] and PF=0.989			
STF, PQ	PQ/OFF	PQ/OFF	PQ/ON		STF-PQ/ON
THDi_{s1}, %	28.14	25.14	2.6	8.8	2.72
THDi_{f1}, %	0	1.85	13.1	14.5	16.7
P_s, W	80	–95	–95	–89	–95
Q_s, VAR	6	6	0	0	0
P_{ch}, W	80	80	80	82	82
P_{pv}, W	0	175	175	175	176

Testing performance of the system under distorted and unbalanced grid voltage with irradiation 900 W/m². At the instant 0.2 s, under solar irradiation of 900 W/m² and under grid voltage distorted and unbalanced condition we observe that as the grid current is distorted and in phase with the grid voltage (Fig. 16), which is justified by the harmonic spectrum of the grid current that take the value of 16.7 % (Fig. 17,*a*).
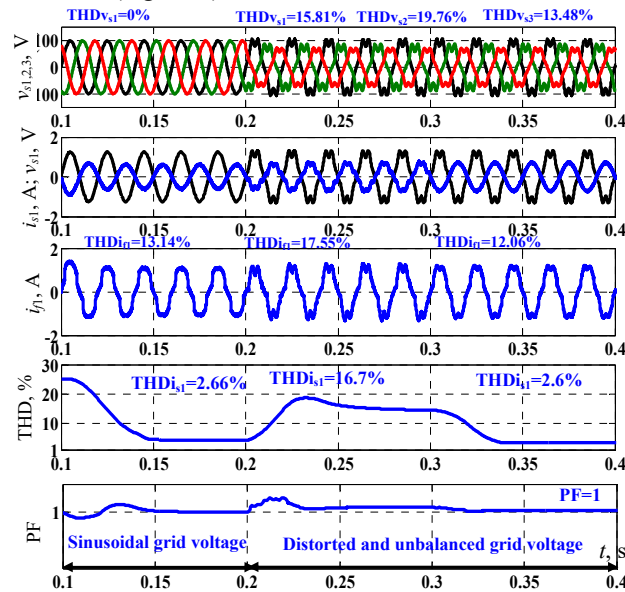
Fig. 16. Performance of the system under distorted unbalanced grid voltage
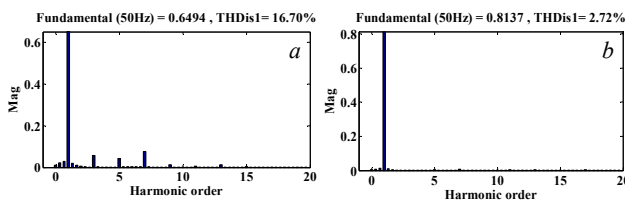
Fig. 17. Harmonic spectrums of i_{s1} without (*a*) and with (*b*) using the STF based PQ algorithm

That means that the PQ algorithm is not efficient in this condition, and after having activated the STF-PQ algorithm at the instant 0.3 s, the grid current recover its sinusoidal wave form, and we can say that the proposed system has become robust to this change. Additionally, the predictive current controller proves its faster response time to quickly generate the switching signal for the VSI of the SAPF. The performances guaranteed by this test have been specified in Table 5.

Table 5
Performance of the system under distorted unbalanced voltage

| G, W/m²	900 W/m² [0 – 0.6 s]			
V_s, V	Distorted unbalanced THD=15.81 % [0.2 – 0.6 s]			
State/SAPF	SAPF/ON [0.1 – 0.3 s] and PF = 1			
STF, PQ	PQ/OFF	PQ/ON		STF-PQ/ON
THDi_{s1}, %	25.14	2.72	16.7	2.6
THDi_{f1}, %	1.85	13.1	17.5	12.06
P_s, W	–95	–95	–89	–88.9
Q_s, VAR	6	0	0	0
P_{ch}, W	80	80	82	60
P_{pv}, W	175	175	175	175

Testing performance of the proposed system under NL change. In this test (Fig. 18, 19), the dynamic performance of proposed system is investigated under solar irradiation $G = 900$ W/m² and under step change of NL, where a capacitor of 15 µF is inserted in parallel with the inductance load at the instant of 0.4 s and disconnected at the instant 0.45 s, we notice that the value of the grid current is decreased to 0.016 A (Fig. 19,*a*), and the filter current provided by the SAPF is similar to the NL current, which mean that the NL is supplied by the PV generator and all the active power generated is provide to the NL.
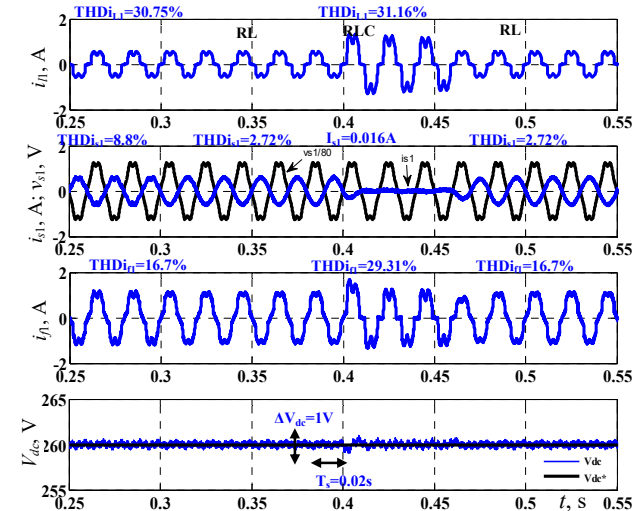
Fig. 18. Waveforms of i_{L1}, v_{s1}, i_{s1}, i_{f1} and V_{dc} under NL change
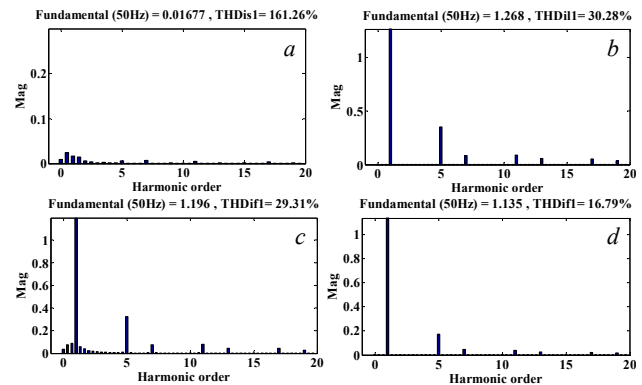
Fig. 19. Harmonic spectrum of i_{s1}, i_{L1} and i_{f1} under NL fluctuations

In this case the grid does not provide any active power, also, when we disbranched the capacitor load at the instant of 0.45 s. The an extra sinusoidal current is appeared into

grid with a THD of 2.72 %, and through these very satisfactory results we confirm the good operation of the proposed system in this case, and the PI controller with PCC reached its main role to manage the flow of active power between the grid, the NL and PV generator.

Testing performance test under gradual change of solar irradiation and NL change. From Fig. 20, when we proceed a step change of solar irradiation from $G = 900$ W/m^2 to 200W/m^2 (between the instant time of 0.6 s and 0.85 s), when the STF-PQ/ON and under distorted grid voltage (THDv_{s1} = 9.45 %), we remark that the source current drops to 0 after one period ($I_{s1} = 0.00667$ A) as depicted by the harmonics spectrum in Fig. 21,a, indicating that all the active power generated by the PV array is entirely consumed by the NL, and grid no provide any active power as can be seen in Fig. 22. For the second test, under $G = 200$ W/m^2 and when we increasing the NL current by decreasing the value of the value of NL between the instants (0.7 s – 0.8 s), we observe that grid current is sinusoidal and in phase with the grid voltage which confirm that the PF is unity, also proved the capability and the robustness of the controllers to precisely track their reference current. And by reading the value of spectrum of the grid current in this test, it can be noticed that the THD take the value of 2.66 % as depicted in Fig. 21,b.
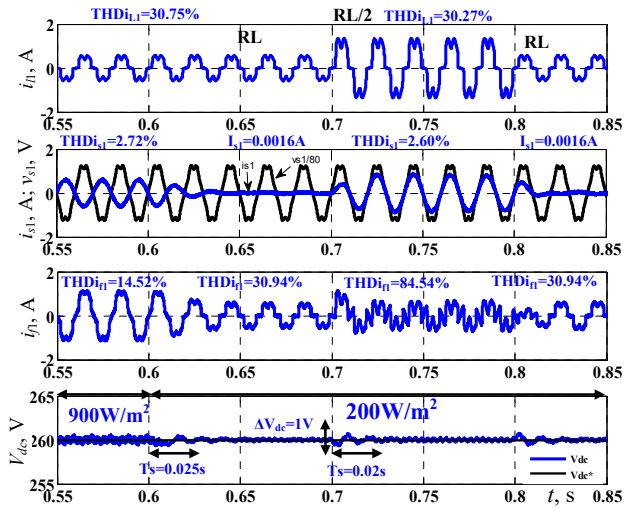
Fig. 20. Performance under step change in solar irradiation and NL
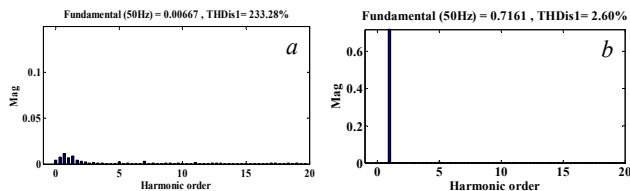
Fig. 21. Harmonic spectrum of i_{s1} and i_{f1} under step change of solar irradiation

Additionally, Fig. 22 illustrates that both active and reactive power sources become null, indicating that the grid does not supply any power to the load. These findings provide insights into the system's robust performance under varying irradiation conditions, showcasing its ability to adapt and maintain stable operation, and all the obtained results of this sever test are presented in Table 6.

Table 6
Performance of the system under distorted unbalanced voltage

G, W/m^2	900	200	
Load type	$(R_d+L_d+C_d)$	(R_d+L_d)	$(R_d+L_d)/2$
t, s	[0.4–0.45]	[0.6–0.7]	[0.7–0.8]
THDi_{s1}, %	0 ($I_s{\approx}0$)	0 ($I_s{=}0$)	2.66 %, PF=1
THDi_{f1}, %	29.31	30.94	84.54
THDi_{L1}, %	31.16	30.75 %	30.75
P_s, W	0.05	0	128
Q_s, VAR	0.05	0	0
P_{ch}, W	175	82	192
P_{pv}, W	175	82	82
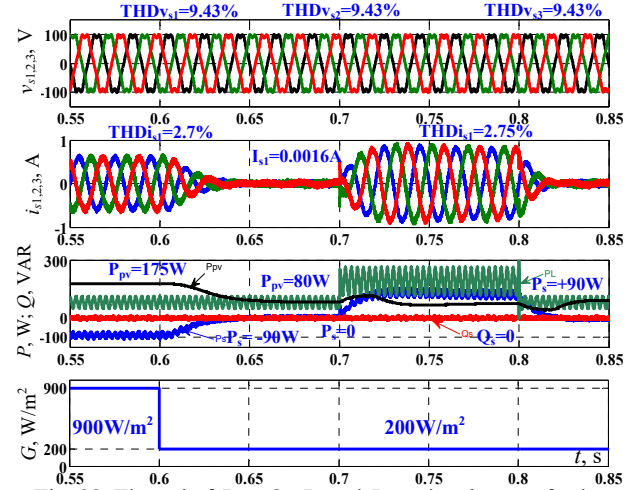
Fig. 22. Flowed of P_{PV}, Q_s, P_s and P_L under change of solar irradiation and NL

Testing performance of the proposed system under fluctuations of solar irradiation. At the instant 0.9 s, when solar radiation increased from 200 W/m² to 900 W/m², we noticed from Fig. 23 that the SAPF is capable of cleaning the grid from the current harmonics generated by the NL and the grid current will be in opposite phase with the grid voltage, which means that the unity PF is reached in this operation condition. In addition, the efficiency the SAPF's algorithm control is confirmed by injecting filter current to compensate the harmonic load current and injecting the fundamental current in the grid, this results is justified by reading the THD of the grid current, it passes from 28.14 % to 3.51 % after switching ON the SAPF as depicted in Fig. 22, then the IEEE-519 standard is satisfactory.
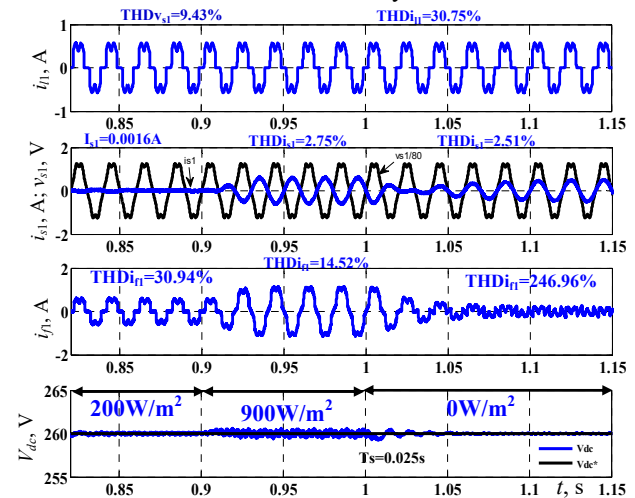
Fig. 23. Behavior of the system when the solar irradiation change (200 / 0 / 900) W/m^2

Its can be observed that the reactive source is drawn to 0, which justify the good behavior of the proposed system to compensate the reactive power generated by the NL. Also the active power is 90 W, which illustrate that the SAPF inject into grid the surplus of the active power provided by the PV system and the NL is fed from the PV system.

The third test is carried out at the instant 1 s, when the solar irradiation is drawn to G=0, it can be observed from Fig. 23 that the grid current is become positive and in phase with the grid voltage, and kept its sinusoidal waveform and its THD pass to 2.52 % (Fig. 24,*a*), the filter current is high distorted and contain only the reactive fundamental and harmonic current (its THD pass from 14.52 % to 246.9 %), then we can say the unity PF is obtained in this condition and the harmonic current are suppression.
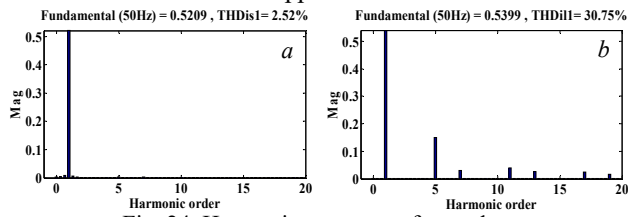
Fig. 24. Harmonic spectrum of i_{s1} and i_{L1}

On the other hand, from Fig. 25, it can be remarked that the active power source become positive, which signify that the PV system no provide any power and the NL is supplied by the grid (P_s = 90 W). We can prove, through these performance tests, that the control algorithms applied to the proposed system have fulfilled their main roles, for which they were designed, under different solar radiations, different types of loads and under non-optimal grid voltage. The results of this performance test are given in Table 7.
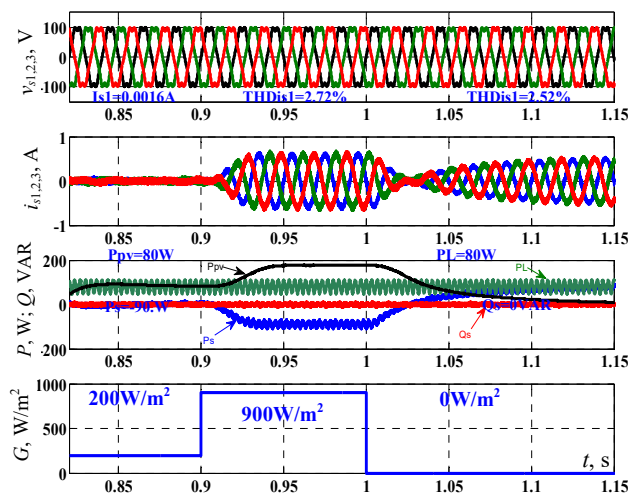
Fig. 25. Flowed of the P_{pv}, Q_s, P_s and P_L under solar irradiation changes

Table 7
Performance of the system under distorted unbalanced voltage

G, W/m^2	0 W/m^2 [1–1.2 s] STF-PQ	900 W/m^2 [1.2–1.3 s] STF-PQ
THDi_{L1}, %	30.75	30.75
THDi_{s1}, %	2.52 % and PF=1	2.72 % and PF=1
THDi_{f1}, %	246.96	14.52
P_s, W	81	–90
Q_s, VAR	0	0
P_{ch}, W	81	81
P_{pv}, W	0	175

Conclusions. In this work, a dual functionality of a double stage grid connected PV system has been performed, analyzed and examined. The majors' tasks of the proposed system have been realized desired target throughout inserting a series active filter concept with injection of the surplus active power into the grid during periods of low overall demand.

From electrical network side, a novel PCC based on discrete-time model for controlling source voltage inverter of the SAPF has been developed. Moreover, modified PQ algorithm, which based on the STF was used for accurately extracting the reference filter currents required for PCC, of which turn, facilitates the generation of the SAPF's switching signals.

From the PV generator side, a P&O based MPPT algorithm has been used to extract MPP generated by the PV array which governs the duty cycle of the DC-DC boost converter. To prove the efficiency of the proposed framework, multiples comprehensive testing has been undergone considering the variations in nonlinear loads and solar radiation fluctuations.

Simulated results highlight superior performance in both transient and stable states, affirming the robustness and effectiveness of the proposed controllers, and thanks to them, we achieved impressive results, by reading the power supply current distortion index, which reduced the THD to less than 5 % according to IEEE-519 standard, which indicates that the proposed system is robust, homogeneous, and performs its assigned role with distinction.

Conflict of interest. The authors declare that they have no conflicts of interest.

REFERENCES
1. El-Habrouk M., Darwish M.K., Mehta P. Active power filters: A review. *IEE Proceedings - Electric Power Applications*, 2000, vol. 147, no. 5, pp. 403-413. doi: https://doi.org/10.1049/ip-epa:20000522.
2. Hamouda N., Babes B., Kahla S., Hamouda C. Uwe R. An optimized FO-PID controller and predictive current control of the APF connected AWPS for power quality improvement. *Przeglad Elektrotechniczny*, 2023, vol. 99, no. 5, pp. 102-107. doi: https://doi.org/10.15199/48.2023.05.19.
3. Dash D.K., Sadhu P.K. A Review on the Use of Active Power Filter for Grid-Connected Renewable Energy Conversion Systems. *Processes*, 2023, vol. 11, no. 5, art. no. 1467. doi: https://doi.org/10.3390/pr11051467.
4. Patidar R.D., Singh S.P., Khatod D.K. Single-phase single-stage grid-interactive photovoltaic system with active filter functions. *IEEE PES General Meeting*, 2010, pp. 1-7. doi: https://doi.org/10.1109/PES.2010.5588185.
5. Shah P.K., Kotwal C.D., Giri A.K., Chitti Babu B. Study of multi-objective photovoltaic grid connected system using SOGI-FLL and NL-SOGI-FLL-APF based DQ hysteresis method. *Electrical Engineering*, 2023, vol. 105, no. 5, pp. 2735-2749. doi: https://doi.org/10.1007/s00202-023-01817-3.
6. Bourouis B., Djeghloud H., Benalla H. Energy efficiency of a 3-level shunt active power filter powered by a fuel-cell / battery DC bus with regulated duty cycles. *Electrical Engineering & Electromechanics*, 2021, no. 5, pp. 30-38. doi: https://doi.org/10.20998/2074-272X.2021.5.05.
7. Ouchen S., Betka A., Abdeddaim S., Menadi A. Fuzzy-predictive direct power control implementation of a grid connected photovoltaic system, associated with an active power filter. *Energy Conversion and Management*, 2016, vol. 122, pp. 515-525. doi: https://doi.org/10.1016/j.enconman.2016.06.018.
8. Reisi A.R., Moradi M.H., Showkati H. Combined photovoltaic and unified power quality controller to improve power quality. *Solar Energy*, 2013, vol. 88, pp. 154-162. doi: https://doi.org/10.1016/j.solener.2012.11.024.

9. Nordin A.H.M., Omar A.M. Modeling and simulation of Photovoltaic (PV) array and maximum power point tracker (MPPT) for grid-connected PV system. *2011 3rd International Symposium & Exhibition in Sustainable Energy & Environment (ISESEE)*, 2011, pp. 114-119. doi: https://doi.org/10.1109/ISESEE.2011.5977080.

10. Zerzouri N., Ben Si Ali N., Benalia N. A maximum power point tracking of a photovoltaic system connected to a three-phase grid using a variable step size perturb and observe algorithm. *Electrical Engineering & Electromechanics*, 2023, no. 5, pp. 37-46. doi: https://doi.org/10.20998/2074-272X.2023.5.06.

11. Elgendy M.A., Zahawi B., Atkinson D.J. Assessment of Perturb and Observe MPPT Algorithm Implementation Techniques for PV Pumping Applications. *IEEE Transactions on Sustainable Energy*, 2012, vol. 3, no. 1, pp. 21-33. doi: https://doi.org/10.1109/TSTE.2011.2168245.

12. Babes B., Albalawi F., Hamouda N., Kahla S., Ghoneim S.S.M. Fractional-Fuzzy PID Control Approach of Photovoltaic-Wire Feeder System (PV-WFS): Simulation and HIL-Based Experimental Investigation. *IEEE Access*, 2021, vol. 9, pp. 159933-159954. doi: https://doi.org/10.1109/ACCESS.2021.3129608.

13. Salmeron P., Herrera R.S. Distorted and Unbalanced Systems Compensation Within Instantaneous Reactive Power Framework. *IEEE Transactions on Power Delivery*, 2006, vol. 21, no. 3, pp. 1655-1662. doi: https://doi.org/10.1109/TPWRD.2006.874115.

14. Abdusalam M., Poure P., Saadate S. Study and experimental validation of harmonic isolation based on High Selectivity Filter for three-phase active filter. *2008 IEEE International Symposium on Industrial Electronics*, 2008, pp. 166-171. doi: https://doi.org/10.1109/ISIE.2008.4676991.

15. Biricik S., Redif S., Khadem S.K., Basu M. Improved harmonic suppression efficiency of single-phase APFs in distorted distribution systems. *International Journal of Electronics*, 2016, vol. 103, no. 2, pp. 232-246. doi: https://doi.org/10.1080/00207217.2015.1036318.

16. Chemidi A., Benhabib M.C., Bourouis M.A. Performance improvement of shunt active power filter based on indirect control with a new robust phase-locked loop. *Electrical Engineering & Electromechanics*, 2022, no. 4, pp. 51-56. doi: https://doi.org/10.20998/2074-272X.2022.4.07.

17. Rodriguez J., Pontt J., Silva C.A., Correa P., Lezana P., Cortes P., Ammann U. Predictive Current Control of a Voltage Source Inverter. *IEEE Transactions on Industrial Electronics*, 2007, vol. 54, no. 1, pp. 495-503. doi: https://doi.org/10.1109/TIE.2006.888802.

18. Boukezata B., Gaubert J.-P., Chaoui A., Hachemi M. Predictive current control in multifunctional grid connected inverter interfaced by PV system. *Solar Energy*, 2016, vol. 139, pp. 130-141. doi: https://doi.org/10.1016/j.solener.2016.09.029.

19. Zine H.K.E., Abed K. Smart current control of the wind energy conversion system based permanent magnet synchronous generator using predictive and hysteresis model. *Electrical Engineering & Electromechanics*, 2024, no. 2, pp. 40-47. doi: https://doi.org/10.20998/2074-272X.2024.2.06.

20. Bouafia A., Gaubert J.-P., Krim F. Predictive Direct Power Control of Three-Phase Pulse Width Modulation (PWM) Rectifier Using Space-Vector Modulation (SVM). *IEEE Transactions on Power Electronics*, 2010, vol. 25, no. 1, pp. 228-236. doi: https://doi.org/10.1109/TPEL.2009.2028731.

21. Hamouda N., Benalla H., Hemsas K., Babes B., Petzoldt J., Ellinger T., Hamouda C. Type-2 fuzzy logic predictive control of a grid connected wind power systems with integrated active power filter capabilities. *Journal of Power Electronics*, 2017, vol. 17, no. 6, pp. 1587-1599. doi: https://doi.org/10.6113/JPE.2017.17.6.1587.

Assam Zorig[1], *Associate Professor,*
Badreddine Babes[2], *Senior Researcher,*
Noureddine Hamouda[2], *Senior Researcher,*
Souhil Mouassa[3], *Professor,*
[1] Department of Electrical Engineering,
Faculty of Technology, Mohamed Boudiaf University, Algeria,
e-mail: assam.zorig@univ-msila.dz
[2] Research Center in Industrial Technologies, Algeria,
e-mail: b.babes@crti.dz; n.hamouda@crti.dz
[3] University of Bouira, Algeria,
e-mail: souhil.mouassa@univ-bouira.dz (Corresponding Author)

How to cite this article:
Zorig A., Hamouda N., Babes B., Mouassa S. Improving the efficiency of a non-ideal grid coupled to a photovoltaic system with a shunt active power filter using a self-tuning filter and a predictive current controller. *Electrical Engineering & Electromechanics*, 2024, no. 6, pp. 33-43. doi: https://doi.org/10.20998/2074-272X.2024.6.05

M. Manohara, S. Muthukaruppasamy, R. Dharmaprakash, S. Sendilkumar, D. Dattatreya Bharadwaj, E. Parimalasundar

Power quality enhancement of grid-integrated solar photovoltaic system with unified power quality conditioner

*Introduction. To enhance the quality of power and ensure a consistent electricity supply, this study proposes the utilization of a unified power quality conditioner (UPQC) system integrated with solar photovoltaic (PV) technology. The innovation involves single DC-link connecting back-to-back voltage-compensating components arranged in series and shunt, forming the PV-UPQC. The shunt compensator utilizes energy from a PV array to address harmonics in the load current. The objective is to mitigate voltage dips and spikes by injecting voltage that is either in phase with or out of phase with the common coupling point through a series compensator. The method combines the benefits of generating renewable energy to enhance electrical quality. The **goal** of the paper is the power quality enhancement of grid-integrated solar PV system. The **novelty** of the proposed work consists of enhancement of grid-integrated solar PV system with UPQC. The purpose of integrating a UPQC into a grid-connected solar PV system is to enhance power quality by mitigating issues such as voltage fluctuations, harmonics and reactive power imbalance. **Methods.** The proposed topology is implemented in MATLAB/Simulink with grid-integrated solar PV system with UPQC. **Results.** Integrating UPQC with a grid-connected solar PV system yields substantial improvements in power quality. This includes effectively mitigating voltage fluctuations and harmonics, resulting in smoother operation and reduced disturbances on the grid. **Practical value.** The proposed topology has proven to be extremely useful for grid-integrated solar PV system with UPQC applications.* References 15, table 2, figures 9.
Key words: **grid integration, unified power quality conditioner, power quality, photovoltaic array.**

*Вступ. Для підвищення якості електроенергії та забезпечення безперебійного електропостачання пропонується використовувати систему уніфікованого стабілізатора якості електроенергії (UPQC), інтегровану із сонячною фотоелектричною (PV) технологією. Інновація включає одиночну лінію постійного струму, що з'єднує зустрічно-паралельні компоненти компенсації напруги, розташовані послідовно, і шунт, утворюючи PV-UPQC. Шунтуючий компенсатор використовує енергію від масиву PV батарей для усунення гармонік струму навантаження. Мета полягає в тому, щоб пом'якшити провали та стрибки напруги шляхом подачі напруги, яке або збігається по фазі із загальною точкою з'єднання, або не збігається по фазі з нею через послідовний компенсатор. Метод поєднує переваги генерації відновлюваної енергії підвищення якості електроенергії. **Метою** статті є підвищення якості електроенергії інтегрованої в мережу сонячної фотоелектричної системи. **Новизна** запропонованої роботи полягає у покращенні інтегрованої у мережу сонячної PV системи за допомогою UPQC. Метою інтеграції UPQC у мережеву сонячну PV систему є підвищення якості електроенергії за рахунок пом'якшення таких проблем, як коливання напруги, гармоніки та дисбаланс реактивної потужності. **Методи.** Запропонована топологія реалізована у MATLAB/Simulink з інтегрованою в мережу сонячною PV системою з UPQC. **Результати.** Інтеграція UPQC із підключеною до мережі сонячною PV системою дає суттєве покращення якості електроенергії. Це включає ефективне пом'якшення коливань напруги і гармонік, що призводить до більш плавної роботи і зменшення перешкод в мережі. **Практична цінність.** Запропонована топологія виявилася надзвичайно корисною для інтегрованої в мережу сонячної PV системи із застосуваннями UPQC. Бібл. 15, табл. 2, рис. 9.*
Ключові слова: **мережева інтеграція, уніфікований стабілізатор якості електроенергії, якість електроенергії, фотоелектрична батарея.**

Introduction. In contemporary times, digital, electronic, and nonlinear devices under the control of microprocessors find extensive applications in various industries. The incorporation of these technologies has become indispensable across diverse sectors. Such systems can lead to power quality problems such as voltage sag, voltage swell, flickering, harmonics, over-voltage, lower power factor, etc. Data errors, memory loss, automated restarts, uninterruptible power supply alarms, equipment failure, circuit failure, software corruption, and distribution network overheating are occurred at various systems due to poor power quality. The significance of power quality has grown in light of these issues. Sensitive loads such as hospitals particularly diagnostic equipment, and classrooms have been affected severely due to poor power quality. This heightened dependence on digital and electronic devices raises concerns about the quality of electricity supplied to these systems. Consequently, ensuring optimal power quality has become a pressing concern to avoid disruptions and potential damage to sensitive equipment. Batteries, fuel cells, and ultracapacitors have been used for custom power devices so far. Among the most significant power

quality issues is voltage swell, encompassing challenges related to harmonics, transients, flicker, and interruptions [1–4]. Protecting sensitive and important loads requires addressing power quality and voltage disruptions. Custom power devices have emerged as the most effective and efficient technique to addressing and correcting for voltage disturbances in this industry, while other solutions have been offered. Electric vehicles, microgrids, distribution static compensators, high-power and moderate-voltage motors, microcontrollers, and grid-integrated or standalone systems are just a few of the many industrial applications where multilevel inverters (MLIs) play a significant role. They also play a pivotal role in diverse sectors, such as active power filters, photovoltaic (PV) systems, and more. The integration of PV systems with dynamic voltage restorer (DVR) leads to the simultaneous minimization of harmonics, voltage dips, and improvement of power factors, effectively meeting energy requirements. In the context of a PV-supplied DVR, the implementation of a 23-level MLI utilizing a rotating *d-q* reference frame controller [5–8] plays a crucial role. The amalgamation of PV with MLI DVR significantly enhances power quality by reducing

instances of voltage sags and swells. The following features are listed below for improving power quality:

• there are just 3 DC sources and 12 switches (7 unidirectional and 5 bidirectional) throughout the entire 23-level MLI;

• the majority of switches can function at medium voltages because of their minimal voltage stress.

A power quality conditioner with shunt and series compensators can modify load voltage and preserve sinusoidal grid current at one power factor. Active power filters [3] come in 2 main varieties: shunt and series. Using the unified power quality conditioner (UPQC) in conjunction with a PV array might make the system energy-independent and environmentally friendly. Improved grid power quality, protection for critical loads from grid side disturbances, and enhanced converter capacity to ride over faults during transients are just a few of how the solar PV integrated UPQC excels above conventional grid-connected inverters. PV-UPQC control faces a significant challenge in creating the reference signal. Time-domain and frequency-domain approaches are the 2 main subcategories of reference signal generation techniques. Because real-time implementation calls for less processing, time-domain methods are frequently employed. Theories of instantaneous reactive power, synchronous reference frames, and instantaneous symmetrical components are the most often used approaches [9–11]. The main difficulty for the synchronous reference frame theory method is producing a d-axis current with a two-harmonic component. This becomes particularly prominent when uneven loads are present. The double harmonic component is removed using low-pass filtering techniques with incredibly low cut-off frequencies. As a result, dynamic performance is compromised. In this study, the primary load active current is obtained by filtering the d-axis current using a moving average filter (MAF). This provides the best attenuation without affecting the controller's bandwidth [11–14]. Lately, MAF has been used to synchronize the grid utilizing phase-locked loops and increase the performance of DC link controllers.

The goal of the paper is listed below for improving power quality enhancement of grid-integrated solar PV system:

• Power quality improvement and renewable energy generation together.

• Improving both current and voltage quality simultaneously.

• Better load current compensation as a result of d-q PV-UPQC's control using the MAF.

Using PV technology helps provide cleaner, greener power while lowering pollution. In the case of a grid outage, it can keep critical loads operating, improving dependability and tackling energy issues simultaneously.

Grid-integrated solar PV system with UPQC.

DVR setup for solar power input. Figure 1 shows the system's components, which include solar PV array, a three-phase, three-wire digital voltage regulator, a load, and a boost converter. A power source, a voltage-applying transformer, an LC filter, and a DC link capacitor make up the DVR. The second part of the PV system is the DVR equivalent circuit (Fig. 2). It includes both boost and maximum power point tracking controller. A voltage source V_{Comp} is established in the DVR circuit by connecting it to a load voltage V_L, another voltage source V_s and the impedances of the 2 sources (Z_S and Z_L). The current I_S divided in half at the point of common coupling (PCC) source: I_L, which stands for a sensitive load current, and I_{OT}, which stands for a different type of load current [15]. A voltage representation for PCC is V_G and DVR rectifies the voltage, which is V_{DVR}. By integrating the equivalent components of R_{DVR} and X_{DVR} with V_{DVR}, we can determine the resistance R and inductance L from the impedance ratings of the filter and injection transformer. There is an impedance of Z_S for the supply, Z_L for the load, and Z_{DVR} for the DVR. The voltage of a sensitive load is depicted as:

$$V_L(t) = V_{DVR}(t) + V_G(t) + Ri_L(t) + L\frac{di_L}{dt}. \quad (1)$$
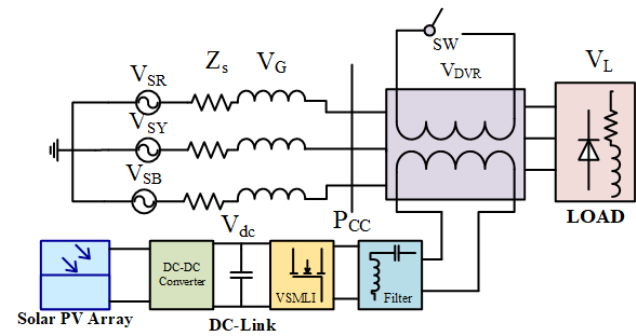
Fig. 1. MLI-DVR setup was merged by PV
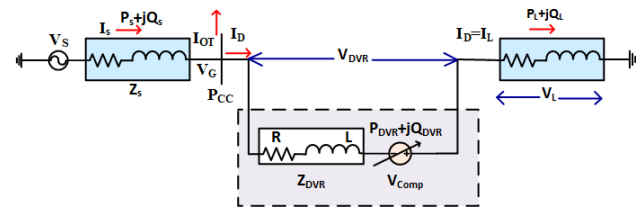
Fig. 2. DVR equivalent circuit

23-level MLI. In this particular setup, 3 DC sources (V_a, V_b and V_c) together with 7 one-way switches and 5 two-way switches are recommended [4] a cross-linked arrangement of 4 bidirectional switches. The DC voltage sources' magnitudes are configured for asymmetric operation as:

$$V_a = 1V_{dc}; \quad V_b = 3V_{dc}; \quad V_c = 7V_{dc}. \quad (2)$$

According to levels N_{Lev}, the following provides the necessary DC sources N_{DC}:

$$N_{DC}^{Asym} = \frac{(N_{Lev} - 5)}{6}. \quad (3)$$

According to the levels N_{Lev}, the number of switches N_{SW} needed is calculated as:

$$N_{SW}^{Asym} = \frac{(N_{Lev} + 1)}{2}. \quad (4)$$

All of the switches in the recommended architecture are unidirectional power switches:

$$N_{GDK}^{Asym} = N_{SW}^{Asym} = \frac{(N_{Lev} + 1)}{2}. \quad (5)$$

The following factors influence the highest voltage output $V_{L.\max}$:

$$V_{L.\max}^{Asym} = \frac{(N_{Lev} - 1)}{2}. \quad (6)$$

By the suggested design, the output voltage has 23 levels and magnitudes that range from 0 V, positive ($+V_{dc}$ to $+11V_{dc}$) and negative ($-V_{dc}$ to $-11V_{dc}$) respectively.

Boost converter analysis for solar PV. Selecting the appropriate PV panel is vital as the voltage and current produced by the solar array are affected by factors such as heat, irradiation, and the configuration of series and parallel strings [5]. In this setup, the series combination of two Trina Solar TSM-200 DC/DA01A solar panels is connected in parallel with another two such stacks to form a PV system.

Output power P_{PV} can be expressed as:

$$P_{PV} = V_{PV} \cdot I_{PV} \quad (7)$$

where V_{pv}, I_{pv} are respective the PV panels output voltage and current.

The current flow can be expressed as:

$$I_{PV} = I_s - I_p - I_d = I_s - I_p - I_0 e^{(V_D/V_T)-1}. \quad (8)$$

Saturation current can be expressed as:

$$I_{s(T)} = I_{s(TR)}[1 + (T - T_R)\beta] \quad (9)$$

where I_p is the photocurrent generated by light; I_d is the recombination current; I_0 is the reverse saturation current; V_D is the voltage across PV; V_T is the thermal voltage; f_s is the switching frequency, and the ripple factors for the output voltage (V_{dc}) and current (I_L) are crucial parameters. It is essential to conduct a thorough assessment of inductors and capacitors.

The change in current (ΔI_L) should be restricted to 30 %, while the variation in voltage (V_{dc}) is conventionally considered as 5 %. Table 1 provides a concise overview of the solar PV and boost converter characteristics.

Table 1
PV module and boost converter's specifications

Module of 200 W		Boost converter	
V, V	37.6	L, mH	1.28
P, W	200	C, µF	1.31
I, A	5.32	$V_{in} = V_{PV}$, V	112.8
V_{oc}, V	46	Duty cycle, D	0.718
I_{sc}, A	5.6	V_{dc}, V	400

Management of PV-fed MLI-DVR. Various compensation techniques are used by DVR to handle different loads and voltage sag scenarios. A PV-fed DVR is an integrated system designed to address voltage fluctuations and provide a stable electricity supply using both PV technology and dynamic voltage restoration capabilities. It is recognized that not all loads are sensitive to changes in voltage magnitude; some respond to both variations and others to changes in phase angle. Depending on the characteristics of the load, a control strategy is chosen. One approach is the pre-sag compensating method, which takes into consideration both the magnitude and phase angles of the voltage sag [6]. The PI controller for a DVR, which makes sure that

the amplitude and phase angle of the load voltage and pre-sag voltage are equal, keeping them at the same level, respectively. The DVR's ability to provide active power from an energy source and inject reactive power during sag becomes increasingly crucial. Moreover, the DVR's regulation of external power consumption impacts the efficiency ratings of batteries and grid electricity.

System construction of UPQC. PV-fed UPQC is a specialized power electronic device used in electrical power systems to mitigate power quality issues while integrating PV systems into the grid.

The proposed system comprises series-shunt compensating converters arranged in a basic block diagram (Fig. 3). These basic blocks serve the purpose of injecting voltage in series with the load to rectify the sinusoidal nature of the voltage, thus mitigating the effects of harmonics.
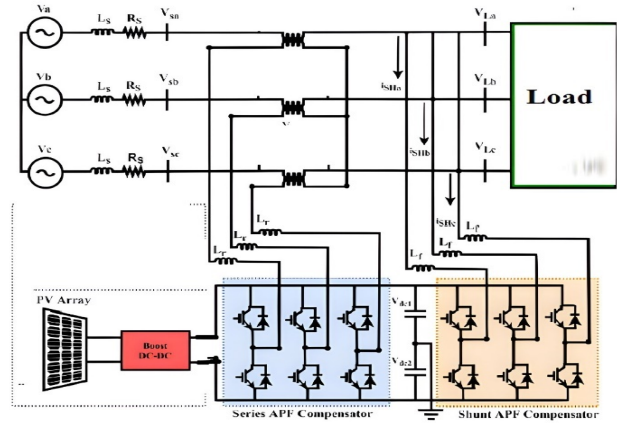
Fig. 3. PV fed UPQC

Additionally, the shunt converter plays a crucial role in regulating the DC link and provides reverse blocking capability for enhanced control. Power filtration is employed to improve the reliability of the power supply. The PV-UPQC is constructed using converters with series-shunt compensation, where shunt and series compensators are interconnected through a single DC bus. The shunt converter is connected to the load side and assists in voltage management. The series compensator addresses grid voltage fluctuations such as sags and swells while operating in voltage management mode. Interface inductors facilitate the connection between the grid and the shunt and series compensators. The proposed system incorporates series-shunt compensating converters to rectify voltage irregularities and mitigate harmonics, with additional features like reverse blocking capability and power filtration to enhance the supply reliability. Since the proposed system is a hybrid system, it meets the load demand from a PV source and from a grid.

Figure 4 illustrates the DVR pre-sag voltage injection method and can be expressed as:

$$V_{DVRp} = \sqrt{2}\sqrt{(V_G^{Sag})^2 + ((V_L)^2) - (2V_L V_{G.p}^{Sag} \cos(\delta_p))}, \quad (10)$$

where V_{DVR} is the DVR injected voltage; φ is the phase angle between V_L and I_L; $V_{G.p}^{Sag}$ is the grid peak voltage at sag; δ is the corresponding angle of phase jump to V_G^{Sag}.
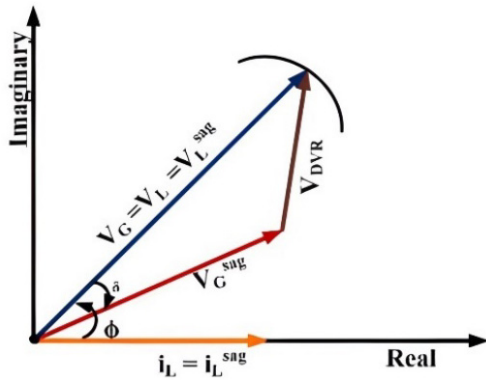
Fig. 4. DVR pre-sag voltage injection method

Results and discussion. PV-fed DVR. 10 kVA injection transformer rated at 400 V (1:1) connects the DVR to the system. The PV array's output voltage is increased to 400 V with the help of a boost converter. An 8 kW linear load running at a 0.85 lag power factor and a regular 400 V battery supply allow the system to maintain a steady DC connection voltage. At maximum power point the PV array's output voltage is 112.8 V; however, with the help of the boost converter, it is increased to 400 V, making it compatible with the DC connector. In addition, the phase voltage of the 23-level MLI is shown in Fig. 5.
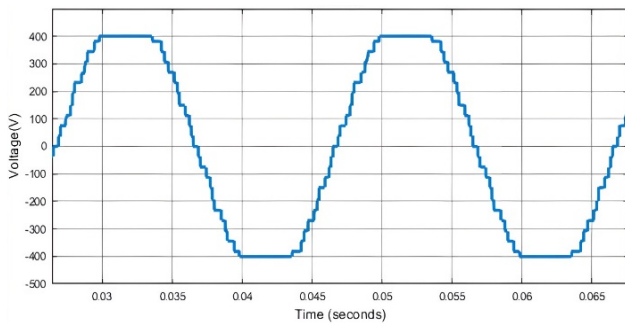
Fig. 5. The phase voltage of a 23-level MLI

Figures 6, 7 display the load voltages at 0.5 pu sag condition and 1.2 pu swell conditions and their associated total harmonic distortion (THD) voltage value at the load side.
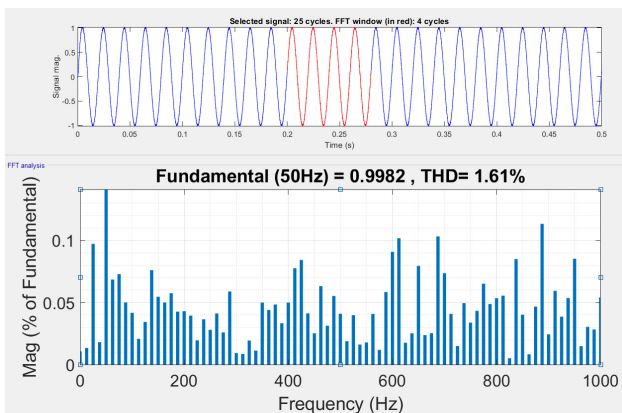
Fig. 6. Load voltages THD at 0.5 pu sag mode
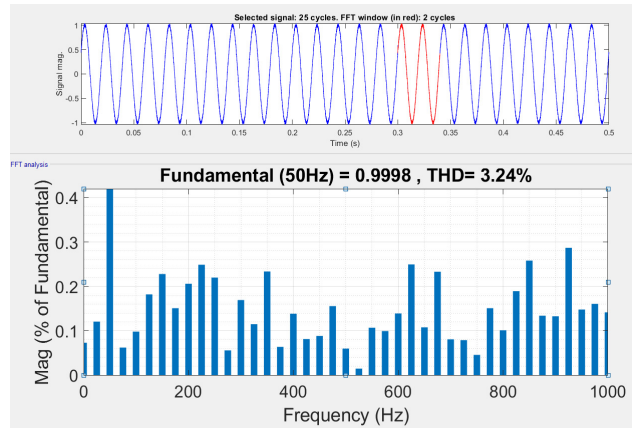
Fig. 7. Load voltage THD at 1.2 pu swell condition

PV fed UPQC. Figures 8, 9 display the load voltages at 0.5 pu sag condition and 1.2 pu swell condition and its associated THD voltage value at the load side.
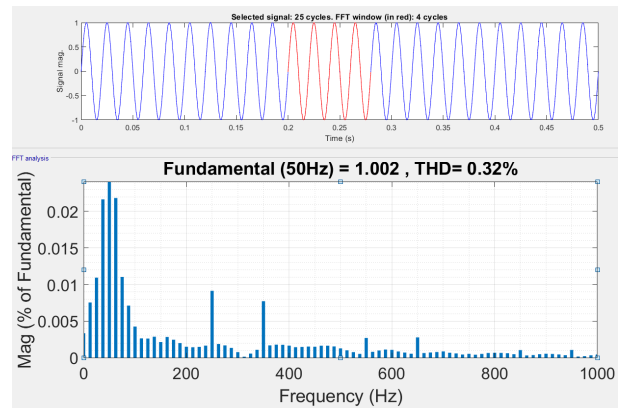
Fig. 8. Load voltage at 0.5 pu sag mode
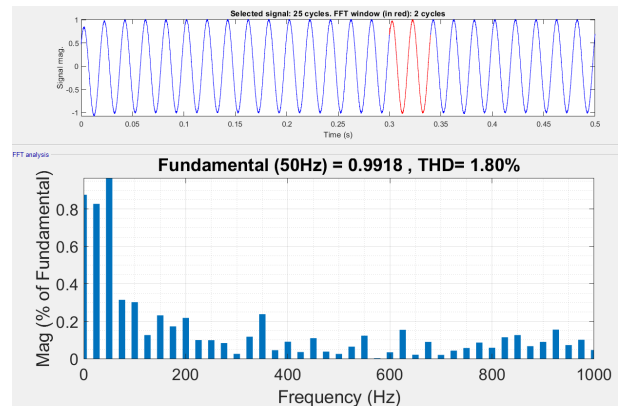
Fig. 9. Load voltage at 1.2 pu swell mode

In Table 2, a thorough comparison of the PV-fed DVR and PV-fed UPQC is shown.

Table 2

Comparison of PV-fed UPQC and PV-fed DVR

Conditions	Load voltage THD	
	PV-fed DVR	PV-fed UPQC
0.5 pu sag	1.61 %	0.32 %
1.2 pu swell	3.24 %	1.80 %

Conclusions. Solar photovoltaic (PV) systems are most impacted when connected to non-linear loads during sag-swell circumstances because harmonics are created. To mitigate these effects of harmonics, the unified power quality

conditioner (UPQC) approaches help to improve the operation of such systems. It is discovered that the PV-fed UPQC system operates effectively while compensating for voltage sag. A solar-powered asymmetrical 23-level multilevel inverter (MLI) with dynamic voltage restorer is equipped with a rotating *d-q* reference frame controller. By using fewer circuit components, the proposed MLI's synthesized output voltage is produced with a lower THD. The PV-UPQC system simulation has been put into practice. It has been demonstrated that with such a configuration, THD is greatly minimized and the system's performance has increased to a decent level.

Conflict of interest. The authors declare that they have no conflicts of interest.

REFERENCES
1. Odeh C., Lewicki A., Morawiec M., Kondratenko D. Three-Level F-Type Inverter. *IEEE Transactions on Power Electronics*, 2021, vol. 36, no. 10, pp. 11265-11275. doi: https://doi.org/10.1109/TPEL.2021.3071359.
2. Parimalasundar E., Kumar N.M.G., Geetha P., Suresh K. Performance investigation of modular multilevel inverter topologies for photovoltaic applications with minimal switches. *Electrical Engineering & Electromechanics*, 2022, no. 6, pp. 28-34. doi: https://doi.org/10.20998/2074-272X.2022.6.05.
3. Parimalasundar E., Senthil Kumar R., Chandrika V.S., Suresh K. Fault diagnosis in a five-level multilevel inverter using an artificial neural network approach. *Electrical Engineering & Electromechanics*, 2023, no. 1, pp. 31-39. doi: https://doi.org/10.20998/2074-272X.2023.1.05.
4. Shahabadini M., Iman-Eini H. Leakage Current Suppression in Multilevel Cascaded H-Bridge Based Photovoltaic Inverters. *IEEE Transactions on Power Electronics*, 2021, vol. 36, no. 12, pp. 13754-13762. doi: https://doi.org/10.1109/TPEL.2021.3084699.
5. Aissaoui M., Bouzeria H., Benidir M., Labed M.A. Harmonics suppression in high-speed railway via single-phase traction converter with an LCL filter using fuzzy logic control strategy. *Electrical Engineering & Electromechanics*, 2024, no. 2, pp. 16-22. doi: https://doi.org/10.20998/2074-272X.2024.2.03.
6. Alluhaybi K., Batarseh I., Hu H. Comprehensive Review and Comparison of Single-Phase Grid-Tied Photovoltaic Microinverters. *IEEE Journal of Emerging and Selected Topics in Power Electronics*, 2020, vol. 8, no. 2, pp. 1310-1329. doi: https://doi.org/10.1109/JESTPE.2019.2900413.
7. Mhiesan H., Wei Y., Siwakoti Y.P., Mantooth H.A. A Fault-Tolerant Hybrid Cascaded H-Bridge Multilevel Inverter. *IEEE Transactions on Power Electronics*, 2020, vol. 35, no. 12, pp. 12702-12715. doi: https://doi.org/10.1109/TPEL.2020.2996097.
8. Jami R., Nakka J., Pulavarthi S.V.K. Grid integration of three phase solar powered fault-tolerant cascaded H-bridge inverter. *International Journal of Circuit Theory and Applications*, 2022, vol. 50, no. 7, pp. 2566-2583. doi: https://doi.org/10.1002/cta.3272.
9. Manohara M., Sravani M., Ganesh K.V., Leela Rani D., Babu M.M., Kavya K. Hybrid Electric Vehicle Voltage Regulation Using Backstepping Sliding Mode Control. *2023 IEEE Renewable Energy and Sustainable E-Mobility Conference (RESEM)*, 2023, pp. 1-6. doi: https://doi.org/10.1109/RESEM57584.2023.10236385.
10. Siddique M.D., Mekhilef S., Rawa M., Wahyudie A., Chokaev B., Salamov I. Extended Multilevel Inverter Topology With Reduced Switch Count and Voltage Stress. *IEEE Access*, 2020, vol. 8, pp. 201835-201846. doi: https://doi.org/10.1109/ACCESS.2020.3026616.
11. Manohara M., Veera Reddy V.C., Vijaya Kumar M. Exploration and mitigation of power quality problems in radial distribution system by placing distributed generation through voltage stability index. *Electrical Engineering & Electromechanics*, 2023, no. 2, pp. 79-85. doi: https://doi.org/10.20998/2074-272X.2023.2.12.
12. Ikhe A., Pahariya Y. Voltage regulation using three phase electric spring by fuzzy logic controller. *Electrical Engineering & Electromechanics*, 2023, no. 4, pp. 14-18. doi: https://doi.org/10.20998/2074-272X.2023.4.02.
13. Davis T.T., Joseph T., Dey A. A Capacitor Voltage Balancing Scheme for Single-Source Fed Switch Optimized Three-Phase Nine-Level Inverter. *IEEE Transactions on Industrial Electronics*, 2021, vol. 68, no. 5, pp. 3652-3661. doi: https://doi.org/10.1109/TIE.2020.2982092.
14. Zine H.K.E., Abed K. Smart current control of the wind energy conversion system based permanent magnet synchronous generator using predictive and hysteresis model. *Electrical Engineering & Electromechanics*, 2024, no. 2, pp. 40-47. doi: https://doi.org/10.20998/2074-272X.2024.2.06.
15. Balakishan P., Chidambaram I.A., Manikandan M. Improvement of power quality in grid-connected hybrid system with power monitoring and control based on internet of things approach. *Electrical Engineering & Electromechanics*, 2022, no. 4, pp. 44-50. doi: https://doi.org/10.20998/2074-272X.2022.4.06.

M. Manohara [1]*, Associate Professor,*
S. Muthukaruppasamy [2]*, Professor,*
R. Dharmaprakash [3]*, Professor,*
S. Sendilkumar [4]*, Professor,*
D. Dattatreya Bharadwaj [1]*, Undergraduate Student,*
E. Parimalasundar [1]*, Professor,*
[1] Department of Electrical and Electronics Engineering,
Mohan Babu University, India,
e-mail: muppirimanohar@yahoo.com;
dattatreyabharadwaj@gmail.com; parimalpsg@gmail.com
[2] Electrical and Electronics Engineering,
Velammal Institute of Technology, Anna University, India,
e-mail: mksamy14@yahoo.com (Corresponding Author)
[3] Department of Electrical and Electronics Engineering,
Panimalar Engineering College, India,
e-mail: rdharmaprakash@yahoo.co.in
[4] Department of Electrical and Electronics Engineering,
S.A. Engineering College, India,
e-mail: sendilkumar2009@gmail.com

F. Saidi, A. Djahbar, E. Bounadja, W.M. Kacemi, K. Fettah

Novel modular multilevel matrix converter topology for efficient high-voltage AC-AC power conversion

Introduction. This paper delves into the practical application of multilevel technology, particularly focusing on the capacitor-clamped converter as a promising solution for medium-to-high voltage power conversion, with specific emphasis on direct AC-AC switching conditions. ***Problem.*** *The limitations of conventional single-cell matrix converters (MC) in efficiency and performance for medium-to-high voltage power conversion applications are well-recognized.* ***Goal.*** *The primary objective is to investigate the performance of the 3 phase modular multilevel matrix converter (3MC) with three flying capacitors (FCs) modeling. This investigation utilizes the Venturini method for gate pulse generation, aiming to compare the performance of the 3MC with standard converter designs.* ***Methodology.*** *To achieve the research goal, the Venturini method is adopted for generating gate pulses for the 3MC, representing a departure from conventional approaches. Detailed simulations employing MATLAB/Simulink are conducted to comprehensively evaluate the performance of the 3MC in comparison to conventional converter designs.* ***Results.*** *The simulation outcomes reveal a significant reduction of 73 % in total harmonic distortion (THD) achieved by the 3MC. This reduction in THD indicates improved robustness and suitability for medium-to-high voltage power conversion systems necessitating direct AC-AC conversion. These results highlight the efficacy of the 3MC in enhancing power conversion efficiency and overall performance.* ***Originality.*** *This paper contributes novel insights into the practical implementation of multilevel technology, particularly within the realm of capacitor-clamped converters. Furthermore, the utilization of the Venturini method for gate pulse generation in the 3MC represents an original approach to enhancing converter performance.* ***Practical value.*** *The research findings present significant advancements in multilevel transformer technology, offering valuable guidance for optimizing transformer design in various industrial and renewable energy applications. These contributions serve to enhance the development of reliable and efficient power systems, addressing critical needs in the energy sector. References 54, tables 3, figures 4.*
Key words: **matrix converter, Venturini method, modular multilevel matrix converter, power conversion.**

Вступ. У цій статті розглядається практичне застосування багаторівневої технології, зокрема, з упором на перетворювач з конденсаторною фіксацією як перспективне рішення для перетворення потужності середньої та високої напруги з особливим акцентом на умовах прямого АС-АС перемикання. Проблема. Обмеження звичайних одноелементних матричних перетворювачів (МС) в ефективності та продуктивності для додатків перетворення потужності середньої та високої напруги загальновідомі. Мета. Основною метою є дослідження продуктивності трифазного багаторівневого модульного матричного перетворювача (3МС) з моделюванням трьох навісних конденсаторів (FC). У цьому дослідженні використовується метод Вентуріні для генерації стробуючих імпульсів з метою порівняння продуктивності 3МС зі стандартними конструкціями перетворювачів. Методологія. Для досягнення мети метод Вентуріні прийнятий для генерації стробуючих імпульсів для 3МС, що є відмінністю від традиційних підходів. Проведено докладну симуляцію з використанням MATLAB/Simulink для всебічної оцінки продуктивності 3МС порівняно з традиційними конструкціями перетворювачів. Результати моделювання показують значне зниження на 73 % загального коефіцієнта гармонічних спотворень (THD), досягнуте 3МС. Це зниження вказує на покращену надійність та придатність для систем перетворення електроенергії середньої та високої напруги, що вимагають прямого АС-АС перетворення. Ці результати підкреслюють ефективність 3МС підвищення ефективності перетворення електроенергії та загальної продуктивності. Оригінальність. Ця стаття робить новий внесок у практичну реалізацію багаторівневої технології, особливо в області перетворювачів з конденсаторною фіксацією. Крім того, використання методу Вентуріні для генерації імпульсів затвора в 3МС є оригінальним підходом до підвищення продуктивності перетворювача. Практична цінність. Результати дослідження представляють значні досягнення в технології багаторівневих трансформаторів, пропонуючи цінні рекомендації щодо оптимізації конструкції трансформаторів у різних промислових та відновлюваних джерелах енергії. Ці вклади служать для поліпшення розробки надійних і ефективних енергосистем, задовольняючи критичні потреби в енергетичному секторі. Бібл. 54, табл. 3, рис. 4.
Ключові слова: **матричний перетворювач, метод Вентуріні, модульний багаторівневий матричний перетворювач, перетворення потужності.**

Introduction. Matrix converters (MC) are widely used to convert AC-AC power and have wide applications in many industrial areas, advantages sinusoidal input-output current, large size reduction, and portable applications to so that eliminates large inertia. An extensive study has shown that MCs are currently considered major candidates for incorrect AC-DC-AC topologies in various industrial settings. MCs act primarily as forced switching cycle converters. Their system has a matrix of switches that can be toggled to either direction, making it easy to connect input and output wires. Regardless of MCs size and frequency, MCs offer many advantages compared to standard AC-DC-AC converters eliminating a DC link capacitor component with different specifications by directly converting AC input voltage to AC output voltage. They allow direct AC-to-AC conversion without intermediate DC phases, resulting in more straightforward configuration and improved performance. Size and weight can be significantly reduced by eliminating bulky parts such as transformers and DC link capacitors. Also, MC offer versatility in the application of different input and output voltages and frequencies, allowing them to quickly adjust to a wide variety of power source loads MCs are ideal for such rapid applications due to their high performance, fast dynamic response and improved reliability Power a precise adjustment is also important, so that fewer things can fail. In addition, they contribute to the reduction of electromagnetic interference, improvement of power quality, and decrease in harmonics, hence boosting compatibility with the grid. MCs are highly adaptable and can be used in various industrial and commercial sectors. They provide practical, flexible, and dependable solutions for power conversion.

MCs are a promising technology that is being evaluated for use in industrial applications. They are seen as a tiny AC-AC solution since they eliminate the need for

large capacitors. The fundamental theory of primarily focused on cycloconverters is presented in [1]. The Venturini method contributed significantly by suggesting a beneficial modulation for the 33 direct MCs (DMC) in [2–4]. This was done after rapidly switching pulse-width modulation (PWM) technologies, and the switches improved. Subsequently, additional versions of MCs, such as indirect MC (IMC) [5], sparse IMC [6], and ultrasparse IMC [7], were subsequently created. The study investigated the impact of impedance (Z) sourced, admittance (Y) sourced, and quasi-Z-sourced MCs on their enhancing effects [8, 9]. These topologies have also been investigated for multiphase and multilevel structures [10, 11]. Additionally, other modulation schemes, such as space vector modulation (SVM), indirect SVM, carrier-based, duty ratio-based and their modified forms have been suggested in [12–17]. Control techniques were designed to address specific difficulties, such as reducing standard mode voltage [18, 19] and optimizing commutation. The study also examined the implementation of overvoltage and overcurrent protection [20] and the inclusion of appropriate input current filters [21, 22].

Literature review. The actual advancement of MC begins with the research conducted by Venturini method, who put out a function analysis and presented the concept of a low-frequency modulation for matrix to explain the low-frequency characteristics of MC. There are two current modulation strategies for MCs that are used on carriers. One has been suggested in [23, 24], and the other was suggested in [25]. As described in [26, 27], successfully implemented indirect SVM. This modulation technique considers the 3-ph modulation constellation as a composite of a 3 phase AC-DC rectifier and a 3 phase DC inverter. Modeling the motor controller in this manner allows for utilizing the widely recognized space vector PWM for both the rectifier and inverter stages. In [28–30] the authors presented direct SVM, which relies on the instantaneous encoding of input current and output voltage using SVM. Unlike indirect SVM, the analysis encompasses all potential switching arrangements in 3 MCs and doesn't require a virtual DC link. A novel modulation technique called delta-sigma modulation, which utilizes a quantizer and a one-sample delay element, has been recently suggested for MCs [31–33]. This modulation technique is based on discrete-time or sample time. When comparing the suggested delta-sigma modulated MC to the saw-tooth and triangle carrier SVM of MC, it is observed that the proposed delta-sigma modulated converter can reduce high-frequency voltage noise peaks and preserve noise regulation [34–36].

A multilevel power converter topology is proposed to achieve high output voltage while reducing voltage stress in semiconductor switches. This enables the use of low voltage switching devices at reduced cost. In [34] the authors invented multilevel DMC by replacing the 9 bidirectional switches in a DMC with 9 H-bridges. The paper provided a comprehensive analysis of a capacitor-clamped multilevel MC, as described in [37, 38]. The voltage that was output's harmonic efficiency was clearly superior, as the findings showed. There is half the stress per switch. The increased number of switches and capacitors, which is concerning because it is twice, is what causes the harm.

Furthermore, an increase in capacitors would diminish the system's dependability. The research on mitigating standard mode voltage is conducted in reference [39]. The researchers have examined an iterative variant of multilevel DMC in [40–50]. This configuration is accomplished by incorporating numerous H-bridges in each line that link the output to the input. The advantage of such schemes is a minimal fluctuation in the output voltage, but this comes with the drawback of requiring many switches and intricate control algorithms. As a result, this topology is best suited for specialized applications. Additional research on fault detection in modular multilevel matrix converter (3MC) can be referenced in [51].

Problem definition. This type of 3MC does not belong to the category of Venturini method, as it lacks a capacitor storage element [23–27]. In [52] they have suggested using the flying capacitor (FCs) topology for the 3MC with bidirectional semiconductor switches. This topology involves the use of two FC per output phase. The charge current in the 3 output phase will experience non-uniform route impedance due to two FC per output phase and variable switching combinations. The authors in [53] have presented a 3MC with 3 FC per output phase. This solution seems effective in minimizing the impedance experienced by the charge current in the 3 output phase. While the study [54] provides a general comparison of capacitor-clamped multilevel MCs for medium-to-high voltage applications, our manuscript offers several novel contributions that distinguish it clearly. Our research specifically focuses on the practical application of a 3 phase 3MC with three FC, utilizing the Venturini method for gate pulse generation – a unique approach that allows for more precise switching control, resulting in a significant 73 % reduction in THD. Unlike the previous work [54], which uses PSCAD for simulations, we employ MATLAB / Simulink to conduct a more comprehensive analysis, providing deeper insights into converter performance under real-world operating conditions. Furthermore, our study emphasizes the practical implementation of multilevel technology in direct AC-to-AC conversion, offering detailed guidance on optimizing power conversion systems for industrial and renewable energy applications. This approach not only demonstrates superior efficiency and robustness but also provides a clear roadmap for enhancing the reliability and performance of high-voltage power systems, thereby filling critical gaps left by earlier studies.

In this study, we introduce a 3MC system featuring three FCs for each output phase, all managed by a Venturini method. This approach effectively reduces the impedance faced by the charging current while also enabling efficient triple-port control.

Goal of the article. The aims of this study are to improve the performance of 3MC to achieve 6 output voltage levels by adding 3 FC at each output stage and to reduce total harmonic distortion (THD) at both output stage and line voltage.

3MC with 3 FC per output phase. Figure 1 [53] illustrates the 3 phase AC-AC 3MC with 3 FC per output phase. IGBT switches in Fig. 1 [53] have the ability to carry current in both directions. Below is the analysis.

There are 4 switches – SAa$_1$, SAa$_2$, SBa$_1$, and SBa$_2$, together with C1. Ensure that all switches are equivalent and have the same resistance when turned off. When all 4 switches are in the off position, the voltage V_{C1} across the FC C1 (Fig. 1), may be determined using the principle of the potential divider [54]:

$$V_{C1} = (V_A - V_B)/2 , \qquad (1)$$

where the upper plate of V_{C1} is positively polarized, while the lower plate is negatively polarized. The same analysis applies to the other FC, C2 to C9. Therefore, $V_{C1} = V_{C4} = V_{C7}$, $V_{C2} = V_{C5} = V_{C8}$, and $V_{C3} = V_{C6} = V_{C9}$. Applying Kirchoff's law to the switch combinations (Fig. 1) the depicted current direction corresponds to the positive half cycle of the 3 phase input voltages [54]. The IGBT bidirectional switches are configured in a shared emitter arrangement [52, 54].

Fig1. 3 phase AC-AC 3MC with 3 FC per output phase

The capacitance C1 of the FC is determined by (2) [53]:

$$C_1 = I_0 / (\Delta V_C \cdot p \cdot f_{sw}), \qquad (2)$$

where I_0 is the maximum value of the load current; p is the number of cells per output phase; f_{sw} is the switching frequency; ΔV_c is the FC voltage ripple.

Control and modeling of 3MC by Venturini method. The input voltage and output voltage are determined as shown in [23–27] and presented as follows:

$$v_i = \begin{bmatrix} v_A \\ v_B \\ v_C \end{bmatrix} = V_{im} \times \begin{bmatrix} \cos(\omega_i t) \\ \cos(\omega_i t + 4\pi/3) \\ \cos(\omega_i t + 2\pi/3) \end{bmatrix}; \qquad (3)$$

$$v_0 = \begin{bmatrix} v_a \\ v_b \\ v_c \end{bmatrix} = q \times V_{im} \times \begin{bmatrix} \cos(\omega_0 t) \\ \cos(\omega_0 t + 4\pi/3) \\ \cos(\omega_0 t + 2\pi/3) \end{bmatrix}, \qquad (4)$$

where q is the voltage transfer ratio [54].

The bidirectional switches (Fig. 1) have a switching function that can be expressed as [54]:

$$S_{ijk} = \begin{cases} 1, \text{ when switch open;} \\ 0, \text{ when switch closed;} \end{cases} \qquad (5)$$

$$S_{Ajk} + S_{Bjk} + S_{Cjk} = 1;$$

where $i \in$ input phase A, B, C; $j \in$ output phase a, b, c and k is the switch column counts 1, 2.

Equation (6) models the output voltage [54]. Similarly, the equation that models the input current can be expressed as (7) [54]. Equation (8) [23–27, 53] provides a straightforward approach for expressing the modulation function in terms of the unity input displacement factor.

$$\begin{bmatrix} v_a \\ v_b \\ v_c \end{bmatrix} = \begin{bmatrix} S_{Aa} & S_{Ba} & S_{Ca} & S_{C1} & S_{C2} & S_{C3} \\ S_{Ab} & S_{Bb} & S_{Cb} & S_{C4} & S_{C5} & S_{C6} \\ S_{Ac} & S_{Bc} & S_{Cc} & S_{C7} & S_{C8} & S_{C9} \end{bmatrix} \times \begin{bmatrix} v_A \\ v_B \\ v_C \\ (v_A + v_B)/2 \\ (v_A + v_B)/2 \\ (v_A + v_B)/2 \end{bmatrix}, (6)$$

where

$S_{Aa} = S_{Aa1} \cap S_{Aa2}$; $S_{Ba} = S_{Ba1} \cap S_{Ba2}$; $S_{Ca} = S_{Ca1} \cap S_{Ca2}$;
$S_{C1} = S_{Aa1} \cap S_{Ba2} \cup S_{Ba1} \cap S_{Aa2}$; $S_{C2} = S_{Ba1} \cap S_{Ca2} \cup S_{Ca1} \cap S_{Ba2}$;
$S_{C3} = S_{Aa1} \cap S_{Ca2} \cup S_{Ca1} \cap S_{Aa2}$;
$S_{Ab} = S_{Ab1} \cap S_{Ab2}$; $S_{Bb} = S_{Bb1} \cap S_{Bb2}$; $S_{Cb} = S_{Cb1} \cap S_{Cb2}$;
$S_{C4} = S_{Ab1} \cap S_{Bb2} \cup S_{Bb1} \cap S_{Ab2}$; $S_{C5} = S_{Bb1} \cap S_{Cb2} \cup S_{Cb1} \cap S_{Bb2}$;
$S_{C6} = S_{Ab1} \cap S_{Cb2} \cup S_{Cb1} \cap S_{Ab2}$;
$S_{Ac} = S_{Ac1} \cap S_{Ac2}$; $S_{Bc} = S_{Bc1} \cap S_{Bc2}$; $S_{Cc} = S_{Cc1} \cap S_{Cc2}$;
$S_{C7} = S_{Ac1} \cap S_{Bc2} \cup S_{Bc1} \cap S_{Ac2}$; $S_{C8} = S_{Bc1} \cap S_{Cc2} \cup S_{Cc1} \cap S_{Bc2}$;
$S_{C9} = S_{Ac1} \cap S_{Cc2} \cup S_{Cc1} \cap S_{Ac2}$;
1 = switch closed; 0 = switch open;
$\cap$= logical AND operator; $\cup$= logical OR operator;

$$\begin{bmatrix} i_A \\ i_B \\ i_C \end{bmatrix} = \begin{bmatrix} (S_{Aa} \cup S_{ABa} \cup S_{ACa}) & (S_{Ab} \cup S_{ABb} \cup S_{ACb}) & (S_{Ac} \cup S_{ABc} \cup S_{ACc}) \\ (S_{Ba} \cup S_{BAa} \cup S_{BCa}) & (S_{Bb} \cup S_{BAb} \cup S_{BCb}) & (S_{Bc} \cup S_{BAc} \cup S_{BCc}) \\ (S_{Ca} \cup S_{CAa} \cup S_{CBa}) & (S_{Cb} \cup S_{CAb} \cup S_{CBb}) & (S_{Cc} \cup S_{CAc} \cup S_{CBc}) \end{bmatrix} \times \begin{bmatrix} i_a \\ i_b \\ i_c \end{bmatrix} (7)$$

where

$S_{Aa} = S_{Aa1} \cap S_{Aa2}$; $S_{ABa} = S_{Aa1} \cap S_{Ba2}$; $S_{ACa} = S_{Aa1} \cap S_{Ca2}$;
$S_{Ba} = S_{Ba1} \cap S_{Ba2}$; $S_{BAa} = S_{Ba1} \cap S_{Aa2}$; $S_{BCa} = S_{Ba1} \cap S_{Ca2}$;
$S_{Ca} = S_{Ca1} \cap S_{Ca2}$; $S_{CAa} = S_{Ca1} \cap S_{Aa2}$; $S_{CBa} = S_{Ca1} \cap S_{Ba2}$;

$S_{Ab} = S_{Ab1} \cap S_{Ab2}$; $S_{ABb} = S_{Ab1} \cap S_{Bb2}$; $S_{ACb} = S_{Ab1} \cap S_{Cb2}$;
$S_{Bb} = S_{Bb1} \cap S_{Bb2}$; $S_{BAb} = S_{Bb1} \cap S_{Ab2}$; $S_{BCb} = S_{Bb1} \cap S_{Cb2}$;
$S_{Cb} = S_{Cb1} \cap S_{Cb2}$; $S_{CAb} = S_{Cb1} \cap S_{Ab2}$; $S_{CBb} = S_{Cb1} \cap S_{Bb2}$;
$S_{Ac} = S_{Ac1} \cap S_{Ac2}$; $S_{ABc} = S_{Ac1} \cap S_{Bc2}$; $S_{ACc} = S_{Ac1} \cap S_{Cc2}$;
$S_{Bc} = S_{Bc1} \cap S_{Bc2}$; $S_{BAc} = S_{Bc1} \cap S_{Ac2}$; $S_{BCc} = S_{Bc1} \cap S_{Cc2}$;
$S_{Cc} = S_{Cc1} \cap S_{Cc2}$; $S_{CAc} = S_{Cc1} \cap S_{Ac2}$; $S_{CBc} = S_{Cc1} \cap S_{Bc2}$.

The signals that control the switches in each cell of the 3MC should be phase-shifted concerning each other by an angle of $2\pi/p$ (p is the number of switching cell, which in this example is 2). The displacement of carrier signals used to control switches S_{ij1} and S_{ij2} is $T_{sw}/2$, where $T_{sw}=1/f_{sw}$ representing the switching period. The duty cycles for the switch group are determined by comparing the modulation.

The mathematical function incorporates a saw-tooth carrier starting from its origin and compares the modulation function with a phase shifted saw-tooth carrier through a set of switches S_{ij2}, as defined by $T_{sw}/2$ [52, 53]:

$$M_{ijk} = \frac{t_{ijk}}{T_s} = \left[\frac{1}{3} + \frac{2 v_i \cdot v_j}{3 \cdot V_{im}^2} \right], \tag{8}$$

for $i \in A, B, C$; and $j \in a, b, c$ and $k \in 1, 2$.

Model of output filter. The output filter circuit shown in Fig. 1 is a RLC circuit, where R_f, L_f, C_f are linked in series. The resonant frequency of this circuit is designed to be equal to the carrier switching frequency f_{sw} [54]:

$$f_{sw} = \frac{1}{2\pi\sqrt{L_f \cdot C_f}}. \tag{9}$$

Simulation results. MATLAB/Simulink model of a 3MC with 3 FC per output stage has been created. The simulation uses the settings specified in Table 1.

Table 1

3MC model parameters

Parameter	Value
Phase to ground input voltage	220 V
Input frequency	50 Hz
Output frequency	50 Hz
Modulation index q	0.5, 0.3, 0.9
Switching frequency	5 kHz
Flying capacitor	10 μF
Series RLC filter	10 Ω, 2 mH, 0.5 μF
RL load	50 Ω, 0.5 H

First test (Case 1: $q = 0.5$). In Fig. 2,*a* the output voltage of a 3MC with 3 FC over a period of 5 s appears to show. The output voltage appears to be a non-sinusoidal waveform, which is common for 3MC. The voltage appears to have several levels, which is characteristic of a 3MC. The voltage waveform appears to be fluctuating slightly over time. This could be due to a number of factors, such as variations in the input voltage or the load current.

Figure 2,*b* shows 3 phase load currents over a time period of 5 s. The current is ranging from –1 A to 1 A. The graph showcases 3 distinct current waveforms designated as I_a, I_b, I_c. These phases are equally spaced across the time axis, signifying a balanced 3 phase system. Each phase current adheres to a sinusoidal wave pattern, a defining characteristic of AC systems.

Figure 2,*c* shows the output voltage characteristics of a 3MC with a 3 FC for phases *A*, *B*, *C*. Each figure shows a comparison between input reference (black line) and output voltage (colored line). The output voltage in each figure V_a(out), V_b(out), V_c(out) show non-sinusoidal waveform with several voltage levels. This characteristic is a defining

characteristic of multilevel converters. It achieves a near-sinusoidal output voltage with reduced THD compared to traditional two-level converters. The black line in each figure likely depicts the reference input voltage V_a(int), V_b(int), V_c(int). By comparing it to the output voltage, we can analyze the modulation strategy employed by the converter regulates the output voltage by manipulating the switching of its internal power electronic elements based on the reference input.

Fig. 2. Results of the first case ($q = 0.5$)
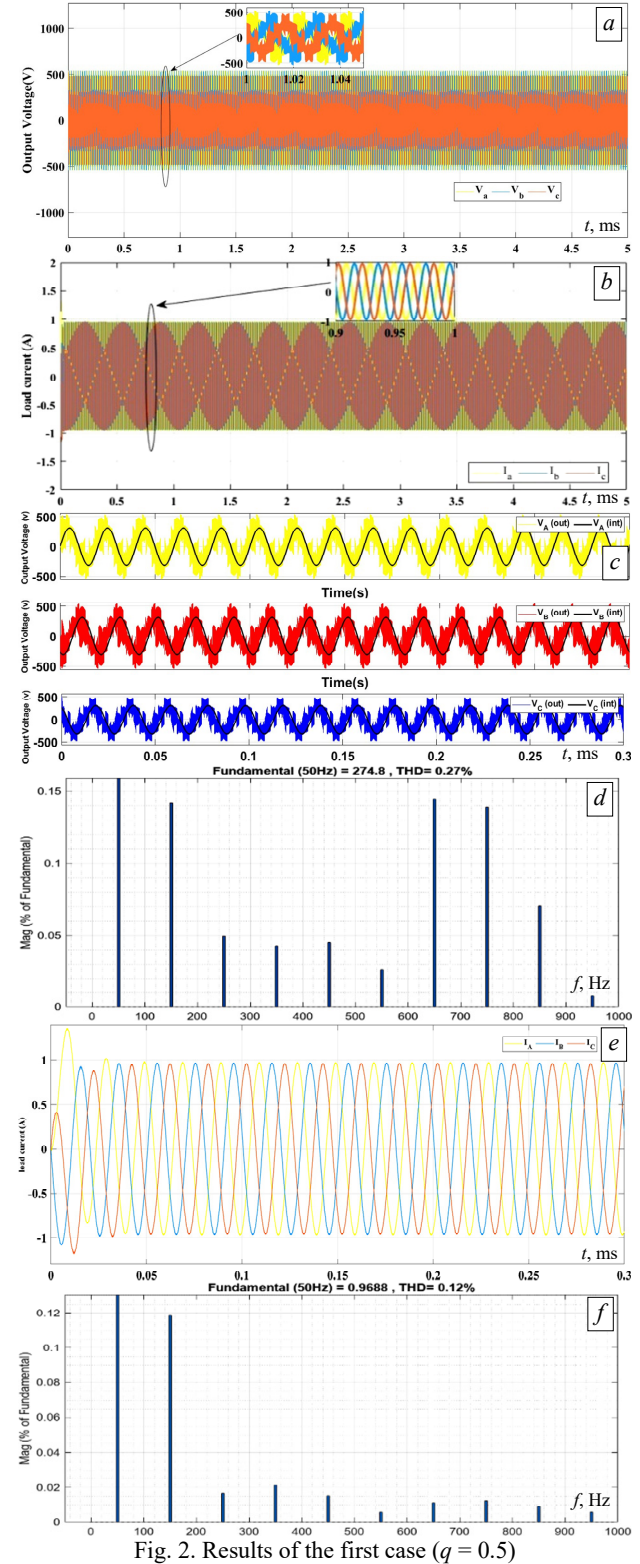
Figure 2,*d* shows the THD for the output voltage (phase *A*) with fundamental value 274.8 V and THD in this

case 0.27 % is a relatively low value. This means the voltage waveform for phase *A* is close to a pure sine wave.

Figure 2,*e* depicts 3 current waveforms, designated as «Load current» for each phase of a 3 phase system. The waveforms closely resemble sinusoids, indicating a balanced linear load with minimal harmonic distortion.

Figure 2,*f* shows the THD for the load current with fundamental value 0.9688 A and THD in this case 0.12 % is a relatively low value. This means the voltage waveform for phase *A* is close to a pure sine wave.

Second test (Case 2: *q* = 0.3). Figure 3,*a* depicts the output voltage behavior of a 3MC with a 3 FC across three phases *A*, *B*, and *C*. Each graph compares the reference input voltage (black line) with the output voltage for each phase (colored line). The output voltage exhibits a non-sinusoidal waveform with multiple voltage levels, a characteristic feature of multilevel converters, aiming to achieve near-sinusoidal output voltage with reduced THD compared to traditional converters. By comparing the reference input with the output voltage, the modulation strategy employed by the converter, which manipulates internal power electronic elements' switching based on the reference input to regulate the output voltage, can be analyzed.
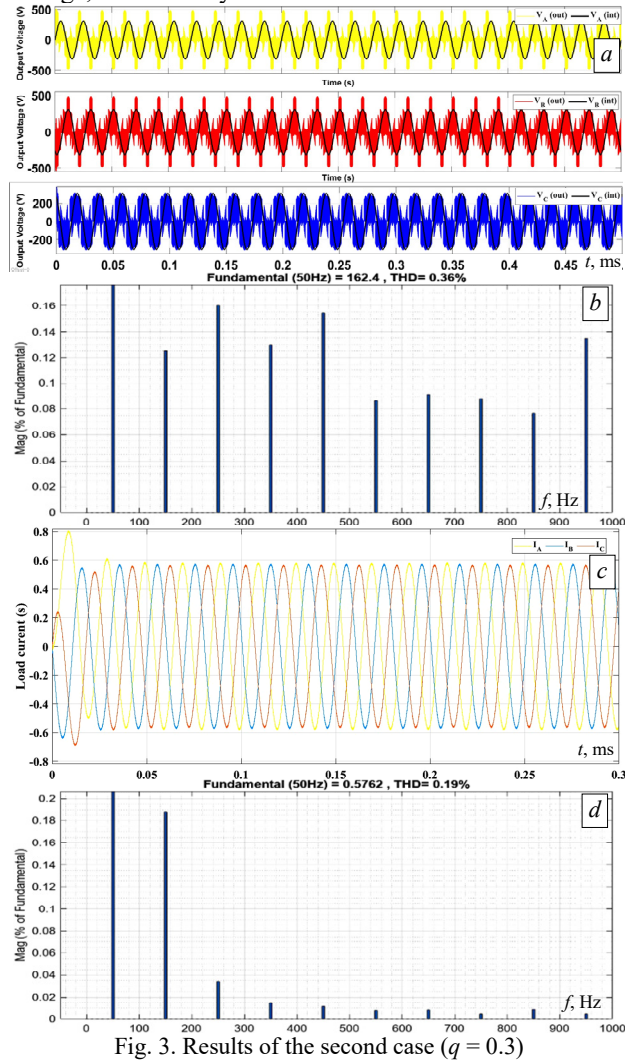
Fig. 3. Results of the second case (*q* = 0.3)

Figure 3,*b* depicts the THD for the output voltage (phase *A*) with value of THD in this case 0.36 % is a relatively low value. This means the voltage waveform for phase *A* is close to a pure sine wave.

Figure 3,*c* illustrates 3 current waveforms for each phase within a 3 phase system. These waveforms exhibit a close resemblance to sinusoidal patterns, suggesting a well-balanced linear load with minimal harmonic distortion. Figure 3,*d* presents the fundamental value 0.5762 A and THD value of 0.19 % is a relatively low value, indicating minimal THD in the load current. This means the current waveform is close to a pure sine wave.

Third test (Case 3: *q* = 0.9). Figure 4,*a* shows that the allure of the output voltage is perturbed compared to the input voltage. The top graph shows the output voltage V_A(out) and the internal voltage V_{int} plotted over time. The output voltage appears to be oscillating more frequently than the input voltage and the same comment for the middle graph and the bottom graph. In all 3 graphs, the output voltage waveform is more complex than the internal voltage waveform. This suggests that the output voltage is being perturbed by some external factor.

Figure 4,*b* depicts the THD for the output voltage (phase *A*) with fundamental value 459.2 V and THD in this case 7.31 %. Figure 4,*c* depicts 3 current waveforms for each phase. The waveforms closely resemble sinusoids, indicating a balanced linear load with harmonic distortion. Figure 4,*d* presents the fundamental value 1.719 A and THD value of 2.6 % is a relatively low value, indicating THD in the load current.
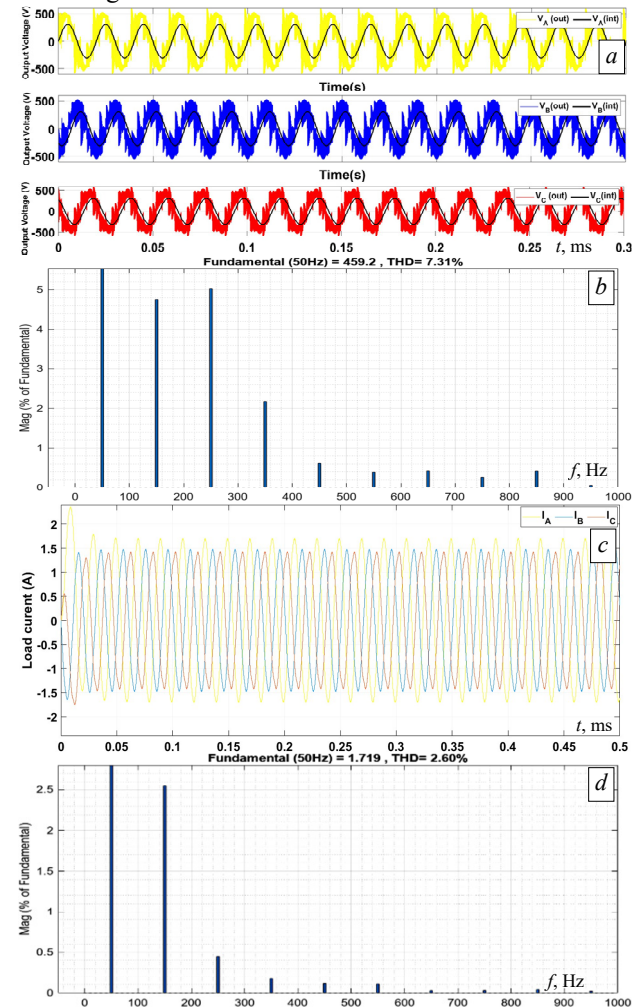
Fig. 4. The results of the third case (*q* = 0.9)

After analyzing Table 2, we conclude that Case 1 (*q* = 0.5) exhibits the best performance among the other

cases, with the lowest THD of phase *A* at 0.27 %, a peak fundamental of 274.8 V, a peak input current of 0.9688 A, and a THD of load current of 0.12 %.

Table 2
Comparison 3MC simulation results

No.	Parameters	Line to line output voltage		Phase *A* input current	
		THD, %	Peak fundamental, V	THD, %	Peak fundamental, A
Case 1	$q = 0.5$	0.27	274.8	0.12	0.9688
Case 2	$q = 0.3$	0.36	162.4	0.19	0.5762
Case 3	$q = 0.9$	7.31	459.2	2.6	1.719

Table 3 presents a comparison between the THD values of proposed 3MC and another converters. The data clearly demonstrates the significant improvement achieved by proposed 3MC in reducing THD compared to the referenced converters. Specifically, the THD reduction ratio of the 3MC, when compared with [54], is 73 %.

Table 3
A comparison between the THD values of proposed 3MC and another converters

Reference	THD of output voltage, %
Article [52]	7.78
Article [53]	23
Article [54]	1.02
Proposed 3MC	0.27

The findings from our study demonstrate notable advancements over previous works, particularly in terms of efficiency and harmonic reduction. Our research shows that the 3 phase 3MC with 3 FC, utilizing the Venturini method for gate pulse generation, achieves a 73 % reduction in THD. This significant improvement surpasses the performance metrics presented in the earlier study, where no such substantial reduction in THD was quantified. Unlike Iyer's work [54], which relied on PSCAD for simulations, our use of MATLAB/Simulink enabled a more detailed and comprehensive assessment of the 3MC's performance across various operating scenarios, allowing for a deeper understanding of its dynamic behavior, stability, and robustness. These enhanced results demonstrate the superior capability of our approach in optimizing power conversion efficiency and minimizing distortion, especially in medium-to-high voltage applications requiring direct AC-AC conversion. Moreover, our study extends the practical application of multilevel converter technology by offering concrete strategies for improving design and performance in industrial and renewable energy contexts, which were not specifically addressed in the previous work.

Conclusions. The adopted multilevel technologies, especially the capacitor-clamped matrix converter (MC), offer promising solutions for medium and high voltage power conversion needs, especially the counter-output stage introduced in this study though made a model on the modular multilevel matrix converter (3MC) of the transformer. The deviation from the conventional methods used in single-cell matrix transformers is demonstrated by the use of a Venturini method to generate gate pulses in this transformer in which using a capacitor-clamp arrangement with 3 flying capacitors.

Simulation results with using MATLAB/Simulink have shown the improved performance of the 3MC. This improvement is evident through comparisons across 3 cases and the tabulated analysis of THD in line-to-line output voltage and input current. These outcomes highlight the effectiveness of the suggested converter design in achieving enhanced performance in power conversion applications.

Recommendations and prospects for further development. To validate the simulation results, real-world implementation and testing of the 3MC under various conditions are recommended. Further optimization of Venturini method control algorithms, exploration of scalability, integration with renewable energy sources, and investigation of thermal management and long-term reliability are essential. Performing a cost-benefit analysis will offer important insights into the economic viability of this technology for industrial applications.

Conflict of interest. The authors declare that they have no conflicts of interest.

REFERENCES
1. Gyugyi L., Pelly B.R. *Static power frequency changers: Theory, performance, and application*. John Wiley and Sons, 1976. 442 p.
2. Alesina A., Venturini M. Solid-state power conversion: A Fourier analysis approach to generalized transformer synthesis. *IEEE Transactions on Circuits and Systems*, 1981, vol. 28, no. 4, pp. 319-330. doi: https://doi.org/10.1109/TCS.1981.1084993.
3. Venturini M., Alesina A. *Method and apparatus for the conversion of a polyphase voltage system*. Patent USA, no. 4628425, 1986.
4. Alesina A., Venturini M.G.B. Analysis and design of optimum-amplitude nine-switch direct AC-AC converters. *IEEE Transactions on Power Electronics*, 1989, vol. 4, no. 1, pp. 101-112. doi: https://doi.org/10.1109/63.21879.
5. Wei L., Lipo T.A. A novel matrix converter topology with simple commutation. *Conference Record of the 2001 IEEE Industry Applications Conference. 36th IAS Annual Meeting (Cat. No.01CH37248)*, 2001, vol. 3, pp. 1749-1754. doi: https://doi.org/10.1109/IAS.2001.955769.
6. Kolar J.W., Schafmeister F., Round S.D., Ertl H. Novel Three-Phase AC–AC Sparse Matrix Converters. *IEEE Transactions on Power Electronics*, 2007, vol. 22, no. 5, pp. 1649-1661. doi: https://doi.org/10.1109/TPEL.2007.904178.
7. Sumiya K., Naito Y., Xu J., Shimosato N., Sato Y. An Advanced Commutation Method for Bidirectional Isolated Three-Phase AC/DC Dual-Active-Bridge Converter Based on Matrix Converter. *2020 IEEE Energy Conversion Congress and Exposition (ECCE)*, 2020, pp. 4158-4164. doi: https://doi.org/10.1109/ECCE44975.2020.9235931.
8. Ellabban O., Abu-Rub H., Bayhan S. Z-Source Matrix Converter: An Overview. *IEEE Transactions on Power Electronics*, 2016, vol. 31, no. 11, pp. 7436-7450. doi: https://doi.org/10.1109/TPEL.2015.2471799.
9. Wang R., Zhao P., Wang J., Hao H. Y-Source Two-Stage Matrix Converter and Its Modulation Strategy. *IEEE Access*, 2020, vol. 8, pp. 214282-214292. doi: https://doi.org/10.1109/ACCESS.2020.3036117.
10. Nabih A., Li Q. A Method to Embed Resonant Inductor Into PCB Matrix Transformer for High-Density Resonant Converters. *IEEE Transactions on Power Electronics*, 2024, vol. 39, no. 2, pp. 2385-2400. doi: https://doi.org/10.1109/TPEL.2023.3330974.
11. Bravo P., Pereda J., Merlin M.M.C., Neira S., Green T.C., Rojas F. Modular Multilevel Matrix Converter as Solid State Transformer for Medium and High Voltage AC Substations. *IEEE Transactions on Power Delivery*, 2022, vol. 37, no. 6, pp. 5033-5043. doi: https://doi.org/10.1109/TPWRD.2022.3166258.
12. Huber L., Borojevic D., Burany N. Voltage space vector based PWM control of forced commutated cycloconverters. *15th Annual Conference of IEEE Industrial Electronics Society*, 1989, pp. 106-111. doi: https://doi.org/10.1109/IECON.1989.69619.
13. Ma C., Shi T., Lin Z., Zhou Z., Xia C. A Novel Wider Range Modulation for Indirect Matrix Converter Utilizing Delta-Sigma and Space Vector. *IEEE Transactions on Power Electronics*, 2023, vol. 38, no. 2, pp. 1429-1434. doi: https://doi.org/10.1109/TPEL.2022.3212673.

14. Saidi F., Bounadja E., Djahbar A. A Comparative Analysis of SVM, Venturini, and PWM with Three Intervals Modulation Techniques for the Control of an AC/AC Three-Phase Matrix Converter. *2023 2nd International Conference on Electronics, Energy and Measurement (IC2EM)*, 2023, pp. 1-6. doi: https://doi.org/10.1109/IC2EM59347.2023.10419515.

15. Haruna J., Wakabayashi M., Yoshihara M., Funato H. A Consideration on Neutral-Point Potential Balancing of 3-Level PWM Rectifier Applying Space Vector Modulation of Matrix Converter. 2021 *24th International Conference on Electrical Machines and Systems (ICEMS)*, 2021, pp. 1-5. doi: https://doi.org/10.23919/ICEMS52562.2021.9634302.

16. Wang X., Wei T., Wang R., Hu Y., Liu S. A Novel Carrier-Based PWM Without Narrow Pulses Applying to High-Frequency Link Matrix Converter. *IEEE Access*, 2020, vol. 8, pp. 157654-157662. doi: https://doi.org/10.1109/ACCESS.2020.3019086.

17. Solemanifard S., Chen Y.-X., Lak M., Lee T.-L. A Commutation Method Free from Inrush Current for the Carrier-Based PWM Controlled Direct Matrix Converter. *2021 IEEE Energy Conversion Congress and Exposition (ECCE)*, 2021, pp. 3253-3260. doi: https://doi.org/10.1109/ECCE47101.2021.9595330.

18. Mir T.N., Singh B., Bhat A.H. FS-MPC-Based Speed Sensorless Control of Matrix Converter Fed Induction Motor Drive With Zero Common Mode Voltage. *IEEE Transactions on Industrial Electronics*, 2021, vol. 68, no. 10, pp. 9185-9195. doi: https://doi.org/10.1109/TIE.2020.3020031.

19. Mei Y., Zhang J., Wei Z., Meng Q. An Analytic Hierarchy Process Based Weighting Factor Tuning Method for Model Predictive Controlled Indirect Matrix Converter - Induction Motor Drives. *IECON 2023 - 49th Annual Conference of the IEEE Industrial Electronics Society*, 2023, pp. 1-6. doi: https://doi.org/10.1109/IECON51785.2023.10312526.

20. Hothongkham P., Suathed S. Simulation of Three-phase PWM AC-AC Matrix Converter without the DC-Link Testing with the Passive Loads and without input filter. *2022 19th International Conference on Electrical Engineering/Electronics, Computer, Telecommunications and Information Technology (ECTI-CON)*, 2022, pp. 1-4. doi: https://doi.org/10.1109/ECTI-CON54298.2022.9795562.

21. Song J., Duan B., Li X., Wan D., Ding W., Zhang C., Du C. A Modified Space Vector Modulation for DC-Side Current Ripple Reduction in High-Frequency Link Matrix Converter. *IEEE Transactions on Transportation Electrification*, 2022, vol. 8, no. 4, pp. 4470-4481. doi: https://doi.org/10.1109/TTE.2022.3183860.

22. Nguyen H.-N., Nguyen M.-K., Duong T.-D., Tran T.-T., Lim Y.-C., Choi J.-H. A Study on Input Power Factor Compensation Capability of Matrix Converters. *Electronics*, 2020, vol. 9, no. 1, art. no. 82. doi: https://doi.org/10.3390/electronics9010082.

23. Xie J., Suberski M., Henneberg D., Rädel U., Petzoldt J. A Study on Simplification of Commutation Methods for Three-Phase Direct Matrix Converters. *2023 25th European Conference on Power Electronics and Applications (EPE'23 ECCE Europe)*, 2023, pp. 1-7. doi: https://doi.org/10.23919/EPE23ECCEEurope58414.2023.10264260.

24. Soyed A., Ameni K., Hasnaoui O., Bacha F. DTC-SVM Control for Induction Motor Drives Fed by Sparse Matrix Converter. *2021 IEEE 2nd International Conference on Signal, Control and Communication (SCC)*, 2021, pp. 126-131. doi: https://doi.org/10.1109/SCC53769.2021.9768397.

25. Saniman M.H., Muhammad K.S., Baharom R. Fault-Tolerant Single-Phase AC-DC Boost Matrix Converter. *2021 IEEE Industrial Electronics and Applications Conference (IEACon)*, 2021, pp. 213-218. doi: https://doi.org/10.1109/IEACon51066.2021.9654733.

26. Muduli U.R., Kumar Behera R. High Performance Finite Control Set Model Predictive DTC for Three-to-Five Phase Direct Matrix Converter Fed Induction Motor Drive. *2021 22nd IEEE International Conference on Industrial Technology (ICIT)*, 2021, pp. 198-202. doi: https://doi.org/10.1109/ICIT46573.2021.9453475.

27. Boukadoum A., Bouguerne A., Bahi T. Direct power control using space vector modulation strategy control for wind energy conversion system using three-phase matrix converter. *Electrical Engineering & Electromechanics*, 2023, no. 3, pp. 40-46. doi: https://doi.org/10.20998/2074-272X.2023.3.06.

28. Fang F., Tian H., Li Y. Finite Control Set Model Predictive Control for AC–DC Matrix Converter With Virtual Space Vectors. *IEEE Journal of Emerging and Selected Topics in Power Electronics*, 2021, vol. 9, no. 1, pp. 616-628. doi: https://doi.org/10.1109/JESTPE.2019.2937330.

29. Aissaoui M., Bouzeria H., Benidir M., Labed M.A. Harmonics suppression in high-speed railway via single-phase traction converter with an LCL filter using fuzzy logic control strategy. *Electrical Engineering & Electromechanics*, 2024, no. 2, pp. 16-22. doi: https://doi.org/10.20998/2074-272X.2024.2.03.

30. Ye G., Kumar A., Deng Y. A Modified Space Vector Modulation and Phase-Shifted Modulation Coordination Strategy for Isolated AC-DC Matrix Converter. *2023 IEEE 2nd International Power Electronics and Application Symposium (PEAS)*, 2023, pp. 380-385. doi: https://doi.org/10.1109/PEAS58692.2023.10395749.

31. Tawfiq K.B., Ibrahim M.N., Sergeant P. An Enhanced Fault-Tolerant Control of a Five-Phase Synchronous Reluctance Motor Fed From a Three-to-Five-Phase Matrix Converter. *IEEE Journal of Emerging and Selected Topics in Power Electronics*, 2022, vol. 10, no. 4, pp. 4182-4194. doi: https://doi.org/10.1109/JESTPE.2022.3148188.

32. Sayed M.A., Takeshita T., Iqbal A., Alaas Z.M., Ahmed M.M.R., Dabour S.M. Modulation and Control of a DC-AC Converter With High-Frequency Link Transformer for Grid-Connected Applications. *IEEE Access*, 2021, vol. 9, pp. 166058-166070. doi: https://doi.org/10.1109/ACCESS.2021.3134813.

33. Themozhi G., Srinivasan K., Arun Srinivas T., Prabha A. Analysis of suitable converter for the implementation of drive system in solar photovoltaic panels. *Electrical Engineering & Electromechanics*, 2024, no. 1, pp. 17-22. doi: https://doi.org/10.20998/2074-272X.2024.1.03.

34. Erickson R.W., Al-Naseem O.A. A new family of matrix converters. *IECON'01. 27th Annual Conference of the IEEE Industrial Electronics Society (Cat. No.37243)*, 2001, vol. 2, pp. 1515-1520. doi: https://doi.org/10.1109/IECON.2001.976015.

35. Utvic M., Bontemps P., Dujic D. Direct Arm Energy Control of the Modular Multilevel Matrix Converter. *IEEE Access*, 2023, vol. 11, pp. 1793-1805. doi: https://doi.org/10.1109/ACCESS.2023.3234013.

36. Sangsuwan P., Kiatsookkanatorn P., Sangwongwanich S., Sangwongwanich A. New Switching Patterns Based on Current Space-Vector Diagram Viewpoint to Reduce Input Current Ripple for Three-Level Inverters. *2022 25th International Conference on Electrical Machines and Systems (ICEMS)*, 2022, pp. 1-6. doi: https://doi.org/10.1109/ICEMS56177.2022.9982904.

37. Yagup V.G., Yagup K.V. Acceleration of exit to steady-state mode when modeling semiconductor converters. *Electrical Engineering & Electromechanics*, 2023, no. 3, pp. 47-51. doi: https://doi.org/10.20998/2074-272X.2023.3.07.

38. Jiang J., Hu S., Liu S., Lu Z., Huang H., Wu W. Smooth Transition of Modular Multilevel Matrix Converter to Hexverter During Single-Arm Failure. *2022 IEEE 6th Conference on Energy Internet and Energy System Integration (EI2)*, 2022, pp. 50-56. doi: https://doi.org/10.1109/EI256261.2022.10116395.

39. Xu Y., Zhao Z., Zhao G., Li W., Lu Z. A Novel Branch Energy Balancing Control Method for Modular Multilevel Matrix Converter Under Unbalanced System Conditions. *IECON 2023 - 49th Annual Conference of the IEEE Industrial Electronics Society*, 2023, pp. 1-6. doi: https://doi.org/10.1109/IECON51785.2023.10311906.

40. Mohamad A.S. A Three-Phase, 41-Level Matrix Inverter Based on Modular Multilevel Converter Half-Bridge Modules. *2021 IEEE 9th Conference on Systems, Process and Control (ICSPC 2021)*, 2021, pp. 114-118. doi: https://doi.org/10.1109/ICSPC53359.2021.9689208.

41. Himker R., Mertens A. Reduced 8-Branch Modular Multilevel Matrix Converter with an Operating Point Optimised Control Strategy in a Branch Failure Event. *2023 25th European Conference on Power Electronics and Applications (EPE'23 ECCE Europe)*, 2023, pp. 1-9. doi: https://doi.org/10.23919/EPE23ECCEEurope58414.2023.10264234.

42. Wu W., Jiang J., Hu S., Liu S., Zhu Z., Huang H. Harmonic Circulating Analysis of Modular Multilevel Matrix Converter based on Two-Dimensional Phasor Method. *2023 Panda Forum on Power and Energy (PandaFPE)*, 2023, pp. 866-871. doi: https://doi.org/10.1109/PandaFPE57779.2023.10141340.

43. Li Y., Jiang Y., Wu Q., Chen J., Zhou Q. Control Strategy for Frequency Support Based on Modular Multilevel Matrix Converter with Emulation Inertia. *2023 8th International Conference on Power and Renewable Energy (ICPRE)*, 2023, pp. 1258-1263. doi: https://doi.org/10.1109/ICPRE59655.2023.10353793.

44. Cuzmar R.H., Mora A., Pereda J., Aguilera R.P., Poblete P., Neira S. Computationally Efficient MPC for Modular Multilevel Matrix Converters Operating With Fixed Switching Frequency. *IEEE Open*

Journal of the Industrial Electronics Society, 2023, vol. 4, pp. 748-761. doi: https://doi.org/10.1109/OJIES.2023.3347101.

45. Ni X., Qiu P., Lin J., Lu Y., Jin Y., Xu H. Selection Methods of Main Circuit Parameters for Modular Multilevel Matrix Converters. *2021 International Conference on Power System Technology (POWERCON)*, 2021, pp. 1304-1309. doi: https://doi.org/10.1109/POWERCON53785.2021.9697737.

46. Cheng Q., Xie Y., Ma X., Cheng Y. Dual-Flatness-Based-Control Strategy of Modular Multilevel Matrix Converter. *2021 6th International Conference on Power and Renewable Energy (ICPRE)*, 2021, pp. 62-66. doi: https://doi.org/10.1109/ICPRE52634.2021.9635218.

47. Wang C., Zheng Z., Wang K., Li Y. Fault Detection and Tolerant Control of IGBT Open-Circuit Failures in Modular Multilevel Matrix Converters. *IEEE Journal of Emerging and Selected Topics in Power Electronics*, 2022, vol. 10, no. 6, pp. 6714-6727. doi: https://doi.org/10.1109/JESTPE.2022.3150166.

48. Siva Ramkumar M., Kannagopalan M., Amudha A., Divyapriya S. Wind Energy Conversion Control for a Double Fed Induction Generator with Modular Multi-Level Matrix Converter. *2022 International Conference on Edge Computing and Applications (ICECAA)*, 2022, pp. 759-767. doi: https://doi.org/10.1109/ICECAA55415.2022.9936090.

49. Purwanto E., Murdianto F.D., Basuki G. Venturini Modulation Method For Matrix Converter. *2019 International Electronics Symposium (IES)*, 2019, pp. 601-605. doi: https://doi.org/10.1109/ELECSYM.2019.8901606.

50. Gokdag M., Gulbudak O. Improving Grid Current Quality of Direct Matrix Converter for Induction Motor. *2021 IEEE 30th International Symposium on Industrial Electronics (ISIE)*, 2021, pp. 1-6. doi: https://doi.org/10.1109/ISIE45552.2021.9576352.

51. Cuzmar R., Montenegro A., Mora A., Pereda J., Aguilera R.P. Constrained MPC for Intercluster Energy Control of Modular Multilevel Matrix Converters. *IEEE Transactions on Industrial Electronics*, 2024, vol. 71, no. 7, pp. 7766-7776. doi: https://doi.org/10.1109/TIE.2023.3303641.

52. Kurtoğlu M., Vural A.M. A Novel Nearest Level Modulation Method with Increased Output Voltage Quality for Modular Multilevel Converter Topology. *International Transactions on Electrical Energy Systems*, vol. 2022, art. no. 2169357, pp. 1-17. doi: https://doi.org/10.1155/2022/2169357.

53. Padhee V., Sahoo A.K., Mohan N. Modulation Techniques for Enhanced Reduction in Common-Mode Voltage and Output Voltage Distortion in Indirect Matrix Converters. *IEEE Transactions on Power Electronics*, 2017, vol. 32, no. 11, pp. 8655-8670. doi: https://doi.org/10.1109/TPEL.2016.2645944.

54. Iyer N.P.R. Performance comparison of a three-phase multilevel matrix converter with three flying capacitors per output phase with a three-phase conventional matrix converter. *Electrical Engineering*, 2017, vol. 99, no. 2, pp. 775-789. doi: https://doi.org/10.1007/s00202-016-0500-4.

Fayssal Saidi[1]*, PhD Student,*
Abdelkader Djahbar[1]*, Professor,*
Elhadj Bounadja[1]*, Assistant Professor,*
Walid Mohammed Kacemi[1]*, PhD Student,*
Khaled Fettah[2]*, PhD Student,*
[1] Laboratoire de genie electrique et energies renouvelables (LGEER),
Hassiba Benbouali University of Chlef,
B. P 78C, OuledFares, Chlef, 02180, Algeria,
e-mail: f.saidi@univ-chlef.dz (Corresponding Author);
a.djahbar@univ-chlef.dz; e.bounadja@univ-chlef.dz;
w.kacemi@univ-chlef.dz;
[2] Laboratoire des Nouvelles technologies et le developpement local
(LNTDL), University El Oued, El Oued, Algeria,
e-mail: khaled-fettah@univ-eloued.dz

B.I. Kuznetsov, A.S. Kutsenko, T.B. Nikitina, I.V. Bovdui, K.V. Chunikhin, V.V. Kolomiets

Method for prediction magnetic silencing of uncertain energy-saturated extended technical objects in prolate spheroidal coordinate system

*Aim. Development of method for prediction by energy-saturated extended technical objects magnetic silencing based on magnetostatics geometric inverse problems solution and magnetic field spatial spheroidal harmonics calculated in prolate spheroidal coordinate system taking into account of technical objects magnetic characteristics uncertainties. **Methodology.** Spatial prolate spheroidal harmonics of extended technical objects magnetic field model calculated as magnetostatics geometric inverse problems solution in the form of nonlinear minimax optimization problem based on near field measurements for prediction far extended technical objects magnetic field magnitude. Nonlinear objective function calculated as the weighted sum of squared residuals between the measured and predicted magnetic field COMSOL Multiphysics software package used. Nonlinear minimax optimization problems solutions calculated based on particle swarm nonlinear optimization algorithms. **Results.** Results of prediction extended technical objects far magnetic field magnitude based on extended technical objects spatial prolate spheroidal harmonics of the magnetic field model in the prolate spheroidal coordinate system using near field measurements with consideration of extended technical objects magnetic characteristics uncertainty. **Originality.** The method for prediction by extended technical objects magnetic cleanliness based on spatial prolate spheroidal harmonics of the magnetic field model in the prolate spheroidal coordinate system with consideration of magnetic characteristics uncertainty is developed. **Practical value.** The important practical problem of prediction extended technical objects magnetic silencing based on the spatial prolate spheroidal harmonics of the magnetic field model in the prolate spheroidal coordinate system with consideration of extended technical objects magnetic characteristics uncertainty solved. References 48, figures 2.*
Key words: **energy-saturated extended technical objects, magnetic field model, magnetic silencing, extended spheroidal coordinate system, spatial extended spheroidal harmonics, prediction, measurements, uncertainty.**

Мета. Розробка методу прогнозування магнітної тиші енергонасичених витягнутих технічних об'єктів на основі розв'язку обернених геометричних задач магнітостатики та обчислення просторових сфероїдальних гармонік магнітного поля в витягнутій сфероїдній системі координат з врахуванням невизначеностей магнітних характеристик технічних об'єктів. Методологія. Просторові витягнуті сфероїдні гармоніки моделі магнітного поля витягнутих технічних об'єктів розраховані як розв'язок обернених геометричних задач магнітостатики в формі нелінійної задачі мінімаксної оптимізації на основі вимірювань ближнього поля для прогнозування величини магнітного поля витягнутих технічних об'єктів. Нелінійна цільова функція розрахована як зважена сума квадратів залишків між виміряним і прогнозованим магнітним полем, яке обчислено з використанням програмного пакету COMSOL Multiphysics. Розв'язки задач нелінійної мінімаксної оптимізації розраховані на основі алгоритмів нелінійної оптимізації роєм частинок. Результати. Результати прогнозування величини дальнього магнітного поля витягнутих технічних об'єктів на основі просторових витягнутих сфероїдальних гармонік моделі магнітного поля в витягнутій сфероїдній системі координат з використанням вимірювань ближнього поля та з врахуванням невизначеності магнітних характеристик витягнутих технічних об'єктів. Оригінальність. Розроблено метод прогнозування магнітної тиші витягнутих технічних об'єктів на основі просторових витягнутих сфероїдальних гармонік моделі магнітного поля в витягнутій сфероїдній системі координат з врахуванням невизначеності магнітних характеристик. Практична цінність. Вирішено важливу практичну задачу магнітної тиші витягнутих технічних об'єктів на основі просторових витягнутих сфероїдальних гармонік моделі магнітного поля в розширеній сфероїдній системі координат з врахуванням невизначеності магнітних характеристик витягнутих технічних об'єктів. Бібл. 48, рис. 2.
Ключові слова: **енергонасичені витягнуті технічні об'єкти, модель магнітного поля, магнітна тиша, витягнута сфероїдна система координат, просторові витягнуті сфероїдні гармоніки, прогноз, вимірювання, невизначеність.**

Introduction. The development of energy-saturated technical objects with a given distribution of the generated magnetic field is an urgent problem for many science and industry branches. The strictest requirements for the accuracy of the spatial distribution of the magnetic field are imposed when ensuring the magnetic silencing of spacecraft, the development of anti-mine magnetic protection of naval vessels and submarines, the creation of magnetometry devices including for medical diagnostic devices and other fields [1–5].

The practice of designing of technical objects with standardized levels of their external magnetic field required the development of scientific foundations for their design, production, methodological and metrological support. The foundation of these scientific foundations is the mathematical modeling of a three-dimensional quasi-stationary external magnetic field generated by a technical object.

The main advantage of applying the methods of spatial harmonic analysis to the study and targeted influence on the external magnetic field of technical objects is the maximum simplification of the calculation of the external magnetic field of a technical object based on a limited number of spatial harmonics.

When energy-saturated technical objects design with a given magnetic field spatiotemporal characteristic, two interrelated problems are solved [6, 7]. First, based on measurements of the real magnetic field of a technical object in the near zone, it is necessary to design a mathematical model of the magnetic field of a technical object, on the basis of which the magnetic field in the far zone can be calculated. This problem is called prediction [6].

To measure the real technical objects magnetic field in the near zone often use point magnetic field sensors [8]. In particular, to measure the magnetic field of ships in the ship magnetism laboratory (France) 39 magnetic field sensors used and located in close proximity to the ship's hull [9]. To design such a mathematical model of a technical object, it is necessary to solve the inverse magnetostatics problem [6]. Based on this mathematical model, the magnetic field in the far zone calculated. For naval vessels a control depth is specified, and for a spacecraft the installation point for the onboard

magnetometer is specified. In addition, for spacecraft, the resulting spacecraft magnetic moment also calculated based on this model.

The second problem is to ensure the specified spatial-temporal characteristics of the magnetic field of a technical object. This is a control problem [6]. Based on the designed mathematical model of the initial magnetic field of a technical object, it is necessary to calculate the spatial location and values of compensating magnetic units in such a way that the resulting magnetic field generated by the technical object satisfies the requirements [10, 11].

The basis of such developments is the design of a mathematical model of the magnetic field of a technical object. If the geometric dimensions of a technical object in an orthogonal coordinate system are approximately the same, then a spherical coordinate system is used.

In particular, the «MicroSAT» spacecraft have the shape of a cube. Moreover, on this spacecraft with the «IonoSAT-Micro» equipment, the on-board magnetometer are coordinate system in the form of a multi-dipole model mounted on rods 2 m long [3]. Therefore mathematical model of such technical object represented with sufficient accuracy on the basis of a spherical.

The KS5MF2 spacecraft and the MS-2-8 spacecraft of the «Sich 2» family also have cube shape [3]. However onboard magnetometer LEMI-016 located at 0.35 m distance from from the sensor KPNCSP.

Then mathematical model of such technical object designed based on spherical coordinate system, but in the form of a multipole model taking into account dipoles, quadrupole and octupole harmonics [12].

If the technical object has an extended shape with a predominant size along one coordinate in the orthogonal coordinate system, then it is necessary to use an elongated spheroidal coordinate system [13–16].

Over the past decade, the development of small satellites, nanosatellites such as «CubeSats», has increased exponentially for Earth observation and deep space missions in the Solar System, mainly due to their lower cost and faster development. The GS-1 spacecraft of the «CUBESAT» family has geometric dimensions 0.371 m by 0.114 m by 0.11 m, so the length more than 3 times other dimensions [3]. Then mathematical model of such technical object presented on the basis of prolate spheroidal coordinate system [12].

Strict requirements are also imposed on the maximum level of the magnetic field created by naval vessels, minesweepers and submarines near their hull [17–19]. Sea Minesweepers has a length more than 6 times the other dimensions. Naval vessels are even more elongated so the length is more than 10 times the other dimensions.

To compensate magnetic field of naval vessels and submarines compensation windings system used in three orthogonal coordinates – longitudinal, transverse and vertical directions and solenoid windings [17–19]. A feature of the technical objects under consideration is the uncertainty of the magnetic characteristics of their elements and their change in different operating modes [2]. Naturally for such elongated extended technical objects mathematical models of the magnetic field must be designed in a prolate spheroidal coordinate system [13–16].

The aim of the work is to develop the method for prediction by energy-saturated extended technical objects magnetic silencing based on solution of geometric inverse magnetostatics problems and calculation magnetic field spatial prolate spheroidal harmonics in a prolate spheroidal coordinate system taking into account the technical objects magnetic characteristics uncertainties.

Direct geometric magnetostatics problems of an energy-saturated extended technical object in prolate spheroidal coordinate system. Usually, to ensure the specified magnetic characteristics, units in a special low-magnetic design are installed at such important technical objects [1–5]. At the same time, at the stage of production and adjustment of high-grade low-magnetic units, compensating magnetic elements are installed in the form of permanent magnets or electromagnet windings. In this case, the magnitudes of the magnetic moments of such units become incredibly small. However, in the magnetic field of such units, harmonics of higher orders appear – quadropoles, octopoles, etc.

The practical solution complexity of these problems is associated with the need to use a sufficient number of integral characteristics of the magnetic field, which could serve as a quantitative criterion for the quality of the field distribution. The method that would allow in practice to use the integral characteristics of the magnetic field – spatial harmonics, and to associate them with the parameters of the technical object – remain insufficiently developed. The need to develop such method is confirmed by one of the latest standards of the European Space Agency ECSS-E-HB-20-07A (2012), which recommends using them to ensure the magnetic cleanliness of space vehicles as integral characteristics of the spatial distribution of the magnetic field its spherical harmonics [2].

The application of spatial harmonic analysis methods is based on the study of the harmonic composition of the magnetic field. The result of this application is the transition from the measured values of the induction vector to the integral characteristics of the magnetic field harmonics – multipole coefficients. Then, based on the obtained values of the multipole coefficients, the magnetic field can be described in the entire external region. The accuracy of the description depends both on the accuracy of determining the multipole coefficients themselves and on the number of spatial harmonics used in the expansion of the source function. The choice of the type of basic solutions and coordinate system depends on the specific conditions of the problem being solved and makes it possible to analytically describe the magnetic field of a wide class of technical objects.

The basis for integral characteristics and methods for their control near objects of extended shape are methods of spatial harmonic analysis in an elongated spheroidal coordinate system, where the shape of the coordinate surfaces makes it possible to bring the description area closer to the surface of the object itself.

Let's consider a mathematical model of an extended energy-saturated technical object in an elongated spheroidal coordinate system ξ, η, φ [16]. A feature of the prolate spheroidal coordinate system is the use of the parameter c, which determines the linear scale for the unit vectors of all three coordinates. The value of the

parameter c is equal to half the interfocal distance of the spheroid, the foci of which lie on the z axis at points $\pm c$.

The solution to the Laplace equation of the scalar magnetic potential for the external region outside the coordinate surface ξ = const containing the source in accordance with [16] written in the following form

$$U = \sum_{n=1}^{\infty} \sum_{m=0}^{n} Q_n^m(\xi) \begin{Bmatrix} c_n^m \cdot \cos(m\varphi) \\ s_n^m \cdot \sin(m\varphi) \end{Bmatrix} P_n^m(\eta), \qquad (1)$$

where P_n^m, Q_n^m are associated Legendre functions of the first and second kind, respectively, with degree n and

order m; c_n^m, s_n^m – constant coefficients characterizing the amplitudes of external spheroidal harmonics of the magnetic field.

Similar to spherical harmonic analysis, the magnetic field strength of a source limited by a spheroidal surface specified by ξ_o outside the spheroid can be determined as the sum of the projections of the magnetic field strength of spheroidal spatial harmonics, determined by the corresponding coefficients. For spheroidal projections, the magnetic field strength in the external region will take the form

$$H_\xi = -\frac{\sqrt{\xi^2-1}}{c\sqrt{\xi^2-\eta^2}} \sum_{n=1}^{\infty} \sum_{m=0}^{n} \frac{dQ_n^m(\xi)}{d\xi} \left\{ c_n^m \cos(m\varphi) + s_n^m \sin(m\varphi) \right\} P_n^m(\cos(\eta));$$

$$H_\eta = -\frac{\sqrt{1-\eta^2}}{c\sqrt{\xi^2-\eta^2}} \sum_{n=1}^{\infty} \sum_{m=0}^{n} Q_n^m(\xi) \frac{dP_n^m(\cos(\eta))}{d\eta} \left\{ c_n^m \cos(m\varphi) + s_n^m \sin(m\varphi) \right\}; \qquad (2)$$

$$H_\varphi = \frac{m}{c\sqrt{(\xi^2-1)(1-\eta^2)}} \sum_{n=1}^{\infty} \sum_{m=0}^{n} Q_n^m(\xi) P_n^m(\cos(\eta)) \left\{ c_n^m \sin(m\varphi) - s_n^m \cos(m\varphi) \right\}.$$

It is more convenient to carry out practical measurements and calculations of magnetic field strength components in the orthogonal coordinate system, the transition to which for the strength components is carried out using the formulas:

$$H_x = \xi \cdot \frac{\sqrt{1-\eta^2}}{\sqrt{\xi^2-\eta^2}} \cdot \cos(\varphi \cdot H_\xi) -$$

$$- \eta \cdot \frac{\sqrt{\xi^2-1}}{\sqrt{\xi^2-\eta^2}} \cdot \cos(\varphi \cdot H_\eta) - \sin(\varphi \cdot H_\varphi);$$

$$H_y = \xi \cdot \frac{\sqrt{1-\eta^2}}{\sqrt{\xi^2-\eta^2}} \cdot \sin(\varphi \cdot H_\xi) - \qquad (3)$$

$$- \eta \cdot \frac{\sqrt{\xi^2-1}}{\sqrt{\xi^2-\eta^2}} \cdot \sin(\varphi \cdot H_\eta) + \cos(\varphi \cdot H_\varphi);$$

$$H_z = \eta \cdot \frac{\sqrt{\xi^2-1}}{\sqrt{\xi^2-\eta^2}} \cdot H_\xi + \xi \cdot \frac{\sqrt{1-\eta^2}}{\sqrt{\xi^2-\eta^2}} \cdot H_\eta,$$

where the coordinates x, y, z in the orthogonal coordinate system are related to coordinates ξ, η, φ in the elongated sphepridal coordinate system by the following relation

$$x = c \cdot \sqrt{\xi^2-1} \cdot \sqrt{1-\eta^2} \cdot \cos\varphi;$$

$$\xi \in [1, \infty[;$$

$$y = c \cdot \sqrt{\xi^2-1} \cdot \sqrt{1-\eta^2} \cdot \sin\varphi; \Rightarrow \eta \in [0,1]; \qquad (4)$$

$$\varphi \in [0, 2\pi];$$

$$z = c \cdot \xi \cdot \eta;$$

Practical harmonic analysis in elongated spheroidal coordinate system based on (2) requires the calculation of associated Legendre polynomials of the first and second kind. Polynomials of the second kind calculated using the well-known formula with a limitation on the number of terms of the infinite series [16]

$$Q_n^m(\xi) = \frac{(-1)^m \cdot (2)^{m-1} \cdot (\xi^2-1)^{m/2}}{\xi^{n+m+1}} \times$$

$$\times \sum_{k=0}^{\infty} \frac{\Gamma\left(\frac{n}{2} + \frac{m}{2} + k + \frac{1}{2}\right)! \cdot \Gamma\left(\frac{n}{2} + \frac{m}{2} + k + 1\right)}{\Gamma(k+1) \cdot \Gamma\left(n+k+\frac{3}{2}\right) \cdot \xi^{2k}}. \qquad (5)$$

The region $\xi \in [\xi_o, 4]$ places strict demands on the accuracy of $Q_n^m(\xi)$ function calculations. In the work [16] algorithms for direct calculation $Q_n^m(\xi)$ obtained in the form of finite sums

$$Q_n^m(\xi) = \frac{P_n(\xi)}{2} \cdot \ln\left(\frac{\xi+1}{\xi-1}\right) - \sum_{k=1}^{n} \frac{1}{k} \cdot \sum_{\lambda=0}^{m} C_m^\lambda \cdot P_{k-1}^\lambda(\xi) \cdot P_{n-k}^{m-\lambda}(\xi) + \frac{(1-\delta(m,0))}{2} \times \ldots \times \sum_{q=0}^{m-1} C_m^q \cdot P_n^q(\xi) \cdot (m-q-1)! \cdot \frac{(\xi-1)^{m-q} - (\xi+1)^{m-q}}{(-1)^{m-q-1}(\xi^2-1)^{\frac{m-q}{2}}};$$

$$(6)$$

$$Q_n^m(\xi) = \frac{(\xi^2-1)^{\frac{m}{2}} n! m!}{2^{n+1}} \sum_{k=0}^{m} \frac{(k+n)! \Omega(m-k,\xi)}{k!(m-k)!} \sum_{\lambda=k}^{n} \frac{(\xi-1)^{n-\lambda}(\xi+1)^{\lambda-k}}{\lambda!(n+k-\lambda)!(\lambda-k)!(n-\lambda)!} - \sum_{k=1}^{n} \frac{1}{k} \sum_{\lambda=0}^{m} C_m^\lambda P_{k-1}^\lambda(\xi) P_{n-k}^{m-\lambda}(\xi);$$

where

$$\Omega(\nu,\xi) = \begin{cases} \nu = 0 & \ln\left(\frac{\xi+1}{\xi-1}\right) \\ \nu \neq 0 & (-1)^{\nu-1}(\nu-1)! \frac{(\xi-1)^\nu - (\xi+1)^\nu}{(\xi^2-1)^\nu} \end{cases}, \quad C_n^k = \frac{n!}{(n-k)!k!}.$$

Direct geometric magnetostatics problems of energy-saturated units in spherical coordinate system. Usually inside extended energy-saturated technical object main sources of the magnetic field in form of N units of energy-saturated units installed. The sources of the magnetic field on naval vessels and submarines are electric motors, generators, distribution boards, semiconductor converters, transformers, etc. At the design and manufacturing stage, each such unit undergoes mandatory testing for its magnetic cleanliness. As a rule, these units represent compact devices and, therefore, mathematical models of the magnetic field of these units are conveniently represented in spherical coordinate systems [22–28].

Let us assume that during the testing process, for each magnetic unit, a model of its magnetic field is determined in a spherical coordinate system in the form of a Gaussian series

$$U = \frac{1}{4\pi} \cdot \sum_{n=1}^{\infty} \left(\frac{1}{r}\right)^{n+1} \cdot \sum_{m=0}^{n} \binom{g_n^m \cdot \cos(m\varphi)+}{+ h_n^m \cdot \sin(m\varphi) \cdot P_n^m(\cos\theta)}. \quad (7)$$

In this case, the spherical coordinates r, φ, and θ models of the magnetic field of the unit n are associated with the magnetic center of this units, and the spatial harmonics g_n^m, h_n^m are a comprehensive characteristic of the magnetic field generated by this unit n only.

Then the components H_r, H_φ, H_θ of the magnetic field strengths generated by all N units at the point with coordinates r, φ, and θ in the spherical coordinate system associated with the geometric center of this unit n calculated from spherical spatial harmonics, taken with the corresponding multipole coefficients:

$$H_r = \sum_{n=1}^{\infty} \sum_{m=0}^{n} \frac{n+1}{r^{n+2}} \left\{ g_n^m \cos(m\varphi) + h_n^m \sin(m\varphi) \right\} P_n^m(\cos\theta);$$

$$H_\theta = -\sum_{n=1}^{\infty} \sum_{m=0}^{n} \frac{1}{r^{n+2}} \left\{ g_n^m \cos(m\varphi) + h_n^m \sin(m\varphi) \right\} \frac{dP_n^m(\cos\theta)}{d\theta}; \quad (8)$$

$$H_\varphi = \sum_{n=1}^{\infty} \sum_{m=0}^{n} \frac{m}{r^{n+2}} \left\{ g_n^m \sin(m\varphi) - h_n^m \cos(m\varphi) \right\} \frac{P_n^m(\cos\theta)}{\sin\theta}.$$

Typically, when testing the magnetic characteristics of unit measurements are carried out in the orthogonal coordinate system x, y, z, which are related to the spherical coordinates r, φ, and θ the following dependence

$$x = r \cdot \sin(\vartheta)\cos(\varphi);$$
$$r \in [0, \infty[;$$
$$y = r \cdot \sin(\vartheta) \cdot \sin(\varphi); \Rightarrow \vartheta \in [0, \pi]; \quad (9)$$
$$\varphi \in [0, 2\pi];$$
$$z = r \cdot \cos(\vartheta).$$

Then, using the calculated values (6) of the magnetic field strength components H_r, H_φ, H_θ in spherical coordinates r, φ, and θ calculate the components H_x, H_y, H_z of this magnetic field strength vector in the rectangular coordinate system x, y, z, associated with the magnetic units centers [29–34]

$$H_x = H_r \sin(\theta_0)\cos(\varphi_0) + H_\theta \cos(\theta_0)\cos(\varphi_0) - H_\varphi \sin(\varphi_0);$$

$$H_y = H_r \sin(\theta_0)\sin(\varphi_0) + H_\theta \cos(\theta_0)\sin(\varphi_0) + H_\varphi \cos(\varphi_0); \quad (10)$$

$$H_z = H_r \cos(\theta_0) - H_0 \sin(\theta_0).$$

Naturally, some of the units are also extended sources of a magnetic field and it is advisable to describe them in the spheroidal coordinate system ξ, η and φ associated with the centers of these blocks. In particular, on a naval vessels such elongated energy-saturated units are distribution boards, semiconductor converters, etc., installed in a row. The components H_x, H_y, H_z of magnetic field generated by these extended energy-saturated units calculated using (8) for direct geometric magnetostatics problems in an elongated spheroidal coordinate system.

Let us set the coordinates ξ_k, η_k, φ_k of k – points for calculating magnetic field strengths in an elongated spheroidal coordinate system ξ, η, φ, associated with the center of the technical object. Based on (9) calculated the coordinates x_k, y_k, z_k of these points in the orthogonal coordinate system associated with the center of the technical object. Let's set the coordinates x_n, y_n, z_n of n location points of energy-saturated units in the same orthogonal coordinate system, also associated with the center of the technical object.

Let us choose the directions of the axes of the orthogonal coordinate systems of individual units parallel to the directions of the axes of the orthogonal coordinate system associated with the center of the technical object.

Then, based on (8) the components H_{rkn}, $H_{\varphi kn}$, $H_{\theta kn}$ of the magnetic field strength vector, generated by separate n units in a current with coordinates x_k, y_k, z_k can be calculated in spherical coordinate systems associated with the magnetic centers of individual units. When calculating the component H_{rkn}, $H_{\varphi kn}$, $H_{\theta kn}$ of the magnetic field strength vector it is necessary to use the following values of the spherical coordinates r_k, φ_k, and θ_k of the location of the magnetic field measurement point with coordinates r_k, φ_k, and θ_k relative to the location point of units n with coordinates r_n, φ_n, and θ_n in (2)

$$r_{kn} = \sqrt{((x_k - x_n)^2 + (y_k - y_n)^2 + (z_k - z_n)^2)};$$
$$\cos(\theta_{kn}) = (z_k - z_n)/r_{kn}; \quad (11)$$
$$\mathrm{tg}(\varphi_{kn}) = (y_k - y_n)/(x_k - x_n).$$

Then, from the calculated based on (8) components H_{rkn}, $H_{\varphi kn}$, $H_{\theta kn}$ of the magnetic field strength vector generated by individual n units at a point with coordinates x_k, y_k, z_k in spherical coordinate systems associated with the magnetic centers of individual blocks, the components H_{rkn}, $H_{\varphi kn}$, $H_{\theta kn}$ of the magnetic field strength vector generated by these n units in a current with coordinates x_k, y_k, z_k in a rectangular coordinate system associated with the magnetic center of a technical object according can be calculated based on (8). Naturally, in (2) it is necessary to use the values r, φ, and θ coordinates in the spheroidal coordinate system calculated from (2).

From the obtained components H_{rkn}, $H_{\varphi kn}$, $H_{\theta kn}$ of the magnetic field strength vector generated by n blocks in a point with coordinates x_k, y_k, z_k in a rectangular coordinate system associated with the magnetic center of a technical object, the components H_{xk}, H_{yk}, H_{zk} can be calculated total magnetic field generated by all N energy-saturated objects at the measurement point with coordinates x_k, y_k, z_k in a rectangular coordinate system associated with the center of the technical object, in the form of the following sums of components H_{xkn}, H_{ykn}, H_{zkn} magnetic field strength generated by individual n energy-saturated blocks

$$H_{xk} = \sum_{n=1}^{n=N} H_{xkn}; \ H_{yk} = \sum_{n=1}^{n=N} H_{ykn}; \ H_{zk} = \sum_{n=1}^{n=N} H_{zkn} \ . \ (12)$$

Prediction geometric inverse magnetostatics problems of an energy-saturated extended technical object in prolate spheroidal coordinate system. A feature of the energy-saturated extended technical objects are the uncertainty of the magnetic characteristics of their elements and their change in different operating modes [35–40]. Let us introduce the vector G of uncertainties of the parameters of energy-saturated extended technical object unit's magnetic cleanliness [41–44]. It should be noted that the values of external spheroidal harmonics c_n^m, s_n^m of magnetic field model (2), (3) of an elongated energy-saturated object in an elongated spheroidal coordinate system ξ, η, φ and the values of the spatial spherical harmonics g_n^m, h_n^m of magnetic field model (8) of the spherical coordinates r, φ, and θ for all N units of the energy-saturated extended technical object determined in the course of testing the magnetic cleanliness of all energy-saturated extended technical object units depend on the operating modes of the microsatellite and, therefore, are functions of the components of the vector G of uncertainties of the parameters of the magnetic cleanliness of the energy-saturated extended technical object units.

Then for a given value of the vector G of uncertainties of the parameters of the magnetic cleanliness of energy-saturated extended technical object units, given coordinates r_n, φ_n, and θ_n of spatial arrangement of N energy-saturated extended technical object units with given values of the spatial spherical harmonics g_n^m, h_n^m of magnetic field model (8) components $H_{xk}(G)$, $H_{yk}(G)$, $H_{zk}(G)$ of the magnetic field generated by all N units of the energy-saturated extended technical object at the point with coordinates r_k, φ_k and θ_k calculated based on (6) – (8). Since the results of measuring the magnetic field depend on the operating modes of the V, the components $H_{xk}(G)$, $H_{yk}(G)$, $H_{zk}(G)$ of the measurement vector also are functions of the vector G.

Let us now consider the prediction geometric inverse magnetostatics problems of calculating the values of external spheroidal harmonics c_n^m, s_n^m of magnetic field model (2) of an elongated energy-saturated object in an elongated spheroidal coordinate system ξ, η, φ, associated with the magnetic center of an energy-saturated object based on the results of measurements of magnetic field $H_{xk}(G)$, $H_{yk}(G)$, $H_{zk}(G)$ generated by all N energy-saturated units this energy-saturated extended technical object at the K point with coordinates r_k, φ_k and θ_k [36, 37].

For convenience, we will perform the calculations in an orthogonal coordinate system associated with the center of the technical object so that instead of the measured values of the magnetic field $H_{\xi k}(G)$, $H_{\eta k}(G)$, $H_{\varphi k}(G)$ in an elongated spheroidal coordinate system at points ξ_k, η_k, φ_k we will use the magnetic field components $H_{xk}(G)$, $H_{yk}(G)$, $H_{zk}(G)$ in an orthogonal system with coordinates x_k, y_k, z_k. Naturally, the coordinates ξ_k, η_k, φ_k in the spheroidal coordinate system and the coordinates x_k, y_k, z_k in the orthogonal coordinate

system correspond to the same points K of measurement of the magnetic field of a technical object.

Let us introduce the vector $Y_M(G)$, components $H_{xk}(G)$, $H_{yk}(G)$, $H_{zk}(G)$ of which are the measured values of the magnetic field in an orthogonal system with coordinates x_k, y_k, z_k, at the K measurement points [10, 48].

Let us introduce the vector X of the desired parameters of the mathematical model of the energy-saturated extended technical object, the components of which are the desired coordinates x_n, y_n, z_n in the orthogonal coordinate system associated with the center of the technical object of spatial arrangement of N energy-saturated extended units as well as the desired values of c_n^m, s_n^m of external spheroidal harmonics of this units.

Then for a given vector value X and for a given vector value G, the components $H_{xkn}(X,G)$, $H_{ykn}(X,G)$, $H_{zkn}(X,G)$ of the magnetic field in the orthogonal coordinate system generated by these N energy-saturated extended units at measurement points with coordinates x_k, y_k, z_k calculated based on (8). When calculating these components $H_{xkn}(X,G)$, $H_{ykn}(X,G)$, $H_{zkn}(X,G)$ of magnetic field parameter c_{kn} and the corresponding angles ξ_{kn}, η_{kn}, φ_{kn} location of measurement points with coordinates x_k, y_k, z_k from points and location of n blocks with coordinates x_n, y_n, z_n an elongated spheroidal coordinate system it is necessary to calculate in the form of solving the following system of equations

$$x_k - x_n = c_{kn}\sqrt{\xi_{kn}^2 - 1} \cdot \sqrt{1 - \eta_{kn}^2} \cdot \cos(\varphi_{kn});$$

$$y_k - y_n = c_{kn}\sqrt{\xi_{kn}^2 - 1} \cdot \sqrt{1 - \eta_{kn}^2} \cdot \sin(\varphi_{kn}); \Rightarrow \begin{matrix} \xi_{kn} \in [1,\infty[; \\ \eta_{kn} \in [0,1]; \\ \varphi_{kn} \in [0,2\pi]; \end{matrix} \quad (13)$$

$$z_{kn} - z_{kn} = c_{kn} \cdot \xi_{kn} \cdot \eta_{kn}.$$

Then, based on the calculated components $H_{xkn}(X,G)$, $H_{ykn}(X,G)$, $H_{zkn}(X,G)$ of the magnetic field generated by each element n, the components $H_{xk}(X,G)$, $H_{yk}(X,G)$, $H_{zk}(X,G)$ of the rezalting magnetic field generated by all N units at the measurement points K can be calculated similarly to (10).

Let us introduce the vector $Y_C(G)$, components of which are the calculated values components $H_{xk}(X,G)$, $H_{yk}(X,G)$, $H_{zk}(X,G)$ of the magnetic field at the K measurement points with the coordinates x_k, y_k, z_k.

For vector X of the desired parametersand and for vector G of parameters uncertainties of the mathematical model of the spacecraft magnetic field, then, based on (3) – (8) the initial nonlinear equation $Y_C(G)$ for the spacecraft multipole magnetic dipole model calculated

$$Y_C(X, G) = F(X, G), \quad (14)$$

where the vector nonlinear function $F(X,G)$ obtained on the basis of expression (3) – (8) with respect to the vector X of unknown variables, whose components are desired coordinates x_n, y_n, z_n of spatial arrangement N energy-saturated extended units as well as the desired values of values c_n^m, s_n^m of external spheroidal harmonics of this units.

Naturally that the vector nonlinear function $F(X,G)$ also is a function of the vector G of uncertainties of the parameters of microsatellite units magnetic cleanliness.

Let us introduce the $E(X,G)$ vector of the discrepancy between the vector $Y_M(G)$ of the measured

magnetic field and the vector $Y_C(X,G)$ of the predicted by model (3) magnetic field

$$E(X, G) = Y_M(G) - Y_C(X, G) = Y_M(G) - F(X, G). \quad (15)$$

The nonlinear vector objective function (12) is obtained on the basis of expression (3) with respect to the vector X of unknown variables, whose components are the values coordinates unknown variables, whose components are desired coordinates x_n, y_n, z_n of spatial arrangement N energy-saturated extended units as well as the desired values of values c_n^m, s_n^m of external spheroidal harmonics of this units and the vector G of uncertainties of the parameters of the magnetic cleanliness of microsatellite units.

This approach is standard when designing robust mathematical model of the spacecraft magnetic field, when the coordinates of the spatial arrangement and the magnitudes of the magnetic moments of the dipoles are found from the conditions for minimizing the vector of the discrepancy between the vector of the measured magnetic field and the vector of the predicted by model magnetic field, but for the «worst» the vector of uncertainty parameters of the spacecraft magnetic moments are found from the conditions for maximizing the same vector of the discrepancy between the vector of the measured magnetic field and the vector of the predicted by model magnetic field.

As a rule, when optimizing the nonlinear objective function (15), it is necessary to take into account restrictions as vector inequalities [41–44]

$$G(X, G) \leq G_{max}. \quad (16)$$

Then the magnitude of the magnetic field at any point P_j of the far zone of a technical object with coordinates x_j, y_j, z_j can be calculated and predicted based on the obtained model (9).

Inverse problem solving method. In course of geometric inverse magnetostatic's problem solving it is necessary to repeatedly solve the direct problem (2) during the iterative calculation of spatial harmonics g_n^m, h_n^m of nanosatellite initial magnetic field mathematical model when prediction geometric inverse magnetostatic's problem solution (3) calculated and during iterative calculation component g_n^m, h_n^m of spherical harmonics of the magnetic field generated by this C compensating magnetic units with unknown coordinates r_c, φ_c and θ_c when control geometric inverse magnetostatic's problem (15) solution calculated.

Components of the vector games (15) are nonlinear functions of the vector X of required parameters and the vector G of uncertainty parameters of geometric inverse magnetostatic's problem for prediction and control by nanosatellite magnetic cleanliness taking into account direct problem uncertainties and calculated by COMSOL Multiphysics software.

Typically geometric inverse magnetostatic's problem for prediction and control by technical objects magnetic cleanliness comes down to solving minimizing optimization problem [6, 7]. When geometric inverse magnetostatic's problem for prediction and control by technical objects magnetic cleanliness taking into account direct problem uncertainties worst-case design approach usually used to impart robustness designed prediction and control by nanosatellite magnetic cleanliness taking into

account direct problem uncertainties. In this cases solution of both prediction and control geometric inverse problem reduced to solving a game in which vector X of required parameters – first player minimizes game payoff (15), but vector G of direct problem uncertainties – second player tries to maximize same game payoff (15).

A feature of the problem of calculated solution under consideration is the multi-extremal nature of game payoff (15) so that the considered region of possible solutions contains local minima and maxima. This due to fact that when minimizing the induction level of the resulting magnetic field at one point in the shielding space, the induction level at another point in this space increases due to under compensation or overcompensation of the original magnetic field. Therefore, to calculate the solution to the vector game under consideration, it is advisable to use stochastic multi-agent optimization algorithms [35, 36].

The main approach to multiobjective optimization is to search for the Pareto set, which includes all solutions that are not dominated by other solutions. To find non-dominated solutions, it is convenient to use specially calculated ranks. However, this raises the problem of comparing several solutions that have the same rank values. To adapt the PSO method in relation to the problem of finding Pareto-optimal solutions on the set of possible values of a vector criterion, it is most simple to use binary preference relations that determine the Pareto dominance of individual solutions.

Inverse problem solving algorithm. Consider algorithm for calculating the solution of the vector game (15). The works [35–37] consider various approaches to computing solutions to vector games based on various heuristic approaches. Unlike works [35, 36], in this work, in order to find a unique solution to a vector game from a set of Pareto-optimal solutions, in addition to the vector payoff (15) we will also use information about the binary relationships of preferences of local solutions relative to each other [38–40].

To calculate one single global solution to the vector game (15) individual swarms exchange information with each other during the calculation of optimal solutions to local games. Information about the global optimum obtained by particles from another swarm used to calculate the speed of movement of particles from another swarm, which allows us to calculate all potential Pareto-optimal solutions [41–46].

In the standard particles swarm optimization algorithm the particle velocities change is carried out according to linear laws [6, 7]. To increase the speed of finding a global solution, special nonlinear algorithms of stochastic multi-agent optimization recently proposed in [45, 46], in which the motion of i particle of j swarm described by the following expressions

$$v_{ij}(t+1) = w_{1j}v_{ij}(t) + c_{1j}r_{1j}(t)H\left(p_{1ij}(t) - \varepsilon_{1ij}(t)\right)\left[y_{ij}(t) - x_{ij}(t)\right] + c_{2j}r_{2j}(t)H\left(p_{2ij}(t) - \varepsilon_{2ij}(t)\right)\left[y_j^*(t) - x_{ij}(t)\right]; \quad (17)$$

$$u_{ij}(t+1) = w_{2j}u_{ij}(t) + c_{3j}r_{3j}(t)H\left(p_{3ij}(t) - \varepsilon_{3ij}(t)\right)\left[z_{ij}(t) - \delta_{ij}(t)\right] + c_{4j}r_{4j}(t)H\left(p_{4ij}(t) - \varepsilon_{4ij}(t)\right)\left[z_j^*(t) - \delta_{ij}(t)\right]; \quad (18)$$

$$x_{ij}(t+1) = x_{ij}(t) + v_{ij}(t+1);$$
$$g_{ij}(t+1) = \delta_{ij}(t) + u_{ij}(t+1), \quad (19)$$

where $x_{ij}(t)$, $g_{ij}(t)$ and $v_{ij}(t)$, $u_{ij}(t)$ is the position and velocity of i particle of j swarm.

In (17) – (19) $y_{ij}(t)$, $z_{ij}(t)$ and $y_j^*(t)$, $z_j^*(t)$ – the best local and global positions of the i–th particle, found respectively by only one i–th particle and all the particles of j swarm. Moreover, the best local position $y_{ij}(t)$ and the global position $y_j^*(t)$ of the i particle of j swarm are understood in the sense of the first player strategy $x_{ij}(t)$ for minimum of component $E_i(\boldsymbol{X},\boldsymbol{G})$ of the vector payoff (15). However, the best local position $z_{ij}(t)$ and the global position z_j^* of the i particle of j swarm are understood in the sense of the second player strategy $g_{ij}(t)$ for maximum of the same component $E_i(\boldsymbol{X},\boldsymbol{G})$ of the vector payoff (15).

Four independent random numbers $r_{1j}(t)$, $r_{2j}(t)$, $r_{3j}(t)$, $r_{4j}(t)$ are in the range of [0, 1], which determine the stochastic particle velocity components.

Positive constants c_{1j}, c_{2j} and c_{3j}, c_{4j} determine the cognitive and social weights of the particle velocity components.

The Heaviside function H is used as a switching function of the motion of a particle, respectively, to the local $y_{ij}(t)$, $z_{ij}(t)$ and global $y_j^*(t)$, $z_j^*(t)$ optimum.

Switching parameters of the cognitive p_{1ij}, p_{3ij} and social p_{2ij}, p_{4ij} components of the particle velocity to the local and global optimum taken in the form of increments changes in the payoff (15) for players' strategies $x_{ij}(t)$, $g_{ij}(t)$ when moving to local and global optimum respectively.

Random numbers $\varepsilon_{1ij}(t)$, $\varepsilon_{2ij}(t)$, $\varepsilon_{3ij}(t)$ and $\varepsilon_{4ij}(t)$ determine the switching parameters of the particle motion, respectively, to local and global optima.

To improve solution finding process quality, the inertia coefficients w_{1j}, w_{2j} used.

In random search, the motion of the particle is carried out in the direction of the maximum growth of the component of the objective function, found in the process of random search. In general, this direction serves as an estimate of the direction of the gradient in a random search. Naturally, such an increment of the objective function serves as an analogue of the first derivative – the rate of change of the objective function.

To take these constraints into account when searching for solutions, we used special particle swarm optimization method for constrained optimization problems [38–40]. To take these binary preference relations into account when searching for solutions, we used special evolutionary algorithms for multiobjective optimizations [45, 46].

Simulation results. The real magnetic signature of naval vessels and submarines are a secret [45–48]. That's why as an example, consider modeling the magnetic signature of an extended energy-saturated object with the following initial data [6]. The sources of the magnetic field are 16 dipoles located at points with coordinates $x = \pm39$ m and ±13 m with $y = \pm4$ m and $z = 3.5$ m. These dipoles have different values of the magnetic moment components M_x, M_y and M_z along the three axes of the rectangular coordinate system.

The magnetic field levels were calculated in the interval $x = -100$ m and $x = +100$ m for three values $y = 0$ and $y = \pm20$ m. Thus, three components of the magnetic field strength were calculated at 303 points, so that the total number

measurements amounted to 909. In this case, calculations were performed for two values $z = 19$ m and $z = 60$ m.

In the example under consideration, the object is elongated along the X coordinate, which corresponds to the real location of the rectangular coordinate system axes of the object in question. However, formulas (2), (3) for calculating the magnetic field in an elongated spheroidal system are given for the case when the object is elongated along the Z coordinate.

Let us consider the model in the form of one magnetic field source located at the beginning of the coordinates. The accuracy of approximation of the magnetic field of an elongated object depends on the number of harmonics taken into account in the magnetic field model.

Let us first consider the approximation in the form of one first harmonic. During the optimization process, the value of the parameter $c = 58.03$ and the magnitude of the first harmonic $c_1^0 = -1.75586$, $c_1^1 = -0.226512$, $s_1^1 = -0.440788$ calculated.

Figure 1 shows magnetic signature projections taking into account only one first harmonic, for three coordinates of the a) $Y = -20$ m, $Z = 19$ m; b) $Y = 0$, $Z = 19$ m and c) $Y = 20$ m, $Z = 19$ m. Note that the components of the magnetic field change most strongly for the passage characteristic at the center of the technical object with coordinates $Y = 0$, $Z = 19$ m.
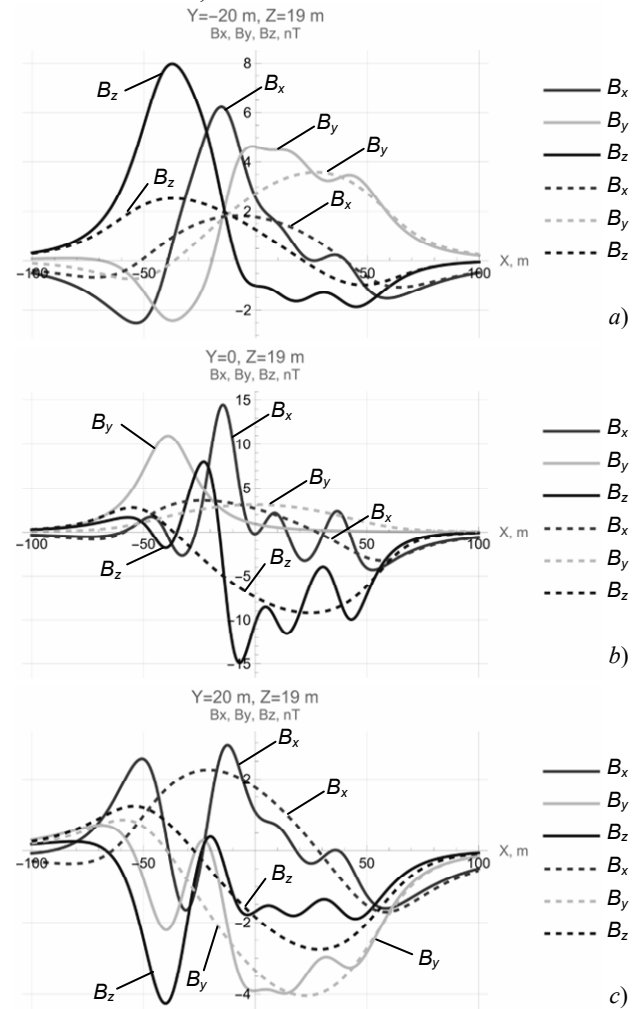

Fig. 1. Magnetic signature projections taking into account only one first harmonic of a real object (solid lines) and models (dashed lines)

Let us consider the approximation in the form of five harmonic. During the optimization process, the value of the parameter $c = 36.5236$ and the magnitude of the five harmonic

$$c_1^0 = -1.17987, \ c_1^1 = -0.524211, \ s_1^1 = -1.28567;$$

$$c_2^0 = 7.0228, \ c_2^1 = 2.34334, \ c_2^2 = -0.0767858, \ s_2^1 = -3.32643,$$

$$s_2^2 = -0.0375657;$$

$$c_3^0 = -64.5892, \ c_3^1 = -3.96332, \ c_3^2 = -0.195524,$$

$$c_3^3 = -0.000181004, \ s_3^1 = -4.36204, \ s_3^2 = -0.0730327,$$

$$s_3^3 = 0.00376364;$$

$$c_4^0 = -112.13, \ c_4^1 = 3.10697, \ c_4^2 = -0.0777715,$$

$$c_4^3 = -0.00120079, \ c_4^4 = 0.0000413822,$$

$$s_4^1 = 7.89786, \ s_4^2 = 0.0941992, \ s_4^3 = 0.00197418,$$

$$s_4^4 = -0.0000144349;$$

$$c_5^0 = 75.3116, \ c_5^1 = -0.894198, \ c_5^2 = 0.0634926,$$

$$c_5^3 = 0.000540308, \ c_5^4 = 3.49849 \cdot 10^{-6}, \ c_5^5 = -7.31748 \cdot 10^{-8},$$

$$s_5^1 = 3.46386, \ s_5^2 = -0.0377943, \ s_5^3 = 0.000859992,$$

$$s_5^4 = 6.01948 \cdot 10^{-6}, \ s_5^5 = -9.39689 \cdot 10^{-8} \text{ calculated.}$$

Figure 2 shows magnetic signature projections taking into account five harmonic, for three coordinates of the magnetic field passage sections: *a*) $Y = -20$ m, $Z = 19$ m; *b*) $Y = 0$, $Z = 19$ m and *c*) $Y = 20$ m, $Z = 19$ m.
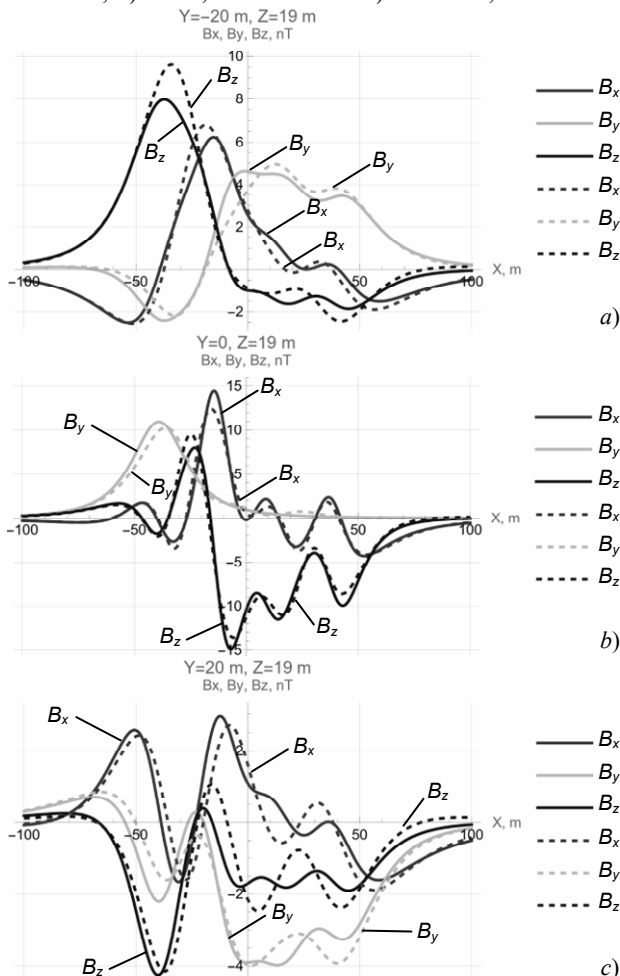

Fig. 2. Magnetic signature projections taking into account five harmonic of a real object (solid lines) and models (dashed lines)

Naturally, that when taking into account the five harmonics shown in Fig. 2 accuracy of the magnetic field prediction is significantly higher than when taking into account only one first harmonic, shown in Fig. 1.

A further increase in accuracy can be achieved both by increasing the number of harmonics taken into account and by increasing the number of magnetic field sources.

Moreover, the coordinates of these sources also need to be calculated in the form of a solution to the optimization problem.

Thus, in the example under consideration, the initial magnetic field of the technical object generated in the form of 16 dipoles located in the space of a technical object. Using these 16 dipoles, the «measured» magnetic field was calculated at 303 points in the near zone of a technical object.

Based on developed method for these 909 values of the «measured» magnetic field in the near zone predictive model designed in the form of one elongated magnetic field source with five spatial spheroidal elongated harmonics. Based on this developed prediction model the magnetic field of a technical object in the far zone calculated in an elongated spheroidal coordinate system to fulfill the technical requirements that apply to the level of the external magnetic field of a technical object.

Conclusions.

1. The method for prediction by extended technical objects magnetic silencing based on spatial prolate spheroidal harmonics magnetic field model in the prolate spheroidal coordinate system with consideration of magnetic characteristics uncertainty developed.

2. Prediction extended technical objects magnetic silencing calculated as solution of geometric inverse magnetostatics problems in the form of nonlinear minimax optimization problem based on near field measurements for prediction far extended technical objects magnetic field magnitude. Nonlinear objective function calculated as the weighted sum of squared residuals between the measured and predicted magnetic field COMSOL Multiphysics software package used. Solutions of this nonlinear minimax optimization problems calculated based on particle swarm nonlinear optimization algorithms.

3. The developed method used to design of prediction extended technical objects magnetic silencing based on the spatial prolate spheroidal harmonics of the magnetic field model in the prolate spheroidal coordinate system with consideration of extended technical objects magnetic characteristics uncertainty. A further increase in accuracy can be achieved both by increasing the number of harmonics taken into account and by increasing the number of magnetic field sources.

4. Obtained prediction model based on experimentally measured magnetic field in the near zone will be used to calculate the magnetic field in the far zone and to solve the control problem by extended technical objects magnetic silencing in the prolate spheroidal coordinate system of monitoring magnetic silence.

of the National Academy of Sciences of Ukraine for the kindly provided materials on the results of experimental measured magnetic field generated by energy-saturated technical objects and also for numerous discussions that allowed the authors to improve the article manuscript.

REFERENCES
1. Rozov V.Yu., Getman A.V., Petrov S.V., Erisov A.V., Melanchenko A.G., Khoroshilov V.S., Schmidt I.R Spacecraft magnetism. *Technical Electrodynamics. Thematic issue «Problems of modern electrical engineering»*, 2010, part 2, pp. 144-147. (Rus).
2. *ECSS-E-HB-20-07A. Space engineering: Electromagnetic compatibility hand-book. ESA-ESTEC. Requirements & Standards Division.* Noordwijk, Netherlands, 2012. 228 p.
3. Droughts S.A., Fedorov O.P. Space project Ionosat-Micro. Monograph. Kyiv, Akademperiodika Publ., 2013. 218 p. (Rus).
4. Holmes J.J. *Exploitation of A Ship's Magnetic Field Signatures.* Springer Cham, 2006. 67 p. doi: https://doi.org/10.1007/978-3-031-01693-6.
5. Woloszyn M., Jankowski P. Simulation of ship's deperming process using Opera 3D. *2017 18th International Symposium on Electromagnetic Fields in Mechatronics, Electrical and Electronic Engineering (ISEF) Book of Abstracts*, 2017, pp. 1-2. doi: https://doi.org/10.1109/ISEF.2017.8090680.
6. Birsan M., Holtham P., Carmen. Using global optimisation techniques to solve the inverse problem for the computation of the static magnetic signature of ships. *Defense Research Establishment Atlantic*, 9 Grove St., PO Box 1012, Dartmouth, Nova Scotia, B2Y 3Z7, Canada.
7. Zuo C., Ma M., Pan Y., Li M., Yan H., Wang J., Geng P., Ouyang J. Multi-objective optimization design method of naval vessels degaussing coils. *Proceedings of SPIE - The International Society for Optical Engineering*, 2022, vol. 12506, art. no. 125060J. doi: https://doi.org/10.1117/12.2662888.
8. Baranov M.I., Rozov V.Y., Sokol Y.I. To the 100th anniversary of the National Academy of Sciences of Ukraine – the cradle of domestic science and technology. *Electrical Engineering & Electromechanics*, 2018, no. 5, pp. 3-11. doi: https://doi.org/10.20998/2074-272X.2018.5.01.
9. Chadebec O., Rouve L.-L., Coulomb J.-L. New methods for a fast and easy computation of stray fields created by wound rods. *IEEE Transactions on Magnetics*, 2002, vol. 38, no. 2, pp. 517-520. doi: https://doi.org/10.1109/20.996136.
10. Rozov V.Yu. Methods for reducing external magnetic fields of energy-saturated objects. *Technical Electrodynamics*, 2001, no. 1, pp. 16-20.
11. Rozov V., Grinchenko V., Tkachenko O., Yerisov A. Analytical Calculation of Magnetic Field Shielding Factor for Cable Line with Two-Point Bonded Shields. *2018 IEEE 17th International Conference on Mathematical Methods in Electromagnetic Theory (MMET)*, 2018, pp. 358-361. doi: https://doi.org/10.1109/MMET.2018.8460425.
12. Rozov V.Yu., Dobrodeev P.N., Volokhov S.A. Multipole model of a technical object and its magnetic center. *Technical Electrodynamics*, 2008, no. 2, pp. 3-8. (Rus).
13. Rozov V.Yu., Getman A.V., Kildishev A.V. Spatial harmonic analysis of the external magnetic field of extended objects in a prolate spheroidal coordinate system. *Technical Electrodynamics*, 1999, no. 1, pp. 7-11. (Rus).
14. Rozov V.Yu. Mathematical model of electrical equipment as a source of external magnetic field. *Technical Electrodynamics*, 1995, no. 2, pp. 3-7. (Rus).
15. Volokhov S.A., Dobrodeev P.N., Ivleva L.F. Spatial harmonic analysis of the external magnetic field of a technical object. *Technical Electrodynamics*, 1996, no. 2, pp. 3-8. (Rus).
16. Getman A.V. *Analysis and synthesis of the magnetic field structure of technical objects on the basis of spatial harmonics.* Dissertation thesis for the degree of Doctor of Technical Sciences. Kharkiv, 2018. 43 p. (Ukr).
17. Xiao C., Xiao C., Li G. Modeling the ship degaussing coil's effect based on magnetization method. *Communications in Computer and Information Science*, 2012, vol. 289, pp. 62-69. doi: https://doi.org/10.1007/978-3-642-31968-6_8.

18. Wołoszyn M., Jankowski P. Ship's de-perming process using coils lying on seabed. *Metrology and Measurement Systems*, 2019, vol. 26, no. 3, pp. 569-579. doi: https://doi.org/10.24425/mms.2019.129582.
19. Fan J., Zhao W., Liu S., Zhu Z. Summary of ship comprehensive degaussing. *Journal of Physics: Conference Series*, 2021, vol. 1827, no. 1, art. no. 012014. doi: https://doi.org/10.1088/1742-6596/1827/1/012014.
20. Getman A.V. Spatial harmonic analysis of the magnetic field of the sensor of the neutral plasma component. *Eastern European Journal of Advanced Technologies*, 2010, vol. 6, no. 5(48), pp. 35-38. doi: https://doi.org/10.15587/1729-4061.2010.3326.
21. Getman A. Ensuring the Magnetic Compatibility of Electronic Components of Small Spacecraft. *2022 IEEE 3rd KhPI Week on Advanced Technology (KhPIWeek)*, 2022, no. 1-4. doi: https://doi.org/10.1109/KhPIWeek57572.2022.9916339.
22. Acuña M.H. *The design, construction and test of magnetically clean spacecraft – a practical guide.* NASA/GSFC internal report. 2004.
23. Junge A., Marliani F. Prediction of DC magnetic fields for magnetic cleanliness on spacecraft. *2011 IEEE International Symposium on Electromagnetic Compatibility*, 2011, pp. 834-839. doi: https://doi.org/10.1109/ISEMC.2011.6038424.
24. Lynn G.E., Hurt J.G., Harriger K.A. Magnetic control of satellite attitude. *IEEE Transactions on Communication and Electronics*, 1964, vol. 83, no. 74, pp. 570-575. doi: https://doi.org/10.1109/TCOME.1964.6539511.
25. Junge A., Trougnou L., Carrubba E. Measurement of Induced Equivalent Magnetic Dipole Moments for Spacecraft Units and Components. *Proceedings ESA Workshop Aerospace EMC 2009 ESA WPP-299*, 2009, vol. 4, no. 2, pp. 131-140.
26. Mehlem K., Wiegand A. Magnetostatic cleanliness of spacecraft. *2010 Asia-Pacific International Symposium on Electromagnetic Compatibility*, 2010, pp. 936-944. doi: https://doi.org/10.1109/APEMC.2010.5475692.
27. Messidoro P., Braghin M., Grande M. Magnetic cleanliness verification approach on tethered satellite. *16th Space Simulation Conference: Confirming Spaceworthiness into the Next Millennium*, 1991, pp. 415-434.
28. Mehlem K., Narvaez P. Magnetostatic cleanliness of the radioisotope thermoelectric generators (RTGs) of Cassini. *1999 IEEE International Symposium on Electromagnetic Compatability*, 1999, vol. 2, pp. 899-904. doi: https://doi.org/10.1109/ISEMC.1999.810175.
29. Eichhorn W.L. *Magnetic dipole moment determination by near-field analysis.* Goddard Space Flight Center. Washington, D.C., National Aeronautics and Space Administration, 1972. NASA technical note, D 6685. 87 p.
30. Matsushima M., Tsunakawa H., Iijima Y., Nakazawa S., Matsuoka A., Ikegami S., Ishikawa T., Shibuya H., Shimizu H., Takahashi F. Magnetic Cleanliness Program Under Control of Electromagnetic Compatibility for the SELENE (Kaguya) Spacecraft. *Space Science Reviews*, 2010, vol. 154, no. 1-4, pp. 253-264. doi: https://doi.org/10.1007/s11214-010-9655-x.
31. Boghosian M., Narvaez P., Herman R. Magnetic testing, and modeling, simulation and analysis for space applications. *2013 IEEE International Symposium on Electromagnetic Compatibility*, 2013, pp. 265-270. doi: https://doi.org/10.1109/ISEMC.2013.6670421.
32. Mehlem K. Multiple magnetic dipole modeling and field prediction of satellites. *IEEE Transactions on Magnetics*, 1978, vol. 14, no. 5, pp. 1064-1071. doi: https://doi.org/10.1109/TMAG.1978.1059983.
33. Thomsen P.L., Hansen F. Danish Ørsted Mission In-Orbit Experiences and Status of The Danish Small Satellite Programme. *Annual AIAA/USU Conference on Small Satellites*, 1999, pp. SSC99-I–8.
34. Kapsalis N.C., Kakarakis S.-D.J., Capsalis C.N. Prediction of multiple magnetic dipole model parameters from near field measurements employing stochastic algorithms. *Progress In Electromagnetics Research Letters*, 2012, vol. 34, pp. 111-122. doi: https://doi.org/10.2528/PIERL12030905.
35. Solomentsev O., Zaliskyi M., Averyanova Y., Ostroumov I., Kuzmenko N., Sushchenko O., Kuznetsov B., Nikitina T., Tserne E., Pavlikov V., Zhyla S., Dergachov K., Havrylenko O., Popov A., Volosyuk V., Ruzhentsev N., Shmatko O. Method of Optimal Threshold Calculation in Case of Radio Equipment Maintenance. *Data Science and Security. Lecture Notes in Networks and Systems*, 2022, vol. 462, pp. 69-79. doi: https://doi.org/10.1007/978-981-19-2211-4_6.

36. Ruzhentsev N., Zhyla S., Pavlikov V., Volosyuk V., Tserne E., Popov A., Shmatko O., Ostroumov I., Kuzmenko N., Dergachov K., Sushchenko O., Averyanova Y., Zaliskyi M., Solomentsev O., Havrylenko O., Kuznetsov B., Nikitina T. Radio-Heat Contrasts of UAVs and Their Weather Variability at 12 GHz, 20 GHz, 34 GHz, and 94 GHz Frequencies. *ECTI Transactions on Electrical Engineering, Electronics, and Communications*, 2022, vol. 20, no. 2, pp. 163-173. doi: https://doi.org/10.37936/ecti-eec.2022202.246878.

37. Havrylenko O., Dergachov K., Pavlikov V., Zhyla S., Shmatko O., Ruzhentsev N., Popov A., Volosyuk V., Tserne E., Zaliskyi M., Solomentsev O., Ostroumov I., Sushchenko O., Averyanova Y., Kuzmenko N., Nikitina T., Kuznetsov B. Decision Support System Based on the ELECTRE Method. *Data Science and Security. Lecture Notes in Networks and Systems*, 2022, vol. 462, pp. 295-304. doi: https://doi.org/10.1007/978-981-19-2211-4_26.

38. Shmatko O., Volosyuk V., Zhyla S., Pavlikov V., Ruzhentsev N., Tserne E., Popov A., Ostroumov I., Kuzmenko N., Dergachov K., Sushchenko O., Averyanova Y., Zaliskyi M., Solomentsev O., Havrylenko O., Kuznetsov B., Nikitina T. Synthesis of the optimal algorithm and structure of contactless optical device for estimating the parameters of statistically uneven surfaces. *Radioelectronic and Computer Systems*, 2021, no. 4, pp. 199-213. doi: https://doi.org/10.32620/reks.2021.4.16.

39. Volosyuk V., Zhyla S., Pavlikov V., Ruzhentsev N., Tserne E., Popov A., Shmatko O., Dergachov K., Havrylenko O., Ostroumov I., Kuzmenko N., Sushchenko O., Averyanova Yu., Zaliskyi M., Solomentsev O., Kuznetsov B., Nikitina T. Optimal Method for Polarization Selection of Stationary Objects Against the Background of the Earth's Surface. *International Journal of Electronics and Telecommunications*, 2022, vol. 68, no. 1, pp. 83-89. doi: https://doi.org/10.24425/ijet.2022.139852.

40. Zhyla S., Volosyuk V., Pavlikov V., Ruzhentsev N., Tserne E., Popov A., Shmatko O., Havrylenko O., Kuzmenko N., Dergachov K., Averyanova Y., Sushchenko O., Zaliskyi M., Solomentsev O., Ostroumov I., Kuznetsov B., Nikitina T. Practical imaging algorithms in ultra-wideband radar systems using active aperture synthesis and stochastic probing signals. *Radioelectronic and Computer Systems*, 2023, no. 1, pp. 55-76. doi: https://doi.org/10.32620/reks.2023.1.05.

41. Maksymenko-Sheiko K.V., Sheiko T.I., Lisin D.O., Petrenko N.D. Mathematical and Computer Modeling of the Forms of Multi-Zone Fuel Elements with Plates. *Journal of Mechanical Engineering*, 2022, vol. 25, no. 4, pp. 32-38. doi: https://doi.org/10.15407/pmach2022.04.032.

42. Hontarovskyi P.P., Smetankina N.V., Ugrimov S.V., Garmash N.H., Melezhyk I.I. Computational Studies of the Thermal Stress State of Multilayer Glazing with Electric Heating. *Journal of Mechanical Engineering*, 2022, vol. 25, no. 1, pp. 14-21. doi: https://doi.org/10.15407/pmach2022.02.014.

43. Kostikov A.O., Zevin L.I., Krol H.H., Vorontsova A.L. The Optimal Correcting the Power Value of a Nuclear Power Plant Power Unit Reactor in the Event of Equipment Failures. *Journal of Mechanical Engineering*, 2022, vol. 25, no. 3, pp. 40-45. doi: https://doi.org/10.15407/pmach2022.03.040.

44. Rusanov A.V., Subotin V.H., Khoryev O.M., Bykov Y.A., Korotaiev P.O., Ahibalov Y.S. Effect of 3D Shape of Pump-Turbine Runner Blade on Flow Characteristics in Turbine Mode. *Journal of Mechanical Engineering*, 2022, vol. 25, no. 4, pp. 6-14. doi: https://doi.org/10.15407/pmach2022.04.006.

45. Sushchenko O., Averyanova Y., Ostroumov I., Kuzmenko N., Zaliskyi M., Solomentsev O., Kuznetsov B., Nikitina T., Havrylenko O., Popov A., Volosyuk V., Shmatko O., Ruzhentsev N., Zhyla S., Pavlikov V., Dergachov K., Tserne E. Algorithms for Design of Robust Stabilization Systems. *Computational Science and Its Applications – ICCSA 2022. ICCSA 2022. Lecture Notes in Computer Science*, 2022, vol. 13375, pp. 198-213. doi: https://doi.org/10.1007/978-3-031-10522-7_15.

46. Zhyla S., Volosyuk V., Pavlikov V., Ruzhentsev N., Tserne E., Popov A., Shmatko O., Havrylenko O., Kuzmenko N., Dergachov K., Averyanova Y., Sushchenko O., Zaliskyi M., Solomentsev O., Ostroumov I., Kuznetsov B., Nikitina T. Statistical synthesis of aerospace radars structure with optimal spatio-temporal signal processing, extended observation area and high spatial resolution. *Radioelectronic and Computer Systems*, 2022, no. 1, pp. 178-194. doi: https://doi.org/10.32620/reks.2022.1.14.

47. Wang D., Yu Q. Review on the development of numerical methods for magnetic field calculation of ships. *Ships Science and Technology*, 2014, vol. 36, no. 3, pp. 1-6.

48. Jin H., Wang H., Zhuang Z. A New Simple Method to Design Degaussing Coils Using Magnetic Dipoles. *Journal of Marine Science and Engineering*, 2022, vol. 10, no. 10, art. no. 1495. doi: https://doi.org/10.3390/jmse10101495.

B.I. Kuznetsov[1]*, Doctor of Technical Science, Professor,*
A.S. Kutsenko[1]*, Doctor of Technical Science, Professor,*
T.B. Nikitina[2]*, Doctor of Technical Science, Professor,*
I.V. Bovdui[1]*, PhD, Senior Research Scientist,*
K.V. Chunikhin[1]*, PhD, Senior Research Scientist,*
V.V. Kolomiets[2]*, PhD, Assistant Professor,*
[1] Anatolii Pidhornyi Institute of Power Machines and Systems of the National Academy of Sciences of Ukraine,
2/10, Komunalnykiv Str., Kharkiv, 61046, Ukraine,
e-mail: kuznetsov.boris.i@gmail.com (Corresponding Author)
[2] Educational scientific professional pedagogical Institute of V.N. Karazin Kharkiv National Univesity,
9a, Nosakov Str., Bakhmut, Donetsk Region, 84511, Ukraine,
e-mail: nnppiuipa@ukr.net

Yu.V. Batygin, T.V. Gavrilova, S.O. Shinderuk, E.O. Chaplygin

Analytical relations for fields and currents in magnetic-pulsed «expansion» of tubular conductors of small diameter

Introduction. *This work was initiated by the problems of cardiovascular diseases, which are one of the main causes of mortality of the population of our planet. More than ten years ago, in 2012, approximately 3.7 million people died of acute coronary syndrome worldwide. The fight against such pathologies is carried out with the help of so-called stents, the manufacture of which can be carried out by the method of magnetic pulse «expansion» from hollow metal cylinders. The limited production possibilities of magnetic pulse «expansion» were caused by the minimum cross-sectional size of the inductor-instrument, which can be practically manufactured. Other tools are required to perform this operation.* ***Novelty.*** *A system of magnetic-pulse expansion of thin-walled pipes of small diameter with an inductor that excites an azimuthal electromagnetic field in the case of direct current passing through the processing object and in the absence of its connection in an electric circuit with an inductor is proposed.* ***Purpose.*** *The main analytical dependencies for the characteristics of the electromagnetic processes taking place in the inductor systems for the expansion of cylindrical conductive pipes of small diameter when direct passage of current through the processed object and when it is not connected to an electric circuit with an inductor (insulated billet) is derived.* ***Methods.*** *The solution of the boundary value problem with given boundary conditions was carried out by applying Laplace transforms and integrating Maxwell's equations.* ***Results.*** *Analytical expressions were obtained for the main characteristics of the processes: the intensities of the excited electromagnetic fields and currents in the system depending on the parameters of the studied systems. The analysis of possible technical schemes for solving the given problem indicated the choice of the optimal variant of an effective system of magnetic-pulse «stretching» of thin-walled cylindrical conductors of small diameter.* ***Practical value.*** *Based on the qualitative analysis of the obtained results, recommendations for the practical implementation of the proposed system were formulated. The obtained dependences allow us to give numerical estimates of the effectiveness of excitation of magnetic pressure forces on the object of processing and to choose directions for further improvement of the magnetic pulse technology for solving such problems.* References 23, figures 2.
Key words: **pulsed electromagnetic fields, cylindrical conductors of small diameter, solution of a boundary value problem, Laplace transforms.**

Вступ*. Ця робота була започаткована проблемами серцево-судинних захворювань, які є однією з основних причин смертності населення нашої планети. Вже більш десяти років тому, в 2012 році, від гострого коронарного синдрому в усьому світі померло приблизно 3,7 мільйона людей. Боротьба з такими патологіями ведеться за допомогою так званих стентів, виготовлення яких може здійснюватися методом магнітно-імпульсного «роздачі» порожнистих металевих циліндрів. Обмежені виробничі можливості магнітно-імпульсної «роздачі» обумовлювалися мінімальним поперечним розміром індуктора-інструмента, який практично можна виготовити. Для виконання цієї операції потрібні інші інструменти.* ***Новизна****. Запропоновано систему магнітно-імпульсного розширення тонкостінних труб малого діаметра з індуктором, який збуджує азимутальне електромагнітне поле, при прямому пропусканні струму через об'єкт обробки та при відсутності його підключення у електричне коло з індуктором.* ***Мета****. Одержано аналітичні вирази для основних характеристик процесів: напруженостей збуджуваних електромагнітних полів і струмів у системі в залежності від параметрів досліджуваних систем.* ***Методи****. Розв'язання крайової задачі із заданими граничними умовами проводилось при застосуванні перетворень Лапласа та інтегрування рівнянь Максвела.* ***Результати****. Отримано аналітичні вирази для основних характеристик процесів, що протікають: напруженості збуджуваних електромагнітних полів і струмів у системі. Аналіз можливих технічних схем вирішення поставленої задачі вказав на вибір оптимального варіанту ефективної системи магнітно-імпульсного «роздачі» тонкостінних циліндричних провідників малого діаметра.* ***Практична цінність****. На основі якісного аналізу отриманих результатів сформульовано рекомендації щодо практичного впровадження запропонованої системи. Отримані залежності дозволяють дати чисельні оцінки ефективності збудження сил магнітного тиску на об'єкт обробки та вибрати напрямки подальшого вдосконалення магнітно-імпульсної технології для вирішення таких задач.* Бібл. 23, рис. 2.
Ключові слова: **імпульсні електромагнітні поля, циліндричні провідники малого діаметра, розв'язання крайової задачі, перетворення Лапласа.**

Introduction. The relevance of this work is determined by many factors, but the first and most significant among them is medicine. So, at present, cardiovascular diseases are one of the main causes of mortality of the population of our planet.

For the work of the cardiovascular system, a large amount of oxygen is needed, for the delivery of which the branched system of the coronary arteries is responsible. Pathological changes in the state of blood vessels, and primarily their narrowing, are one of the main causes of impaired oxygen-rich blood supply and invariably lead to the development of serious and even fatal cardiovascular diseases. The fight against these pathologies is carried out by various methods, among which the so-called stenting is particularly effective [1].

Stenting is a medical minimally invasive surgical intervention to install a stent (a special metal frame that is placed in the lumen of hollow organs and vessels) and provides expansion of the area of the cardiovascular system, which was narrowed by the pathological process.

The history of development of stents began in the late 1970s. But only in the early 1990s, the effectiveness of the stenting method was proven to restore the patency of the coronary artery and keep it in a new state [2, 3].

Stents fabrication is a precision and very expensive technology involving the processing of thin-walled tubular metals [4, 5]. Without dwelling on a detailed criticism of the known methods of manufacturing stents, one can point to the possibility of stamping frameworks from hollow cylindrical conductors using Magnetic Pulse Metal Processing (MPMP, in the west terminology this is Electromagnetic Metal Forming, EMF) methods. Such a non-contact production operation, the so-called «expansion», was successfully tested when processing massive tubular billets with large transverse dimensions in the mode of high-frequency act fields [6, 7].

It should be noted that during magnetic pulse processing of tubular parts, all their parameters are set and all factors that can affect the accuracy of part processing are taken into account [8–10].

The tools of the method (as a rule, single-turn or multi-turn solenoids), also, as in the case of flat stamping [11, 12], were located in the zone subject to deformation [13–15].

As for the processing of thin-walled conductors, the most successful was the production operations to eliminate dents in the low-frequency mode of excited fields, which ensured the attraction of specified damaged areas on the sheet metal's surface [16, 17].

Returning to the magnetic-pulse «expansion», it should be noted that its limitations were established by the minimum transverse dimension of the tool that can be practically made [11, 18]. Nevertheless, if we ignore the traditional approaches and methods of implementing the method, then the magnetic-pulse «expansion» of hollow conducting cylinders, even of small diameter, seems feasible. But other tools are needed to perform this operation. Physically, their principle of operation should be based on the interaction of the azimuthal component of the magnetic field strength with the longitudinal current in the billet metal.

The practical implementation of this proposal can be carried out according to two concepts shown in Fig. 1.
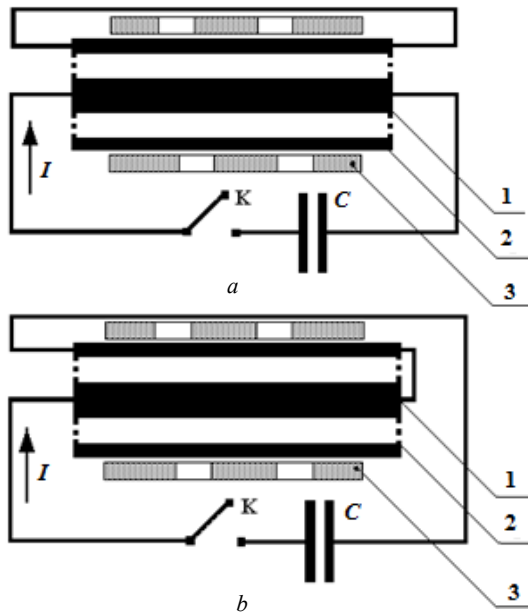

Fig. 1. Principal diagrams of magnetic-pulsed «expansion» of a hollow cylindrical billet: *1* – inductor-current conductor; *2* – tubular billet; *3* – matrix with holes

Problem statement. In the system in Fig. 1,*a*, «expansion» is carried out by the field interaction forces with eddy currents induced in the billet metal.

The difference between this scheme from the analogs known in MPMP is that:

• the source of the magnetic field is a linear conductor, not a solenoid;

• force pressure is excited by the azimuthal rather than the longitudinal component of the magnetic field strength (in traditional designs of inductor systems, the situation is reversed);

• an additional conductor was introduced to ensure the closed circuit for the flow of induced current.

In contrast to the first proposed scheme, the system in Fig. 1,*b* assumes the direct passage of current through the billet. In this case, there must be an electrodynamic interaction between the magnetic field of the current in the inner conductor and the total current (connected and induced) in the billet [19].

A priori, it is obvious that the second scheme is preferable to the first one from the point of view of energy and efficiency of the given technological operation.

The absence of penetration of the magnetic field into the free space through the metal of the processed object is common to the proposed schemes. This means that the force acting on it should be maximal [11, 18, 19].

In fairness, it should be noted that similar technical solutions for the design of magnetic-pulse tools have already been described in the technical literature. Closest to the proposed method (Fig. 1,*b*) is a device for forming pipes of small diameter [20]. This system consists of two electrically conductive pipes isolated from each other and an internal mandrel – a matrix. The discharge current from the capacitor bank is directed through the outer pipe and taken back through the inner pipe. The resulting forces compress it towards the mandrel, which is melted after the operation. As a result, the inner tube takes the required shape of the matrix. Here there is no description of any conditions for the practical performance of the proposed device in the cited publication, although its effectiveness in the case of field penetration through the metal of the inner pipe is doubtful.

It should be noted that from a mathematical point of view, both proposed systems (Fig. 1) require the solution of the same boundary value problem. The features inherent in each of these systems can be taken into account at the final stage of determining the characteristics of the ongoing electromagnetic processes.

In the proposed system with the «direct passage of current», the object of processing is the outer tubular billet. The forces acting on it do not depend on the nature of the ongoing electromagnetic processes and, as already indicated, reach a maximum.

Let us dwell on this design of the inductor system, a characteristic feature of which is the presence of an internal conductor connected in series with an external hollow cylinder. In the terminology familiar to magnetic-pulse processing of metals, we will call the internal current conductor an inductor, a hollow cylinder – a tubular billet to be deformed according to the profile of the matrix. Since we were talking about stents, the holes in the matrix should ensure the punching of the corresponding holes in the tubular billet.

In the future, the proposed system will be called an inductor system for the «expansion» of hollow thin-walled metal cylinders of small diameter with «direct passage of current» through the billet.

The purpose of this work is to derive the main analytical dependencies for the characteristics of the electromagnetic processes taking place in the inductor systems for the expansion of cylindrical conductive pipes of small diameter when direct passage of current through the processed object and when it is not connected to an electric circuit with an inductor (insulated billet).

Fields and currents, analytical dependences. The geometry in the cross-section of the system in Fig. 1,*b*, obtained by a mental cut of a tubular billet with a central internal conductor, is shown in Fig. 2.

Before proceeding to the formulation of the problem, we note the physical feature of the forthcoming consideration. We are talking about the influence of induction effects on the excited fields and currents in the system under consideration. In the simplest approach from the point of view of circuit theory, that is, in the neglect of inductive effects, the magnetic pressure forces are proportional to the square of external currents (from external power sources). But it is obvious that this

assumption significantly distorts the adequacy of the calculations and the characteristics of the processes studied with their help [19]. A priori, we can assume that the fields and currents in the system are always determined by the algebraic sum of external and excited components.
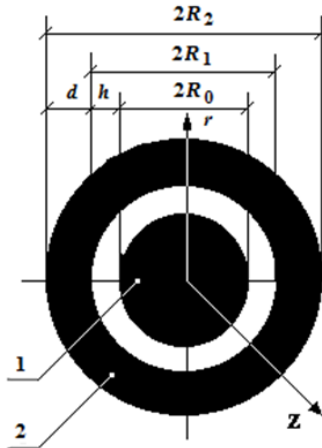

Fig. 2.
Calculation model of the system for magnetic-pulse expansion of a tubular billet of small diameter (cross section Fig. 1,*b*): *1* – central internal conductor; *2* – conductive thin-walled tubular billet

Let us formulate assumptions that establish the level of adequacy of the accepted calculation model and the real inductor system:

• The matrix is made of a dielectric, so there is free space outside the tubular billet.

• A cylindrical coordinate system is acceptable, related to the considered cross-sectional configuration according to Fig. 2.

The system has a sufficiently large length in the longitudinal direction (perpendicular to the plane of the drawing) and azimuth symmetry, so that

$$\partial/\partial\varphi \approx 0.$$

• In the metal of the internal current conductor (this is the inductor) and the external tubular billet $I(t)$ current flows, the time parameters of which are such that the ongoing electromagnetic processes can be considered quasi-stationary and

$$\omega R_{1,2}/c \ll 1,$$

where ω is the cyclic frequency of the acting field; c is the velocity of light in vacuum.

• The billet being processed is rather thin-walled, so that

$$\omega \cdot \tau \ll 1,$$

where $\tau = \mu_0\,\gamma\,d^2$ is the characteristic diffusion time of the field into a conductive layer with specific electrical conductivity γ; $d = R_2 - R_1$ is the thickness of the layer; μ_0 is the magnetic table.

• According to the longitudinal geometry of the system under study (Fig. 1,*b*), the currents in the conductor – the inductor and the tubular billet are equal in magnitude, but oppositely directed.

• An electromagnetic field is being excited with non-zero components $E_z(r, t) \neq 0$ and $H_\varphi(r, t) \neq 0$.

Maxwell's equations for the Laplace-transformed non-trivial components of the electromagnetic field vector in the metal of the processed tubular billet are written in the form [18, 21]:

$$\begin{cases} \dfrac{\partial E_z(r,p)}{\partial r} = p \cdot \mu_0 \cdot H_\varphi(r,p); \\ \dfrac{1}{r} \cdot \dfrac{\partial}{\partial r}\big(r \cdot H_\varphi(r,p)\big) = \gamma \cdot E_z(r,p) + j_z(p,r), \end{cases} \quad (1)$$

where p is parameter of the Laplace transformation; $j_z(p,r)$ is the density of the external current:

$$j_z(p,r) = j(p) \cdot f(r); \quad j(p) \approx \frac{I(p)}{2\pi \cdot R_1 \cdot d},$$

where $f(r)$ is the function of the distribution of the thickness of the pipe.

Within the accepted assumption about its thin walls we have

$$f(r) \approx \begin{cases} 1, & r \in [R_1, R_2]; \\ 0, & r \notin [R_1, R_2]; \end{cases}$$

$$E_z(p, r) = L\{E_z(t, r)\}, \ H_\varphi(p, r) = L\{H_\varphi(t, r)\},$$

where $I(p) = L\{I(t)\}$ are L-images of the electrical and magnetic field intensities, as well the currents in the tubular billet metal.

System (1) is reduced to an inhomogeneous differential equation for the longitudinal component of the electric field [22]:

$$\frac{\partial^2 E_z(p,r)}{\partial r^2} + \frac{1}{r} \cdot \frac{\partial E_z(p,r)}{\partial r} - k^2(p) \cdot E_z(p,r) = \\ = p \cdot \mu_0 \cdot j(p) \cdot f(r), \quad (2)$$

where $k(p) = \sqrt{p \cdot \mu_0 \cdot \gamma}$ is a wave number in the billet metal.

In accordance with the statement of the problem under consideration in the inductor and billet, the currents are equal in magnitude but directed oppositely. From here, the boundary conditions for the excited azimuthal component of the magnetic field intensity will be as follow:

a) on the external side of the tube:

$$H_\varphi(p, r = R_2) = 0; \quad (3)$$

b) on the inner wall of the tube:

$$H_\varphi(p, r = R_1) = \frac{I(p)}{2\pi \cdot R_1}. \quad (4)$$

The general integral of the inhomogeneous equation (2) can be found using the method of variation of arbitrary constants [22, 23]:

$$E(p,r) = C_1(p,r) \cdot I_0(k(p)r) + C_2(p,r) \cdot K_0(k(p)r), \quad (5)$$

where $I_0(k(p)r)$, $K_0(k(p)r)$ are the modified zero-order Bessel functions; $C_{1,2}(p,r)$ are unknown functions involving arbitrary integration constants.

According to the accepted method for variables $r \in [R_1, R_2]$ we write down the system of equations for unknown functions $C_{1,2}(p,r)$ [22]:

$$\begin{cases} \dfrac{dC_1(p,r)}{dr} \cdot I_0(k(p)r) + \dfrac{dC_2(p,r)}{dr} \cdot K_0(k(p)r) = 0, \\ \dfrac{dC_1(p,r)}{dr} \cdot \dfrac{dI_0(k(p)r)}{dr} + \dfrac{dC_2(p,r)}{dr} \cdot \dfrac{dK_0(k(p)r)}{dr} = p\mu_0 j(p). \end{cases} \quad (6)$$

We shall find from the first equation of the differential system (6), that

$$\frac{dC_2(p,r)}{dr} = -\frac{dC_1(p,r)}{dr} \cdot \frac{I_0(k(p)r)}{K_0(k(p)r)}. \quad (7)$$

We substitute expression (7) into the second equation of system (6). After the necessary identical transformations, we obtain, that

$$\frac{dC_1(p,r)}{dr} = p\mu_0 j(p) \cdot r \cdot K_0(k(p)r). \quad (8)$$

Integrating (8), we can find unknown function $C_1(p, r)$:

$$C_1(p,r) = j(p)\sqrt{p\mu_0/\gamma} \cdot r \cdot K_1(k(p)r) + C_1(p), \quad (9)$$

where $K_1(k(p)r)$ is the modified first order Bessel function; $C_1(p)$ is an arbitrary constant of integration.

We substitute the derivative from (8) into expression (7). After integration and identical transformations, we obtain a formula for the second unknown function $C_2(p, r)$:

$$C_2(p,r) = -j(p)\sqrt{p\mu_0/\gamma} \cdot r \cdot I_1(k(p)r) + C_2(p), \quad (10)$$

where $I_1(k(p)r)$ is the modified first order Bessel function; $C_2(p)$ is an arbitrary constant of integration.

Let us substitute dependences (9), (10) into the general integral (5). We get that

$$E_z(p,r) = C_1(p)I_0(k(p)r) + C_2(p)K_0(k(p)r) + \\ + j(p)\sqrt{p\mu_0/\gamma} \cdot r \cdot B_1, \quad (11)$$

where B_1 is defined in the form:

$$B_1 = K_1(k(p)r) \cdot I_0(k(p)r) - I_1(k(p)r) \cdot K_0(k(p)r).$$

The expression for the electric field intensity (11) should be substituted into the first equation of system (1). As a result, we find the magnetic field intensity in the tube metal

$$H_\varphi(p,r) = \sqrt{\gamma/p\mu_0} \cdot B_2 + 2j(p)rK_1(k(p)r) \cdot I_1(k(p)r), \quad (12)$$

where B_2 is defined in the form:

$$B_2 = C_1(p) \cdot I_1(k(p)r) - C_2(p) \cdot K_1(k(p)r).$$

From the given boundary conditions, one can determine unknown arbitrary constants in (12). However, finding them in general requires very cumbersome mathematical transformations. This operation can be somewhat simplified if, according to the accepted formulation of the problem, an additional condition is introduced according to which $|k(p) \cdot R_{1,2}| < 1$ [13, 18].

Actually, this mathematical assumption determines the temporal characteristics of the mode of force impact on the processing object, that is, the frequency range of the active fields.

Let us write down this condition and obtain a quantitative estimate of its fulfillment:

$$|k(p) \cdot R_{1,2}| < 1 \Rightarrow \sqrt{\omega \cdot \mu_0 \cdot \gamma} \cdot R_{1,2} \ll 1$$

and obtain a quantitative estimate of its fulfillment

$$f < \frac{1}{2\pi \cdot \mu_0 \cdot \gamma \cdot R_{1,2}^2}. \quad (13)$$

Thus, inequality (13) determines the range of operating frequencies, the value of which is acceptable in subsequent numerical estimates. It should be noted that, as shown by the authors of the scientific publication [13], at $R_{1,2} \rightarrow d$ (practically corresponds to the ultra-small transverse size of the system), this inequality will simultaneously be the condition for the «transparency» of the processed metal for excited electromagnetic fields.

When (13) is fulfilled, expression (12) takes the form:

$$H_\varphi(p,r) \approx \frac{\gamma \cdot r}{2}\left[C_1(p) - C_2(p)\frac{2}{k^2(p)r^2} \right] + j(p) \cdot r. \quad (14)$$

Now let us determine the unknown constants – $C_{1,2}(p)$.

With help of (3) and (14) we shall find, that

$$C_2(p) = \frac{k^2(p)R_2^2}{2}\left[C_1(p) + \frac{2}{\gamma} \cdot j(p) \right]. \quad (15)$$

We substitute expression (15) into (14), after which we use the second boundary condition from (4). We get:

$$C_1(p) = -\frac{2 \cdot j(p)}{\gamma}\left[1 + \left(\frac{d}{R_1}\right)\frac{1}{(R_2/R_1)^2 - 1} \right]. \quad (16)$$

We substitute formulas (15) and (16) into (14). We obtain an analytical dependence for the strength of the magnetic field excited in the metal of a thin-walled tubular billet

$$H_\varphi(t,r) = I(t) \cdot \frac{r \cdot ((R_2/r)^2 - 1)}{2\pi R_1^2 \cdot ((R_2/R_1)^2 - 1)}. \quad (17)$$

Next, we find the strength of the excited electric field. The fulfillment of constraint (13) allows us to pass in (11) from modified Bessel functions to their representations in the neighborhood of zero [22, 23].

A further estimate of

$$(k(p) \cdot R_{1,2})^2 \ln(k(p) \cdot R_{1,2})\Big|_{(k(p)R_{1,2}) \to 0} \sim (k(p) \cdot R_{1,2})^2$$

sufficiently small of the second order and significantly simplifies the formula (11). In the result obtained, one should introduce expressions for arbitrary constants $C_1(p)$ and $C_2(p)$.

After the transition to the space of originals, we find the strength of the excited electric field [22]:

$$E_z(t,r) \approx -\frac{I(t)}{2\pi R_1 d\gamma}\left[1 + 2\frac{d}{R_1} \cdot \frac{1}{(R_2/R_1)^2 - 1} \right]. \quad (18)$$

Multiplying expression (18) by the electrical conductivity of the metal of the tubular billet, we obtain a formula for the density of the induced current:

$$j_i(t) \approx -\frac{I(t)}{2\pi R_1 d}\left[1 + 2\frac{d}{R_1} \cdot \frac{1}{(R_2/R_1)^2 - 1} \right]. \quad (19)$$

System with «direct passage of current» through the processed billet. Summing up the density of external and induced currents, in accordance with the right side of the second Maxwell equation from the system (1), we find the integral current in the metal of the tubular billet

$$j_s(t) \approx -\frac{I(t)}{\pi R_1^2} \cdot \frac{1}{(R_2/R_1)^2 - 1}. \quad (20)$$

Thus, the obtained expressions (17), (18) and (20) represent the characteristics of electromagnetic processes in the system with «direct passage of current» through the deformation object (Fig. 1,*b*).

A system with a billet that is isolated from inductor.

There is no extraneous current in the tubular billet without its electrical connection to the inductor (Fig. 1,*a*).

With the excited magnetic field – (17) no longer the total, but only the induced signal – formula (19) will interact. In this case, the set of analytical expressions (17) – (19) will already describe electromagnetic processes in a structure with an electrically isolated object of deformation.

A comparative assessment of the effectiveness and efficiency of the proposed systems is interesting from a practical point of view. From this point of view, it is expedient to obtain appropriate ratios.

With the help of expressions (19), (20), we write the formulas for the density of electrodynamic forces (pondermotive forces per unit volume [22]) on the inner surface of the billets in various designs of the proposed systems and the density ratio of the currents excited in them:

$$\begin{cases} f_s = j_s(t) \cdot H_\varphi(t, r = R_1) = j_0^2(t) \cdot d \cdot \left(\frac{R_2 d}{R_1^2}\right) \cdot \frac{1}{(R_2/R_1)^2 - 1}; \\[2mm] f_i = j_i(t) \cdot H_\varphi(t, r = R_1) = j_0^2(t) \cdot d \cdot \left[1 + 2\frac{d}{R_1} \cdot \frac{1}{(R_2/R_1)^2 - 1} \right]; \\[2mm] \dfrac{j_i(t)}{j_s(t)} \approx \dfrac{R_2^2}{2 \cdot d \cdot R_1}, \end{cases} \quad (21)$$

where f_s is the density of electrodynamic forces during the direct passage of current through the processing object;

f_i is the density of electrodynamic forces in the case of an isolated tubular billet; $j_0(t) \approx I(t)/2\pi R_1 d$ is the current density in the billet without taking into account induction effects.

Let us analyze the got results.

• When $r \rightarrow R_1$ the intensity of the excited magnetic field is:

$$H_\varphi \rightarrow \frac{I(t)}{2\pi \cdot R_1},$$

what corresponds to the law of total current and is evidence of the reliability of the formula (17) [21].

• The densities of excited electrodynamic forces depend significantly on the induction effects in both proposed systems ($f_{s,i}$ in (21)).

• The current densities in the treated objects are proportional to the proportionality factor determined by the geometry of each of the proposed systems ($j_{i,s}$ in (21)).

Conclusions.

1. Magnetic pulse systems was proposed for distributing hollow thin-walled metal cylinders of small diameter both with direct current passing through the object of deformation and without connecting the latter to the electric circuit of the inductor.

2. On the basis of a well-founded physical and mathematical model, the main analytical dependencies for the characteristics of electromagnetic processes occurring in the proposed systems were found.

3. The reliability of the found results was shown with the help of boundary transitions.

4. The significant dependence of excited electrodynamic forces on induction effects in both proposed systems was shown.

Conflict of interest. The authors declare no conflict of interest.

REFERENCES

1. Wald D.S., Morris J.K., Wald N.J., Chase A.J., Edwards R.J., Hughes L.O., Berry C., Oldroyd K.G. Randomized Trial of Preventive Angioplasty in Myocardial Infarction. *New England Journal of Medicine*, 2013, vol. 369, no. 12, pp. 1115-1123. doi: https://doi.org/10.1056/NEJMoa1305520.

2. Blero D., Huberty V., Devière J. Novel biliary self-expanding metal stents: indications and applications. *Expert Review of Gastroenterology & Hepatology*, 2015, vol. 9, no. 3, pp. 359-367. doi: https://doi.org/10.1586/17474124.2015.960395.

3. Jang S.I., Lee D.K. Stents with specialized functions: drug-eluting stents and stents with antireflux devices. *Gastrointestinal Intervention*, 2015, vol. 4, no. 1, pp. 50-54. doi: https://doi.org/10.1016/j.gii.2015.03.004.

4. Guerra A.J., Ciurana J. Stent's Manufacturing Field: Past, Present, and Future Prospects. *Angiography*, 2019, 148 p. doi: https://doi.org/10.5772/intechopen.81668.

5. Jiang W., Zhao W., Zhou T., Wang L., Qiu T. A Review on Manufacturing and Post-Processing Technology of Vascular Stents. *Micromachines*, 2022, vol. 13, no. 1, art. no. 140. doi: https://doi.org/10.3390/mi13010140.

6. Qiu L., Li Y., Yu Y., Xiao Y., Su P., Xiong Q., Jiang J., Li L. Numerical and experimental investigation in electromagnetic tube expansion with axial compression. *The International Journal of Advanced Manufacturing Technology*, 2019, vol. 104, no. 5, pp. 3045-3051. doi: https://doi.org/10.1007/s00170-019-04217-9.

7. Qiu L., Zhang W., Abu-Siada A., Liu G., Wang C., Wang Y., Wang B., Li Y., Yu Y. Analysis of Electromagnetic Force and Formability of Tube Electromagnetic Bulging Based on Convex Coil. *IEEE Access*, 2020, vol. 8, pp. 33215-33222. doi: https://doi.org/10.1109/ACCESS.2020.2974758.

8. Belyy I.V., Fertik S.M., Khimenko L.T. *Handbook of magnetic pulse treatment of metals*. Kharkiv, Vyscha Shkola Publ., 1977. 168 p. (Rus).

9. Huei-Huang Lee. *Finite Element Simulations with ANSYS Workbench 2019*. SDC Publications, 2019. 614 p. Available at: https://www.routledge.com/Finite-Element-Simulations-with-ANSYS-Workbench-2019/Lee/p/book/9781630572990 (Accessed 15.08.2019).

10. Lavinsky D.V., Zaitsev Y.I. Computational analysis method of the electromagnetic field propagation and deformation of conductive bodies. *Electrical Engineering & Electromechanics*, 2023, no. 5, pp. 77-82. doi: https://doi.org/10.20998/2074-272X.2023.5.11.

11. Psyk V., Risch D., Kinsey B.L., Tekkaya A.E., Kleiner M. Electromagnetic forming – A review. *Journal of Materials Processing Technology*, 2011, vol. 211, no. 5, pp. 787-829. doi: https://doi.org/10.1016/j.jmatprotec.2010.12.012.

12. Batygin Y.V., Shinderuk S.O., Chaplygin E.O. Mutual influence of currents in plane inductor system with solenoid between two massive conductors. *Electrical Engineering & Electromechanics*, 2021, no. 6, pp. 25-30. doi: https://doi.org/10.20998/2074-272X.2021.6.04.

13. Batygin Y.V., Golovashchenko S.F., Gnatov A.V. Pulsed electromagnetic attraction of sheet metals – Fundamentals and perspective applications. *Journal of Materials Processing Technology*, 2013, vol. 213, no. 3, pp. 444-452. doi: https://doi.org/10.1016/j.jmatprotec.2012.10.003.

14. Qiu L., Yu Y., Xiong Q., Deng C., Cao Q., Han X., Li L. Analysis of Electromagnetic Force and Deformation Behavior in Electromagnetic Tube Expansion With Concave Coil Based on Finite Element Method. *IEEE Transactions on Applied Superconductivity*, 2018, vol. 28, no. 3, pp. 1-5. doi: https://doi.org/10.1109/TASC.2017.2789287.

15. Lavinsky D.V., Zaitsev Y.I. Computational studies of electromagnetic field propagation and deforming of structural elements for a thin-walled curved workpiece and an inductor. *Electrical Engineering & Electromechanics*, 2024, no. 2, pp. 55-60. doi: https://doi.org/10.20998/2074-272X.2024.2.08.

16. Batygin Y.V., Chaplygin E.A., Shinderuk S.A., Strelnikova V.A. Numerical estimates of currents and forces in linear tools of the magnetic-pulse attraction of metals. Part 1: Low electrical conductance metals. *Electrical Engineering & Electromechanics*, 2019, no. 5, pp. 40-44. doi: https://doi.org/10.20998/2074-272X.2019.5.07.

17. Volontsevich D.O., Barbashova M.V., Eremina E.F. Diffusion processes during «crimping» of tubular billets in magnetic-pulse processing of metals. *Scientific Bulletin of Kherson State Maritime Academy*, 2017, no. 2(17), pp. 149-160. (Rus).

18. Batygin Yu.V., Lavinsky V.I. Peculiarities of the magnetic pulsed expansion of the thin-walled tube samples. *Electricity*, 2005, no. 11, pp. 62-68. (Rus).

19. Batygin Y., Shinderuk S., Chaplygin E. Induction Effects In The Flat System «Circular Solenoid - Sheet Metal». *2021 IEEE 2nd KhPI Week on Advanced Technology (KhPIWeek)*, 2021, pp. 185-190. doi: https://doi.org/10.1109/KhPIWeek53812.2021.9570048.

20. Erickson G.F. *Device for forming pipes of small diameter*. Patent Germany, no. 1452934, 1965.

21. Thomson J.J., *Elements of the Mathematical Theory of Electricity and Magnetism*. London, Wentworth Publ., 2016. 560 p.

22. Kantorovich L. *Mathematics for Natural Scientists. Fundamentals and Basics*. Springer Nature Publ., 2018. 526 p.

23. Abramowitz M., Stegun I.A. *Handbook of Mathematical Functions*. Courier Corporation Publ., 1964. 1046 p.

Yu.V. Batygin[1]*, Doctor of Technical Science, Professor,*
T.V. Gavrilova[1]*, PhD, Associate Professor,*
S.O. Shinderuk[1]*, PhD, Associate Professor,*
E.O. Chaplygin[1]*, PhD, Associate Professor,*
[1] Kharkiv National Automobile and Highway University,
25, Yaroslava Mudrogo Str., Kharkiv, 61002, Ukraine.
e-mail: yu.v.batygin@gmail.com (Corresponding Author);
gavrilova.hnadu@gmail.com; s.shinderuk.2016102@ukr.net;
chaplygin.e.a@gmail.com

N.A. Shydlovska, S.M. Zakharchenko, M.F. Zakharchenko, M.A. Kulida, S.A. Zakusilo

Spectral and optic-metric methods of monitoring parameters of plasma channels caused by discharge currents between metals granules in working liquids

*Introduction. Spark-erosion processing of metals and alloys granules in working liquids is the basis of a several technological processes. Efficiency of energy use in them and parameters of the resulting product largely depend on the accuracy of stabilization and regulation of pulse power in each plasma channel between the granules. To achieve this, until now only the voltage and current of the discharge pulses in the entire layer of granules have been controlled. **Problem.** The measurement methods, which are used, are not effective enough for monitoring the parameters of individual plasma channels and predicting the size distribution of eroded metals particles at the stage of their formation. The **aim** of the work is to develop a method for determining the volumes of components of plasma channels in layers of metals granules during their spark-erosion treatment to predict the size distribution of eroded metal particles at the stage of their formation, as well as to simplify the method of spectrometric analysis of the elemental composition of substances surrounding plasma channels for the operational prediction of the chemical composition of resulting products. **Methodology.** A series of experiments were carried out on spark-erosion processing of Al and Ag granules layers in distilled water. Using a digital camera, images of the plasma channels in them were obtained. Based on the theory of pulsed electrical breakdown of liquid dielectrics, an analysis of the components of plasma channels was carried out. Using the specialized ToupView program, the volumes of equivalent ellipsoids of rotation were determined, approximating the halos of colored radiation likely arising from streamers, as well as the spark cores of plasma channels emitting white light. The shades of the resulting radiation were studied for several metals and working liquids. The obtained data were compared with the known results of spectrometric studies for the same elements excited by similar mechanisms. **Results.** The theory of discharge-pulse systems for spark-erosion processing of granular conductive media has been developed in the direction of new methods for monitoring the parameters of discharge pulses and predicting the chemical composition and size distribution parameters of eroded metal particles at the stage of their production. An optic-metric method has been developed for determining the volumes of halos and cores of plasma channels. A simplified spectral method for determining the chemical composition of erosion particles based on the shade of the resulting radiation was proposed. **Originality.** The developed new optic-metric method makes it possible to obtain information about almost every plasma channel, which refines predictions of the size distribution of erosion particles. To implement the method, general-purpose hardware and specialized software that is freely available are used. The developed method of simplified spectral analysis of excited atoms makes it possible to make preliminary predictions of the chemical composition of the obtained erosion particles already at the stage of their formation without the use of expensive specialized equipment. **Practical significance.** The ratio of the volumes of halos and cores of plasma channels between Al and Ag granules in distilled water was measured. An analysis of the emission spectra of plasma channel halos between Al, Ag and Cu granules in distilled water, Fe in ethyl alcohol, Ni-Mn-Ga and Ti-Zr-Ni alloys in liquid nitrogen, and Ti-Zr-Ni in liquid argon was carried out. Based on spectrometry data, the resulting shades of these radiations were substantiated and their description in the RGB system is given. References 56, table 1, figures 4.*
Key words: **discharge current, plasma channels, metal granules, optical emission spectrum.**

Обґрунтовано актуальність та доцільність розроблення та застосування оптичних методів контролю параметрів плазмових каналів у шарах металевих гранул під час їх іскро- та плазмоерозійного оброблення з метою підвищення точності керування процесами і якості продукції, яка отримується. Розроблено оптикометричний метод визначення відношення об'ємів кольорових ореолів, імовірно спричинених стримерами, та іскрових ядер плазмових каналів між гранулами металів у робочій рідині, який не потребує спеціалізованого спектрометричного обладнання, а базується на використанні апаратних засобів загального призначення та спеціалізованого програмного забезпечення, яке є у вільному доступі. Даним методом проведено аналіз відношення об'ємів кольорових ореолів та іскрових ядер плазмових каналів між гранулами Al та Ag у дистильованій воді, що дало додаткову інформацію для прогнозів співвідношення нано- та мікророзмірних фракцій ерозійних частинок металів на етапі їх формування. Проведено аналіз спектрів випромінювання кольорових ореолів плазмових каналів у дистильованій воді між гранулами Al, Ag, Fe та Cu, а також Ni-Mn-Ga та Ti-Zr-Ni у рідкому азоті і Ti-Zr-Ni у рідкому аргоні. Обґрунтовано і узагальнено відтінки результуючого випромінювання у цих випадках та наведено їх опис за RGB-кодами. Обґрунтовано можливість спрощення спектрометричного методу аналізу плазми та оточуючої її парогазової фази у шарах металевих гранул за аналізом відтінку результуючого випромінювання, який базується на отриманих раніше спектрометричних даних. Бібл. 56, табл. 1, рис. 4.
Ключові слова: **розрядний струм, плазмові канали, металеві гранули, оптичний спектр випромінювання.**

The current state of research, definition and relevance of the problem. Spark and plasma erosion processing of layers of metal granules (LMGs) in working liquids with relatively low specific electrical conductivity is the basis of four groups of technological processes. The first one is the production of microdispersed powders of metals and alloys with special properties: refractory and heat-resistant, with magnetic [1] and temperature [2] shape memory, with amorphous [3] and amorphous-crystalline structure [4], with a giant magnetoresistive effect [5], soft-magnetic [6], hydrogen-absorbing [7],

solid [8], corrosion-resistant [9], etc. [10, 11]. The second one is spark plasma or electric discharge sintering under pressure of micro-sized powders of metals and alloys in composites, ceramics and other heterogeneous media [12]. The third one is the production of coagulant-forming hydroxides of metals (*Al* and *Fe*) for purification, including for the needs of thermal power energy industry [13] and disinfection [14] of natural waters and industrial waste water. The fourth one is the production of sedimentation-resistant nanodisperse hydrosols of biologically active metals (*Ag, Cu, Zn, Fe, Mg, Mn, Mo,*

Co) [15, 16] for use in in plant breeding [17] and animal breeding [18].

The process is as follows. As a result of the supply from the generator of discharge pulses of electrical energy to the LMG immersed in the working liquid, a current begins to flow in it. The conditions in the contacts between the granules change rapidly and to some extent stochastically even during one discharge pulse, which leads to the branching and migration of current flow channels in the LMG, the direction of which is determined by the smallest electrical resistance of the circuit, and not by the shortest distance between the electrodes. In LMG, as a rule, there are simultaneously several parallel paths of current flow from one electrode to another.

Under the conditions of low values of the amplitude of the discharge voltage pulses (up to ≈ 40 V), plasma channels between the surfaces of the granules do not appear. In this case, the current between the granules flows through the working liquid, which is characterized by low ionic conductivity, or through ohmic contacts with low resistance between the granules, which happens less often. With a further increase in the amplitude of the voltage pulses between some pairs of granules, first streamer, and later spark channels, begin to form.

A further increase in the voltage of the discharge pulses leads to an increase in the number of both serially and parallel connected plasma channels in the LMG. When the average amplitude of voltage pulses is greater than ≈ 36 V for each consecutively connected contact between granules, plasma channels appear in the direction from electrode to electrode throughout the LMG. In operation modes, the amplitude of voltage pulses usually does not exceed 20 V on average for each contact connected in series. The duration of pulses is from units to tens of microseconds, and the average power during this time is from tens to hundreds of kilowatts.

Depending on a number of conditions [19], part of the streamer channels evolves in the spark, and the rest stops at the pre-spark stages of the streamer or leader [20]. One of the significant differences between streamer-leader channels and spark channels is the orders of magnitude lower energy released in them [20, 21]. As a result, eroded metal particles formed due to the action of streamers or leaders most often have sizes from tens to hundreds of nanometers [16], and those formed as a result of the action of sparks – from units to tens of micrometers [10]. Forced limitation of the evolution of most plasma channels by pre-spark stages with the help of special measures [15, 16, 22] made it possible to create new ones – plasma erosion, based on earlier spark-erosion technologies, in particular, the third and fourth groups. Their energy and material efficiency largely depend on the ratio of streamer-leader and spark channels in LMG.

Until now, in most cases, this ratio was controlled indirectly by measuring the amplitude and duration of the discharge current pulses throughout the LMG [22], which is the sum of all branches of the discharge currents in the gap between the electrodes. But this method does not take into account changes during the discharge pulse of the number of plasma channels in the LMG and the plane of their cross sections, as a result of which it does not provide comprehensive information about the current density in them. Therefore, it is insufficient to control the above ratio. In addition, visual observation of plasma channels by the process operator without the use of special devices is used, but it is subjective and not sufficiently accurate. Therefore, an urgent and important task is the search for objective and sufficiently accurate methods of controlling the ratio of streamer-leader and spark channels in LMG.

The goal of the article is to develop a method of objective optical determination of the volumes of streamer-leader and spark components of plasma channels in LMG during their spark and plasma erosion processing, the ratio of these volumes, as well as to simplify the method of spectrometric research of the elemental composition of the surrounding plasma channel of a steam-gas phase and working liquid and impurities in it for some metals and working liquids by analyzing the resulting shade of radiation. These methods are new in operational control of electrotechnological processes of spark- and plasma-erosion processing of LMG and allow more accurate prediction of the granulometric and chemical composition of erosion particles even at the stage of their production. The development of laws for regulating the distribution of erosion particles by size using the results of the analysis of the specified volumes of plasma channel elements and their ratio as information parameters, and the parameters of discharge pulses as controls, and the creation of automatic regulation systems with their involvement will allow to improve the accuracy of property control in the future erosion particles.

Methodology of experiments, equipment, modes and materials. The objects of research were plasma channels in layers of aluminum and silver granules immersed in distilled water. The experiments were carried out on a laboratory installation for spark and plasma erosion processing of LMG, the functional diagram of which is presented in Fig. 1. The installation included: a thyristor discharge pulse generator (marked DPG). A generator control unit (CU), a discharge chamber (DC) with a LMG immersed in the working liquid (marked DCham), a vibration bench (VB), on which it was located, a C8-17 memory oscilloscope (Osc), a voltage divider 1:10 (Voltage probe, VProbe), a high-frequency measuring current transformer (Current probe, CProbe), a web camera (WCam), connected to a personal computer (PC).

The generator was powered by a single-phase network with voltage of 220 V and frequency of 50 Hz (220V). The network voltage was rectified, regulated and stabilized by a controlled thyristor-diode rectifier (CR) and filtered from the alternating component by capacitor C1.

The operating capacitor C was charged to almost twice the voltage of the filter capacitor C1 at the command of the generator control unit through a charging circuit with Q factor greater than 20, which included

thyristor VS1 and choke L1. The charge voltage of the operating capacitor C, the capacity of which in our experiments was 100 μF, was adjusted by adjusting the voltage on the filter capacitor C1. After the end of the discharge process and closing thyristor VS1 in a natural way, according to the next command of the control unit, discharge thyristor VS2 was opened. The voltage of the operating capacitor through VS2 and the connecting cable with inductance L, which in our experiments was ≈2 μH, was applied to the discharge chamber, where it caused the appearance of plasma channels in the LMG. After the end of the discharge, according to the commands of the control unit, the charge of the next pulse-following cycle began.
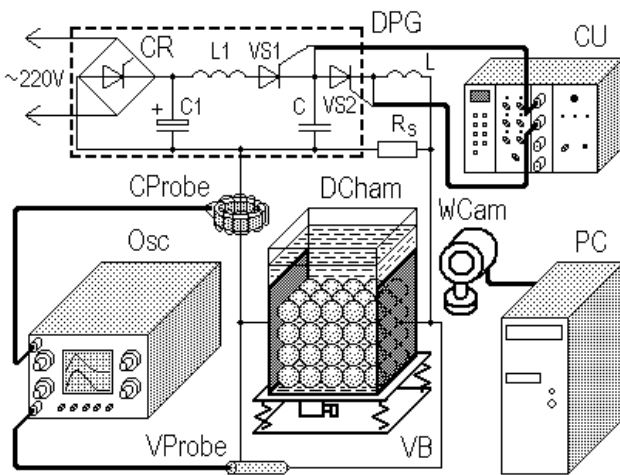

Fig. 1. Functional diagram of the laboratory installation

The discharge current was almost always aperiodic. Oscillating discharges could occur due to the stochastic decrease in the equivalent electrical resistance of the LMG, but they were almost never observed in our experiments. More dangerous for such thyristor generators (Fig. 1) is a stochastic increase in the resistance of the LMG, as a result of which a current flows through it, which slightly exceeds the holding current of the discharge thyristor VS2. If the duration of the discharge process under such conditions exceeds the duration of the pause between the discharge and charge pulses, a situation may arise when the discharge thyristor VS2 has not yet closed, and the charge thyristor VS1 has already opened. That is, a situation may arise when all thyristors will be open for a long time and not only the energy of capacitor C will enter the load, but also almost all the energy of capacitor C1, and in the worst case, even the energy of the power supply network, the current of which will be limited only by the parameters of the choke L1 and the load.

Such modes can cause not only an overload by current of the thyristors of the generator, but also the fusion of metal granules in the DC with each other, which will make their further processing impossible. To prevent these modes, a resistive shunt R_S is connected in parallel with the load in Fig. 1. In our experiments, its resistance was 3 Ω, which ensured an almost complete discharge of the operating capacitor C and the closing of the thyristor VS2 in a natural way before the arrival of the next charging pulse, despite the stochastic increase in the resistance of the LMG. The pulse repetition rate in these experiments was 50 Hz.

In more detail, the operation of laboratory equipment for spark and plasma erosion processing of LMG, on which experiments were carried out with aluminum granules, is described in [23], and with silver granules in [16]. A7E aluminum granules were quasi-spherical in shape with diameter of ≈4 mm, and their surface had previously undergone spark electroerosion treatment. The distance between the vertical aluminum electrodes of the AD0 brand in the discharge chamber No. 1 was 52 mm. The height of the LMG is 30 mm, the width is 22 mm. The flow of water in this case was directed from the bottom up and was ≈12 ml/s, which ensured the stability of the process and removed eroded particles from the active zone of the DC. Forced vibration activation [15] with frequency of ≈90 Hz was applied to the LMG. Since the equivalent electrical resistance of the LMG changes rapidly even during one discharge pulse, and even more so from pulse to pulse [24], the amplitude values of the voltage on the LMG and the current in it, as well as the total duration of the modes of the discharge pulses changed noticeably, and we can only talk about approximate average values of these parameters. For aluminum LMG, they were 220 V, 180 A and 100 μs, respectively.

The pieces of 999 silver were irregularly shaped. They were bitten off with wire cutter from a sheet 3 mm thick so that the size of the sides was from 3 to 7 mm. Their surface was pre-treated by spark erosion. The height of their layer in DC No. 2 with vertical silver electrodes was 6 mm, the width was 120 mm, and the distance between the electrodes was 60 mm. There was no water flow in this series of experiments. The frequency of forced vibration activation of the LMG in this case was ≈40 Hz. The average values of duration of discharge pulses were 30 μs, the voltage amplitude of the pulses was 130 V, and the current was 120 A.

In the absence of complex expensive specialized and not very common optical equipment, such as a monochromator (for example, MDR-2), a photoelectronic multiplier (for example, FEU-106), a high-speed analog-to-digital converter, etc. [25], optical studies were carried out using an ordinary household web camera (WCam in Fig. 1) with mediocre characteristics (matrix 640 by 480 pixels). The images of streamer-leader and spark channel projections obtained with its help were saved on a PC, and then analyzed using the specialized ToupView program of the ToupTek Company [26], which is freely available and designed for working with digital optical cameras of microscopes and telescopes. The program has a wide functionality and, which is important for our research, allows to enlarge the image up to 1600 %, approximate the image of objects with a number of geometric shapes, the parameters of which can be adjusted, as well as measure and calculate their indicators such as area, perimeter, length of axes, etc. [27]. At the time of writing this article, the latest version of the ToupView program 4.11.19728 dated 22.10.2021 has an option to construct ellipses by three points, which is very

convenient and allows to quickly and fairly accurately approximate image elements. The program automatically measures the length of their axes, based on which the values of the volumes of the corresponding ellipsoids of rotation were then calculated, which were used to approximate the areas with colored radiation and spark channels of white color.

Spectral analysis of streamer-leader and spark channels between aluminum granules in water. A photography of the plasma channels between the surfaces of aluminum granules immersed in distilled water in DC No. 1 in the dark (to increase image contrast) is presented in Fig. 2.

As you can see, the vast majority of channels have a white core and a colored halo, in this case, blue-violet. One of the qualitative criteria for distinguishing spark channels from streamers and leaders is the continuous spectrum of their white radiation. This kind of radiation spectrum is caused by high temperature (about 10,000 K) and pressure (about 100 MPa) in spark channels in such processes, as researchers write about [6].
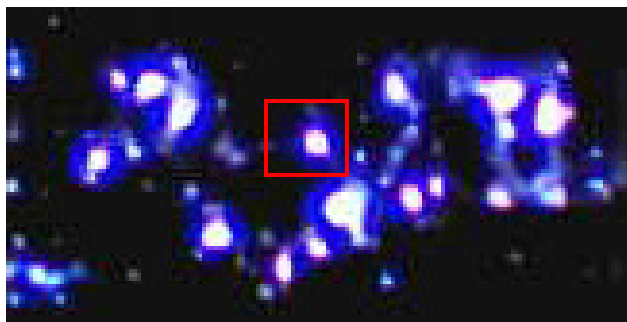

Fig. 2. Plasma channels in the layer of aluminum granules

The temperature of the streamer-leader channels and their pressure are orders of magnitude lower. The main part of their radiation is caused by transitions of electrons in excited atoms to lower orbitals, which causes a linear color spectrum. This makes it possible to carry out a spectral analysis of the chemical composition of excited atoms in and near such channels and to make assumptions about chemical reactions that can occur in such conditions.

The emergence of a halo with colored radiation can occur according to three main mechanisms. According to the first one, the source of excitation of electrons of atoms of the vapor-gas or liquid phase of substances that surround the spark cores can be the ultraviolet radiation of the spark core. That is, the emission of the halo is secondary, induced as a result of higher-energy radiation of the core [28]. The following facts testify in favor of this mechanism: 1) almost all halos have a spark core and almost all spark cores are surrounded by colored halos; 2) in the vast majority of cases, the halos are located around the spark cores quasi-uniformly from all sides.

According to the second mechanism, the excitation of atoms around the spark core is caused by their collisions with fast electrons and ions in streamer-leader avalanches [29]. Even in a homogeneous gas dielectric, streamers and leaders spread along a zigzag path, which ensures the smallest drop in electric voltage across it [30]. This way of expansion of electronic and ion avalanches of

streamers and leaders is all the more characteristic of heterogeneous dielectrics. As long as one of the leaders does not evolve into a spark channel, they can repeatedly appear, change their position in space, and even disappear in a relatively long time (on the order of 30 ms), during which a slow digital household camera captures a frame. Due to the migration and branching of streamers and leaders, the volume they permeate during this time is usually greater than the volume of the spark channel. This mechanism is supported by the fact that there is no strict spatial symmetry of the halo relative to the core.

According to the third mechanism, ionization of atoms occurs in an electric field of high intensity, especially near eroded metal particles in the working liquid, which has a relatively low specific electrical conductivity, and microprotrusions on the surface of metal granules, as occurs in dielectrics near inclusions with higher electrical conductivity [31, 32]. Obviously, this ionization mechanism is primary and can lead to the occurrence of the two discussed above. In our opinion, to one degree or another, all three mechanisms of ionization or excitation of atoms are present in the considered conditions. That is, the second mechanism should occur in a statistically significant number of cases. Then it is logical to assume that the volume and intensity of emission of colored halos are related to the energy that is released specifically in the streamer and leader channels and the distribution of their volumes can be correlated with the size distribution of the nanosized fraction of eroded metal particles.

If the first mechanism of excitation or ionization of atoms prevails, then the volume and intensity of radiation of each colored halo will be proportional to the energy released in the corresponding spark cores. In this case, the ratio of the halo volumes to the core volumes will not change significantly, and only the analysis of the distribution of the spark core volumes will be sufficient to predict the size distribution of the eroded metal particles.

Spectrometric analysis of halo radiation requires appropriate equipment capable of accurately determining the length of all radiation wavelengths, which allows atoms to be identified by their spectral lines, comparing them with reference data [33]. But an approximate spectral analysis based on the resulting shade of the brightest emission lines can also provide certain information about the predominant atoms in the excited state and allows predicting possible chemical reactions involving them.

In the general case, excited electrons of neutral atoms of aluminum (Al) and its ions (Al^+ and Al^{2+}), as well as molecules of its compounds, for example, oxide (Al_2O_3), returning to their orbitals, emit photons in the ultraviolet and visible ranges of the spectrum of electromagnetic waves [33–38]. According to the analysis of scientific publications, the highest intensity of radiation (in order of its decrease in various experiments) is observed for waves of the following lengths: 396.15, 394.4, 308.21, 309.27 and 309.28 nm for Al (in the literature on spectrometry it is designated as $Al\ I$) [34–37], 466.4, 499.8, 484.5, 487, 489, 467, 470, 472, 456, and 474 nm for Al^+ (accepted to be denote as $Al\ II$) [34], 510.5, 508, 512.5, 514.5, 516, 519 and 520.5 nm for

Al_2O_3 (accepted to be denote as *AlO I*) [35] and 451.3 nm for Al^{2+} (accepted to be denote as *Al III*) and 358.7 nm for Al^+ [38].

The objects of emission spectra research and the conditions of the experiments described in the literature were as follows. In [34] – plasma formations that arose in a hydrogen atmosphere with pressure of 13.3 kPa due to the irradiation of an aluminum plate with neodymium laser with power density of 300 GW/cm². In [35] – the flame of combustion in the air flow of aluminum particles with average diameter of 4.2 μm. Plasma channels in strong aqueous electrolytes H_3BO_3 and $Na_2B_4O_7$ [36] and KOH and Na_2SiO_3 [37] in the processes of plasma-electrolytic anodization of aluminum. In [38] – plasma formations that arose as a result of the bombardment of aluminum target with Xe^+ ions with energies of the order of 10 ke·V in a vacuum of 10^{-6} Pa.

Nanoporous Al_2O_3 is capable of luminescent radiation in a relatively wide range of wavelengths, approximately from 380 to 500 nm (at the half-maximum level) [40, 41] due to the action of near-ultraviolet radiation [39] or electric currents of plasma channels in it. This radiation can last several hundreds of microseconds longer than the action of its exciting factor [42].

Electromagnetic radiation with wavelength of approximately 390 to 440 nm is interpreted by the human eye as violet, from 440 to 480 as blue, and from 480 to 510 as cyan [43]. That is, the vast majority of the relaxation radiation of Al, Al^+, Al^{2+} and Al_2O_3 forms light of blue and violet colors and only a small part of it forms blue light, or belongs to the ultraviolet range. Therefore, the halos in Fig. 2 have a blue-violet color, which indirectly indicates the presence of aluminum ions, its atoms and their compounds, primarily oxide and hydroxide, in the plasma channels and in their immediate vicinity. Given the fact that the processes take place in water, the most likely chemical reactions of aluminum hydroxide formation take place [13]:

$$2Al + 6H_2O = 2Al(OH)_3 + 3H_2 \uparrow. \qquad (1)$$
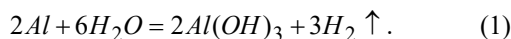
This is possible only under conditions of destruction of the surface oxide film, for example, under the influence of electrical energy. After the formation of aluminum hydroxide according to reaction (1), the processes of further dehydration of a small part of it under the influence of high temperature of plasma channels are possible, according to the reaction:

$$2Al(OH)_3 \xrightarrow{T>575°C} Al_2O_3 + 3H_2O. \qquad (2)$$
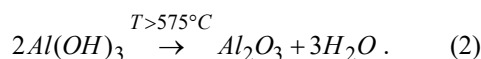
Since in the described processes aluminum hydroxide and oxide are formed according to reactions (1) and (2), ultraviolet radiation from spark cores is also present, the luminescent radiation described in [39–41] also occurs.

Development of a method of optometric analysis of the ratio of the volumes of colored halos and spark channels in LMG. The shape of most plasma channels between two spherical metal electrodes, in the absence of other inhomogeneities, of all known stereometric bodies, the geometric location of surface points of which is easily described analytically, most resembles an ellipsoid [20, 44]. Due to the uniformity of conditions in homogeneous environments, this ellipsoid can be an ellipsoid of rotation around an axis that coincides with the resulting direction of current flow from one electrode to another. Although in LMG the plasma channels between their surfaces do not always have the correct and symmetrical shape, with a certain approximation they can also be represented by ellipsoids of rotation of equivalent volume.

Since the dimensions of the DC are small enough to significantly attenuate the radiation of plasma channels in the working liquid, and the walls of DC No. 1 made of organic glass and DC No. 2 made of polyethylene are thin enough and transparent in the visible part of the spectrum of electromagnetic radiation, it can be assumed that the photographs show full projections both a bright spark core and a dim colored halo around it, presumably caused by streamer-leader channels. To determine the volume of the ellipsoid of rotation V_r, it is enough to know only the length of its semi-axis of rotation o_r and the length of one of the other two equal semi-axes o_p: $V_r = 4\pi o_r o_p^2/3$. This is very appropriate, since in order to determine the length of all three semi-axes of an ellipsoid, in general, it is necessary to have at least two pictures of it synchronized in time in different (preferably orthogonal) projections, which is impossible to do with one camera without additional mirrors or prisms.

The projection of an ellipsoid onto any plane is an ellipse. The camera is located so that the directions of the resulting currents in all vertical layers of granules are in planes parallel to the plane of its image. This creates the conditions for the majority of images of plasma channels to display the axes of ellipsoids of equivalent volume in their natural size without distortion. Since the direction of current flow in the local elements of the LMG is determined not by the shortest geometric distance between the DC's electrodes, but by the smallest electrical resistance of these elements, there is a possibility that it may be located at an angle to the picture plane.

Let us denote the angles between the plane of the image and the semi-axis of rotation of such an ellipsoid α, and between this plane and one of its other two semi-axes β. Then the length of the projections of these semi-axes on the image plane will be $o'_r = o_r \cdot \cos\alpha$ and $o'_p = o_p \cdot \cos\beta$, respectively. The volume of the spark core approximated by such an ellipsoid calculated from the projections of the semi-axes will be $V_S = 4\pi \cdot o'_{rs} \cdot o'_{ps}{}^2/(3 \cdot \cos\alpha \cdot \cos^2\beta)$. If the directions of the corresponding axes of the equivalent ellipsoids of the spark core o_{rs} and o_{ps} and the color halo o_{rl} and o_{pl} coincide, then its volume will be $V_L = 4\pi(o'_{rl} \cdot o'_{pl}{}^2 - o'_{rs} \cdot o'_{ps}{}^2)/(3 \cdot \cos\alpha \cdot \cos^2\beta)$. The ratio of the volumes of the equivalent ellipsoids of the halo and core in this case will be $V_L/V_s = (o'_{rl} \cdot o'_{pl}{}^2)/(o'_{rs} \cdot o'_{ps}{}^2) - 1$. Therefore, if we analyze the ratio of volumes, and not their absolute values, then under the assumptions described above, the angles of inclination of the axes of the ellipsoids of rotation of the equivalent volume to the image plane do not matter. Also in this case, the units of measurement of length (pixels or millimeters) do not matter, and instead of the length of the semi-axes, it is possible to use the length of the axes, since their

coefficients of 0.5 cancel each other, which is convenient for working with the ToupView program, which measures the length of the axes, not the semi-axes of ellipses.

The question of which of the two axes of the elliptic projection is the projection of the axis of rotation of the ellipsoid remains open. If the distance between the electrodes significantly exceeds the size of the irregularities on their surface, then with greater probability, the larger axis is the axis of rotation of the ellipsoid and it is elongated. If the distance between the electrodes is commensurate to the size of the irregularities on their surface, then with a greater probability the smaller axis is the axis of rotation of the ellipsoid and it is flattened. Since the pressure on the granules is lower in the upper part of the LMG, the probability of the appearance of plasma channels increases, the shape of which resembles an elongated ellipsoid of rotation, while in the lower part of the LMG, on the contrary, it is flattened. Therefore, under the described conditions, both options are possible, therefore, one should find appropriate relations for both elongated (index 1) and flattened (index 2) ellipsoids of rotation.

One of the factors that significantly affects the mass and size of eroded metal particles is the energy of individual plasma channels, which is spent on heating, melting, vaporizing, and evacuating the metal from the granule zones that are in direct contact with the plasma channels [13]. In streamer-leader channels, this energy is orders of magnitude lower than in spark channels [20]. Therefore, the mass and size of erosion particles obtained as a result of the action of streamer-leader channels are orders of magnitude smaller than those of particles obtained as a result of the action of spark channels. The volume of channels, their brightness and time of existence are related to the energy released in them. An increase in the volume and brightness of channels leads to an increase the quantity, and in some cases, the size of erosion particles. Therefore, an increase the quantity and size of streamer-leader channels leads to an increase increase the quantity of submicron erosion particles, and a corresponding increase in spark channels leads to an increase increase the quantity of particles with unit sizes of tens of micrometers. Accordingly, the ratio of the volumes of streamer-leader and spark channels affects the ratio of the quantity of submicron erosion particles to erosion particles of larger sizes.

By reducing the size of spark channels, which have a white emission color, it is possible to reduce the quantity, and in some cases, the size of larger erosion particles. However, it should be remembered that the productivity of the process of obtaining them will also decrease. By increasing the size of colored streamer-leader channels, the quantity of small submicron erosion particles can be increased. An increase in the volume ratio of streamer-leader channels to spark channels contributes to an increase in the share of submicron erosion particles.

The energy of individual plasma channels depends on the voltage $u_1(t)$ applied to them, their electrical resistance $r_1(u_1(t))$, which also depends on it, and the time of their existence τ_1 and can be calculated by the formula:

$$E_1 = \int_0^{\tau_1} \left[u_1^2(t) / r_1(u_1(t)) \right] dt . \tag{3}$$

As practice has shown, the voltage of the discharge pulses is the parameter that most affects the size, brightness, and number of spark channels during spark erosion treatment of LMG. Therefore, control of energy (3), brightness and volumes of streamer-leader and spark channels, as well as the ratio of their volumes in these modes occurs, first of all, with the help of the voltage of discharge pulses. Controlling these parameters using the duration of discharge pulses (by changing the capacity of the working capacitor in thyristor generators or the time of the open state of the key in transistor generators) during spark erosion treatment is less effective. In the case of plasma erosion treatment of LMG, the voltage of the discharge pulses is kept as low as possible for the established process and is almost not subject to regulation. Therefore, in this case, a more effective parameter for adjusting the volumes of streamer-leader and spark channels, as well as their ratio, is the duration of discharge pulses.

One of the plasma channels with a size close to the statistical average in Fig. 2 is marked with a red rectangle. This section of the image is shown on a larger scale (800 % in ToupView) in Fig. 3. Approximation of the projection of the spark core in Fig. 3 is represented by a red ellipse and labeled E1. The length of its axes of 6 and 5 pixels (px) is automatically calculated in the ToupView program and presented in Fig. 3. Approximation of the projection of the colored halo in Fig. 3 is represented by a fuchsia ellipse and is labeled E2. The length of its axes is 14 and 12 pixels. Crosses of the corresponding colors in Fig. 3 mark the characteristic points by which the ToupView program built these ellipses.
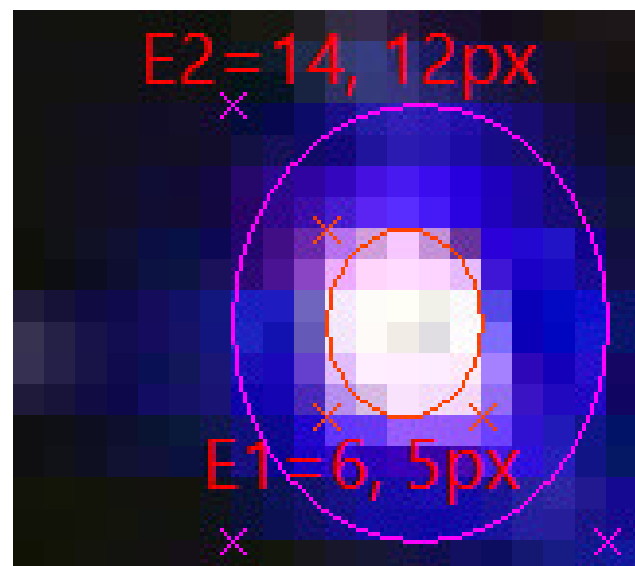

Fig. 3. Plasma channel between aluminum granules

In the hypothesis of elongated ellipsoids, the ratio of the volumes of the halo and core is $V_{L1}/V_{S1} = (14 \cdot 12^2)/(6 \cdot 5^2) - 1 \approx 12.44$, and in the hypothesis

of flattened ellipsoids: $V_{L2}/V_{S2}=(12 \cdot 14^2)/(5 \cdot 6^2)-1 \approx 12.07$. Since, in this particular case, the length of the major and minor axes of each ellipsoid differs slightly, the results obtained in different hypotheses are almost identical. To accurately determine the energy released in the core and halo, it is necessary to know the power density distributions in their volumes, their dependence on time, and the duration of the channels' existence. Such research requires more sophisticated equipment. Here, we can only qualitatively estimate the energy ratio of the colored halo, presumably caused by the streamers, and the spark core, based on the ratio of their volumes and brightness.

A situation is possible when some plasma channels do not have a spark core, but consist entirely of streamer-leader halos, or very bright spark cores have almost no streamer-leader halos. Then it makes sense to determine separately the sums of the volumes of all streamer-leader haloes and spark cores presented in the image, and then find their ratio.

The developed method consists in measuring the volumes of colored halos and spark cores of plasma channels in the LMG by images of their projections and the involvement of specialized software and finding their ratios. The obtained information is used for predictions of size distributions of eroded metal particles, including the ratio of their nano- and micro-sized fractions and correction of their properties during the production process by adjusting the voltage and duration of discharge pulses.

Analysis of parameters of color halos and spark channels between silver granules in water. One of the characteristic plasma channels in the LMG of silver on a scale of 250 % is presented in Fig. 4. Unlike the previous picture, this picture was taken in a lit laboratory, because not only the spark core, but also the colored halo in this case were bright enough and did not need darkness to photograph them. As in the experiments with LMG of aluminum, the projection of the bright spark core in Fig. 4 is approximated by a red ellipse with axis lengths of 22 and 17 pixels, which is labeled E1. Approximation of the projection of the colored halo in Fig. 4 is represented by a fuchsia ellipse with axis lengths of 50 and 45 pixels and labeled E2. Crosses of the corresponding colors mark the characteristic points at which the ToupView program built these ellipses.

In the hypothesis of elongated ellipsoids, the ratio of the volumes of the halo and core in this case is $V_{L1}/V_{S1}=(50 \cdot 45^2)/(22 \cdot 17^2)-1 \approx 14.92$, and in the hypothesis of flattened ones: $V_{L2}/V_{S2}=(45 \cdot 50^2)/(17 \cdot 22^2)-1 \approx 12.67$. In this case, the results obtained under different hypotheses differ from each other a little more than in the previous one, since the differences between the lengths of the axes of the ellipsoids are also larger. The greater the ratio of the volume of the colored halo to the volume of the spark core, the greater the probability of obtaining eroded metal particles of smaller sizes, which in the case of silver increases the biocidal activity of hydrosols based on them [15, 16].
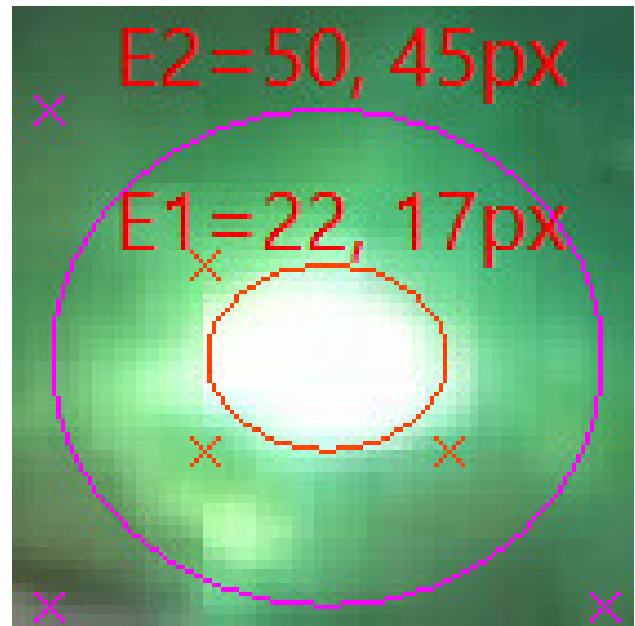

Fig. 4. Plasma channel between silver granules

The halo of the plasma channel between the silver granules is green. Near the white spark core, there is a shade of green mint, and further away from it, an emerald shade, which may be associated with a decrease in the intensity of the white radiation of the core with distance from it. Under the conditions of an underwater spark discharge between Ag granules, the highest radiation intensity of its neutral atoms (accepted to be denote as *Ag I*) is observed at two wavelengths: 546.5 and 520.9 nm (transitions of electrons from the $5d^2D$ levels to the $5p^2P^0$ levels) [45, 46]. The radiation intensity of excited neutral *Ag* atoms is also observed at wavelengths 466.8 and 447.6 nm (transitions from $7s^2S$ to $5p^2P^0$) and at 768.8 and 827.4 nm (transitions from $6s^2S$ to $5p^2P^0$) [45, 46]. There is also a relatively low intensity emission of excited silver ions Ag^+ (denoted *Ag II*) at wavelengths of 540.01 nm (transition from $4d^94f$ to $4d^95d$) and 489.13 nm (transition from $4d^85s^2$ to $4d^95p$) [45].

It is described in [45] that relatively low-intensity radiation with wavelengths of 656.3 nm, which belongs to the first (alpha) transition of the Balmer series in hydrogen atoms (H_α) and 777.42 nm, which belongs to excited neutral oxygen atoms (*O I*) [33]. It is known that molecular oxygen at altitudes from 80 to 150 km under the influence of the solar wind emits a green aurora with wavelength of 557.7 nm [47]. Oxygen molecules are formed on the silver anode as a result of the electrochemical decomposition of water under the action of unipolar discharge pulses [48], since oxygen does not react very actively with silver:

$$2H_2O \xrightarrow{I} 2H_2 \uparrow + O_2 \uparrow. \qquad (4)$$
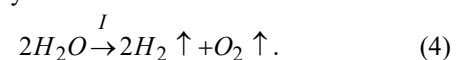
Under the influence of electric currents and radiation of the spark core, electrons in oxygen molecules can move to higher energy levels, and after returning from them – emit photons with the specified wavelength. That is, radiation with wavelength of 557.7 nm can be an indirect indication of the existence or formation of oxygen molecules in plasma channels, for example, as a result of reaction (4).

Electromagnetic radiation with wavelength of approximately 510 to 550 nm is interpreted by the human eye as green, and from 550 to 575 nm as yellow-green [43]. That is, the brightest spectral lines of radiation in the LMG of silver form shades of the resulting green color.

Simplification of the method of spectral estimation of plasma between granules of a number of metals in some working liquids. When the amplitude of the voltage pulses in the aluminum LMG is increased to ≈400 V, the character of the plasma channels between them changes somewhat. First, the linear dimensions of the channels increase by 2–5 times. Secondly, the intensity of light and the specific size of the spark core, which now occupies almost the entire volume of the plasma channel, increase significantly. Thirdly, outside the spark core, sometimes in addition to the blue-violet halo, and sometimes instead of it, a halo strip of pale purple or pale pink hue appears. The probability of its occurrence increases slightly in the case of an increase in the speed of the flow of water directed from the bottom up, which contributes to an increase in the average distance between the surfaces of neighboring granules.

The color of this additional halo is similar to the color of the radiation of excited hydrogen atoms both in the composition of the H_2 gas molecule and in the composition of the H_2O molecule of water vapor, which are formed as a result of heating water by plasma channels. This color is determined by the combination of radiation of the most intense lines of the Balmer series in the visible part of the spectrum with wavelengths of H_α=656.3 nm red, H_β=486.1 nm blue, and violet colors: H_γ=434.1 nm, H_δ=410.2 nm and H_ε=397.0 nm. If the intensity of all these lines is equal, the result will be a pale purple hue, and if the intensity of the H_α line predominates, it will be pale pink.

In our experiments on spark erosion treatment of low-alloy steel LMG both in water and in ethanol [49], under the conditions of voltage pulse amplitude values of more than 300 V, a narrow pale yellow halo was observed with the naked eye around the bright spark core of the plasma channels. The increase in its size and light intensity was caused by an increase in the energy of the pulses, the frequency of their repetition, as well as the flow rate of the working liquid and the intensity of air purging of the LMG, the direction of which was from the bottom up, which contributed to an increase in the average distance between the granules.

Spectral studies of the radiation of plasma channels in water between iron granules showed that the most intense emission lines of neutral *Fe* atoms (denoted *Fe I*) have wavelengths in the range from 560 to 590 nm [46, 50], which corresponds to the yellow color (575–585 nm) and its shades from yellow-green (550–575 nm) to orange (585–620 nm) [43]. The radiation also contains the above-described H_α=656.3 nm and *O I*=777.1 nm lines, and a group of low-intensity lines with wavelengths in the range from 490 to 540 nm, which belong to *Fe I* [45, 50].

In the processes of spark- and plasma-erosion production of copper hydrosols resistant to sedimentation

[15], we observed a narrow, dull strip of halo of malachite-nephrite green color around the spark core of the channel. Spectral studies of the radiation of such channels showed that the highest intensity (in decreasing order) was the emission lines of neutral *Cu* atoms (denoted *Cu I*) with wavelengths of 521.8, 515.3, 510.5, 465.1, 529.3, and 458.6 nm [51], which corresponds to the short-wavelength region of the green color range (510–550 nm) and the blue color range (480–510 nm) [43]. As in the case of plasma channels in water between the granules of some other metals, there are H_α, H_β, *O I*=777.41 nm lines and lines of low intensity *Cu I* radiation: 570.0, 578.2, 793.3 and 809.2 nm [51], whose contribution to the color of the total radiation is insignificant.

When we obtained spark-erosion particles of *Ni-Mn-Ga* alloys with magnetic shape memory [1] and hydrogen-absorbing *Ti-Zr-Ni* alloys [7] in liquid nitrogen, bright and large halos of plasma channels of the resulting blue-blue in color, and in liquid argon of *Ti-Zr-Ni* alloys [7] – violet-blue color of lower brightness. In liquid nitrogen, the lines of the ionized nitrogen molecule N_2^+ (denoted N_2 *II*) with wavelengths of 391.4 and 427.8 nm have the highest radiation intensity [52, 53]. In descending order of radiation intensity, the spectral lines of the neutral nitrogen molecule N_2 (denoted *N2 I*) with wavelengths of 394.3, 575.5, 470.9, 551.6, and 537.3 nm follow [54]. There is also a series of low-intensity spectral lines with wavelengths in the range from 457.4 to 470.9 nm [54], which the human eye interprets as blue [43].

In neutral *Ar* atoms (denoted *Ar I*), lines with wavelengths of 420.07, 415.86, 427.22, 419.83, 425.94, 430.01, 433.36, 426.63, 404.44, 418.19, 394.9, 416.42, 433.53, 434.52 and 425.12 nm have the highest radiation intensity (in descending order) [55]. The radiation of these lines is interpreted by the human eye as a violet color, the wavelength of which is in the range from 390 to 440 nm [43]. In the radiation of argon ions Ar^+ (denoted *Ar II*), in order of decreasing radiation intensity, there are lines with wavelengths of 459.0, 472.7, 440.1, 501.7, 476.5, 461.0, 488.0, 427, 8, 434.8, 480.6, 454.5 nm, etc. [56], which correspond to violet (390–440 nm), blue (440–480 nm), and cyan (480–510 nm) colors [43]. The results of spectral studies are summarized in Table 1.

The first column presents atoms, ions and molecules of chemical elements that were present in the plasma channels and had spectral lines of radiation of noticeable intensity. Their designations adopted in spectrometry are given in parentheses. The second column shows the wavelengths of the five brightest spectral emission lines of these elements. A more complete list of spectral emission lines of these elements is given above. The third column presents the common name of the shade that most closely matches the color of the resulting radiation in the subjective opinion of the authors, as well as the approximate range of wavelengths of radiation of the main colors of this shade.

An approximate view of the shade of radiation is presented in the fourth column. The shade of the resulting radiation is affected by many factors: the brightness of the spark core of the plasma channels and the distance of the

observation point from it, the degree and frequency dependence of radiation absorption by the working liquid and the material of the walls of the discharge chamber, their reflection of external light, its spectrum and brightness, etc. In addition, the appearance of the shade on the monitor screen is also affected by its settings (brightness, contrast, gamma correction, color temperature) and the corresponding graphics card settings. Listed in Table 1 examples are correct for the initial values of the video card settings of the Samsung R508 laptop on which they were reproduced: gamma = 1, brightness = 0, contrast = 50.

Table 1

Results of spectral studies of plasma channels halos radiation

Atom, ion, molecule	The wavelength of the brightest lines λ, nm	Name of the resulting shade of radiation	Approximate appearance of the shade	RGB shade code
Al ($Al\ I$), Al^+ ($Al\ II$), Al^{2+} ($Al\ III$), Al_2O_3 ($AlO\ I$)	396,2, 394,4, 484,5, 466,4, 451,3	Blue-violet (390–480 nm)		R=60, G=0, B=255
Ag ($Ag\ I$), Ag^+ ($Ag\ II$)	546,5, 520,9, 540,0, 489,1	Emerald (510–550 nm)		R=75, G=170, B=90
		Green mint (510–550 nm)		R=150, G=230, B=140
Cu ($Cu\ I$)	521,8, 515,3, 510,5, 465,1, 529,3	Malachite-jade (510–530 nm)		R=30, G=145, B=50
Fe ($Fe\ I$), Fe^+ ($Fe\ II$)	558,6, 557,2, 562,4, 576,3, 591,4	Pale yellow (575–585 nm)		R=255, G=255, B=170
H ($H\ I$)	656,3, 486,1, 434,1, 410,2, 397,0	Pale purple (397–656 nm)		R=220, G=90, B=255
	656,3	Pale pink (656 nm)		R=255, G=195, B=195
N_2 ($N_2\ I$), N_2^+ ($N_2\ II$)	391,4, 427,8, 394,3, 575,5, 470,9, 551,6	Blue-cyan (440–510 nm)		R=100, G=150, B=255
Ar ($Ar\ I$)	420,1, 415,9, 427,2, 459,0, 472,7, 440,1	Violet-blue (390–480 nm)		R=150, G=120, B=255

To increase the objectivity of the reproduction of shades on different devices, their RGB code is given in the fifth column. Values are obtained using Photoshop's eyedropper tool for the most characteristic areas of colored halos in their digital photographs. If the shades of the halos differed significantly when moving away from the spark cores of the plasma channels, as in the case of Ag, or due to a change in the power and conditions in the local plasma channels, as in the case of H, then the fourth and fifth columns present the two most characteristic shades and their RGB codes respectively.

Analysis of the shade of the resulting radiation is much simpler than its spectrometric analysis, which requires expensive and complex highly specialized equipment. The proposed analysis is based on the previously obtained results of the spectrometric analysis of the radiation of excited atoms of specific metals and their surrounding working liquids in conditions close to the modes of their spark and plasma erosion processing.

Generalization and conclusions.

1. An optometric method was developed for determining the volumes of colored halos, presumably caused by streamers, and spark cores of plasma channels between metal granules immersed in the working liquid and their ratio, which does not require specialized spectrometric equipment. The obtained values indicate the energies of streamer-leader and spark channels between metal granules and their ratio, which affect the size distribution of erosion particles, including the ratio of their nano- and micro-sized fractions. Their use is expedient when adjusting the modes of spark- and plasma-erosion electrotechnological processes in order to increase the specific share of erosion particles of the required sizes.

2. In spark erosion technologies, the voltage of the discharge pulses has the greatest influence on the size, brightness and quantity of spark channels, so its use to control these parameters is of primary importance compared to the duration of the discharge pulses. In plasma erosion technologies, the voltage of the discharge pulses is kept as low as possible for the steady-state process and is almost not subject to regulation. Instead, the main adjustment parameter in this case is the duration of discharge pulses.

3. The possibility of simplifying the spectrometric method of analyzing the plasma and its surrounding vapor-gas phase in the LMG based on the analysis of the shade of the resulting radiation, which is based on previously obtained spectrometric data, is substantiated.

4. An analysis of the emission spectra of colored halos of plasma channels in distilled water between Al, Ag, Fe and Cu granules and Ni-Mn-Ga and Ti-Zr-Ni in liquid nitrogen and Ti-Zr-Ni in liquid argon is carried out. The shades of the resulting emission of halos in these cases are substantiated and summarized, and their description by RGB codes is provided.

5. Based on the analysis of the emission spectra of colored halos of plasma channels in distilled water, which are caused by an electric current, it was confirmed that the reactions of hydrogen gas formation, and in the case of silver granules, also oxygen as a result of the electrochemical decomposition of water, took place.

During the spark-erosion dispersion of aluminum granules in water, the occurrence of chemical reactions of the formation of its hydroxide, as well as a small part of the oxide under the influence of high temperatures of the spark channels, was indirectly confirmed.

Conflict of interest. The authors of the article declare that there is no conflict of interest.

REFERENCES

1. Ochin P., Gilchuk A.V., Monastyrsky G.E., Koval Y., Shcherba A.A., Zaharchenko S.N. Martensitic Transformation in Spark Plasma Sintered Compacts of Ni-Mn-Ga Powders Prepared by Spark Erosion Method in Cryogenic Liquids. *Materials Science Forum*, 2013, vol. 738-739, pp. 451-455. doi: https://doi.org/10.4028/www.scientific.net/MSF.738-739.451.
2. Monastyrsky G. Nanoparticles formation mechanisms through the spark erosion of alloys in cryogenic liquids. *Nanoscale Research Letters*, 2015, vol. 10, no. 1, art. no. 503. doi: https://doi.org/10.1186/s11671-015-1212-9.
3. Aur S., Egami T., Berkowitz A.E., Walter J.L. Atomic Structure of Amorphous Particles Produced by Spark Erosion. *Physical Review B*, 1982, vol. 26, no. 12, pp. 6355-6361. doi: https://doi.org/10.1103/PhysRevB.26.6355.
4. Hong J.I., Parker F.T., Solomon V.C., Madras P., Smith D.J., Berkowitz A.E. Fabrication of spherical particles with mixed amorphous/crystalline nanostructured cores and insulating oxide shells. *Journal of Materials Research*, 2008, vol. 23, no. 06, pp. 1758-1763. doi: https://doi.org/10.1557/JMR.2008.0199.
5. Wang W., Zhu F., Weng J., Xiao J., Lai W. Nanoparticle morphology in a granular Cu–Co alloy with giant magnetoresistance. *Applied Physics Letters*, 1998, vol. 72, no. 9, pp. 1118-1120. doi: https://doi.org/10.1063/1.120942.
6. Berkowitz A.E., Hansen M.F., Parker F.T., Vecchio K.S., Spada F.E., Lavernia E.J., Rodriguez R. Amorphous soft magnetic particles produced by spark erosion. *Journal of Magnetism and Magnetic Materials*, 2003, vol. 254-255, pp. 1-6. doi: https://doi.org/10.1016/S0304-8853(02)00932-0.
7. Kolbasov G.Ya., Ustinov A.I., Shcherba A.A., Perekos A.Ye., Danilov M.O., Vyunova N.V., Zakharchenko S.N., Hossbah G. Application of volumetric electric-spark dispersion for the fabrication of Ti-Zr-Ni hydrogen storage alloys. *Journal of Power Sources*, 2005, vol. 150, pp. 276-281. doi: https://doi.org/10.1016/j.jpowsour.2005.02.025.
8. Jin C.H., Si P.Z., Xiao X.F., Feng H., Wu Q., Ge H.L., Zhong M. Structure and magnetic properties of Cr/Cr2O3/CrO2 microspheres prepared by spark erosion and oxidation under high pressure of oxygen. *Materials Letters*, 2013. vol. 92, pp. 213-215. doi: https://doi.org/10.1016/j.matlet.2012.10.126.
9. Harrington T., McElfresh C., Vecchio K.S. Spark erosion as a high-throughput method for producing bimodal nanostructured 316L stainless steel powder. *Powder Technology*, 2018, vol. 328, pp. 156-166. doi: https://doi.org/10.1016/j.powtec.2018.01.012.
10. Berkowitz A.E., Walter J.L. Spark Erosion: A Method for Producing Rapidly Quenched Fine Powders. *Journal of Materials Research*, 1987, no. 2. pp. 277-288. doi: https://doi.org/10.1557/JMR.1987.0277.
11. Carrey J., Radousky H.B., Berkowitz A.E. Spark-eroded particles: influence of processing parameters. *Journal of Applied Physics*, 2004, vol. 95, no. 3, pp. 823-829. doi: https://doi.org/10.1063/1.1635973.

12. Shen B., Inoue A. Fabrication of large-size Fe-based glassy cores with good soft magnetic properties by spark plasma sintering. *Journal of Materials Research*, 2003, vol. 18, no. 9, pp. 2115-2121. doi: https://doi.org/10.1557/jmr.2003.0297.
13. Shydlovska N.A., Zakharchenko S.M., Zakharchenko M.F., Mazurenko I.L., Kulida M.A. Physical and Technical-economic Aspects of Modern Methods of Water Treatment for Thermal and Nuclear Power Engineering. *Technical Electrodynamics*, 2022, no. 4, pp. 69-77. (Ukr). doi: https://doi.org/10.15407/techned2022.04.069.
14. Goncharuk V.V., Shcherba A.A., Zakharchenko S.N., Savluk O.S., Potapchenko N.G., Kosinova V.N. Disinfectant action of the volume electrospark discharges in water. *Khimiia i tehnologiia vody*, 1999, vol. 21, no. 3, pp. 328-336. (Rus).
15. Shcherba A.A., Zakharchenko S.N., Lopatko K.G., Aftandilyants E.G. Application of volume electric spark dispersion for production steady to sedimentation hydrosols of biological active metals. *Pratsi Instytutu Elektrodynamiky Natsionalnoi Akademii Nauk Ukrainy*, 2009, no. 22, pp. 74-79. (Rus).
16. Zakharchenko S.M., Shydlovska N.A., Perekos A.O., Lopatko K.G., Savluk O.S. Features of Obtaining of Plasma-Erosion Nanodispersed Silver Hydrosols and Their Bactericidal and Fungicidal Properties. *Metallofizika i Noveishie Tekhnologii*, 2020, vol. 42, no. 6, pp. 829-851. (Rus). doi: https://doi.org/10.15407/mfint.42.06.0829.
17. Batsmanova L., Taran N., Konotop Ye., Kalenska S., Novytska N. Use of a Colloidal Solutions of Metal and Metal Oxide-Containing Nanoparticles as Fertilizer for Increasing Soybean Productivity. *Journal of Central European Agriculture*, 2020, vol. 21, no. 2, pp. 311-319. doi: https://doi.org/10.5513/JCEA01/21.2.2414.
18. Youssef F.S., El-Banna H.A., Elzorba H.Y., Gabal A.M. Application of Some Nanoparticles in the Field of Veterinary Medicine. *International Journal of Veterinary Science and Medicine*, 2019, vol. 7, no. 1. pp. 78-93. doi: https://doi.org/10.1080/23144599.2019.1691379.
19. Shydlovska N.A., Zakharchenko S.M., Cherkaskyi O.P. Physical Prerequisites of Construction of Mathematical Models of Electric Resistance of Plasma-erosive Loads. *Technical Electrodynamics*, 2017, no 2, pp. 5-12. (Ukr) doi: https://doi.org/10.15407/techned2017.02.005.
20. Raizer Yu.P. *Gas Discharge Physics*. Berlin, Springer, 1991. 449 p.
21. Lo A., Cessou A., Lacour C., Lecordier B., Boubert P., Xu D., Laux C.O., Vervisch P. Streamer-to-spark transition initiated by a nanosecond overvoltage pulsed discharge in air. *Plasma Sources Science and Technology*, 2017, vol. 26, no. 4. art. no. 045012. doi: https://doi.org/10.1088/1361-6595/aa5c78.
22. Shcherba A.A., Zakharchenko S.N., Yatsyuk S.A., Kucheryavaya I.N., Lopatko K.G., Aftandilyants E.G. Analysis of the Methods of Increasing the Efficiency of Electric-erosive Coagulation During Cleaning of Aqueous Media. *Technical Electrodynamics. Thematic Issue «Power Electronics and Energy Efficiency»*, 2008, part 2, pp. 120-125. (Rus).
23. Shcherba A.A., Zakharchenko S.N., Suprunovskaya N.I., Shevchenko N.I. The influence of repetition rate of discharge pulses on electrical resistance of current-conducting granular layer during its electric-spark treatment. *Technical Electrodynamics*, 2006, no. 2, pp. 10-14.
24. Shcherba A.A., Suprunovska N.I., Ivashchenko D.S. Determination of Probabilistic Properties of Electrical Characteristics of Circuits of Electric Discharge Installations Taking into Account their Stochastically Changing Parameters. *Technical Electrodynamics*, 2019, no. 4, pp. 3-11. (Rus). doi: https://doi.org/10.15407/techned2019.04.003.

25. Shuaibov O.K., Malinina A.O., Hrytsak R.V., Malinin O.M., Bilak Yu.Yu., Gomoki Z.T., Vatrala M.I. Characteristics and Parameters of Overstressed Nanosecond Discharge Plasma Between Copper Electrodes in Argon. *Metallofizika i Noveishie Tekhnologii*, 2021, vol. 43, no. 12. pp. 1683-1706. (Ukr). doi: https://doi.org/10.15407/mfint.43.12.1683.

26. *ToupTek. Download.* Available at: https://www.touptek.com/download (Accessed 15 March 2023).

27. *ToupTek. Download. Software Download. Help files for ToupCam camera.* Available at: http://www.touptek.com/download/showdownload.php?lang=en&id=7 (Accessed 15 March 2023).

28. Medvedev N., Zastrau U., Forster E., Gericke D.O., Rethfeld B. Short-Time Electron Dynamics in Aluminum Excited by Femtosecond Extreme Ultraviolet Radiation. *Physical Review Letters*, 2011, vol. 107, art. no. 165003. doi: https://doi.org/10.1103/PhysRevLett.107.165003.

29. Kim S.J., Lee Y.S., Cho Ch.H., Choi M.S., Seong I.H., Lee J.J., Kim D.W., You Sh.J. Observation of prior light emission before arcing development in a low-temperature plasma with multiple snapshot analysis. *Scientific Reports*, 2022, no. 12, art. no. 20976. doi: https://doi.org/10.1038/s41598-022-25550-2.

30. Baranov M.I. A generalized physical principle of development of plasma channel of a high-voltage pulse spark discharge in a dielectric. *Electrical Engineering & Electromechanics*, 2024, no. 1, pp. 34-42. doi: https://doi.org/10.20998/2074-272X.2024.1.05.

31. Shcherba A.A., Shcherba M.A., Peretyatko Ju.V. Electro-Physical Processes of Degradation of Cross-Linked Polyethylene Insulation of Power Cables and Self-Carrying Insulated Wires under Non-Sinusoidal Voltages and Currents. *Technical Electrodynamics*, 2023, no. 1. pp. 3-6. (Ukr). doi: https://doi.org/10.15407/techned2023.01.03.

32. Bereka V.O., Bozhko I.V., Kondratenko I.P. Influence of Parameters of Water Movement at its Treatments on Energy Efficiency Pulse Barrier Discharge. *Technical Electrodynamics*, 2022, no. 3, pp. 62-68. (Ukr). doi: https://doi.org/10.15407/techned2022.03.062.

33. Zaidel' A.N., Prokof'ev V.K., Raiskii S.M., Slavnyi V.A., Shreider E.Ya. *Tables of Spectral Lines.* New York, Springer, 1970. 782 p. doi: https://doi.org/10.1007/978-1-4757-1601-6.

34. Parigger C.G., Hornkohl J.O., Nemes L. Measurements of aluminum and hydrogen microplasma. *Applied Optics*, 2007, vol. 46, no. 19, pp. 4026-4031. doi: https://doi.org/10.1364/AO.46.004026.

35. Soo M., Goroshin S., Glumac N., Kumashiro K., Vickery J., Frost D.L., Bergthorson J.M. Emission and Laser Absorption Spectroscopy of Flat Flames in Aluminum Suspensions. *Combustion and Flame*, 2017, vol. 180, pp. 230-238. doi: https://doi.org/10.1016/j.combustflame.2017.03.006.

36. Sarvan M., Radić-Perić J., Kasalica B., Belča I., Stojadinović S., Perić M. Investigation of Long-duration Plasma Electrolytic Oxidation of Aluminum by Means of Optical Spectroscopy. *Surface & Coatings Technology*, 2014, vol. 254, pp. 270-276. doi: https://doi.org/10.1016/j.surfcoat.2014.06.029.

37. Liu R., Wu J., Xue W., Qu Ya., Yang Ch., Wang B., Wu X. Discharge Behaviors During Plasma Electrolytic Oxidation on Aluminum Alloy. *Materials Chemistry and Physics*, 2014, vol. 148, no. 1-2, pp. 284-292. doi: https://doi.org/10.1016/j.matchemphys.2014.07.045.

38. Qayyum A., Akhtar M.N., Riffat T. Light Emission from Sputtered Aluminum Atoms and Ions Produced by Ion Bombardment. *Radiation Physics and Chemistry*, 2005, vol. 72, no. 6, pp. 663-667. doi: https://doi.org/10.1016/j.radphyschem.2004.05.048.

39. Stojadinovic S., Vasilic R., Petkovic M., Nedic Z., Kasalica B., Belca I., Zekovic Lj. Luminescence properties of oxide films formed by anodization of aluminum in 12-tungstophosphoric acid. *Electrochimica Acta*, 2010, vol. 55, no. 12, pp. 3857-3863. doi: https://doi.org/10.1016/j.electacta.2010.02.011.

40. Staninski K., Piskuła Z., Kaczmarek M. Photo- and electroluminescence properties of lanthanide tungstatedoped porous anodic aluminum oxide. *Optical Materials*, 2017, vol. 64, pp. 142-146. doi: https://doi.org/10.1016/j.optmat.2016.12.003.

41. Stepniowski W.J., Norek M., Michalska-Domanska M., Bombalska A., Nowak-Stepniowska A., Kwasny M., Bojar Z. Fabrication of Anodic Aluminum Oxide with Incorporated Chromate Ions. *Applied Surface Science*, 2012, vol. 259, pp. 324-330. doi: https://doi.org/10.1016/j.apsusc.2012.07.043.

42. Shcherba A.A, Shtompel I.V. Analysis electrical parameters and dynamics of spark discharges in a layer of current-conducting granules. *Stabilizatsiia parametrov elektricheskoi energii*, 1991, pp. 65-74. (Rus).

43. *Abcibc.com. Light wavelengths.* Available at: http://abcibc.com/photo-reference-tables.php?art=19 (Accessed 15 March 2023). (Rus).

44. Nijdam S., Teunissen J., Ebert U. The physics of streamer discharge phenomena. *Plasma Sources Science and Technology*, 2020, vol. 29, no. 10, art. no. 103001. doi: https://doi.org/10.1088/1361-6595/abaa05.

45. Ninyovskij V., Murmantsev A., Veklich A., Boretskij V. Plasma spectroscopy of electric spark discharge between silver granules immersed in water. *Energetika*, 2022, vol. 68, no. 1, pp. 107-114. doi: https://doi.org/10.6001/energetika.v68i1.4862.

46. Veklich A., Tmenova T., Zazimko O., Trach V., Lopatko K., Titova L., Boretskij V., Aftandiliants Ye., Lopatko S., Rogovskiy I. Regulation of Biological Processes with Complexions of Metals Produced by Underwater Spark Discharge. *Nanooptics and Photonics, Nanochemistry and Nanobiotechnology and Their Applications: Selected Proceedings of the 7th International Conference Nanotechnology and Nanomaterials (NANO2019),* pp. 283-306. doi: https://doi.org/10.1007/978-3-030-52268-1_23.

47. *Aurora.* Available at: https://en.wikipedia.org/wiki/Aurora (Accessed 15 March 2023).

48. Shydlovska N.A., Zakharchenko S.M., Cherkassky O.P. The Analysis of Electromagnetic Processes in Output Circuit of the Generator of Discharge Pulses with Non-linear Model of Plasma-erosive Load at Change Their Parameters in Wide Ranges. *Technical Electrodynamics*, 2016, no. 1. pp. 87-95. (Rus). doi: https://doi.org/10.15407/techned2016.01.087.

49. Zakharchenko S.M., Perekos A.O., Shydlovska N.A., Ustinov A.I., Boytsov O.F., Voynash V.Z. Electrospark Dispersion of Metal Materials. I. Influence of Velocity of Flow of Operating Fluid on Dispersity of Powders. *Metallofizika i Noveishie Tekhnologii*, 2018, vol. 40, no. 3, pp. 339-357 (Rus). doi: https://doi.org/10.15407/mfint.40.03.0339.

50. Murmantsev A., Veklich A., Boretskij V. Optical emission spectroscopy of plasma of electric spark discharge between metal granules in liquid. *Applied Nanoscience*, 2023, vol. 13, no. 7, pp. 5231-5237. doi: https://doi.org/10.1007/s13204-022-02744-8.

51. Tmenova T.A., Veklich A.N., Boretskij V.F., Cressault Y., Valensi F., Lopatko K.G., Aftandilyants Y.G. Optical Emission Spectroscopy of Plasma Underwater Electric Spark Discharges Between Metal Granules. *Problems of Atomic Science and Technology*, 2017, vol. 107, no. 1, pp. 132-135.

52. Li S.-Y., Li S.-C., Sui L.-Z., Jiang Y.-F., Chen A.-M., Jin M.-X. Contribution of nitrogen atoms and ions to the

luminescence emission during femotosecond filamentation in air. *Physical Review A*, 2016, vol. 93, no. 1, art. no. 013405. doi: https://doi.org/10.1103/PhysRevA.93.013405.

53. Lianzhu Z., Shuxia Z., Xiulan M. Characterization of Nitrogen Glow Discharge Plasma via Optical Emission Spectrum Simulation. *Plasma Science and Technology*, 2008, vol. 10, no. 4, pp. 455-462. doi: https://doi.org/10.1088/1009-0630/10/4/11.

54. Wang Z., Cohen S.A., Ruzic D.N., Goeckner M.J. Nitrogen atom energy distributions in a hollow-cathode planar sputtering magnetron. *Physical Review E*, 2000, vol. 61, no. 2, pp. 1904-1911. doi: https://doi.org/10.1103/PhysRevE.61.1904.

55. Bogaerts A., Gijbels R., Vlcek J. Modeling of glow discharge optical emission spectrometry: Calculation of the argon atomic optical emission spectrum. *Spectrochimica Acta Part B: Atomic Spectroscopy*, 1998, vol. 53, no. 11, pp. 1517-1526. doi: https://doi.org/10.1016/S0584-8547(98)00139-6.

56. Saloman E.B. Energy Levels and Observed Spectral Lines of Ionized Argon, Ar II through Ar XVIII. *Journal of Physical and Chemical Reference Data*, 2010, vol. 39, no. 3, art. no. 033101. doi: https://doi.org/10.1063/1.3337661.

N.A. Shydlovska[1]*, Corresponding Member of NAS of Ukraine, Doctor of Technical Science, Chief Research Scientist,*
S.M. Zakharchenko[1]*, Doctor of Technical Science, Leading Research Scientist,*
M.F. Zakharchenko[2]*, Candidate of Chemical Sciences,*
M.A. Kulida[3]*, Candidate of Veterinary Sciences,*
S.A. Zakusilo[1]*, Postgraduate Student,*
[1] Institute of Electrodynamics
of the National Academy of Sciences of Ukraine,
56, Prospect Beresteiskyi, Kyiv, 03057, Ukraine,
e-mail: snzakhar@ukr.net (Corresponding Author)
[2] V.I. Vernadsky Institute of General and Inorganic Chemistry
of the National Academy of Sciences of Ukraine,
32/34, Prospect Palladina, Kyiv, 03142, Ukraine.
[3] National University of Life and Environmental Sciences of Ukraine,
16, Vystavkova Str., Kyiv, 03041, Ukraine.

M. Si Ahmed, Y. Guettef, A. Mokaddem, A. Mokhefi, A. Hamid, P. Spiteri, F.Z. Medjaoui

Design optimization for enhancing performances of integrated planar inductor for power electronics applications

*Goal. In this work, the performance of an integrated planar inductor with a square geometric shape using different materials for the substrate: Ni-Fe, Mn-Zn and Ni-Zn have been analyzed and investigated in order to assess the impact of the substrate material on the performance of the integrated planar inductor and to determine the optimal material in the various applications of power modules in power electronics. **Methods**. To this end, we carried out an in-depth analysis of the geometric dimensions of the integrated planar inductor, by calculating all the geometric parameters of the proposed structure, to establish an equivalent physical model of the integrated planar inductor in order to evaluate its different electrical specifications. The numerical simulation, based on the three-dimensional mathematical model of the system using Maxwell's equations, was realized by COMSOL Multiphysics software. **Results** show the importance of the substrate material for the performance of the integrated planar inductor, and specify that the use of Ni-Fe ferrite as a substrate of the integrated planar inductor gives very interesting performance compared to other materials studied. The presented results provide valuable information on the influence of substrate material on the performance of embedded integrated planar inductor and can help to design and optimize these components for use in power electronic systems. **Practical value**. These results are significant for a wide range of applications, where the integrated planar inductor performance and efficiency can have a significant impact on the overall performance and cost-effectiveness of the power electronic device. References 37, tables 2, figures 7.*
Key words: **integrated square micro-coil, electrical characteristics, thermal modeling, electromagnetic phenomena, substrate material.**

*Мета. У цій роботі проаналізовано та досліджено характеристики вбудованого планарного індуктора квадратної геометричної форми з використанням різних матеріалів підкладки: Ni-Fe, Mn-Zn та Ni-Zn для оцінки впливу матеріалу підкладки на продуктивність вбудованого планарного індуктора та визначення оптимального матеріалу для різних силових застосувань модулів у силовій електроніці. **Методи**. З цією метою проведено поглиблений аналіз геометричних розмірів вбудованого планарного індуктора, розраховано всі геометричні параметри запропонованої конструкції для встановлення еквівалентної фізичної моделі вбудованого планарного індуктора та оцінки його електричних характеристик. Чисельне моделювання, що базується на тривимірній математичній моделі системи з використанням рівнянь Максвелла, було реалізовано за допомогою COMSOL Multiphysics. **Результати** показують важливість матеріалу підкладки для роботи вбудованого планарного індуктора і вказують на те, що використання фериту Ni-Fe у якості підкладки вбудованого планарного індуктора дає дуже цікаві характеристики порівняно з іншими вивченими матеріалами. Представлені результати надають важливу інформацію щодо впливу матеріалу підкладки на характеристики вбудованого планарного індуктора та можуть допомогти спроєктувати та оптимізувати дані компоненти для використання у силових електронних системах. **Практична цінність**. Отримані результати важливі для широкого спектра застосувань, де продуктивність та ефективність вбудованого планарного індуктора можуть істотно вплинути на загальну продуктивність та економічну ефективність силового електронного пристрою. Бібл. 37, табл. 2, рис. 7.*
Ключові слова: **вбудована квадратна мікрокотушка, електричні характеристики, теплове моделювання, електромагнітні явища, матеріал підкладки.**

1. Introduction. The advantages of integrating passive components, in particular integrated planar inductor, in power electronics are multiple and numerous, namely: improved performance and better profitability in a wide range of power electronics applications, including static converters and power systems. The low weight and small size of integrated planar inductor make them particularly suitable for use in compact and lightweight power electronics converters where they can reduce the overall size and weight of the device while improving its performance [1–4]. The integration of planar inductors makes it possible to add other functions on a single chip, more efficient designs and simplifying the manufacturing process [5, 6]. To this end, researchers are exploring various approaches to optimize the design and performance of integrated planar inductor, including the use of new materials, new advanced manufacturing techniques and innovative design methodologies [7]. These efforts allow the adoption of integrated planar inductor in complex power electronic systems, and further improve the efficiency, performance and profitability of the systems produced [8].

The integrated planar inductor is particularly used in low-power converters operating at high frequencies [9, 10]. Where they can be used to transform and transfer electrical energy efficiently with low losses. The choice of substrate material is an important factor in the design

and optimization of integrated planar inductors [11, 12], as different materials can exhibit different electrical, magnetic and mechanical properties which can impact on the performance of the integrated planar inductor in terms of efficiency, stability and response time [13–16]. The best choice of the substrate material and its optimal parameters for the design of low-power converters is a crucial factor in order to improve the energy efficiency and the performance of the designed systems [17–23], the integrated planar inductor must be able to transfer energy with high efficiency and low losses, while preserving good stability and an ideal response time [19–26].

The experimental and numerical studies during the design phase of electronic equipment allow the understanding of the magneto-thermal behavior of its equipment and the optimization of their designs and guarantee of their performance and safety. In order to realize the circuits and electronic components with improved performance, it is essential to know all the electrical and thermal properties, which help to predict and understand the local temperature conditions and optimize the design of its components [27, 28]. In this context, the several methods have been used to study the electrical and thermal properties of electronic devices, for example, the finite-element method has been used to numerically study the thermal behavior of a circular-coil

inductor integrated in a micro DC-DC step-down converter [29–35]. In [32] investigated the temperature-dependent characteristics of cryogenic planar multilayer inductors. The autors [6, 32] predicted by numerical simulation the thermal-magnetic behavior of a square planar coil placed between two magnetic materials. In [34], the authors conducted a theoretical study on the design of an octagonal planar inductor and transformer for use in a converter, with the aim of improving the performance and efficiency of the conversion system. Overall, these research efforts have contributed to a better understanding of the electrical and thermal behavior of electronic equipment and have enabled the development of more efficient and better performing devices.

Goal. The work aim is to investigate, analyze and compare the performance of an integrated planar inductor with a planar topology of square geometric shape using three different materials for the substrate: Ni-Fe, Mn-Zn and Ni-Zn, in order to evaluate the impact of the best substrate material on the performance of the integrated planar inductor and identify the best performing material in terms of increasing the efficiency, stability and response time of the integrated planar inductor as well as their optimal design parameters in order to obtain the best performance of the integrated planar inductor.

The results of this study will undoubtedly provide useful information to experimenters on the influence of substrate material, the performances of the integrated planar inductor and present the design and optimization of these components for use in a wide range of specific power electronics applications.

It should be noted that the various numerical models proposed by the researchers often assume a stable state of the ambient air and tend to focus on the electrical and magnetic aspects of the passive components. Our main contribution is to provide a new thermal model that takes into account the real effects of buoyancy on the thermal behavior of a square integrated planar inductor using COMSOL software [36, 37]. Additionally, this study includes the effect of coil conductor width on electromagnetic and thermal properties by mathematically coupled the Navier-Stokes momentum and Maxwell's electromagnetism equations.

The current state of research in the field of integrated planar inductors for power electronics applications mostly ignores the effects of air motion and buoyancy on thermal behavior. The numerical models proposed by researchers often assume a stable state of the surrounding air and tend to focus on the electrical and magnetic aspects of passive components. The aim of this study is to provide a new thermal model that takes into account the real effects of buoyancy on the thermal behavior of a planar micro-coil. Additionally, this study investigates the effect of the width of the coil conductor on the electromagnetic and thermal properties. This research aims to offer a more realistic view of thermal phenomenon in electrical equipment by mathematically coupling of Navier-Stokes momentum equations and Maxwell's electromagnetism.

2. Development of a physical model for the micro-coil.
2.1. Defining the study area. Micro-coil Modeling.
The current study focuses on the examination of a planar micro inductor with a square spiral shape, the performance of a planar inductor depends on its geometric parameters such as the number of turns (n), inner diameter (d_{in}), outer diameter (d_{out}), initial width (w_i), final width (w), thickness (t), and total length (L_t). This micro-coil is placed on a ferrite substrate that also has a square shape with a side length of L and thickness of t_{sub}. Additionally, the micro-coil is elevated by a height of H.

2.2. Determining the geometric parameters of inductors for calculation. In order to optimize the geometric characteristics of an inductor, to improve its performance, the several methods and mathematical models have been used for this purpose. Among these methods, the calculation method developed by Wheeler [14] makes it possible to evaluate the inductance for coils of hexagonal, octagonal or square shapes, which are built using discrete methods. This theoretical model is easy to implement, thanks to its accuracy compared to other methods and will always remain valid even for coils with a limited number of turns. The geometrical parameters of the micro-coil and the substrate are detailed in Fig. 1, and the specific values used in this investigation are listed in Table 1.
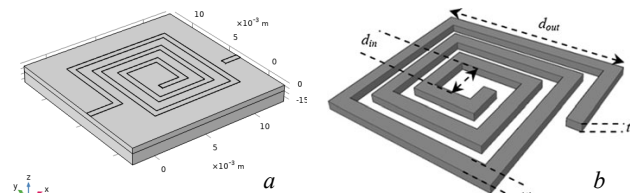

Fig. 1. Study area of the micro-coil deposited on substrate (*a*) geometrical parameters of the micro-inductor (*b*)

Table 1

The recommended parameters

Inner diameter d_{in}, mm	3	Spires thickness t, μm	35
Outer diameter d_{out}, mm	10	Spires number n	3
Spires width w, mm	0.55	Turn spacing s, μm	925

From a specification, we will size, using Wheeler's modified method, the square spiral coil, in order to minimize losses [35]. Additionally, the physical and electrical parameters of the different materials involved in Fig. 2 [3] including air, copper and ferrite are also given in Table 2.
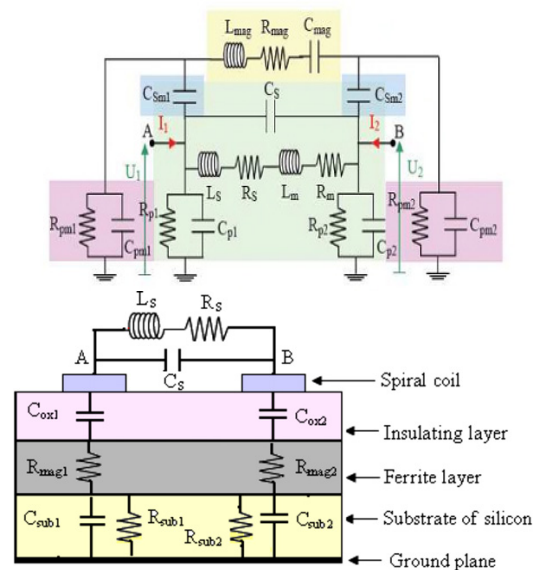

Fig. 2. The ferromagnetic inductor (*a*) and cross-section of planar inductor on ferrite (*b*)

The physical and electrical parameters of different components

Properties	Air	Copper	Ni-Fe (sub1)	Mn-Zn (sub2)	Ni-Zn (sub3)
Density γ, kg/m^3	1.225	8700	4000	4700	4800
Viscosity η, Pa·s	$1.8 \cdot 10^{-5}$	–	–	–	–
Thermal conductivity k, W·m^{-1}·K^{-1}	0.0257	400	30	3.9	6.3
Heat capacity C, J·kg^{-1}·K^{-1}	1005.4	385	700	1050	710
Electrical resistivity ρ, Ω·m	$1.3 \cdot 10^{16}$	$1.75 \cdot 10^8$	–	–	–
Relative permittivity ε_r	1.0	1.0	11.8	270	12
Relative permeability μ_r	1.0	1.0	800	5000	1500
Thermal expansion α, K^{-1}·10^{-3}	3.43	–	–	–	–

3. Mathematical formulation of the problem.

3.1. Basic mathematical equations. The inductance L given by Wheeler method is represented by:

$$L = k_1 \cdot \mu_0 \cdot \frac{n^2 \cdot d_{avg}}{1 + k_2 \cdot A_m}, \tag{1}$$

where d_{avg} is the average diameter; A_m is the form factor; n is the number of turns; μ_0 is the vacuum permeability.

By using the Wheeler method for the square shape, the coefficients $k_1 = 2.34$, $k_2 = 2.75$. So we have:

$$d_{avg} = (d_{out} + d_{in}) / 2; \tag{2}$$
$$A_m = (d_{out} - d_{in}) / (d_{out} + d_{in}). \tag{3}$$

Based on the form factor A_m, we have the option to create either hollow or full inductors. Consequently, the hollow inductor exhibits higher inductance than a full one due to the turns situated near the center of the spiral, which help to reduce the positive mutual inductances and increase the negative mutual inductances [12].

The electric current i flowing through the conductors is dependent on both the current density J_{avg} and the cross-sectional area S_c of the conductor:

$$i = S_c \cdot J_{avg}. \tag{4}$$

The cross-sectional area is determined by the width w and the thickness t of the planar coil:

$$S_c = w \cdot t. \tag{5}$$

The spacing between turns is given by:

$$s = \frac{d_{out} - d_{in} - 2 \cdot w \cdot n}{2 \cdot (n-1)}. \tag{6}$$

The width w is equal to

$$w = \frac{d_{out} - d_{in} - 2 \cdot s \cdot (n-1)}{2 \cdot n}. \tag{7}$$

And the total lengths l_t:

$$l_t = 4 \cdot n \cdot (d_{out} - s \cdot (n-1) - n \cdot w) - s. \tag{8}$$

In this study, a mathematical model was developed to understand the behavior of integrated micro-coil. The model combines Maxwell's equations for electrical and magnetic phenomena with a thermal conduction equation to determine the temperature profile in the coil conductors. Additionally, to take into account the effect of air on the thermal performance, a computational fluid dynamics approach was used. This approach considers the convective heat transfer and includes the Navier-Stokes equations for laminar flow that are strongly coupled with the convection-diffusion equation for air. The buoyancy term of the air is introduced in the Navier-Stokes momentum (11) in the direction along the vertical Z (Fig. 1,*a*). The resulting mathematical model is a strong coupling between the Maxwell's equations, the combined convection-conduction equation of the air, and the Navier-Stokes momentum equation.

Maxwell's equations are:

$$\boldsymbol{J} = \nabla \times \boldsymbol{H}; \quad \boldsymbol{B} = \nabla \times \boldsymbol{A}; \quad \boldsymbol{E} = -j\omega\boldsymbol{A};$$
$$\boldsymbol{J} = \sigma\boldsymbol{E} + j\omega\boldsymbol{D}; \quad \nabla \cdot \boldsymbol{J} = 0; \quad \boldsymbol{E} = -\nabla V - j\omega\boldsymbol{D}, \tag{9}$$

where $\boldsymbol{H}$ is the magnetic field intensity; $\boldsymbol{J}$ is the current density; $\boldsymbol{B}$ is the magnetic flux density; $\boldsymbol{A}$ is the magnetic vector potential; $\boldsymbol{E}$ is the electric field intensity; ω is the angular frequency; σ is the electrical conductivity; $\boldsymbol{D}$ is the electric displacement field; V is the electric potential.

Heat equation in the air and the solid parts:

$$k_s\nabla^2 T_s + \rho_0\boldsymbol{J} \otimes \boldsymbol{J} = 0 \quad \text{with } k_s = k_{Cu} \text{ or } k_s = k_{sub}, \tag{10}$$

where k_s is the thermal conductivity of the solid; k_{Cu} is the thermal conductivity of the copper; k_{sub} is the thermal conductivity of the substrate; T_s is the temperature in the solid; ρ_0 is the mass density of the solid.

Navier-Stokes equations in air part:

$$\rho_{air}(\boldsymbol{u} \cdot \nabla)\boldsymbol{u} = -\nabla \cdot (P\boldsymbol{I}) + (\nabla\boldsymbol{u} + (\nabla\boldsymbol{u})^T) +$$
$$+ A\rho_{air}\beta\boldsymbol{g}(T - T_c)\boldsymbol{e}, \tag{11}$$

where ρ_{air} is the mass density of the air; $\boldsymbol{u}$ is the velocity of the flow of the air; P is the pressure in the air; $\boldsymbol{I}$ is the identity matrix; A is the coefficient for the buoyancy term; β is the thermal expansion coefficient; $\boldsymbol{g}$ is the gravitational acceleration; T is the temperature of the air; T_c is the reference temperature; $\boldsymbol{e}$ is the unit vector in the direction of gravitational force.

Heat equation in the air parts:

$$\rho_{air}Cp_{air} \cdot \boldsymbol{u} \cdot \nabla T = k_{air}\nabla^2 T, \tag{12}$$

where Cp_{air} is the specific heat capacity of air at constant pressure; k_{air} is the thermal conductivity of air.

The coupling between the electromagnetic, thermal, and Navier-Stokes equations involves several steps: solving Maxwell's equations to obtain the electric field and current density, calculating heat generation in solid materials due to Joule heating, solving the heat equation in solid materials to determine temperature distribution, solving the Navier-Stokes equations to find airflow around the inductor, and solving the heat equation in the air to account for convective heat transfer, using the velocity field obtained from the Navier-Stokes equations.

3.2. Boundary conditions. The solving of the above system equations (9)–(12) requires the boundary conditions such as:

• For the copper conductor:
- On the input:

$$I = I_0 \quad \text{or} \quad \boldsymbol{J} = I_0 / S_{via}, \tag{13}$$

where I is the the electric current; I_0 is the input current at the boundary of the copper conductor; $\boldsymbol{J}$ is the current density; S_{via} is the cross-sectional area.

- On the output:

$$V = 0. \tag{14}$$

This boundary condition implies that the electric potential is zero at the output boundary.

• At the copper boundary:

$$n \cdot \boldsymbol{J} = 0, \quad -k_{Cu}\partial n T_s = h \cdot (T_c - T_s), \quad \text{and} \quad T = T_s, \tag{15}$$

where $n \cdot \boldsymbol{J}$ – this boundary condition implies that there is no normal component of the current density at the boundary, meaning there is no current flowing out of the surface perpendicular to the boundary; k_{Cu} is the thermal conductivity of the copper material; $\partial n T_s$ – this boundary condition implies that there is no normal component of

the current density at the boundary, meaning there is no current flowing out of the surface perpendicular to the boundary; h is the convective heat transfer coefficient; T_c is the temperature of the surrounding air; T_s is the temperature at the surface of the copper conductor; T is the general temperature variable.

• At the substrate boundary:

$$-k_{sub}\partial nT_s = h\cdot(T_c - T_s), \quad \partial nT = 0, \quad \text{and} \quad u = 0, \quad (16)$$

where k_{sub} is the thermal conductivity of the substrate material; u – this boundary condition suggests that the velocity of the air is zero at the substrate boundary, indicating a no-slip condition.

• At the study domain boundary:

$$\partial nT = 0, \quad \text{and} \quad P = 0, \quad (17)$$

where P is the pressure.

4. Numerical and computational methods. The system of governing differential equations (9)–(12), along with the set of boundary conditions (13)–(17), has been solved using the finite element method with Galerkin discretization. For the mesh, we have employed a tetrahedral structure with prisms at the boundary layer (coil and substrate). The multiple tests carried out to ensure result independence have led us to adopt a fine tetrahedral irregular mesh for the coil conductor. The complete mesh consists of 29,888 domain elements and 1,172 boundary elements (Fig. 3). The convergence criterion is set to a relative error of each variable, ensuring their values below 10^{-6}.
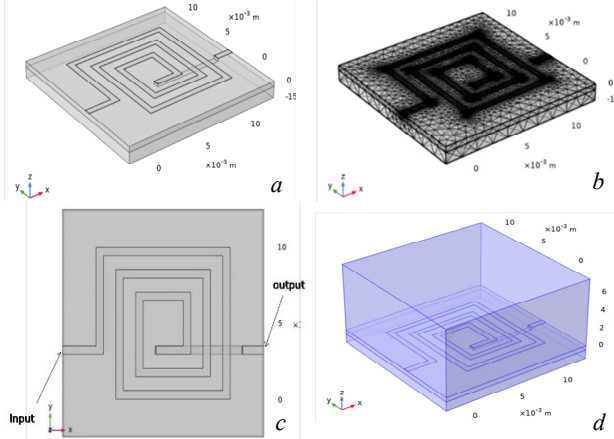

Fig. 3. The physical model (*a*), mesh of micro-coil (*b*), scheme for initial conditions (*c*) and limits of the studied area (*d*)

To ensure the accuracy and reliability of our numerical results, we conducted a comparison with the previous work [34]. We added their simulation conditions to examine the temperature distribution in the study area and along the vertical line passing through the substrate, as depicted in Fig. 4, 5. Upon comparing of our findings with the reference results [34], we observed the strong agreement and consistency, thereby validating of our mathematical model.

The simulation results obtained by solving the Maxwell's equations are applicable to all of the configurations studied. Therefore, in this study we will only focus on presenting the unique physical models and boundary conditions for each case. Figures 3,*a–d* depict the physical model of the square planar coil, the domain mesh, and the initial and boundary conditions, respectively.

4.1. Distribution of magnetic flux density. Figure 4 shows the 3D distribution of the magnetic flux density in planar coil for three materials of ferrite (Ni-Fe, Mn-Zn and Ni-Zn).
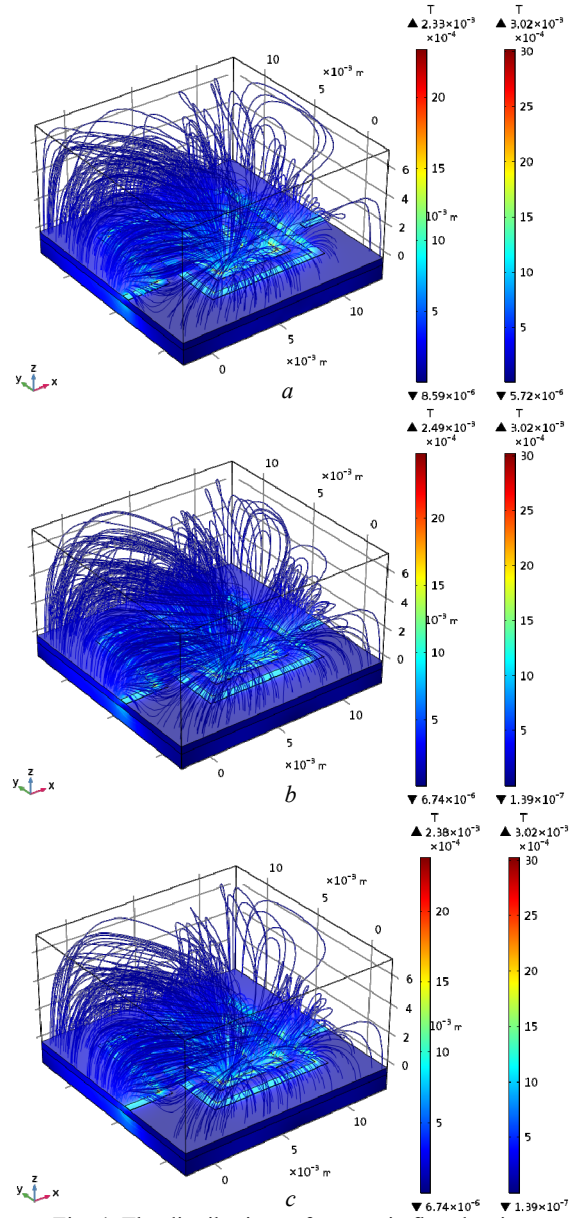

Fig. 4. The distributions of magnetic flux density for Ni-Fe (*a*), Mn-Zn (*b*) and Ni-Zn (*c*)

Figure 4 illustrates the magnetic flux density distribution along the median line ($x = y = 0$) for the micro-inductor made of materials Mi-Zn, Ni-Zn and Ni-Fe. The decreasing of the inner width of the micro-coil results in an increase in the flux value, it particularly evident in the region between 2 mm and 3 mm, corresponding to the line crossing the plane of the micro-coil. The similar magnetic behavior is observed in the neighboring zones with lower variance rates.

To further analyze the effect of changing the inner width of the micro-inductance on electromagnetic behavior, we have plotted curves that show casing variations in key parameters like maximum flux density, maximum field modulus, and maximum potential. The same figure illustrates the distribution of maximum magnetic flux density and maximum electric field for the inner width of the inductor ($w = 0.6$ mm). It reveals a evident increase in magnetic flux with decreasing w and predominant increase in the maximum electric field. The active zone of direct influence of the electric field is observed when the internal width is below 0.3 mm.

4.2. Temperature distribution. Regarding the temperature evolution in the study area, it is essential to plot the temperature distribution curves along the lines defined in the next diagrams. This is evident in Fig. 5, where we observe a rapid temperature increase in the kapton material along the median line ($x = y = 0$). The temperature is sharp until it reaching a peak at the micro-coil plane, exhibiting a perfect fit. This behavior can be attributed to the influence of the buoyancy force.
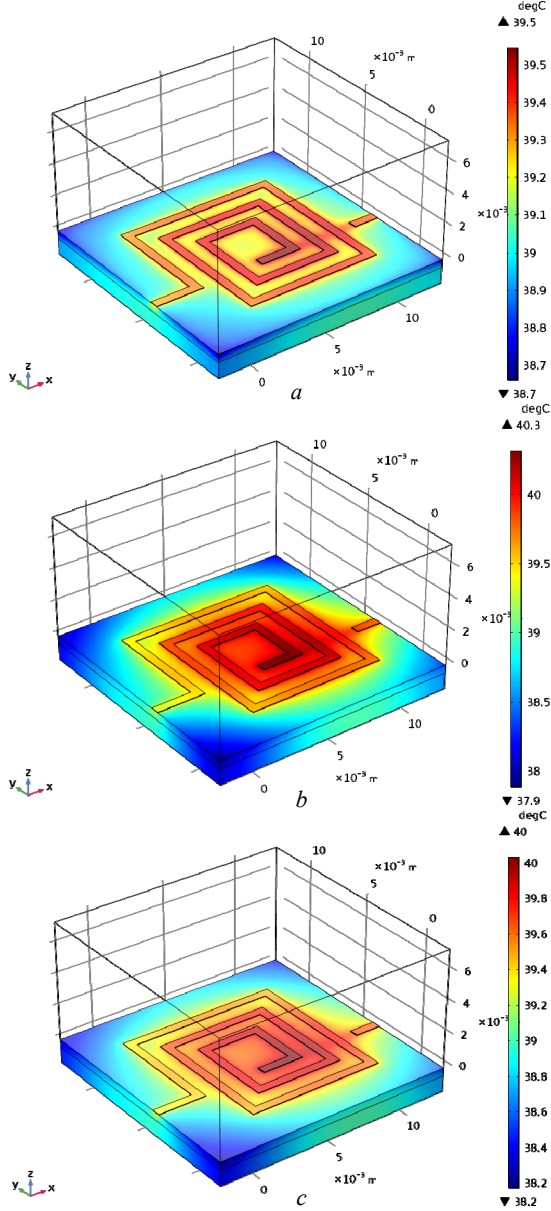

Fig. 5. The temperature distributions for
Ni-Fe (*a*), Mn-Zn (*b*) and Ni-Zn (*c*)

As we move upward, the temperature begins to decrease, and a slight difference between the two curves becomes evident, indicating the minor effect of the buoyancy force in this particular region. Along the lateral line shown in Fig. 5, a noticeable change in the thermal distribution shape occurs, particularly at the plane where the coil turns are placed. The thermal peak rises at non-availability of buoyancy, and then the curves start to diverge by 1 °C as they move upward, with natural convection resulting in the lowest temperatures. The temperature distribution on the horizontal line presented in Fig. 5 confirms the earlier observation regarding the narrowing of

the isothermal lines. We observe a reduction of the temperature values on both sides above the coil, where the maximum temperature value is directly recorded on the area of the inner diameter of the coil in both cases, with a higher value for this peak when considering the buoyancy force.

4.3. Comparison between three materials on the temperature and the flux magnetic distribution. The flux magnetic density and temperature distribution were compared for three different ferrite materials: Ni-Fe, Mn-Zn and Ni-Zn (Fig. 6, 7). In terms of magnetic flux density, it was observed that Mn-Zn exhibited the highest magnetic flux density, followed by Ni-Zn and Ni-Fe. The differences in magnetic flux density were attributed to the varying magnetic properties of the different ferrite materials.

a) the vertical line $x = L/2$, $y = L/2$

b) the horizontal line $y = L/2$, $z = 0$

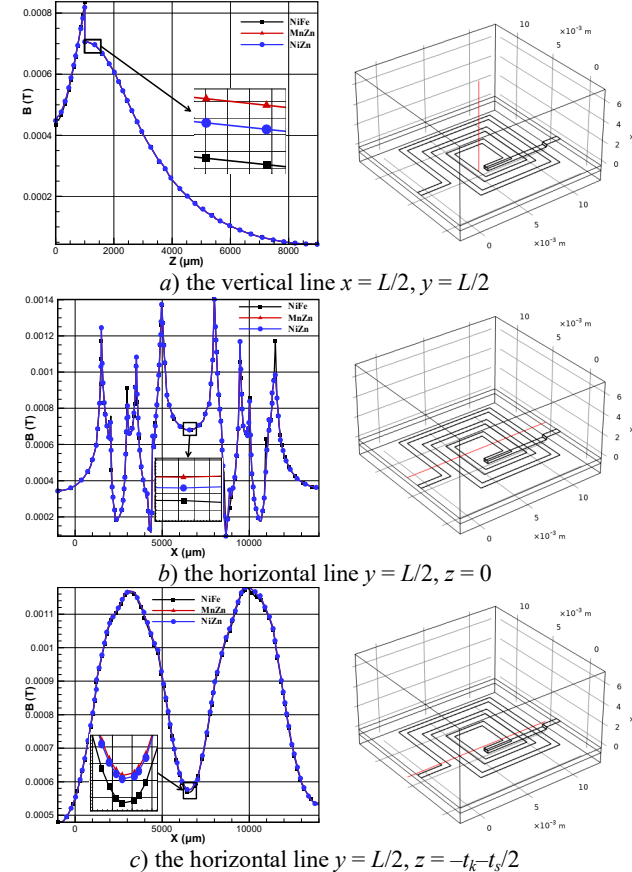*c*) the horizontal line $y = L/2$, $z = -t_k - t_s/2$

Fig. 6. The comparison between three ferrite materials
(Ni-Fe, Mn-Zn and Ni-Zn) on flux magnetic density

Regarding the temperature distribution, the results showed that Ni-Fe had the lowest temperature, indicating better thermal performance compared to the other two materials. Ni-Zn had a moderate temperature distribution, while Mn-Zn exhibited the highest temperature, indicating relatively poorer thermal behavior.

Summarizing the comparison between the three ferrite materials, Mn-Zn exhibited the highest magnetic flux density but also the highest temperature distribution, indicating potential trade-offs between magnetic performance and thermal behavior. Ni-Fe, on the other hand, showed the lowest temperature distribution, making a favorable choice for applications where thermal considerations are crucial. Ni-Zn is between the two materials, offering a balanced compromise between magnetic and thermal properties. The selection of the most suitable ferrite material would depend on the specific requirements of the application, considering factors such as magnetic performance, temperature sensitivity and overall efficiency.

a) the vertical line $x = L/2$, $y = L/2$

b) the horizontal line $y = L/2$, $z = 0$

c) the horizontal line $y = L/2$, z $= -t_k - t_s/2$

d) the horizontal line $y = L/2$, *z*= height air/2

e) the horizontal line $y = L/2$, z = height air
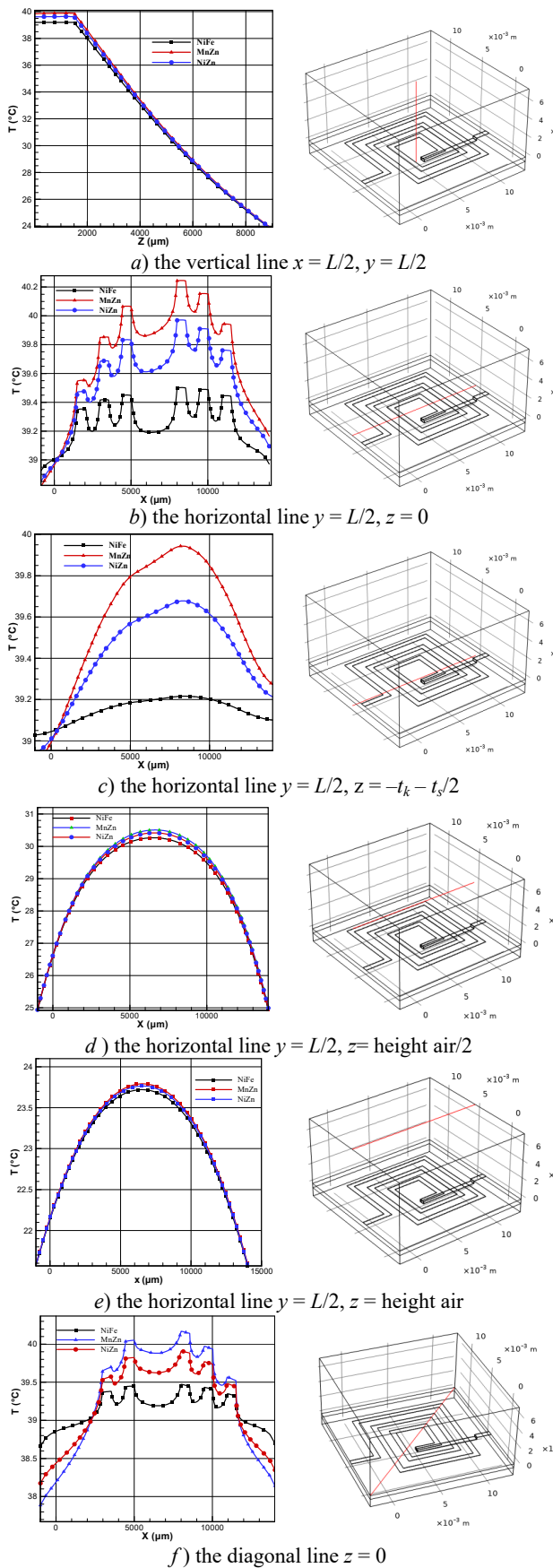

f) the diagonal line $z = 0$

Fig. 7. The comparison between three ferrite materials
(Ni-Fe, Mn-Zn and Ni-Zn) on the temperature distribution

5. Conclusions. After conducting an in-depth study on the magnetic and thermal properties of three ferrite materials (Ni-Fe, Mn-Zn, Ni-Zn) we have found valuable characteristics regarding their performance and behavior across diverse applications.

Firstly, Mn-Zn emerged as the preferential material in terms of magnetic flux density, showing the highest values among the three. This exceptional magnetic performance holds immense significance for applications like transformers and inductors, where upper magnetic properties are crucial for optimal efficiency and performance.

Secondly, our observations of the temperature distribution revealed significant distinctions among the materials. Ni-Fe exhibited the lowest temperature distribution; giving the exceptional thermal performance compared to the other two. Its ability to efficiently dissipate heat makes it as the best choice for applications where thermal considerations play a basic role, such as high-power integrated circuits, where temperature management is critical for reliability.

On the other hand, Ni-Zn displayed a moderate temperature distribution, striking a favorable balance between the magnetic performance of Mn-Zn and the thermal performance of Ni-Fe. This characteristic makes Ni-Zn a viable option for applications demanding a harmonious convergence of both magnetic and thermal properties.

Nonetheless, when selecting the most suitable ferrite material, the careful consideration of specific application requirements becomes essential. Factors like the required magnetic flux density, temperature sensitivity, thermal constraints and energy losses should be diligently evaluated to ensure optimal performance in the intended application.

As a conclusion, this comprehensive study facilitated an in-depth comparison of Ni-Fe, Mn-Zn and Ni-Zn ferrite materials, their different magnetic flux density and temperature distribution characteristics. Each material presents unique advantages and drawbacks, and the optimal choice relies on the precise demands of the application. Our research significantly contributes to advancing our understanding of ferrite material properties and proposes the potential to optimize the design of electronic and electromagnetic systems, enhancing overall efficiency and performance. Moving forward, future research can further explore the additional properties of ferrite materials and their specific impacts on applications, expanding the boundaries of technological innovation to achieve even more advanced solutions.

Conflict of interest. The authors declare that they have no conflicts of interest.

REFERENCES
1. Kharbouch H., Guettaf Y., Hamid A., Bley V., Benhadda Y. Design and Implementation of Inductors with Variable Conductor Width Integrated in a Boost Micro Converter. *Transactions on Electrical and Electronic Materials*, 2021, vol. 22, no. 4, pp. 519-530. doi: https://doi.org/10.1007/s42341-020-00261-5.
2. Guettaf Y., Flitti A., Bensaci A., Kharbouch H., Rizouga M., Hamid A. Simulation of the operation of a DC–DC converter containing an inductor of planar type. *Electrical Engineering*, 2018, vol. 100, no. 2, pp. 953-969. doi: https://doi.org/10.1007/s00202-017-0558-7.
3. Derkaoui M., Benhadda Y., Hamid A. Modeling and simulation of an integrated octagonal planar transformer for RF systems. *SN Applied Sciences*, 2020, vol. 2, no. 4, art. no. 656. doi: https://doi.org/10.1007/s42452-020-2376-1.
4. Namoune A., Taleb R., Mansour N., Benzidane M.R., Boukortt A. Integrated through-silicon-via-based inductor design in buck converter for improved efficiency. *Electrical Engineering & Electromechanics*, 2023, no. 6, pp. 54-57. doi: https://doi.org/10.20998/2074-272X.2023.6.09.
5. Xu D., Guan Y., Wang Y., Wang W. A review of high frequency resonant DC-DC power converters: Topologies and planar magnetic technologies. *Science China Technological Sciences*, 2020, vol. 63, no. 8, pp. 1335-1347. doi: https://doi.org/10.1007/s11431-020-1665-3.
6. Medjaoui F.Z., Hamid A., Guettaf Y., Spiteri P., Bley V. Conception and Manufacturing of a Planar Inductance on NiFe Substrate. *Transactions on Electrical and Electronic Materials*, 2019, vol. 20, no. 3, pp. 269-279. doi: https://doi.org/10.1007/s42341-019-00105-x.
7. Kim S.-G., Yun E.-J., Kim J.-Y., Kim J., Cho K.-I. Microfabrication and characteristics of double-rectangular spiral type thin-film inductors

with an upper NiFe magnetic core. *Journal of Applied Physics*, 2001, vol. 90, no. 7, pp. 3533-3538. doi: https://doi.org/10.1063/1.1399026.

8. Liu X., Wang T., Gao F., Khan M.M., Yang X., Rogers D.J. A Resonant Inductor Integrated-Transformer-Based Receiver for Wireless Power Transfer Systems. *IEEE Transactions on Industrial Electronics*, 2023, vol. 70, no. 4, pp. 3616-3626. doi: https://doi.org/10.1109/TIE.2022.3174286.

9. Meshkat A., Dehghani R., Farzanehfard H., Khajehoddin S.A. Improved On-Chip Inductor Design for Fully Integrated Voltage Regulators. *IEEE Journal of Emerging and Selected Topics in Power Electronics*, 2022, vol. 10, no. 6, pp. 7397-7409. doi: https://doi.org/10.1109/JESTPE.2022.3199692.

10. Shaltout A.H., Gregori S. Layout optimization of planar inductors for high-efficiency integrated power converters. *Analog Integrated Circuits and Signal Processing*, 2020, vol. 102, no. 1, pp. 155-167. doi: https://doi.org/10.1007/s10470-019-01494-y.

11. Shetty C., Smallwood D.C. Design, Modeling, and Analysis of a 3-D Spiral Inductor With Magnetic Thin-Films for PwrSoC/PwrSiP DC-DC Converters. *IEEE Access*, 2022, vol. 10, pp. 92105-92127. doi: https://doi.org/10.1109/ACCESS.2022.3200335.

12. Jiao D., Ni L., Zhu X., Zhe J., Zhao Z., Lyu Y., Liu Z. Measuring gaps using planar inductive sensors based on calculating mutual inductance. *Sensors and Actuators A: Physical*, 2019, vol. 295, pp. 59-69. doi: https://doi.org/10.1016/j.sna.2019.05.025.

13. Freitas W.J., Manera L.T., Swart J.W. Functional cyclic bending test for integrated inductors on flexible Kapton substrate. *Microelectronics Reliability*, 2022, vol. 135, art. no. 114592. doi: https://doi.org/10.1016/j.microrel.2022.114592.

14. Khan F., Younis M.I. Investigation of on-chip integrated inductors fabricated in SOI-MUMPs for RF MEMS ICs. *Analog Integrated Circuits and Signal Processing*, 2020, vol. 102, no. 3, pp. 585-591. doi: https://doi.org/10.1007/s10470-020-01627-8.

15. Anthony R., Wang N., Casey D.P., Mathuna O.C., Rohan J.F. MEMS based fabrication of high-frequency integrated inductors on Ni–Cu–Zn ferrite substrates. *Journal of Magnetism and Magnetic Materials*, 2016, vol. 406, pp. 89-94. doi: https://doi.org/10.1016/j.jmmm.2015.12.099.

16. Murali P., Alvarez C., Suresh S., Losego M.D., Swaminathan M., Oishi Y., Uemura T., Nagatsuka R., Watanabe N. Semi-additive patterning process based fabrication of miniaturized, package-embedded high conversion ratio inductors for DC-DC converters. *Power Electronic Devices and Components*, 2022, vol. 3, art. no. 100023. doi: https://doi.org/10.1016/j.pedc.2022.100023.

17. Shetty C. A detailed study of Q_{dc} of 3D micro air-core inductors for integrated power supplies: Power supply in package (PSiP) and power supply on chip (PSoC). *Power Electronic Devices and Components*, 2022, vol. 2, art. no. 100006. doi: https://doi.org/10.1016/j.pedc.2022.100006.

18. Liu S., Zhu L., Allibert F., Radu I., Zhu X., Lu Y. Physical Models of Planar Spiral Inductor Integrated on the High-Resistivity and Trap-Rich Silicon-on-Insulator Substrates. *IEEE Transactions on Electron Devices*, 2017, vol. 64, no. 7, pp. 2775-2781. doi: https://doi.org/10.1109/TED.2017.2700022.

19. Ouyang Z., Thomsen O.C., Andersen M.A.E. Optimal Design and Tradeoff Analysis of Planar Transformer in High-Power DC–DC Converters. *IEEE Transactions on Industrial Electronics*, 2012, vol. 59, no. 7, pp. 2800-2810. doi: https://doi.org/10.1109/TIE.2010.2046005.

20. Zhang W., Su Y., Mu M., Gilham D.J., Li Q., Lee F.C. High-Density Integration of High-Frequency High-Current Point-of-Load (POL) Modules With Planar Inductors. *IEEE Transactions on Power Electronics*, 2015, vol. 30, no. 3, pp. 1421-1431. doi: https://doi.org/10.1109/TPEL.2014.2320857.

21. Musunuri S., Chapman P.L., Zou J., Liu C. Design Issues for Monolithic DC–DC Converters. *IEEE Transactions on Power Electronics*, 2005, vol. 20, no. 3, pp. 639-649. doi: https://doi.org/10.1109/TPEL.2005.846527.

22. Hsiang H.-I. Progress in materials and processes of multilayer power inductors. *Journal of Materials Science: Materials in Electronics*, 2020, vol. 31, no. 19, pp. 16089-16110. doi: https://doi.org/10.1007/s10854-020-04188-8.

23. Ahmed B., Yacine G., Rabah D., Hamid M.-H.-A. Design and electromagnetic modeling of integrated LC filter in a buck converter. *Facta Universitatis - Series: Electronics and Energetics*, 2020, vol. 33, no. 2, pp. 289-302. doi: https://doi.org/10.2298/FUEE2002289A.

24. Pordanjani S.R., Mahseredjian J., Naïdjate M., Bracikowski N., Fratila M., Rezaei-Zare A. Electromagnetic modeling of inductors in EMT-type software by three circuit-based methods. *Electric Power Systems Research*, 2022, vol. 211, art. no. 108304. doi: https://doi.org/10.1016/j.epsr.2022.108304.

25. Sagar P., Gour A.S., Karunanithi R. A multilayer planar inductor based proximity sensor operating at 4.2 K. *Sensors and Actuators A: Physical*, 2017, vol. 264, pp. 151-156. doi: https://doi.org/10.1016/j.sna.2017.07.042.

26. Zhou G., Zhang W., He D., Li X., Wang S., Hong Y., Chen Y., Wang C., He W., Miao H., Zhou J. A novel structured spiral planar embedded inductor: Electroless-plating NiCoP alloy on copper coil as magnetic core. *Journal of Magnetism and Magnetic Materials*, 2019, vol. 489, art. no. 165363. doi: https://doi.org/10.1016/j.jmmm.2019.165363.

27. Bechir M.H., Yaya D.D., Kahlouche F., Soultan M., Youssouf K., Capraro S., Chatelon J.P., Rousseau J.J. Planar inductor equivalent circuit model taking into account magnetic permeability, loss tangent, skin and proximity effects versus frequency. *Analog Integrated Circuits and Signal Processing*, 2016, vol. 88, no. 1, pp. 105-113. doi: https://doi.org/10.1007/s10470-016-0697-1.

28. Benhadda Y., Hamid A., Lebey T. Thermal Modeling of an Integrated Circular Inductor. *Journal of Nano- and Electronic Physics*, 2017, vol. 9, no. 1, art. no. 01004. doi: https://doi.org/10.21272/jnep.9(1).01004.

29. Rizou M.E., Prodromakis T. Electrothermal deterioration factors in gold planar inductors designed for microscale bio-applications. *Microelectronic Engineering*, 2018, vol. 197, pp. 61-66. doi: https://doi.org/10.1016/j.mee.2018.05.006.

30. Vellvehi M., Jorda X., Godignon P., Ferrer C., Millan J. Coupled electro-thermal simulation of a DC/DC converter. *Microelectronics Reliability*, 2007, vol. 47, no. 12, pp. 2114-2121. doi: https://doi.org/10.1016/j.microrel.2006.10.009.

31. Sagar P., Hassan H.K., Lakshmi E.D.A., Akber K., Girish P.S., Gour A.S., Karunanithi R. Investigation on Temperature Dependent Inductance (TDI) of a planar Multi-Layer Inductor (MLI) down to 4.2 K. *Review of Scientific Instruments*, 2020, vol. 91, no. 8. doi: https://doi.org/10.1063/5.0008901.

32. Medjaoui F.Z., Mokhfi A., Guettaf Y., Spetiri P., Hamid A. Magnetothermal behavior of a planar coil. *Transactions on Electrical and Electronic Materials*, 2022, vol. 23, no. 2, pp. 171-181. doi: https://doi.org/10.1007/s42341-021-00337-w.

33. Derkaoui M., Benhadda Y., Hamid A., Temmar A. Design and Modeling of Octagonal Planar Inductor and Transformer in Monolithic Technology for RF Systems. *Journal of Electrical Engineering & Technology*, 2021, vol. 16, no. 3, pp. 1481-1493. doi: https://doi.org/10.1007/s42835-021-00692-x.

34. Fatna B., Mokhefi A., Hamid A., Yacine G., Fatima Zohra M., Spiteri P. Numerical investigation of the thermal convective phenomenon around a circular micro-coil with variable internal width. *Production Engineering*, 2023, vol. 17, no. 5, pp. 653-668. doi: https://doi.org/10.1007/s11740-023-01195-6.

35. Namoune A., Taleb R., Mansour N. Simulation of an integrated spiral inductor and inter-digital capacitor in a buck micro converter. *Automatika*, 2023, vol. 64, no. 2, pp. 268-276. doi: https://doi.org/10.1080/00051144.2022.2142572.

36. Gans S., Molnár J., Kováč D. Estimation of electrical resistivity of conductive materials of random shapes. *Electrical Engineering & Electromechanics*, 2023, no. 6, pp. 72-76. doi: https://doi.org/10.20998/2074-272X.2023.6.13.

37. Zablodskiy M.M., Pliuhin V.E., Kovalchuk S.I., Tietieriev V.O. Indirect field-oriented control of twin-screw electromechanical hydrolyzer. *Electrical Engineering & Electromechanics*, 2022, no. 1, pp. 3-11. doi: https://doi.org/10.20998/2074-272X.2022.1.01.

Mohammed Si Ahmed [1], *PhD Student,*
Yacine Guettaf [1], *Full Professor,*
Allel Mokaddem [1], *Full Professor,*
Abderrahim Mokhefi [2], *Full Professor,*
Azzedine Hamid [1], *Full Professor,*
Pierre Spiteri [3], *Full Professor,*
Fatima Zohra Medjaoui [4], *Associate Professor,*
[1] Centre Universitaire Nour Bachir El-Bayadh, Algeria,
e-mail: medsiahmed95@gmail.com (Corresponding Author)
[2] Ecole Nationale Polytechnique d'Oran, Algeria,
[3] Institut de Recherche en Informatique de Toulouse, France,
[4] Universite des Sciences et de la Technologie d'Oran Mohamed-Boudiaf, Algeria.

Передплатний індекс: 01216